

INFORMATION TO USERS

This manuscript has been reproduced from the microfilm master. UMI films the text directly from the original or copy submitted. Thus, some thesis and dissertation copies are in typewriter face, while others may be from any type of computer printer.

The quality of this reproduction is dependent upon the quality of the copy submitted. Broken or indistinct print, colored or poor quality illustrations and photographs, print bleedthrough, substandard margins, and improper alignment can adversely affect reproduction.

In the unlikely event that the author did not send UMI a complete manuscript and there are missing pages, these will be noted. Also, if unauthorized copyright material had to be removed, a note will indicate the deletion.

Oversize materials (e.g., maps, drawings, charts) are reproduced by sectioning the original, beginning at the upper left-hand corner and continuing from left to right in equal sections with small overlaps.

Photographs included in the original manuscript have been reproduced xerographically in this copy. Higher quality 6" x 9" black and white photographic prints are available for any photographs or illustrations appearing in this copy for an additional charge. Contact UMI directly to order.

**Bell & Howell Information and Learning
300 North Zeeb Road, Ann Arbor, MI 48106-1346 USA
800-521-0600**

UMI[®]

**COLLECTIVITY IN $A \sim 60$ NUCLEI:
SUPERDEFORMED AND SMOOTHLY TERMINATING
ROTATIONAL BANDS**

By

CARL EDWARD SVENSSON, B.Sc.

A Thesis

Submitted to the School of Graduate Studies

in Partial Fulfillment of the Requirements

for the Degree

Doctor of Philosophy

McMaster University

© Copyright by Carl Edward Svensson, November 1998

COLLECTIVITY IN $A \sim 60$ NUCLEI

DOCTOR OF PHILOSOPHY (1998)
(Physics)

McMaster University
Hamilton, Ontario

TITLE: Collectivity in $A \sim 60$ Nuclei:
 Superdeformed and Smoothly Terminating Rotational Bands

AUTHOR: Carl E. Svensson, B.Sc. (McMaster University)

SUPERVISOR: Professor J.C. Waddington

NUMBER OF PAGES: xv, 264

Abstract

The proton-rich nuclei in the $A \sim 60$ mass region provide an excellent laboratory for studying the interplay between single-particle and collective nuclear excitations. In order to increase the sensitivity of spectroscopic studies of these nuclei, a new method of channel selection based on the measurement of the total energy of all γ rays and charged particles emitted in fusion-evaporation reactions has been developed. This method has been used to identify and study deformed and superdeformed (SD) rotational bands in ^{62}Zn and the $N = Z$ nucleus ^{60}Zn .

Two sets of strongly coupled rotational bands have been identified in ^{62}Zn and have been observed up to the terminating states of their respective configurations. Lifetime measurements indicate that the transition quadrupole moments in these bands decrease as termination is approached. These results represent the first observation of the terminating states of rotational bands in the $A \sim 60$ mass region and confirm the predicted loss of collectivity associated with the phenomenon of smooth band termination. The first superdeformed rotational band in the $A \sim 60$ mass region has also been identified in ^{62}Zn , establishing a new region of superdeformation for nuclei with neutron and proton numbers $N, Z \approx 30$.

The doubly-magic superdeformed band in the $N = Z$ nucleus ^{60}Zn has been identified. This band corresponds to filling the single-particle orbitals up to the large SD shell gaps at $N, Z = 30$ and is the natural reference core for the study of $A \sim 60$ superdeformation. In addition, the observation of linking transitions connecting this band to normal deformed (ND) states provides the first spin, parity, and excitation energy measurements for $A \sim 60$ SD states. The stretched- $E2$ character and relatively large $B(E2)$ values of these linking transitions indicate that the decay-out mechanism in ^{60}Zn differs significantly from that observed in heavier nuclei.

Acknowledgements

Throughout my graduate studies I have benefited from the opportunity to interact with, and learn from, a large number of friends and colleagues. Although I will not attempt to mention all of them here, I would like to acknowledge the special contributions of several individuals.

First, I thank Joanne for her companionship throughout the past three years, for her careful reading of most of this manuscript and helpful suggestions regarding its presentation, and particularly for her constant support, encouragement, and patience, and for generally maintaining my sanity, during the writing of this thesis.

No graduate student could ask for a better supervisor than Dr. Jim Waddington. His contagious enthusiasm for research is outdone only by his passion for sharing his knowledge with others. It was many years ago that Jim taught me introductory electricity and magnetism as an undergraduate, and since then no other individual has had such a large impact on my development as a scientist. The excellence of Jim's supervision during my undergraduate thesis project led me to graduate studies in nuclear structure physics, and his direction and insight have formed the foundation upon which this work is built. It has truly been a pleasure being your student, Jim.

During my studies at McMaster I have had the opportunity to interact with many members of the nuclear structure group. Gracious thanks go to Dr. John Cameron and Dr. Stephane Flibotte for shedding light on many of the secrets of the nucleus, to Dr. Jonathan Wilson for all the lessons on computers and data analysis and for never turning down an evening of Guinness at the Phoenix, and to my fellow graduate and undergraduate students, Dean, John, Tim, Bryan, Guillaume, Roby, Tom, and Conrad, with whom I have shared both ideas and good times.

The experimental work presented in this thesis was conducted at several in-

ternational heavy-ion accelerator facilities and involved the participation of many people. I will not attempt to mention everyone here, but my special thanks go to the 8π guys, Gordon Ball, Alfredo Galindo-Uribarri, Victor Janzen, David Radford, and David Ward, for their time and guidance during my first experiments at the TASCC facility, to Cyrus Baktash for inviting the McMaster group to participate in the GS-90 experiment and for our successful $A \sim 60$ collaborations ever since, to Demetrios Sarantites and the Washington University group for perfect operation of the Microball during all our experiments, and to I.-Yang Lee, Augusto Macchiavelli, and Randy MacLeod at LBNL and Michael Carpenter and Robert Janssens at ANL for all their efforts above and beyond the call of duty to ensure smooth operation during our experiments with Gammasphere.

This work has benefited greatly from a close collaboration between experimentalists and theorists. My gracious thanks go to Anatoli Avanasjev and Ingemar Ragnarsson for the calculations that have provided much of the theoretical framework for interpreting the results presented in this thesis, and for taking the time to explain many of the subtler aspects of nuclear structure to me.

I gratefully acknowledge the Natural Sciences and Engineering Research Council of Canada (NSERC), both for personal support during my graduate studies through PGS A and PGS B scholarships, and for the grants of the nuclear structure group at McMaster, which have provided funding for this research.

Finally, I thank my parents, Eric and Patricia Svensson, for everything.

This thesis is dedicated to the memory of my faithful companion Chelsea, who never once declined a late-night walk to school to do some physics.

Contents

Abstract	iii
Acknowledgements	iv
1 Introduction	1
1.1 Nuclear Models	3
1.1.1 The Shell Model	4
1.1.2 The Collective Model	8
1.2 Population and Decay of High-Spin States	10
1.2.1 Heavy-Ion Fusion-Evaporation Reactions	10
1.2.2 The Yrast Line and γ -Decay	15
1.3 Superdeformation	18
1.3.1 Shell Effects and Deformation	18
1.3.2 SD Mass Regions	21
1.3.3 Population and Decay of Superdeformed Bands	24
1.4 The $A \sim 60$ Mass Region	27
2 Theoretical Background	30
2.1 Deformation, Rotation, and Angular Momenta	30
2.1.1 Deformation Parameters	31

2.1.2	Nuclear Rotation	35
2.1.3	Collective and Single-Particle Angular Momenta	37
2.2	The Deformed Mean Field	42
2.2.1	The Nilsson Model	42
2.2.2	The Deformed Woods-Saxon Potential	46
2.2.3	Strutinsky Shell Correction	48
2.2.4	Other Mean Field Methods	50
2.3	The Cranking Model	51
2.3.1	The Cranking Hamiltonian	51
2.3.2	Signature	53
2.3.3	Routhians	54
2.3.4	Shell Correction and Configurations	57
2.4	Pairing	61
2.4.1	The Pairing Interaction	62
2.4.2	Backbending	63
2.5	Band Termination	66
2.5.1	Smooth Termination	67
2.5.2	Shape Changes and Collectivity	69
3	Gamma-Ray Spectroscopy	70
3.1	Gamma-Ray Detection	70
3.1.1	Interactions of Gamma Rays with Matter	70
3.1.2	Gamma-Ray Detectors	72
3.1.3	Compton Suppression	74
3.1.4	Calibration	76
3.2	Detector Arrays	79

3.2.1	The 8π Spectrometer	79
3.2.2	Gammasphere	81
3.2.3	Efficiency, Resolution, and Sensitivity	83
3.3	Coincidence Spectroscopy	87
3.3.1	The $\gamma - \gamma$ Coincidence Matrix	87
3.3.2	Higher Folds	92
3.3.3	Spins and Parities	93
3.4	Lifetime Measurements	95
3.4.1	The Doppler Shift Attenuation Method	95
3.4.2	Stopping Powers	99
3.4.3	Side Feeding	101
4	Channel Selection	102
4.1	Gamma-Ray Multiplicity and Sum Energy	102
4.1.1	Entry Distributions	103
4.1.2	H and K Gating	105
4.1.3	The $A \sim 60$ Mass Region	107
4.2	Charged-Particle Detection	109
4.2.1	Detector Arrays	109
4.2.2	Charged-Particle Identification	112
4.2.3	Energy Calibration	115
4.2.4	Efficiency and Particle Gating	119
4.2.5	Kinematic Reconstruction	122
4.3	Total Energy Channel Selection	124
4.3.1	The Total Energy Method	124
4.3.2	Implementation: $8\pi + \text{Miniball}$	128

4.3.3	Implementation: Gammasphere + Microball	139
4.4	Other Channel Selection Methods	142
4.4.1	Neutron Detection	142
4.4.2	Recoil Detection	143
5	Smooth Band Termination in ^{62}Zn	145
5.1	Motivation	145
5.2	Experiments	147
5.3	Results: Rotational Bands in ^{62}Zn	150
5.4	Interpretation	155
5.5	Evidence for a Loss of Collectivity	159
5.6	Summary	169
6	Superdeformation in ^{62}Zn	170
6.1	Motivation	170
6.2	Results: A Superdeformed Band in ^{62}Zn	172
6.3	Interpretation	183
6.4	Summary	192
7	The Doubly-Magic Superdeformed Band in ^{60}Zn	193
7.1	Motivation	194
7.2	Experiments	196
7.3	Results: Superdeformation in ^{60}Zn	199
7.4	Interpretation	211
7.5	Decay Out of the ^{60}Zn SD Band	217
7.6	Summary	223

8 Conclusions and Future Prospects	224
8.1 Summary	224
8.2 Future Research	227
A Electromagnetic Transitions	231
B Symbols	236
Bibliography	241

List of Figures

1.1	Woods-Saxon potential	5
1.2	Shell model energy levels	6
1.3	Heavy-ion fusion-evaporation reaction	11
1.4	Angular momentum distribution in a compound nucleus	13
1.5	Yrast diagram	16
1.6	Deformed harmonic oscillator energy levels	20
1.7	Fission isomers and the second well	22
1.8	Yrast diagram for SD bands	24
1.9	Decay out of SD bands	26
1.10	The $A \sim 60$ mass region	28
2.1	$\beta - \gamma$ deformation plane	33
2.2	Angular momenta in rotating nuclei	38
2.3	Limiting coupling schemes of the particle-rotor model	40
2.4	Nilsson diagram for $N, Z \leq 50$	44
2.5	Single-particle energies in the deformed Woods-Saxon potential	47
2.6	Routhian diagram for ^{60}Zn	55
2.7	Identification of high- j Routhians	60
2.8	Backbending plots for ^{168}Hf	64
2.9	Characteristics of smooth band termination	68

3.1	Linear attenuation coefficients for Ge and BGO	71
3.2	8π HPGe detector and Compton suppression shield	74
3.3	Compton suppression	75
3.4	Gamma-ray energy calibration	77
3.5	Gamma-ray efficiency calibration	78
3.6	The 8π Spectrometer	80
3.7	Gammasphere	81
3.8	Consequences of removing the Hevimet collimators	82
3.9	Doppler broadening of γ -ray energy resolution	85
3.10	Coincidence matrix for low-spin transitions in ^{62}Zn	88
3.11	Gated spectra for low-spin transitions in ^{62}Zn	90
3.12	Coincidence matrix for a rotational band	91
3.13	Angular distributions for dipole and quadrupole transitions	94
3.14	Doppler shifts for ^{60}Cu band 1	96
3.15	Thin-target DSAM quadrupole moment measurements	98
4.1	Statistical model calculation of particle evaporation	104
4.2	Channel selection by H and K gating	106
4.3	Particle evaporation in the $A \sim 60$ mass region	108
4.4	The Microball inside Gammasphere	110
4.5	Schematic of the Microball	111
4.6	Particle identification: zero-crossing time versus energy	113
4.7	Particle identification: E_{slow} versus energy	114
4.8	Particle identification: energy ratio versus zero-crossing time	115
4.9	Proton energy calibration	116
4.10	Alpha-particle energy calibration	118

4.11	Channel selection by charged-particle gating	121
4.12	Kinematic reconstruction	123
4.13	“Theoretical” total energy plane	126
4.14	Total energy resolution, 8π + Miniball	129
4.15	$3p$ total energy plane	130
4.16	Gamma-ray gated $3p$ total energy planes	131
4.17	Total energy gated $3p$ γ -ray spectrum	132
4.18	Total energy gated $2p$ γ -ray spectrum	133
4.19	$2p$ total energy plane	134
4.20	Pure $2p$ γ -ray spectrum	135
4.21	Pure $3p$ and $3pn$ γ -ray spectra	138
4.22	Total energy resolution, Gammasphere + Microball	140
4.23	$4p$ total energy plane	141
5.1	Total γ -ray spectra for ^{62}Zn	149
5.2	Decay scheme of ^{62}Zn	151
5.3	Gamma-ray spectra of bands 1 and 2 in ^{62}Zn	152
5.4	Single-particle configurations in ^{62}Zn	156
5.5	Calculated shape trajectory for ^{62}Zn band 1	157
5.6	Calculated shape trajectory for ^{62}Zn band 2	158
5.7	Doppler-shift measurements for band 1 in ^{62}Zn	160
5.8	Doppler-shift measurements for band 2 in ^{62}Zn	161
5.9	Transition quadrupole moments for bands 1 and 2 in ^{62}Zn	163
5.10	$B(M1)$ values for bands 1 and 2 in ^{62}Zn	167
6.1	Gamma-ray spectrum of the ^{62}Zn SD band	174

6.2	A decay-out transition for the ^{62}Zn SD band	176
6.3	Entry excitation energy feeding the ^{62}Zn SD band	178
6.4	Fractional Doppler shifts for the SD band in ^{62}Zn	180
6.5	Systematics of $\mathcal{J}^{(2)}$ values for superdeformed bands	182
6.6	Potential energy surfaces for ^{62}Zn	184
6.7	Nilsson-Strutinsky calculations for SD bands in ^{62}Zn	185
6.8	Single-particle Routhians for ^{62}Zn	186
6.9	Hartree-Fock calculations for SD bands in ^{62}Zn	188
6.10	Relativistic mean field calculations for SD bands in ^{62}Zn	189
7.1	Selection of the ^{60}Zn channel	200
7.2	Gamma-ray spectrum of the ^{60}Zn SD band	201
7.3	Decay scheme of ^{60}Zn	202
7.4	Angular distributions for ^{60}Zn SD linking transitions	206
7.5	Fractional Doppler shifts for the ^{60}Zn SD band	209
7.6	Single-particle configurations in ^{60}Zn	212
7.7	Relativistic mean field calculations for the ^{60}Zn SD band	215

List of Tables

5.1	Gamma-ray energies and intensities in ^{62}Zn band 1	153
5.2	Gamma-ray energies and intensities in ^{62}Zn band 2	154
6.1	Gamma-ray energies and intensities in the ^{62}Zn SD band	175
7.1	Gamma-ray energies and intensities in ^{60}Zn	203
A.1	Weisskopf estimates of single-particle transition rates	233

Chapter 1

Introduction

The atomic nucleus provides an excellent laboratory for studying a many-body, yet finite, quantum system. The number of strongly interacting protons and neutrons in an intermediate mass nucleus consisting of a few tens to a few hundreds of nucleons is sufficiently large to build up the correlations necessary for collective excitations, yet is sufficiently small that single-particle effects remain important. The resulting interplay between collective and single-particle degrees of freedom leads to a variety of excitation modes and to rich patterns of nuclear behaviour as functions of particle numbers, excitation energy, and angular momentum.

Much of the intellectual challenge associated with the study of nuclear structure stems from the fact that the number of interacting particles is too large to permit “first principle” calculations based on the mutual interactions of all the particles, yet is too small to permit a statistical treatment. Models of the nucleus must therefore be developed which are capable of describing both macroscopic nuclear properties and single-particle effects, but which involve a sufficiently small number of parameters to yield meaningful insight into the physics of the nucleus. As ever more sensitive experimental measurements of nuclear properties are carried out, these models are refined and our understanding of the structure of the nucleus, and the quantum many-body

problem in general, deepens.

As a bound quantum system, the allowed states of the nucleus consist of a ground state and series of excited levels characterized by their excitation energy and quantum numbers such as parity π and total angular momentum I^\dagger (commonly called “spin”). Although the variety of experimental techniques that have been developed to study the nucleus is even more vast than the number of nuclear properties which can be measured, much of our understanding of nuclear structure has been attained through studies of the γ rays emitted when excited nuclear states decay to other nuclear levels by electromagnetic transitions. In this work, the techniques of γ -ray spectroscopy have been employed to study collectivity in proton-rich nuclei in the $A \sim 60$ mass region. In particular, high-spin states in ^{62}Zn and ^{60}Zn have been studied by their γ -ray decay following heavy-ion fusion-evaporation reactions.

This chapter provides a brief introduction to aspects of nuclear physics necessary to set the stage for the remainder of this thesis. In Chapter 2, a more detailed treatment of the nuclear structure theory relevant to this work is given. Chapter 3 describes the experimental apparatus and techniques of high-spin γ -ray spectroscopy. In Chapter 4, auxiliary detector systems and reaction channel selection are discussed and a new channel selection method which has been developed as part of this work is presented. The experimental results for smoothly terminating bands in ^{62}Zn , superdeformation in ^{62}Zn , and the doubly-magic superdeformed band in the $N = Z$ nucleus ^{60}Zn are presented and discussed in Chapters 5, 6, and 7, respectively. Conclusions drawn from this work and future prospects for nuclear structure studies in the $A \sim 60$ mass region are given in Chapter 8.

[†]See Appendix B for a complete list of symbols used in this thesis.

1.1 Nuclear Models

The natural starting point for a theory of nuclear eigenstates is a stationary Schrödinger equation of the form

$$H\Psi = E\Psi. \quad (1.1)$$

Noting that the nucleus is comprised of A interacting nucleons, it at first seems reasonable to write Ψ as a product of single-particle wavefunctions and, assuming that a two-body interaction $v(i, j)$ is sufficient to describe the interaction between nucleons i and j , express the nuclear Hamiltonian in the form

$$H = \sum_{i=1}^A -\frac{\hbar^2}{2m} \nabla_i^2 + \sum_{i<j} v(i, j). \quad (1.2)$$

The task of nuclear structure theory is then to solve the many-body Schrödinger equation 1.1 with the Hamiltonian 1.2.

Two notable difficulties with this approach to nuclear structure immediately become apparent. Firstly, unlike atomic physics where quantum electrodynamics provides the fundamental description of the interaction potential, no fundamental theory of the strong nucleon-nucleon interaction yet exists and $v(i, j)$ must be parametrized from empirical data. Secondly, even with modern computers the many-body Schrödinger equation is completely intractable for large A , and even if such calculations were possible the complex nuclear wavefunctions resulting from them would be unlikely to provide meaningful insight into the structure of the nucleus.

It therefore becomes necessary to develop simplified models which contain the essential physics of the nucleus, yet remain mathematically tractable. In the following sections, brief introductions are given to two such models of nuclear structure, the shell model and the collective model.

1.1.1 The Shell Model

The great simplifying assumption of the shell model is that individual nucleons move in an average one-body potential V which is produced by all of the other nucleons. The nuclear Hamiltonian 1.2 may then be decomposed into

$$H = H_0 + V_R, \quad (1.3)$$

with the shell model Hamiltonian

$$H_0 = \sum_{i=1}^A \left\{ -\frac{\hbar^2}{2m} \nabla_i^2 + V(i) \right\}, \quad (1.4)$$

and the one-body potential V chosen to minimize the residual interactions

$$V_R = \sum_{i < j} v(i, j) - \sum_{i=1}^A V(i). \quad (1.5)$$

Neglecting these residual interactions for the moment, one thereby replaces Eq. 1.1 with the much simpler equation

$$H_0 \Psi = \left\{ \sum_{i=1}^A h_i \right\} \Psi = \sum_{i=1}^A \left\{ -\frac{\hbar^2}{2m} \nabla_i^2 + V(i) \right\} \Psi = E \Psi. \quad (1.6)$$

The solutions Ψ to Eq. 1.6 are simply anti-symmetrized products of the eigenfunctions ϕ_n of the single-particle Schrödinger equation

$$h_i \phi_n(i) = \epsilon_n \phi_n(i). \quad (1.7)$$

In direct analogy with the filling of atomic shells by electrons, the nuclear eigenstates in this independent-particle shell model are simply obtained by filling the single-nucleon energy levels with the Z protons and N neutrons that make up the nucleus, remembering that protons and neutrons are fermions and obey the Pauli principle. In fact, it was the similarity between abrupt changes in atomic properties such as ionization energies at atomic shell closures, and abrupt changes in nuclear

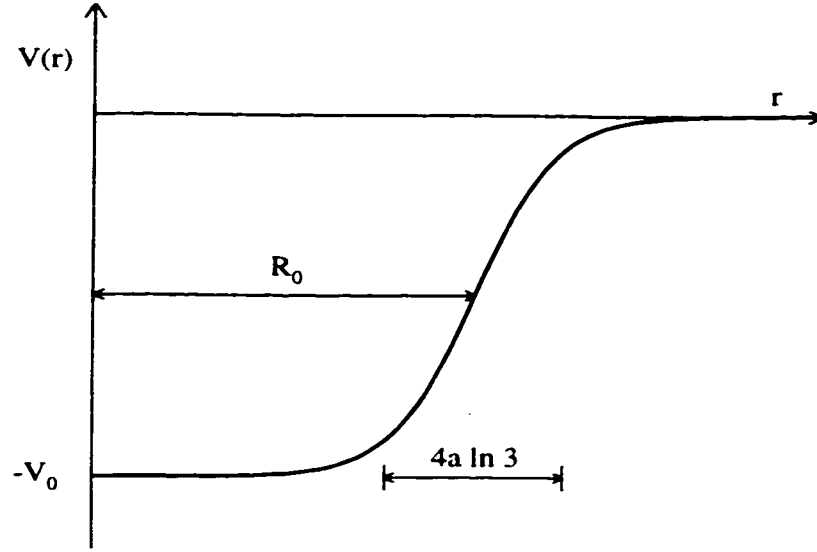


Figure 1.1: The Woods-Saxon potential showing the well depth V_0 , half-value radius R_0 , and “skin thickness” $4a \ln 3$.

properties such as nucleon separation energies at the magic nucleon numbers 2, 8, 20, 28, 50, 82, and 126 which provided much of the initial motivation and rational for the development of the nuclear shell model.

To proceed with the development of the shell model it is necessary to chose a form for the one-body potential V . As this potential is generated by the nucleons themselves, its radial dependence should be approximately that of the nucleon density. A commonly used form is the Woods-Saxon potential [WS 54] (Fig. 1.1)

$$V(r) = -V_0 \left[1 + \exp \left(\frac{r - R_0}{a} \right) \right]^{-1}, \quad (1.8)$$

where the well depth V_0 is of order 50 MeV, R_0 is the half-value radius which, because of the incompressibility of nuclear matter, is related to the mass number A by

$$R_0 = r_0 A^{1/3} \quad (1.9)$$

with $r_0 \approx 1.2$ fm, and the “skin thickness” over which the potential changes from $0.9 V_0$ to $0.1 V_0$ is given by $4a \ln 3$ with $a \approx 0.5$ fm.

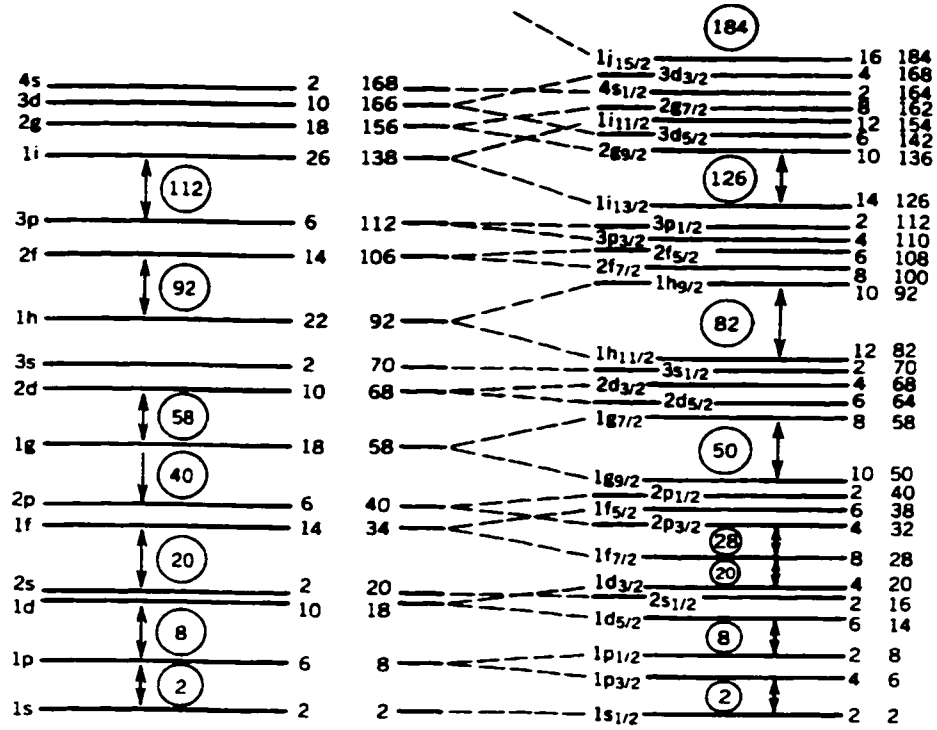


Figure 1.2: Energy levels of the Woods-Saxon potential without (left) and with (right) the spin-orbit interaction. The degeneracy of each level and the cumulative number of nucleons up to that level are shown to the right of each figure. Circled numbers indicate the cumulative capacity up to the major shell closures, i.e. the magic numbers. The labeling of the energy levels is discussed in the text. From [Kra 88].

As shown on the left side of Fig. 1.2, the shell gaps in the energy levels of this potential reproduce only the lowest three magic numbers, 2, 8, and 20. A major advance in the nuclear shell model occurred when it was realized [May 49, HJS 49] that a strong nuclear spin-orbit interaction splits the energy levels according to their total angular momentum j and, as shown on the right side of Fig. 1.2, exactly reproduces all of the magic numbers. The resulting energy levels of the spherical shell model, which remain $2j+1$ degenerate, are labeled by the quantum numbers l, j, π and n , where the orbital angular momentum l is represented by a letter (s, p, d, f, g, h, \dots for $l = 0, 1, 2, 3, 4, 5, \dots$), $j = l \pm \frac{1}{2}$ for nucleons which are spin- $\frac{1}{2}$ fermions, the parity

π is given by $(-1)^l$, and n simply counts the occurrences of a given l value. For example, the first $l = 3$ orbital with $j = l + \frac{1}{2} = \frac{7}{2}$ is labeled $1f_{7/2}$ and has negative parity. In cases where there is no ambiguity, the n value is often omitted.

A second simplifying assumption of the shell model is that the low-energy structure of the nucleus is dominated by a relatively small number of valence nucleons. Again drawing an analogy with closed atomic shells, completely filled nucleon shells form an “inert” core, and the detailed nuclear structure is determined primarily by the valence nucleons outside this core. Despite the simplicity of this model, it has enjoyed tremendous success, especially in describing the low-lying states of light nuclei. In cases such as ^{17}O and ^{41}Ca , with a single valence nucleon outside a doubly-magic spherical core, the assumptions of the extreme independent particle model are largely justified and the application of the shell model is both straightforward and particularly successful. With more than one valence nucleon, however, it must be remembered that distributing the nucleons over the energy levels of Fig. 1.2 corresponds to an eigenstate of the shell-model Hamiltonian 1.4, not the complete Hamiltonian 1.3. The residual interactions between the valence nucleons mix the pure shell-model states and must be taken into account in order to obtain an accurate description of the nuclear structure. In such multi-nucleon configurations, a shell model calculation typically proceeds by the following steps:

- (i) A model space consisting of an inert core and a limited set of orbitals over which the valence particles and holes may be distributed is chosen.
- (ii) The energies of the valence nucleon orbitals in the model space are determined, usually from the energies of levels in a nucleus with a single valence particle or hole outside the core. The level energies in the independent-particle approximation are then obtained by summing the energies of the occupied orbitals for

each possible configuration of the valence nucleons.

- (iii) A realistic form for the residual interaction between the valence nucleons (of which there are many variants) is chosen and for each value of I^π the Hamiltonian 1.3 is diagonalized using the independent particle states as a basis.

Using modern computers to diagonalize the very large matrices which can result in step (iii) above, large-scale spherical shell model calculations can now be performed for nuclei up to the $A \sim 50$ mass region. Taking ^{40}Ca as the doubly-magic core and including the full pf -shell (the $1f_{7/2}$, $1f_{5/2}$, $2p_{3/2}$, and $2p_{1/2}$ orbitals) in the valence space, such shell model calculations have been very successful in describing the structure of nuclei like the $A = 48$ [Cau 94] and $A = 47$ and 49 [Mar 97] isobars.

1.1.2 The Collective Model

Although the shell model is often considered the “fundamental” microscopic model of nuclear structure and is, in principle, applicable to all nuclei, in practice this approach rapidly becomes limited by computational power. As one considers heavier nuclei, the number of orbitals between major shell gaps increases, the number of valence nucleons outside of a doubly-magic core can become large, and the number of levels of a given I^π in the model space can rapidly become enormous. To quote an example given by Casten [Cas 90], approximately 3×10^{14} states with $I^\pi = 2^+$ can be constructed in $^{154}_{62}\text{Sm}_{92}$ with 12 valence protons in the $Z = 50$ –82 shell and 10 valence neutrons in the $N = 82$ –126 shell. In such cases one cannot even conceive of calculating all the matrix elements of the Hamiltonian 1.3, let alone diagonalize such a matrix. For nuclei heavier than about $A \sim 50$ with more than a few valence nucleons outside a doubly-magic core, a different approach to nuclear structure becomes essential.

In describing the structure of heavy and medium-mass nuclei, one simplify-

ing assumption which has enjoyed tremendous success is that the nucleus undergoes collective excitations in which all, or at least a substantial fraction, of the nucleons participate coherently. This model, developed in detail by Bohr and Mottelson [BM 75], treats the nucleus as a quantum liquid drop which can become deformed and which can undergo collective excitations such as vibrations and, if deformed, rotations about an axis perpendicular to the nuclear symmetry axis[†]. Although such a macroscopic model of nuclear structure at first seems completely removed from the microscopic approach discussed in the previous section, it has, at least in some cases, been possible to provide a microscopic justification for the collective model through approaches such as the random phase approximation (RPA) [Zaw 78] and interacting boson approximation (IBA) [Ari 77]. Thus, although treating the nucleus as a (possibly) deformed liquid drop subject to macroscopic excitations such as rotations and vibrations is a phenomenological model, this microscopic justification, combined with the success of this model in describing and predicting the behaviour of many nuclei, leaves little doubt that it embodies much of the essential physics of the nucleus.

It should also be noted that the collective and shell models are by no means mutually exclusive. Perhaps the most successful and broadly applicable approach to nuclear structure results from a combination of these complementary models in a microscopic-macroscopic treatment where the bulk properties and excitations of the nucleus are described in the collective model and the detailed nuclear structure is determined by valence nucleons in a deformed shell model. A more detailed description of this approach, which forms the theoretical basis for the interpretation of the experimental results presented in this thesis, is given in Chapter 2.

[†]The nuclear wavefunction is invariant under rotations about a symmetry axis. Quantum mechanically, there is no means to tell whether such a rotation occurs and collective rotations about symmetry axes are therefore forbidden. Although spherical nuclei can undergo collective vibrations, collective rotation of a spherical nucleus is not possible.

1.2 Population and Decay of High-Spin States

This thesis focuses on the study of nuclear states at high angular momentum, commonly referred to as “high-spin” states. In order to study the structure of such states experimentally it is, of course, necessary to impart a large angular momentum to the nucleus. The following sections introduce the experimental method of populating high-spin states employed in this work, namely heavy-ion fusion-evaporation reactions, as well as some of the basic ideas and terminology relevant to high-spin nuclear structure studies.

1.2.1 Heavy-Ion Fusion-Evaporation Reactions

Although several methods of populating high-spin states are available to the experimentalist (e.g. Coulomb excitation, transfer reactions, etc.), the most commonly used technique, and the method employed in this work, is the heavy-ion fusion-evaporation reaction. A schematic diagram depicting the main sequence of events in such a reaction is shown in Fig. 1.3. A beam of accelerated heavy ions is directed onto a target and a small fraction of the projectile nuclei pass close enough to a nucleus of the target material to undergo fusion reactions. The target and projectile nuclei are, of course, both positively charged and thus repel each other by the Coulomb interaction. However, if the energy of the projectile is sufficient to overcome this Coulomb repulsion and the nuclei approach within a distance R_{int} , their mutual strong nuclear attraction can lead to fusion and the formation of a compound nucleus, as illustrated in the upper panels of Fig. 1.3.

In typical fusion-evaporation reactions above the Coulomb barrier, the center-of-mass bombarding energy E_{CM} is sufficiently high that the de Broglie wavelength

$$\lambda = \frac{\hbar}{\sqrt{2\mu E_{CM}}} \quad (1.10)$$

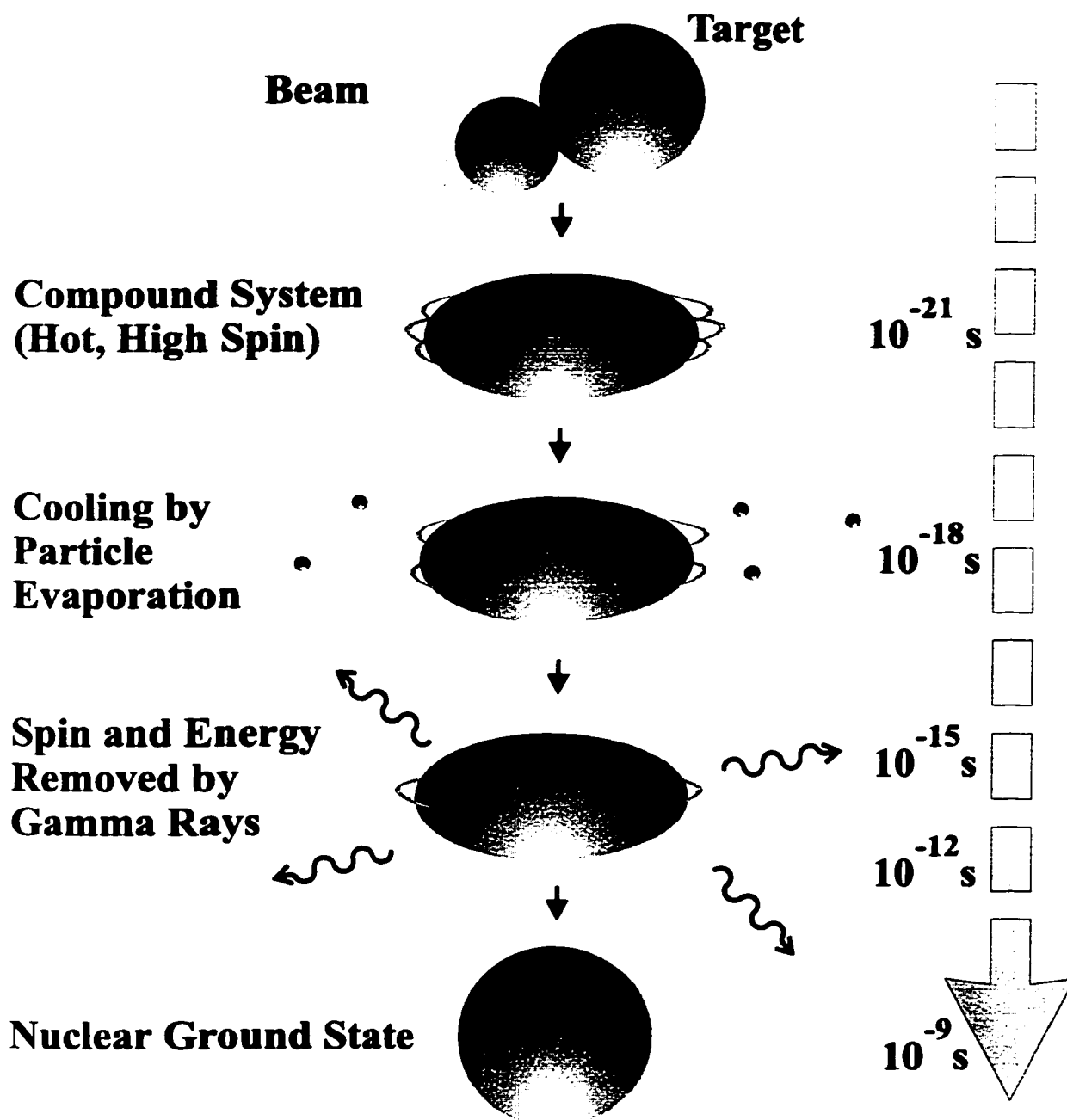


Figure 1.3: Schematic illustration of the main sequence of events in a heavy-ion fusion-evaporation reaction. An accelerated projectile nucleus and a target nucleus fuse to form a hot and (possibly) rapidly rotating compound system. The compound system first cools by evaporating particles (protons, neutrons, and alpha particles). The remaining angular momentum and excitation energy of the final nucleus is then removed by a cascade of γ -ray transitions until the nuclear ground state is reached. Approximate time scales for the various steps are shown at right.

where μ is the reduced mass, is small compared to the dimensions of the nuclei themselves. It is thus reasonable to estimate R_{int} as the sum of the target and projectile nuclear radii (given by Eq. 1.9) plus a small correction to account for the diffuse nature of the nuclear surfaces and the finite range of the strong nuclear force [Bas 80],

$$R_{int} = R_1 + R_2 + 2 \text{ fm.} \quad (1.11)$$

The bombarding energy (in the center of mass frame) needed to overcome the Coulomb barrier is then

$$E_{CB} = 1.44 \frac{Z_1 Z_2}{R_{int}} \text{ MeV.} \quad (1.12)$$

Although subbarrier fusion reactions at energies below E_{CB} are made possible by quantum-mechanical tunneling through the Coulomb barrier, all of the reactions employed in this work were conducted at energies well above E_{CB} .

The excitation energy E^* of a compound nucleus formed in a fusion reaction is fixed at

$$E^* = E_{CM} + Q \quad (1.13)$$

by the center of mass bombarding energy E_{CM} and the Q -value for the reaction. There is, however, a distribution of compound nuclear angular momenta given by the partial wave cross section [Szy83]

$$\sigma(l) = \pi \lambda^2 (2l + 1) T_l, \quad (1.14)$$

where T_l is the transmission coefficient for angular momentum l .

In the “sharp cut-off” approximation the T_l are assumed to be unity up to a maximum angular momentum l_{max} which corresponds to a grazing collision of the target and projectile nuclei, and are taken as zero for angular momenta above l_{max} .

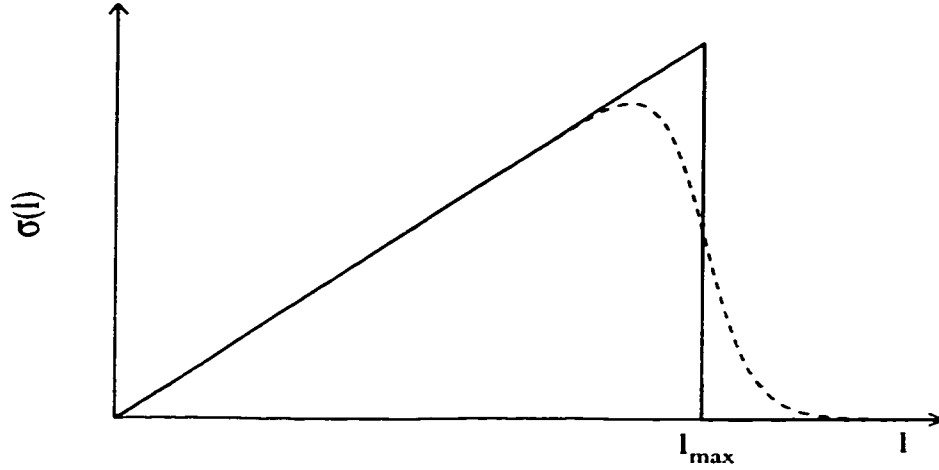


Figure 1.4: Schematic diagram of the angular momentum distribution for a compound nucleus formed in a heavy-ion fusion reaction. The “sharp cut-off” approximation is shown by the solid line, and deviations from this model due to nuclear surface diffuseness and quantum-mechanical barrier penetration are indicated by the dashed line. After [Bas 80].

The value of l_{max} is estimated as [DS 80]

$$l_{max} = 0.219 R_{int} \sqrt{\mu(E_{CM} - E_{CB})}, \quad (1.15)$$

where R_{int} is in fm, μ is in atomic mass units, and E_{CM} and E_{CB} are in MeV.

The cross section as a function of l then takes the triangular form shown by the solid line in Fig. 1.4. As indicated by the dashed line in Fig. 1.4, the nuclear surface diffuseness and a full treatment of the quantum-mechanical barrier penetration have the effect of smoothing $\sigma(l)$ close to l_{max} . Nonetheless, the important point that the largest cross sections occur for angular momenta close to l_{max} remains valid.

Summing the $\sigma(l)$ (Eq. 1.14) from zero to l_{max} with $T_l = 1$, one obtains the total reaction cross section

$$\sigma_R = \pi \lambda^2 (l_{max} + 1)^2. \quad (1.16)$$

Although the actual dynamics of heavy-ion fusion reactions are considerably more complicated than implied by the simplified discussion presented here, the above

equations do provide reasonable approximations to the magnitudes of parameters relevant in these reactions. As an example, consider a 125-MeV ^{28}Si beam directed onto a target of ^{40}Ca . The center of mass bombarding energy of 73.5 MeV in this reaction is well above the 41.8 MeV Coulomb barrier at $R_{int} = 9.65$ fm. The Q -value is -2.2 MeV, so that the compound nucleus ^{68}Se is formed at an excitation energy of 71.3 MeV. From Eqs. 1.15 and 1.16 we estimate $l_{max} = 48\hbar$ and a reaction cross section of 1.3 b^\dagger . It is thus clear that such heavy-ion fusion reactions provide an effective means of producing compound nuclear systems with large amounts of both excitation energy and angular momentum.

Following a heavy-ion fusion reaction, the most likely decay modes of the compound system are fission and particle evaporation. The latter, which is illustrated in Fig. 1.3, typically occurs with partial lifetimes on the order of 10^{-17} to 10^{-18} seconds, while the fission lifetime depends sensitively on the height of the potential energy barrier which must be tunneled through in order for fission to occur [DS 80]. This fission barrier decreases with angular momentum, producing an effective upper limit on the compound nucleus angular momenta which lead to particle evaporation. The importance of this fission cut-off depends on the mass region being studied. For heavy nuclei, the fissility parameter Z^2/A becomes large and, although very large values of l_{max} (in excess of $100\hbar$) are possible in heavy-ion fusion reactions producing these nuclei, the highest angular momenta are immediately lost to fission. For the relatively light nuclei ($A \sim 60$, $Z \sim 30$) studied in this thesis, however, the fission cut-off is roughly equal to the l_{max} of the reactions employed and the majority of the compound nuclei thus decay by particle evaporation.

The evaporation of particles (protons, neutrons, and alpha particles) from a

[†]A "barn" b is defined as 10^{-28} m^2 and is a convenient unit for describing nuclear cross sections and quadrupole moments.

hot compound system formed in a heavy-ion fusion reaction is a complex statistical process governed by level densities, particle binding energies, Coulomb and centrifugal barriers, etc., and a large number of different final nuclei (or “evaporation residues”) may be produced in a given reaction depending on the number and type of evaporated particles. A more detailed discussion of the characteristics of particle evaporation relevant to the proton-rich $A \sim 60$ mass region will be given in Chapter 4. Here it is simply noted that each evaporated particle removes both its kinetic energy and its binding energy from the nucleus, thereby rapidly cooling the hot compound system. At the same time, the evaporated particles remove angular momentum from the nucleus. This angular momentum is generally quite small ($\sim 1\text{--}2\hbar$) for protons and neutrons, but may be substantial ($\sim 5\text{--}10\hbar$) for alpha particles.

1.2.2 The Yrast Line and γ -Decay

The state of lowest excitation energy E^* for a given angular momentum I in a particular nucleus is referred to as the yrast[†] state at that spin, and the line in (E^*, I) space connecting these states is referred to as the yrast line. At high-spin the yrast line is expected [BM 75] to be approximately that of a rigid rotor with E^* proportional to $I(I + 1)$. Below this line there are no states available to the nucleus.

As noted in the previous section, particle evaporation from the hot compound system removes large amounts of excitation energy but a limited amount of angular momentum. In the yrast diagram of E^* versus I (Fig. 1.5) evaporated particles are thus represented by nearly vertical arrows. This evaporation continues until the nuclear excitation energy is within approximately one particle binding energy ($\sim 8\text{ MeV}$) of the yrast line. Emission of an additional particle is then no longer possible because

[†]Alternatively such a level may be described as the state of highest angular momentum at a given energy, hence the name “yrast”, which means “dizziest” in Swedish.

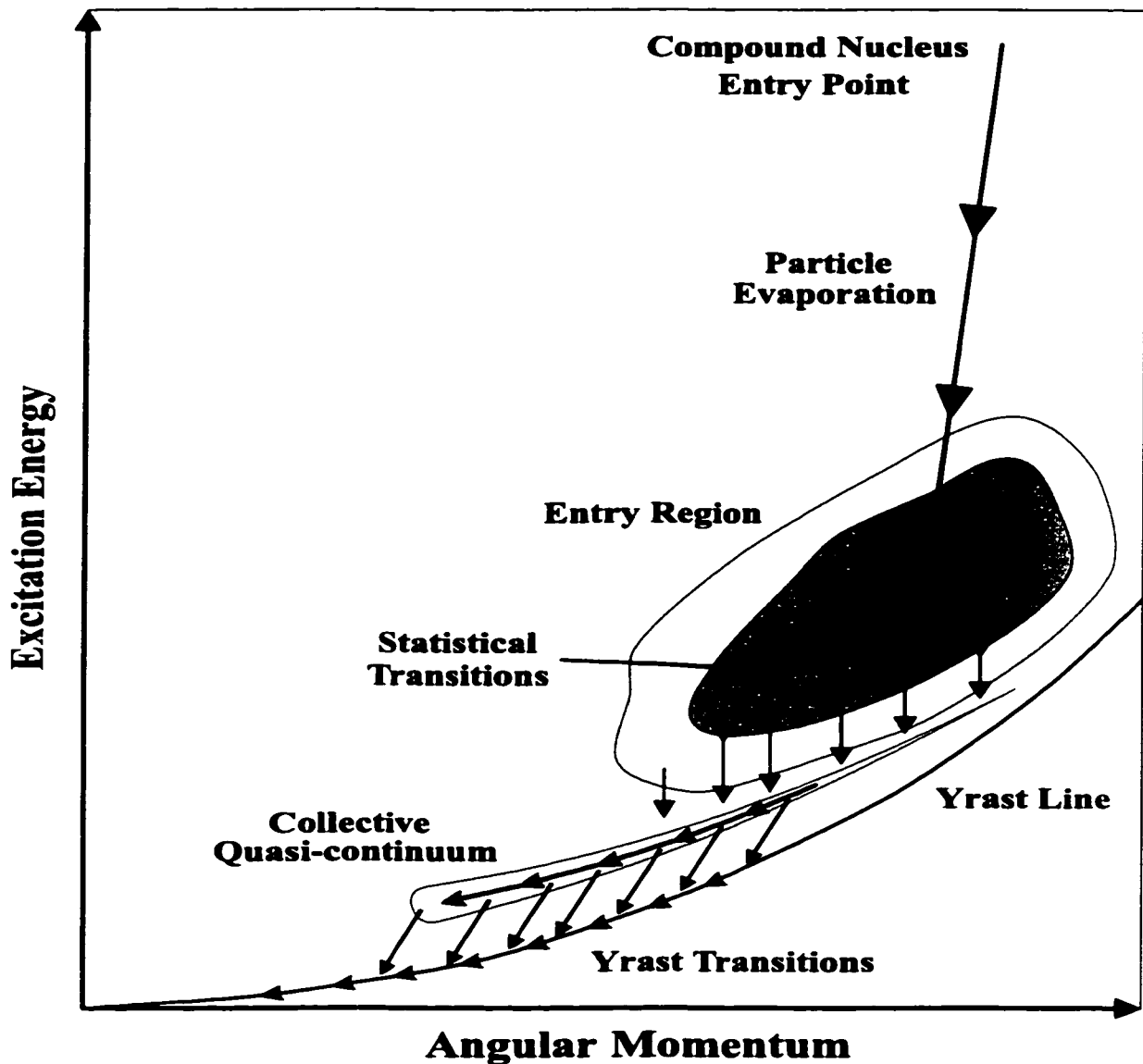


Figure 1.5: Schematic illustration of particle and γ -ray decay following a heavy-ion fusion reaction in a plot of excitation energy E^* versus angular momentum I (an "yrast" diagram). A compound nucleus entry point in (E, I) space leads to an entry region in the final nucleus depending on the energies and angular momenta of the evaporated particles. Statistical γ -ray transitions, which remove energy but little angular momentum from the nucleus, are shown by vertical arrows. Collective quasi-continuum transitions run parallel to and above the yrast line. The yrast and near-yrast transitions have a high probability of occurring each time a particular final nucleus is populated and can thus be observed as discrete peaks in the γ -ray spectrum. Adapted from [Wil 94].

it would lead to a non-existent state below the yrast line of the daughter nucleus. The remaining excitation energy and angular momentum in the final nucleus are then removed by a cascade of γ -ray transitions.

The γ -ray transitions which follow particle evaporation can be roughly divided into three categories (shown schematically in Fig. 1.5). As noted above, the entry region in the final nucleus extends ~ 8 MeV above the yrast line. At these high excitation energies, both the density of nuclear levels and the energy available for γ -ray transitions are large, and statistical dipole transitions which remove energy but little angular momentum are favoured[†]. The number of possible pathways for the γ -decay in this region is extremely large and these statistical transitions thus form a continuum in the γ -ray spectrum. As the excitation energy is reduced to within a few MeV of the yrast line, the level density decreases and collective transitions in rotational bands begin to compete with the statistical transitions. Transitions in these rotational cascades result in energy and angular momentum losses such that the γ decay in the yrast diagram follows a path parallel to the yrast line, as shown in Fig. 1.5. In this region the level density is, however, still large enough that the probability of populating a particular rotational structure is small. These collective transitions thus form a quasi-continuum of correlated, yet unresolved, γ rays. Eventually the majority of the γ -ray flux is collected by transitions close to the yrast line. The probability that such yrast and near-yrast transitions occur in each event that populates a particular final nucleus becomes substantial and these transitions thus appear as discrete peaks in the γ -ray spectrum. It is primarily through analysis of such discrete yrast and near-yrast transitions that the nuclear structure studies presented in this thesis have been accomplished.

[†]See Appendix A for a formal discussion of electromagnetic transition rates in nuclei.

1.3 Superdeformation

A substantial fraction of this thesis deals with the study of superdeformed rotational bands, in which the nucleus takes on an ellipsoidal shape approximately twice as long as it is wide. The following sections provide a brief introduction to, and history of, the study of superdeformed nuclei.

1.3.1 Shell Effects and Deformation

If the nucleus is considered as a liquid drop consisting of A mutually attracting nucleons, the surface energy is minimized, and hence the lowest energy state of the nucleus is attained, for a spherical shape. It may thus seem surprising at first that many nuclei take on shapes which deviate substantially from spherical symmetry. The stability of such deformed shapes results from the limited number of particles in the nucleus and the importance of shell effects which modify the liquid-drop energy and can lead to potential energy minima at finite deformations.

A detailed discussion of single-particle states in deformed nuclei will be given in Chapter 2. A simple and intuitive, if somewhat unrealistic, impression of the importance of shell effects on deformation and of the particular stability of superdeformed shapes can, however, be obtained by considering the nucleons to be confined in a harmonic oscillator potential

$$V(x, y, z) = \frac{1}{2}m \left(\omega_x^2 x^2 + \omega_y^2 y^2 + \omega_z^2 z^2 \right), \quad (1.17)$$

where m is the nucleon mass and the frequencies $\omega_x, \omega_y, \omega_z$ are inversely proportional to the half axes a_x, a_y, a_z of a nucleus with an ellipsoidal shape:

$$\omega_\nu = \omega_0 \frac{R_0}{a_\nu}, \quad (\nu = x, y, z). \quad (1.18)$$

The energy eigenvalues of this potential (with $n_x, n_y, n_z = 0, 1, 2, \dots$) are given by

$$E(n_x, n_y, n_z) = \hbar\omega_x \left(n_x + \frac{1}{2}\right) + \hbar\omega_y \left(n_y + \frac{1}{2}\right) + \hbar\omega_z \left(n_z + \frac{1}{2}\right). \quad (1.19)$$

In the case of a spherically symmetric potential ($\omega_x = \omega_y = \omega_z = \omega_0$), Eq. 1.19 reduces to the familiar result for the three dimensional isotropic harmonic oscillator

$$E(N) = \hbar\omega_0 \left(N + \frac{3}{2}\right), \quad (1.20)$$

where the principle oscillator quantum number $N = n_x + n_y + n_z$ and the degeneracy of the energy levels (including the 2-fold spin degeneracy for spin- $\frac{1}{2}$ fermions) is given by $(N + 1)(N + 2)$. Deformation, however, partially breaks the degeneracy of the spherically symmetric potential. In the case of an axially symmetric shape ($\omega_x = \omega_y = \omega_\perp$), we may introduce the deformation parameter ε through

$$\omega_\perp = \omega_0(\varepsilon) \left(1 + \frac{1}{3}\varepsilon\right), \quad \omega_z = \omega_0(\varepsilon) \left(1 - \frac{2}{3}\varepsilon\right), \quad (1.21)$$

where the condition for the conservation of nuclear volume

$$\omega_x\omega_y\omega_z = \text{constant}. \quad (1.22)$$

requires a slight renormalization of ω_0 with deformation

$$\omega_0(\varepsilon) = \omega_0(0) \left(1 - \frac{1}{3}\varepsilon^2 - \frac{2}{27}\varepsilon^3\right)^{-1/3}. \quad (1.23)$$

The energy eigenvalues (Eq. 1.19) may then be expressed in the form

$$E(N, n_z, \varepsilon) = \hbar\omega_0(\varepsilon) \left[\left(N + \frac{3}{2}\right) + \varepsilon \left(\frac{N}{3} - n_z\right) \right]. \quad (1.24)$$

The energy levels of Eq. 1.24 are shown as a function of the deformation parameter ε in Fig. 1.6, where positive ε values correspond to prolate shapes with two short axes and one long axis, and negative ε values correspond to oblate shapes with

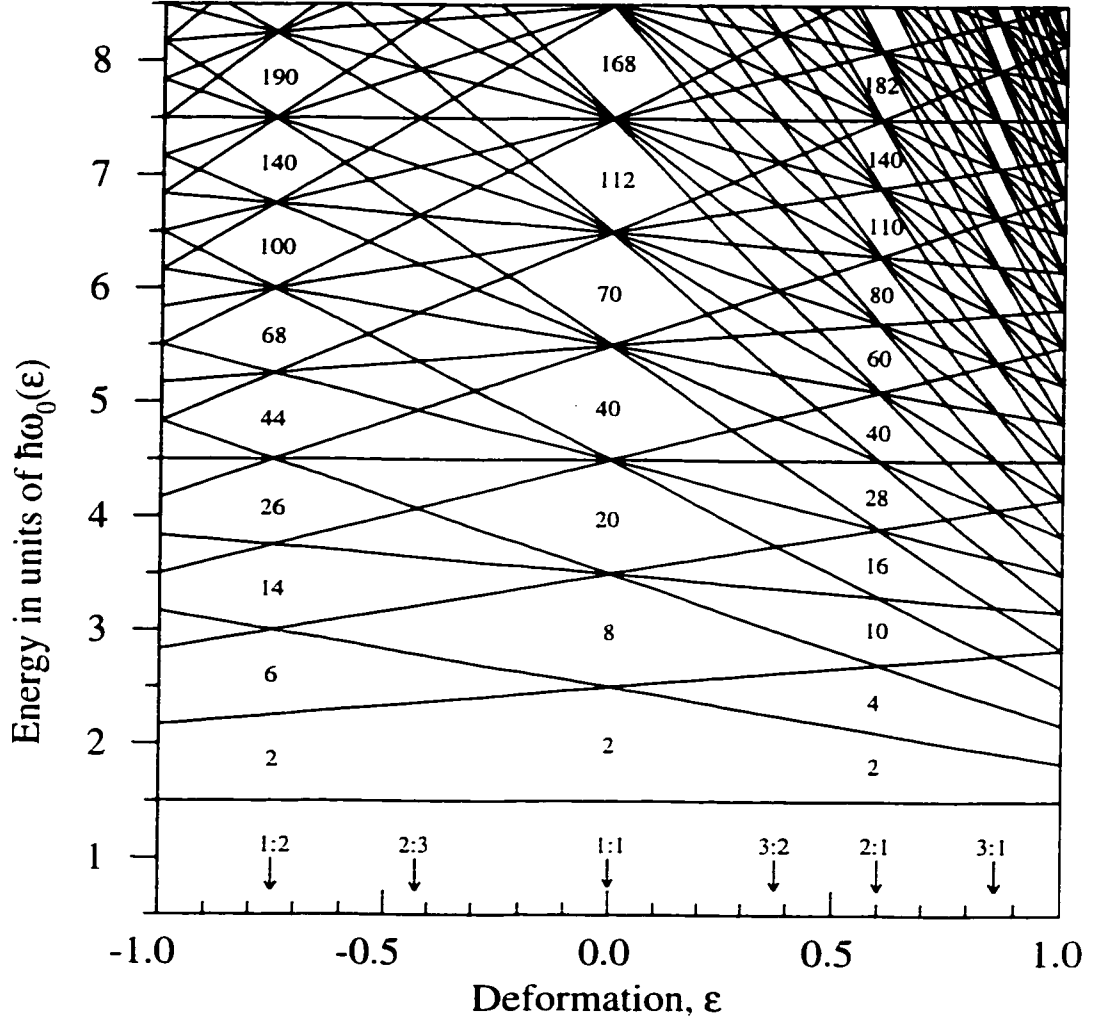


Figure 1.6: Energy levels of the axially symmetric deformed harmonic oscillator potential as a function of the deformation parameter ε . Ratios of the z -axis to the x and y axes are shown at the bottom of the figure. The spherical ($\varepsilon = 0.0$), prolate superdeformed ($\varepsilon = 0.6$), and oblate superdeformed ($\varepsilon = -0.75$) magic numbers are indicated in the shell gaps. After [She 72].

two long axes and one short axis. One immediately notices that for certain nucleon numbers a lower total energy can be achieved if the nucleus becomes deformed. However, this gain in shell energy comes at the expense of liquid-drop surface energy, and the balance between shell effects and this liquid-drop energy generally leads to nuclear ground state deformations with $|\varepsilon| \lesssim 0.3$.

Another feature apparent in Fig. 1.6 is that large gaps appear in the energy levels not only for spherical nuclei, but also when the axis lengths appear in small integer ratios. In particular, new sets of shell gaps and magic numbers appear for the prolate superdeformed ($\epsilon = 0.6$) and oblate superdeformed ($\epsilon = -0.75$) shapes with 2 : 1 axis ratios. Although the nuclear spin-orbit interaction and a more realistic treatment of the nuclear potential modify both the SD magic numbers and the exact deformations at which they occur (see Chapter 2), it is these SD shell gaps, together with the large moment of inertia associated with the superdeformed shape, which stabilize superdeformed nuclei.

1.3.2 SD Mass Regions

Historically, the first examples of superdeformation identified were the fission isomers in the actinide nuclei with neutron numbers $N \sim 142$ –148. Because of the mutual Coulomb repulsion of the large number of protons ($Z \sim 92$ –96) in these nuclei, they are unstable against spontaneous fission. However, the increase in liquid-drop energy with deformation prior to fission produces a substantial potential energy barrier (dashed line in Fig. 1.7) which must be tunneled through in order for fission to occur. Because of this barrier, the spontaneous fission lifetimes of these nuclei are quite long on nuclear time scales, ranging from several minutes to billions of years. It thus came as a considerable surprise when excited states (well below the fission barrier) were discovered (first in ^{242}Am [Pol 62, Per 62]) with fission lifetimes in the range of ns to ms. Not only were the fission lifetimes of these states much shorter than expected from the liquid-drop barrier, but there was also no clear explanation for their isomeric nature, i.e. their long lifetimes against γ -ray decay to the ground state. These fission isomers were successfully explained by Strutinsky [Str 67, Str 68], who noted that shell effects modify the liquid-drop potential energy barrier and, for $N \sim 142$ –148, produce

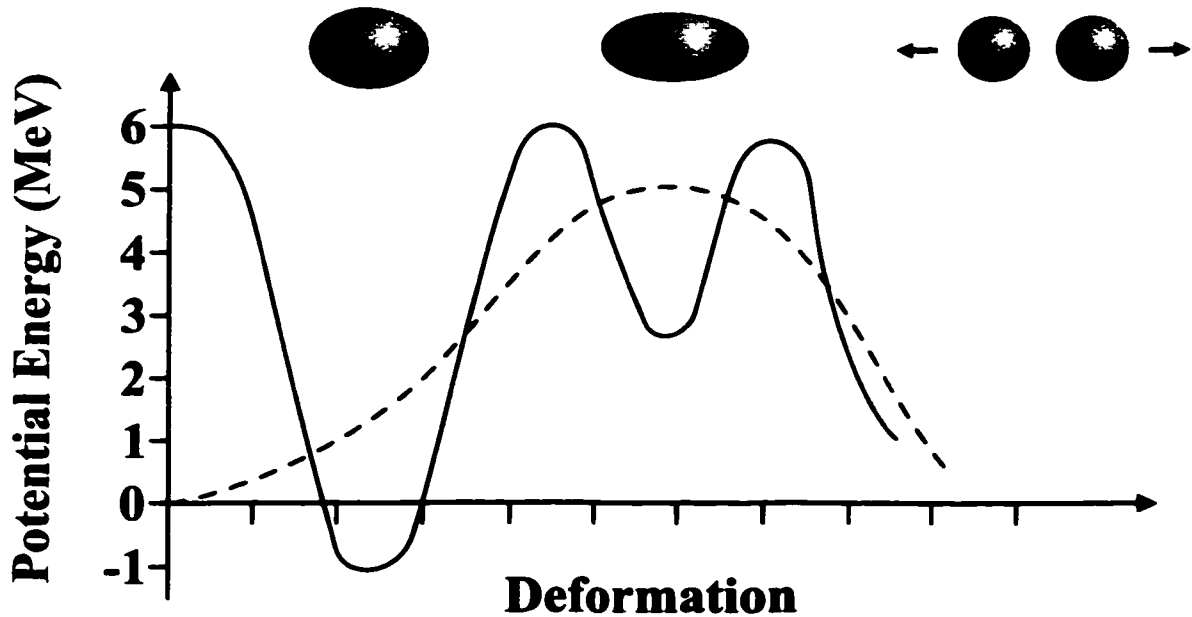


Figure 1.7: Schematic diagram of the potential energy as a function of deformation for a fission-isomer nucleus with neutron number $N \sim 142\text{--}148$. The liquid-drop energy (dashed line) is modified by shell effects to produce a “double-humped” barrier (solid line) with a second minimum for a superdeformed shape. After [PB 75].

a “double-humped” barrier (solid line in Fig. 1.7) with a second minimum for superdeformed shapes. States in this second well not only have a much narrower barrier to tunnel through on their way to fission and thus have much shorter fission lifetimes, but the barrier separating them from the first well also explains the hindrance of their γ -decay to the ground state. The subsequent identification of a rotational band built on such a fission isomer in ^{240}Pu [Spe 72], by measuring fission fragments in delayed coincidence with the conversion electron decays in the rotational band, provided a beautiful confirmation of the superdeformed character of these states.

For many years, the fission isomers were the only known examples of superdeformed nuclei and, to date, they remain the only nuclei in which the superdeformed ground state has been observed. It was, however, soon realized that SD bands in lighter nuclei with proton and neutron numbers in the vicinity of the SD shell gaps

could be stabilized by rapid rotation [Ben 75, Nee 75, Ben 81, Dud 82]. In general, the cost in liquid-drop surface energy associated with the superdeformed shape outweighs the gain in shell energy, and SD states lie at high excitation energy at low spin. However, the larger moment of inertia associated with the superdeformed shape leads to an SD yrast line with a smaller slope than that of the ND yrast line. As shown in Fig. 1.8, the SD yrast line may cross the ND yrast line at high spin, and for angular momenta above this crossing point the superdeformed shape becomes the lowest energy state of the nucleus.

Following evidence for such high-spin SD bands from studies of γ -ray energy correlations in the collective quasi-continuum of ^{152}Dy [Nya 84], the first discrete-line γ decays of SD rotational bands were discovered in ^{132}Ce [Nol 85] and ^{152}Dy [Twi 86]. These discoveries sparked an explosion of experimental and theoretical studies of superdeformation. High-spin superdeformed bands were soon identified in many nuclei in the $A \sim 130$ and $A \sim 150$ mass regions, and the observation of an SD band in ^{191}Hg [Moo 89] opened a third region for the study of high-spin superdeformation [JK 91]. More recently, the observation of superdeformation in ^{83}Sr [Bak 95] has led to intense studies of SD bands in the $A \sim 80$ mass region based on the SD shell gaps at $N, Z \approx 40$. In this thesis, the discovery of a new region of superdeformation for $A \sim 60$ nuclei with $N, Z \approx 30^\dagger$ is presented. High-spin SD bands have been identified in both ^{62}Zn [Sve 97c] and the $N = Z$ nucleus ^{60}Zn [Sve 98b], and these results will be discussed in detail in Chapters 6 and 7.

[†]As will be discussed in Chapter 2, the nuclear spin-orbit interaction and a realistic treatment of the nuclear potential shifts the deformed harmonic oscillator SD shell gap at $N, Z = 28$ shown in Fig. 1.6 to $N, Z = 30$.

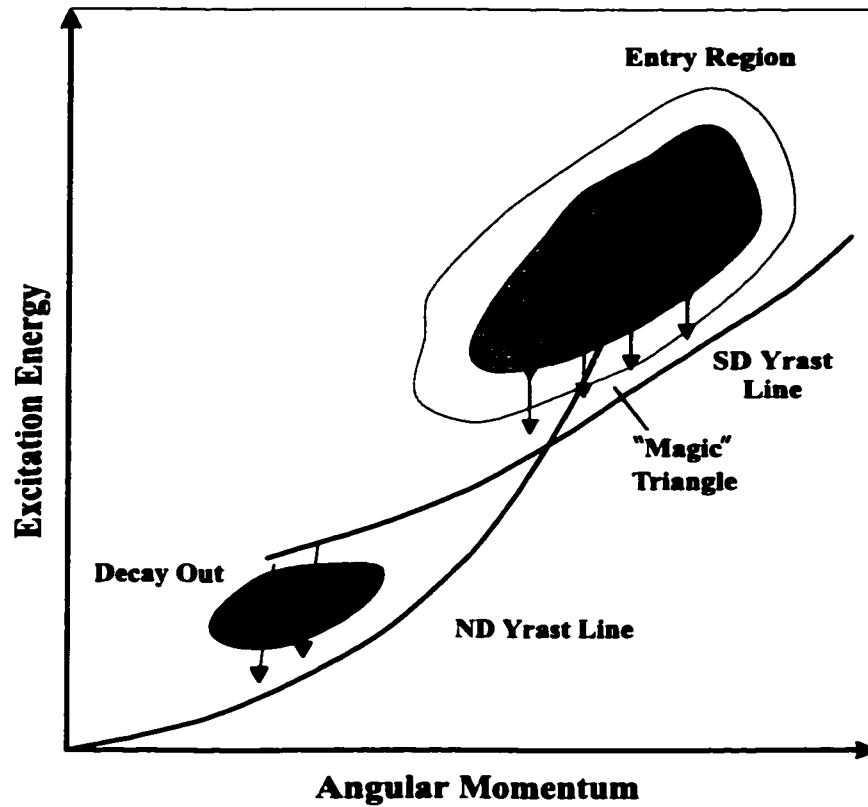


Figure 1.8: Schematic yrast diagram appropriate for the population and decay of SD bands. The ND and SD yrast lines, the “magic triangle” (see text), and the γ -ray continua resulting from the feeding transitions and the decay out of the SD band are indicated. Adapted from [Wil 94].

1.3.3 Population and Decay of Superdeformed Bands

As noted above and shown schematically in Fig. 1.8, SD bands typically lie at high excitation energy at low spin but, because of their large moments of inertia, may become energetically favoured at high angular momentum. Together with the potential energy barrier which separates the first and second wells, this crossing of the SD and ND yrast lines has important consequences for the feeding and decay of SD bands. Beyond the crossing point, the region of the yrast diagram bounded below by the SD yrast line, above and to the left by the ND yrast line, and above and to the right by the fission cut-off limit (not shown in Fig. 1.8), is often referred to

as the “magic triangle”. In order to populate SD bands with sufficient intensity to observe their discrete-line γ -ray decay, it is necessary to maximize the overlap of the entry region following particle evaporation with this magic triangle. In general, this presents a considerable challenge to the experimentalist and, even in the best cases, SD bands are rarely populated with more than a few percent of the channel cross section[†]. The identification of γ rays associated with the decay of SD bands, amidst the large background of γ rays from ND and continuum transitions, thus requires the use of powerful detection systems and data analysis techniques (see Chapter 3).

Once populated, SD rotational bands decay by cascades of in-band γ -ray transitions. Although decay out of the SD band is energetically possible below the crossing of the SD and ND yrast lines, the potential energy barrier separating the first and second minima hinders such decay-out transitions and favours the continuation of decay within the second minimum. However, with decreasing angular momentum the SD and ND yrast lines continue to diverge and the SD states become more and more excited relative to ND states of the same spin. The density of ND levels increases exponentially with excitation energy and, as indicated schematically in Fig. 1.9, the SD states will eventually become embedded in a “sea” of ND levels with similar excitation energies. When an SD state lies close enough in energy to an ND level of the same spin and parity, even a small interaction between these states will be sufficient to mix the SD and ND wavefunctions and lead to the decay out of the SD band [Vig 90a]. At the decay-out point, the high ND level density leads to a large number of possible pathways for the decay to the yrast line. The decay-out transitions thus form a quasi-continuum of unresolved γ rays and, although more

[†]The yrast SD band in ^{60}Zn identified in this work was populated far more strongly than any previously observed SD band, carrying 60(4)% of the ^{60}Zn channel intensity. As discussed in Chapter 7, this amazingly strong population is related to the doubly-magic nature of this SD band.

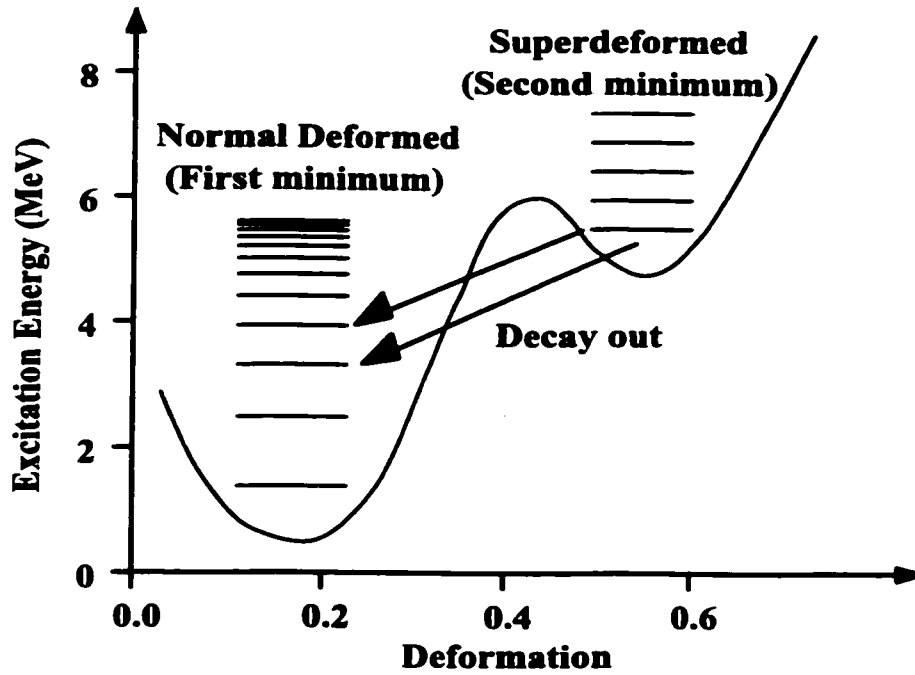


Figure 1.9: Schematic illustration of excitation energy versus deformation relevant for the decay out of SD bands. The “cold” SD states at the bottom of the second minimum are separated by a potential energy barrier from a “sea” of hot ND states. When the ND level density becomes sufficiently high, weak mixing between the SD and ND states results in the decay out of the SD band. Adapted from [Wil 94].

than 150 [Sin 96] SD bands have now been identified, in almost all cases it has not been possible to identify discrete γ -ray transitions connecting these bands to the ND states. The unfortunate consequence of this failure to link the SD and ND decay schemes is that the most fundamental properties of the SD states, namely their spins, parities, and excitation energies, are largely unknown.

Recently, significant progress has been made in studying the decay out of SD bands in the $A \sim 190$ mass region. Discrete linking transitions have been identified for SD bands in ^{194}Hg [Kho 96, Hac 97] and ^{194}Pb [Lop 96a, Hau 97], and these observations have not only provided definite quantum number assignments for SD states in these nuclei, but have also permitted a detailed study of the decay-out

process. In this thesis, the identification of discrete linking transitions connecting the doubly-magic SD band in ^{60}Zn to the ND yrast line is presented. A comparison of the decay-out properties in ^{60}Zn with those observed in the $A \sim 190$ mass region will be given in Chapter 7.

1.4 The $A \sim 60$ Mass Region

This thesis focuses on the study of high-spin states in proton-rich ($N \approx Z$) nuclei in the $A \sim 60$ mass region. An introduction to this region of the chart of the nuclides and the relevant shell-model orbitals that will play a major role in interpreting the experimental results presented in this thesis are shown in Fig. 1.10. High-spin spectroscopic studies of nuclei in this mass region are faced by a number of experimental challenges. The relatively high transition energies in these nuclei lead to low γ -ray detection efficiencies. The combination of these high transition energies, the high recoil velocities typical in the heavy-ion fusion reactions used to populate high-spin states in this mass region, and the substantial recoil given to these light nuclei by the evaporation of charged particles (particularly alpha particles), also lead to severe Doppler-broadening problems and a degradation of the γ -ray energy resolution (see Chapter 3). Furthermore, a relatively low Coulomb barrier and statistical pressures for the proton-rich compound nuclei to decay toward the valley of stability by emitting charged particles lead to a fragmentation of the total fusion cross section into a large number of exit channels with various numbers of evaporated protons, alphas, and neutrons (see Chapter 4). A highly efficient and selective means of identifying the γ rays belonging to particular reaction channels therefore becomes essential for detailed spectroscopic studies in this mass region.

Faced by these experimental challenges, previous γ -ray studies of proton-rich

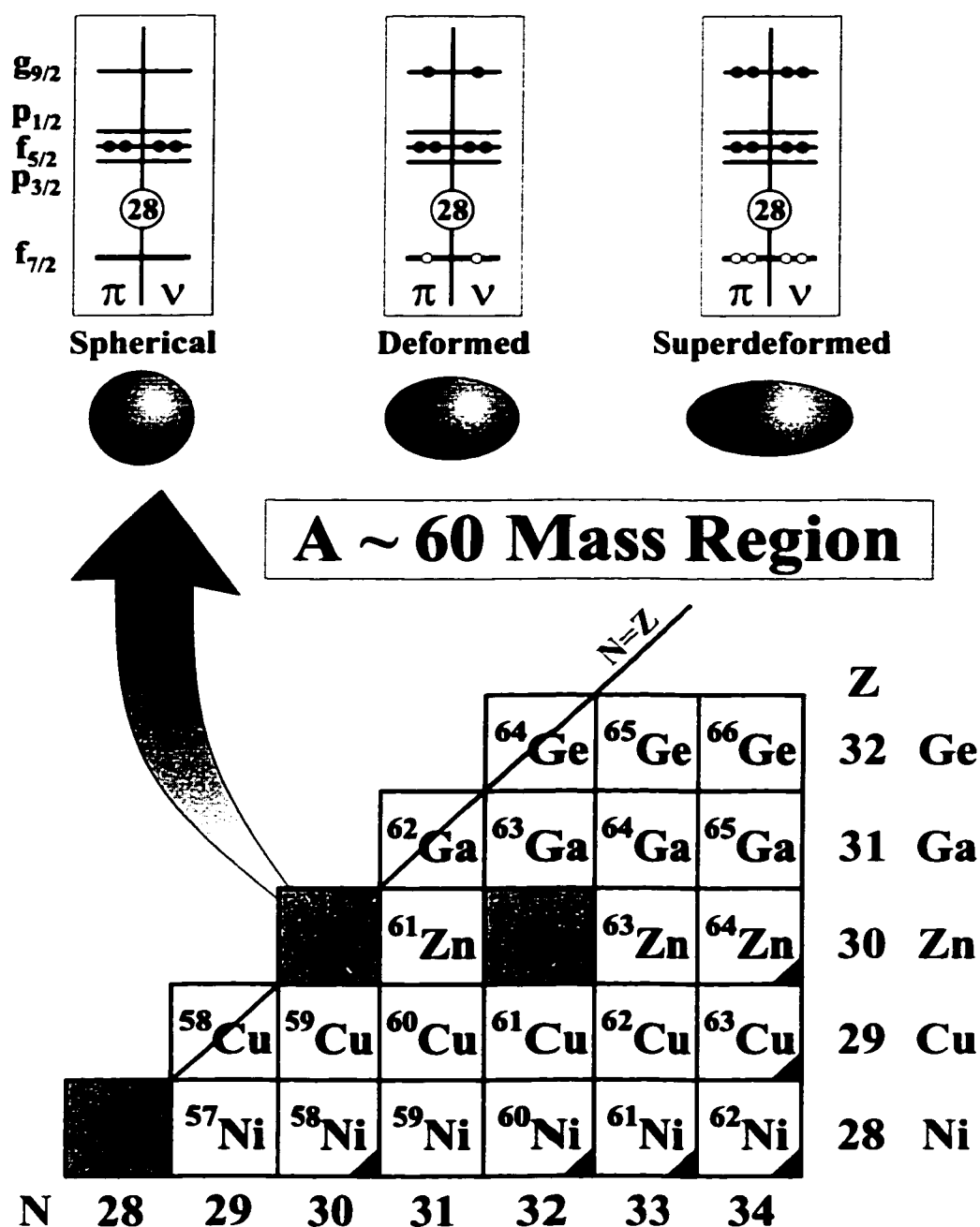


Figure 1.10: The proton-rich $A \sim 60$ mass region. The relevant portion of the chart of the nuclides is shown in the lower half of the figure. The $N = Z$ line is indicated and stable nuclei are marked with small solid triangles. The nuclei which form the focus of this work, namely ^{60}Zn and ^{62}Zn , as well as the doubly-magic spherical nucleus ^{56}Ni , are shaded. The relevant shell-model orbitals in this mass region and schematic single-particle configurations for spherical, deformed, and superdeformed shapes in ^{60}Zn are indicated at the top of the figure.

$A \sim 60$ nuclei (e.g. [Mul 79, Sch 89]) have focused on the spherical shell model states which dominate the low-lying decay schemes of these nuclei. The recent coupling of high efficiency charged-particle detectors with large γ -ray detector arrays has, however, provided new opportunities for detailed high-spin studies in this mass region, and the results presented in this thesis have revealed that these nuclei undergo a rich pattern of shape transformations and noncollective-collective transitions with increasing angular momentum. As indicated by the schematic configurations shown for the $N = Z$ nucleus ^{60}Zn in Fig. 1.10, the presence of high- j orbitals both below ($f_{7/2}$) and above ($g_{9/2}$) the spherical shell gaps at $N, Z = 28$ leads to deformed shapes and collective rotational bands in these nuclei based on particle-hole excitations across these shell gaps. However, with only a small number of valence particles and holes occupying these high- j orbitals, the total angular momentum in these configurations is limited to $20\text{--}30\hbar$. These rotational bands thus gradually exhaust all of the angular momentum available from their single-particle configurations and terminate in fully aligned noncollective states at experimentally observable spins. At still higher spins, the presence of the large SD shell gaps in the single-particle energy levels for particle numbers $N, Z \approx 30$ [She 72, Dud 87] leads to the prediction [Rag 90, She 91] of highly collective superdeformed bands in this mass region.

The experimental results which have illuminated this delicate interplay of single-particle and collective excitations in proton-rich $A \sim 60$ nuclei will be presented in Chapters 5, 6, and 7, following discussions of theoretical and experimental techniques in the next three chapters.

Chapter 2

Theoretical Background

The interplay between collective and single-particle degrees of freedom within the nucleus is one of the major themes of nuclear structure physics. This is particularly the case in high-spin studies, where angular momentum may be associated with each of these excitation modes. As noted in Section 1.1.2, a deformed nucleus can rotate about an axis perpendicular to a symmetry axis, thereby generating collective rotational angular momentum. At the same time, angular momentum is associated with single-particle states in nuclei, and high-spin states can be generated by noncollective couplings of particle and hole excitations. The theoretical description of these two degrees of freedom within the nucleus, and their delicate interplay as a function of variables such as deformation and rotational frequency, form the subject of the present Chapter.

2.1 Deformation, Rotation, and Angular Momenta

The concepts of nuclear deformation, rotation, and angular momentum have already been introduced qualitatively. The following sections provide more formal definitions of a number of parameters which will be used throughout this thesis to describe these concepts quantitatively.

2.1.1 Deformation Parameters

The surface of the nucleus is not well defined. As suggested by the shape of the Woods-Saxon potential shown in Fig. 1.1, the density of nuclear matter smoothly decreases from a rather constant value in the interior of the nucleus to zero over a finite “skin thickness”. Nevertheless, it is instructive to define an effective surface of the nucleus by the radius $R(\theta, \phi)$ where the density of nuclear matter drops to half its central value. For a spherical nucleus, $R(\theta, \phi)$ simply reduces to the constant value R_0 defined in Eq. 1.9, while to describe a general nuclear shape, $R(\theta, \phi)$ may be expressed as an expansion in the spherical harmonics $Y_{\lambda\mu}(\theta, \phi)$

$$R(\theta, \phi) = R_0 \left(1 + \sum_{\lambda=0}^{\infty} \sum_{\mu=-\lambda}^{\lambda} \alpha_{\lambda\mu} Y_{\lambda\mu}(\theta, \phi) \right). \quad (2.1)$$

Considering the lowest multipoles (λ values) in Eq. 2.1, we note that $Y_{00}(\theta, \phi)$ is a constant and α_{00} may thus be absorbed into R_0 so as to conserve the nuclear volume. The dipole ($\lambda = 1$) terms have the effect of shifting the center of mass of the nucleus. Choosing the origin of our coordinate system to correspond with the center of mass of the nucleus, the $\alpha_{1\mu}$ can thus be set equal to zero. The lowest order significant terms in Eq. 2.1, and those with which we will be primarily concerned in this thesis, are thus the quadrupole ($\lambda = 2$) deformations described by the five coefficients $\alpha_{2\mu}$. In fact, three of these coefficients are absorbed in defining the orientation of the nucleus, so that by choosing the axes of our coordinate system to coincide with the body-fixed principal axes of the nucleus (henceforth referred to as the 1, 2, and 3 axes) the shape of a quadrupole deformed nucleus may be completely specified by the two deformation parameters β and γ [HW 53]. These parameters define the $\alpha_{2\mu}$ by:

$$\alpha_{20} = \beta \cos \gamma, \quad \alpha_{2\pm 1} = 0, \quad \alpha_{2\pm 2} = \frac{1}{\sqrt{2}} \beta \sin \gamma, \quad (2.2)$$

so that, evaluating the spherical harmonics, the nuclear surface may be expressed as

$$R(\theta, \phi) = R_0 \left\{ 1 + \beta \sqrt{\frac{5}{16\pi}} \left(\cos \gamma \left[3 \cos^2 \theta - 1 \right] + \sqrt{3} \sin \gamma \sin^2 \theta \cos 2\phi \right) \right\}. \quad (2.3)$$

The parameters β and γ define a polar coordinate system for the description of quadrupole deformed shapes, with the “radial” coordinate β giving the magnitude of the deformation ($\beta = 0$ for a sphere). As shown schematically in Fig. 2.1, prolate (“football-like”) shapes lie along the $\gamma = 0^\circ$ axis and oblate (“disk-like”) shapes have $\gamma = 60^\circ$. These shapes are axially symmetric and have two equivalent principal axes. Between $\gamma = 0^\circ$ and $\gamma = 60^\circ$ the nuclear shape is triaxial with no two principal axes of equal length. Although all quadrupole shapes can be described within the sextant $0^\circ \leq \gamma \leq 60^\circ$, it is conventional to chose the rotation axis to coincide with the body-fixed 1-axis of the nucleus. As shown in Fig. 2.1, collective rotation of prolate and oblate shapes about an axis perpendicular to the nuclear symmetry axis then correspond to $\gamma = 0^\circ$ and $\gamma = -60^\circ$ respectively, while the noncollective axes with “rotation” about the nuclear symmetry axis occur at $\gamma = 60^\circ$ (oblate noncollective) and $\gamma = -120^\circ$ (prolate noncollective).

Two important quantities related to the deformation of the nucleus are its moment of inertia \mathcal{J} and quadrupole moment Q . The moments of inertia \mathcal{J}_κ for rotation of a quadrupole deformed nucleus about the $\kappa = 1, 2, 3$ axes can be readily calculated [RS 80] assuming that the nucleus is either an irrotational superfluid

$$\mathcal{J}_\kappa^{\text{irr}} = \frac{3}{2\pi} m A R_0^2 \beta^2 \sin^2 \left(\gamma - \frac{2\pi}{3} \kappa \right) \quad (2.4)$$

or a rigid rotor

$$\mathcal{J}_\kappa^{\text{rig}} = \frac{2}{5} m A R_0^2 \left\{ 1 - \sqrt{\frac{5}{4\pi}} \beta \cos \left(\gamma - \frac{2\pi}{3} \kappa \right) \right\}. \quad (2.5)$$

The moment of inertia of a real nucleus, which is neither an irrotational superfluid nor a rigid body, generally lies between these extremes, $\mathcal{J}^{\text{irr}} < \mathcal{J}^{\text{nuc}} < \mathcal{J}^{\text{rig}}$.

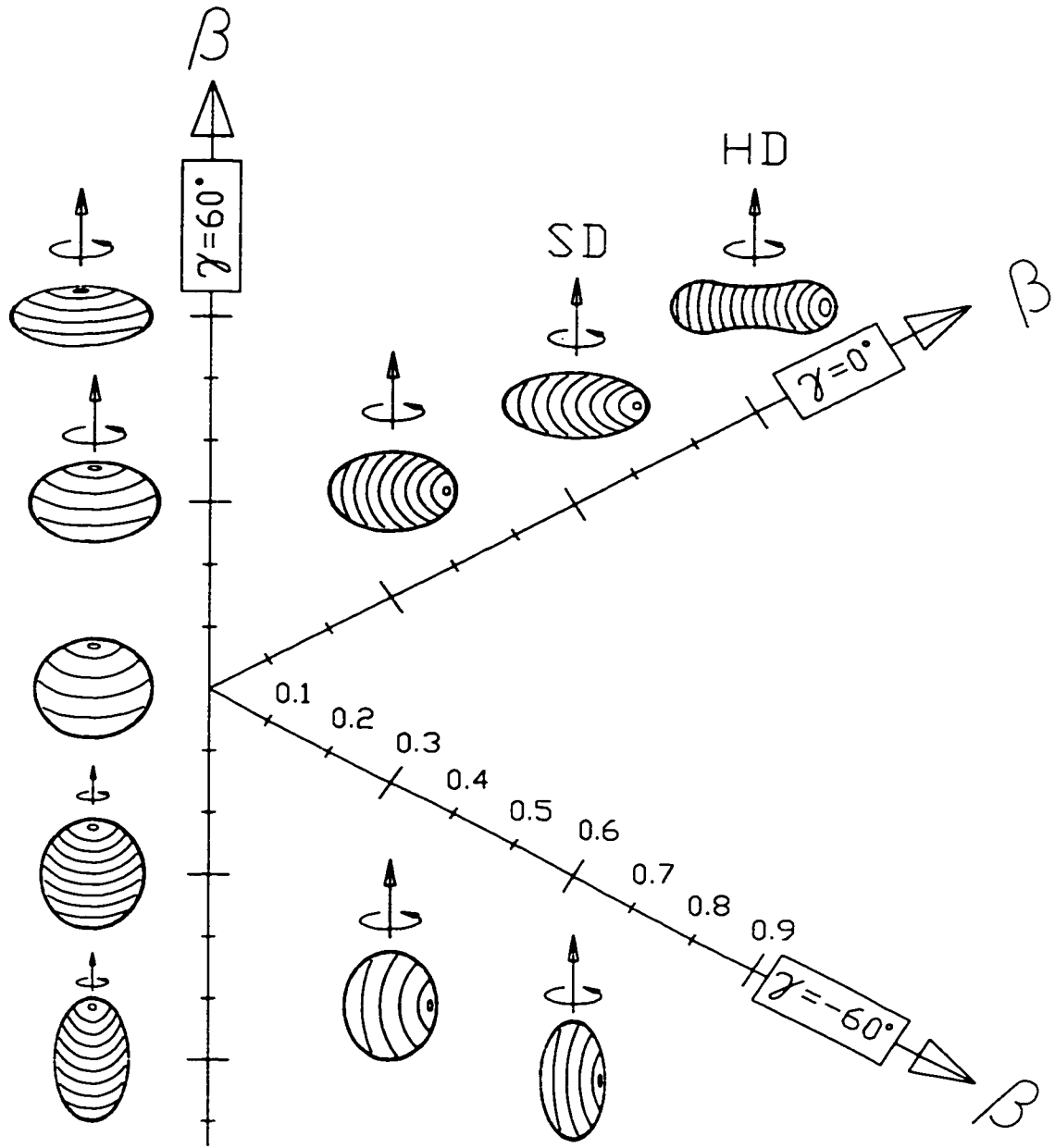


Figure 2.1: Schematic diagram of quadrupole deformed nuclei defined by the deformation parameters β and γ . The rotation axis is assumed to coincide with the body-fixed 1-axis of the nucleus, so that the $\gamma = 60^\circ, 0^\circ, -60^\circ$, and -120° axes correspond to the noncollective oblate, collective prolate, collective oblate, and noncollective prolate axes, respectively. Shapes with γ not equal to an integer multiple of 60° correspond to triaxial shapes with no two equivalent axes. Adapted from [WD 92].

The intrinsic electric quadrupole moment Q_{20} of the nucleus is given by

$$Q_{20} = \sqrt{\frac{16\pi}{5}} \int \rho(\vec{r}) r^2 Y_{20}(\theta, \phi) dV, \quad (2.6)$$

where ρ is the nuclear charge density. Assuming that $\rho = 3Ze/4\pi R_0^3$ is constant within the volume enclosed by $R(\theta, \phi)$, Eq. 2.6 may be integrated to obtain [LVH 70]

$$Q_{20} = \frac{3}{\sqrt{5\pi}} Ze R_0^2 \beta \left(1 + \frac{2}{7} \sqrt{\frac{5}{\pi}} \beta + \frac{1}{14\pi} \beta^2 - \dots \right). \quad (2.7)$$

Two additional points should be made regarding deformation parameters. Firstly, as shown by the “peanut-like” prolate hyperdeformed (HD) shape in Fig. 2.1, the pure quadrupole ($\lambda = 2$) deformations are not equivalent to ellipsoids. Better approximations to ellipsoidal shapes can be obtained by introducing small hexadecapole ($\lambda = 4$) deformations, and the coefficients of the $Y_{4\mu}$ terms in Eq. 2.1 are often related to a single additional deformation parameter β_4 [WD 92]. It is then conventional to denote the quadrupole deformation parameter β by β_2 , and this notation will be adopted for the remainder of this thesis.

Secondly, a number of distinct deformation parameters are used in the nuclear structure literature. While the use of $(\beta_2, \beta_4, \gamma)$ is common, many theoretical calculations, especially those performed within the framework of the Nilsson model (see Section 2.2), employ $(\varepsilon_2, \varepsilon_4, \gamma)$, which generalize the ellipsoidal deformation parameter ε introduced in Section 1.3.1. Although the relationship between these two parametrizations of the nuclear deformation is, in general, non-trivial (graphic conversion tables between (β_2, β_4) and $(\varepsilon_2, \varepsilon_4)$ can be found in [Ben 89]), for the special case of $\gamma = 0^\circ$ and $\beta_4 = \varepsilon_4 = 0$, β_2 and ε_2 can be related by the expansions [LVH 70]:

$$\beta_2 = \sqrt{\frac{\pi}{5}} \left(\frac{4}{3} \varepsilon_2 + \frac{10}{63} \varepsilon_2^2 + \frac{2896}{6615} \varepsilon_2^3 + \dots \right), \quad \varepsilon_2 = \frac{3}{4} \sqrt{\frac{5}{\pi}} \beta_2 - \frac{75}{224\pi} \beta_2^2 - \frac{81}{128\pi} \sqrt{\frac{5}{\pi}} \beta_2^3 + \dots \quad (2.8)$$

Both β_2 and ε_2 will be frequently used throughout this thesis.

2.1.2 Nuclear Rotation

In order to define a number of parameters which characterize the rotation of a nucleus, it is instructive to consider the nucleus as a perfect quantum rotor. The energy levels E are then related to the angular momentum I by

$$E(I) = \frac{\hbar^2}{2\mathcal{J}} I(I+1), \quad (2.9)$$

where \mathcal{J} is the moment of inertia of the nucleus.

Although Eq. 2.9 could, in principle, be used to extract values of \mathcal{J} from the energies and spins of the levels in a rotational band, in practice the lowest energy (or “bandhead”) states of rotational bands in real nuclei often have non-zero values of both energy and spin which depend on the details of the intrinsic nuclear state upon which the rotational band is built. A more useful expression for the moment of inertia is thus obtained by taking the first difference of the rotational energy with respect to spin, which is simply related to the energy E_γ of the γ ray emitted when the nucleus makes a transition in the rotational band from a state of spin I to a state of spin $I - 2$:

$$E_\gamma(I \rightarrow I - 2) = E(I) - E(I - 2) \quad (2.10)$$

$$= \frac{\hbar^2}{\mathcal{J}} (2I - 1). \quad (2.11)$$

Rearranging Eq. 2.11, we define the kinematic moment of inertia $\mathcal{J}^{(1)}$ by

$$\mathcal{J}^{(1)} = \frac{\hbar^2 (2I - 1)}{E_\gamma(I \rightarrow I - 2)}. \quad (2.12)$$

Although $\mathcal{J}^{(1)}$ is independent of the absolute excitation energies of the states in a rotational band, it should be noted that Eq. 2.12 does require a knowledge of the level spins. As discussed in Section 1.3.3, these absolute spin values are not known for

many rotational bands and, in particular, are unknown for almost all superdeformed bands. It is therefore useful to obtain an expression for the moment of inertia which is independent of both the absolute spins and the absolute excitation energies of the levels by taking the second difference of the rotational energy with respect to spin. From Eq. 2.11 we note that the difference in the energies of consecutive γ -ray transitions in a rotational band is given by

$$\Delta E_\gamma(I) = E_\gamma(I + 2 \rightarrow I) - E_\gamma(I \rightarrow I - 2) \quad (2.13)$$

$$= \frac{4\hbar^2}{\mathcal{J}}. \quad (2.14)$$

This constant difference between consecutive γ -ray energies leads to the regular “picket fence” γ -ray spectrum that characterizes the decay of a rotational band. Rearranging Eq. 2.14 we define the dynamic moment of inertia $\mathcal{J}^{(2)}$ by

$$\mathcal{J}^{(2)} = \frac{4\hbar^2}{\Delta E_\gamma(I)}. \quad (2.15)$$

Another parameter which characterizes rotational motion is the rotational frequency ω , usually expressed in terms of the associated energy $\hbar\omega$. In order to relate ω to the experimental observables for a rotational band, the classical expression $\omega = dE/dI$ is replaced by the finite difference equation $\omega = \Delta E/\Delta I$. Noting that ΔE is simply a γ -ray transition energy, and $\Delta I = 2\hbar$ in a rotational band, we have $\hbar\omega = E_\gamma/2$. In accordance with the definition of $\mathcal{J}^{(2)}$ in Eq. 2.15, it is conventional to define $\omega(I)$ by taking the average of the γ -ray energies which feed and decay out of the state of spin I :

$$\hbar\omega(I) = \frac{E_\gamma(I + 2 \rightarrow I) + E_\gamma(I \rightarrow I - 2)}{4}. \quad (2.16)$$

Although rotational frequencies in this thesis will be given in MeV, it is worthwhile to note that a typical rotational frequency in the $A \sim 60$ mass region of $\hbar\omega = 1$ MeV corresponds to a nuclear rotation rate of 2.4×10^{20} revolutions per second.

2.1.3 Collective and Single-Particle Angular Momenta

In the previous section, the intrinsic state of the nucleus was neglected and the nuclear angular momentum was assumed to result entirely from collective rotation. This simple model is extended in the present section to include the angular momentum associated with single-particle states. In the particle-plus-rotor model, the bulk of the nucleons are considered to form a core which undergoes collective rotation and the remaining valence particles are treated separately. As illustrated in Fig. 2.2, the total nuclear angular momentum \vec{I} is then formed by the vector sum of the collective rotational angular momentum \vec{R} of the core and the single-particle angular momentum \vec{j} , which is, in turn, composed of orbital \vec{l} and spin \vec{s} components. The projections of \vec{l} and \vec{s} on the body-fixed 3-axis of the nucleus are denoted by Λ and Σ respectively, and their sum $\Omega = \Lambda + \Sigma$ is the projection of \vec{j} on this axis. The projections of \vec{I} on the body-fixed 3-axis and the laboratory-frame x-axis (the rotation axis) are labeled K and M respectively.

If the Hamiltonian is separated into intrinsic and collective components.

$$H = H_{int} + H_{col} \quad (2.17)$$

$$= H_{int} + \sum_{i=1}^3 \frac{\hbar^2}{2\mathcal{J}_i} R_i^2, \quad (2.18)$$

where the R_i are the body-fixed components of the collective rotational angular momentum, the nuclear eigenstates take the form of products of an intrinsic wavefunction χ_{int} and a rotational wavefunction $\Psi(\vec{\Theta})$, where $\vec{\Theta}$ denotes the three Euler angles which define the orientation of the nucleus. Since the body-fixed components $I_{1,2,3}$ of the total angular momentum commute with the laboratory-frame components $I_{x,y,z}$ (because $I_{1,2,3}$ are independent of the nuclear orientation), I^2 , I_x , and I_3 may be chosen as a set of commuting angular momentum variables and their respective eigenvalues

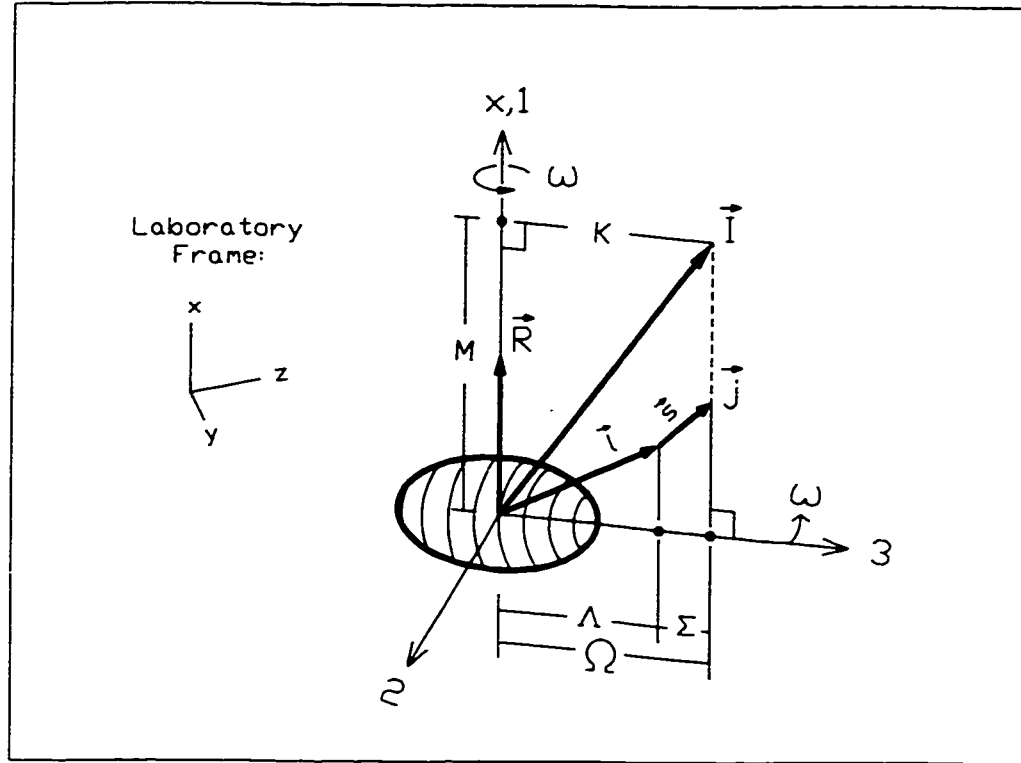


Figure 2.2: Rotational, single-particle, and total angular momenta and their projections for a prolate nucleus. From [Hac 95a].

I , M , and K may be used to label the rotational wavefunctions. For specified values of I , M , and K , these rotational wavefunctions are given by [BM 75]

$$\Psi_{MK}^I(\vec{\Theta}) = \sqrt{\frac{2I+1}{8\pi^2}} \mathcal{D}_{MK}^I(\vec{\Theta}), \quad (2.19)$$

where the $\mathcal{D}_{MK}^I(\vec{\Theta})$ are the Wigner rotation functions. However, for axially symmetric nuclei, the invariance of the Hamiltonian with respect to 180° rotations about an axis perpendicular to the symmetry axis requires the wavefunction to be symmetrized with respect to $\pm K$. For the special case of $K = 0$ bands, this leads to allowed values of the total angular momentum which form the $\Delta I = 2$ sequences $I = 0, 2, 4, \dots$ for positive parity ($K^\pi = 0^+$) bands and $I = 1, 3, 5, \dots$ for negative parity ($K^\pi = 0^-$) bands (see [PB 75], Chapter 9 for a formal derivation). For $K \neq 0$, all values of

$I = K, K + 1, K + 2, \dots$ are allowed. However, the large quadrupole transition matrix elements in such bands are generally between states differing in spin by $2\hbar$ (see Appendix A). It is thus conventional to consider these bands as two separate $\Delta I = 2$ sequences with spins $I = K, K + 2, K + 4, \dots$ and $I = K + 1, K + 3, K + 5, \dots$ referred to as signature partner bands (see Section 2.3).

The particle-plus-rotor definition $\vec{I} = \vec{R} + \vec{j}$ may be used to eliminate R^2 from the collective component of the nuclear Hamiltonian in Eq. 2.18. For the special case of axial symmetry about the body-fixed 3-axis of the nucleus, $\mathcal{J}_1 = \mathcal{J}_2 \equiv \mathcal{J}$, $R_3 = 0$ (since collective rotation about a symmetry axis is forbidden), $K = \Omega$, and H_{col} may be recast in the form

$$H_{col} = \frac{\hbar^2}{2\mathcal{J}}(I^2 - I_3^2) + \frac{\hbar^2}{2\mathcal{J}}(j_1^2 + j_2^2) - \frac{\hbar^2}{\mathcal{J}}(I_1 j_1 + I_2 j_2). \quad (2.20)$$

The first term in Eq. 2.20 is referred to as the rotational term and represents the component of the total angular momentum (collective plus single-particle) perpendicular to the symmetry axis of the nucleus. The second term depends only on the single-particle degrees of freedom and can be absorbed into the intrinsic component of the Hamiltonian. The final term in Eq. 2.20 represents a coupling of the single-particle and rotational motion resulting from the Coriolis and centrifugal forces acting on the nucleons, and is usually referred to simply as the Coriolis term. The standard ladder operators $I_{\pm} = I_1 \pm iI_2$ and $j_{\pm} = j_1 \pm ij_2$ which raise and lower the 3-components of \vec{I} and \vec{j} , respectively, can be used to recast the Coriolis interaction in the form

$$H_{Cor} = -\frac{\hbar^2}{2\mathcal{J}}(I_+ j_- + I_- j_+). \quad (2.21)$$

The only non-zero matrix elements of I_{\pm} and j_{\pm} are (with $\Omega = K$) [Cas 90]

$$\langle I, K | I_{\pm} | I, K \pm 1 \rangle = \sqrt{(I \mp K)(I + K + 1)}, \quad (2.22)$$

$$\langle j, K | j_{\mp} | j, K \pm 1 \rangle = \sqrt{(j \mp K)(j + K + 1)}. \quad (2.23)$$

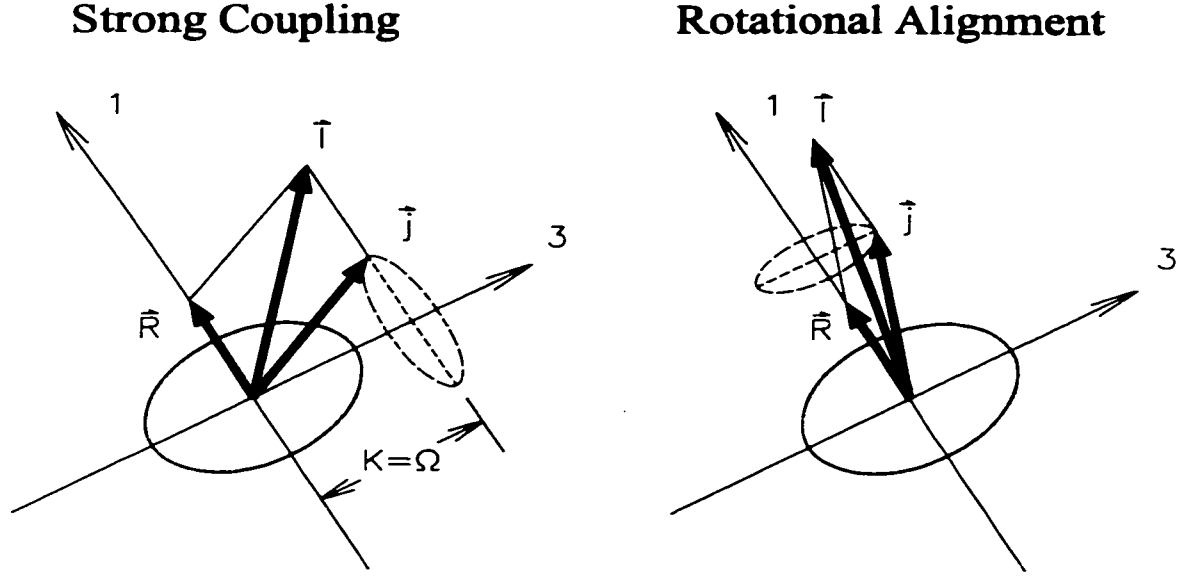


Figure 2.3: Schematic illustration of the strong coupling and rotational alignment limits of the particle-plus-rotor model. Adapted from [RS 80].

It is thus clear that the effect of the Coriolis term is to mix states differing in K by ± 1 . For the special case of $K = \frac{1}{2}$ bands, the symmetry of the wavefunction with respect to $K = \pm \frac{1}{2}$ leads to an important diagonal contribution to the energy eigenstates from this Coriolis interaction.

In the presence of the rotational-particle coupling induced by the Coriolis interaction, a full particle-plus-rotor calculation requires the numerical diagonalization of the Hamiltonian given in Eq. 2.18. A qualitative impression of the importance of the Coriolis interaction can, however, be obtained by considering the two limiting cases illustrated in Fig. 2.3. The strong coupling, or deformation alignment, limit is realized when the matrix elements of the Coriolis interaction are small compared to the splitting of the single-particle energy levels with different K values in the deformed nuclear potential. This limit is expected when either the K -splitting is large (which occurs at large deformation) or the Coriolis interaction is weak (which occurs for small values of I and/or j , or for large values of Ω if j is large). In this limit

the single-particle angular momentum is strongly coupled to the rotating core and, as illustrated in Fig. 2.3, K may be treated as a good quantum number. For $K \neq \frac{1}{2}$ bands, the Coriolis interaction can be neglected and the energy levels of the rotational band are given by

$$E(I) = E_0 + \frac{\hbar^2}{2\mathcal{J}} [I(I+1) - K^2], \quad (2.24)$$

where E_0 is an eigenstate of H_{int} . For $K = \frac{1}{2}$ bands, a perturbative calculation of the Coriolis interaction yields the result [RS 80]

$$E_{K=\frac{1}{2}}(I) = E_0 + \frac{\hbar^2}{2\mathcal{J}} \left[I(I+1) - \frac{1}{4} + a(-1)^{(I+\frac{1}{2})} \left(I + \frac{1}{2} \right) \right], \quad (2.25)$$

where the decoupling parameter a for a $K = \frac{1}{2}$ orbital $|\phi\rangle$ is given by

$$a = i\langle\phi | j_+ e^{-i\pi j_1} | \phi\rangle. \quad (2.26)$$

The rotational alignment limit is realized when the Coriolis interaction is large compared to the deformation-induced splitting of the orbitals with different K values, and is expected when I and j are large and Ω is small. The Coriolis interaction favours the configuration in which the single-particle and total angular momenta are maximally aligned, and in this limit the single-particle angular momentum becomes decoupled from the core and aligns along the rotation axis. As illustrated in Fig. 2.3, in the limit of rotational alignment the projection of the single-particle angular momentum on the rotation axis becomes a good quantum number ($\langle j_x \rangle = j$ for maximally aligned states) and the energy levels in this limit are given by

$$E = E_0 + \frac{\hbar^2}{2\mathcal{J}} R(R+1), \quad (2.27)$$

where $R = I - \langle j_x \rangle = 0, 2, 4, \dots$ is restricted to even values by the aforementioned symmetry considerations.

2.2 The Deformed Mean Field

The concepts of shell structure in a mean-field potential and the effects of deformation on single-particle energy levels were briefly introduced in Sections 1.1.1 and 1.3.1. In the following sections a more detailed discussion of deformed nuclear mean-field models is presented. For a comprehensive review, the reader is referred to [ÄFN 90].

2.2.1 The Nilsson Model

The Nilsson model [Nil 55] extends the deformed harmonic oscillator model introduced in Section 1.3.1 by adding terms proportional to $\vec{l} \cdot \vec{s}$ and $\vec{l}^2 - \langle \vec{l}^2 \rangle_N$ to the single-particle Hamiltonian. As discussed in Section 1.1.1, a strong nuclear spin-orbit ($\vec{l} \cdot \vec{s}$) interaction is required to reproduce the correct magic numbers for spherical nuclei, and this remains true for deformed nuclei. The $\vec{l}^2 - \langle \vec{l}^2 \rangle_N$ term, where $\langle \vec{l}^2 \rangle_N = N(N+3)/2$ is the average value of \vec{l}^2 within an oscillator N -shell, lowers the energies of the higher- l orbitals within a shell and qualitatively has the same effect as a flattening of the oscillator potential to give a radial dependence in the interior of the nucleus similar to the more realistic Woods-Saxon potential. For axially-symmetric deformations, the Nilsson potential thus takes the form

$$V_{\text{Nilss}}(\varepsilon_2) = \frac{1}{2}m\omega_0^2(\varepsilon_2) \left[(x_1^2 + x_2^2) \left(1 + \frac{1}{3}\varepsilon_2 \right)^2 + x_3^2 \left(1 - \frac{2}{3}\varepsilon_2 \right)^2 \right] + C\vec{l} \cdot \vec{s} + D(\vec{l}^2 - \langle \vec{l}^2 \rangle_N) \quad (2.28)$$

where the x_i refer to the body-fixed axes, Eq. 1.23 relates $\omega_0(\varepsilon_2)$ to the spherical frequency ω_0 given by (with the $+$ ($-$) sign applying to neutrons (protons)) [Nil 69]

$$\hbar\omega_0 = 41A^{-\frac{1}{3}} \left(1 \pm \frac{N-Z}{3A} \right) \text{ MeV} \quad (2.29)$$

and C and D are related to two adjustable parameters κ and μ :

$$C = -2\hbar\omega_0\kappa, \quad D = -\hbar\omega_0\kappa\mu, \quad (2.30)$$

which are determined from global fits to experimental data and are usually adjusted independently for protons and neutrons and for each oscillator N -shell. Typical values are in the range 0.05–0.12 for κ and 0.0–0.7 for μ . All of the Nilsson calculations presented in subsequent chapters of this thesis were performed with the κ and μ values given in [Ben 85].

At finite deformations, the only good quantum numbers remaining in the Nilsson model are parity and the projection Ω of the single-particle angular momentum on the symmetry axis of the nucleus. However, in the limit of large deformations the spin-orbit and \vec{l}^2 terms can be neglected relative to the deformation-induced splitting of the energy levels and the Nilsson Hamiltonian is equivalent to a pure deformed harmonic oscillator. In this limit, the single-particle orbitals may be labeled by the asymptotic Nilsson quantum numbers N , n_3 , and Λ , where N is the total number of oscillator quanta, n_3 is the number of oscillator quanta along the 3-axis, and, as defined in Fig. 2.2, Λ is the projection of the orbital angular momentum on the 3-axis. Although these quantum numbers are strictly valid only in the limit of large deformations, it is conventional to use them as labels of the form $\Omega^\pi[N, n_3, \Lambda]$ to distinguish Nilsson orbitals of the same Ω^π even at moderate deformations. Since the parity π is given by $(-1)^N$ this label is often omitted, and it is also worth noting that the sum $n_3 + \Lambda$ takes on only even (odd) values for even (odd) N .

The Nilsson single-particle energy levels for $N, Z \leq 50$ and $|\varepsilon_2| \leq 0.3$ are shown in Fig. 2.4. With deformation, the $2j + 1$ degenerate spherical shell-model energy levels are split into $j + \frac{1}{2}$ orbitals with different values of $|\Omega|$ (a twofold degeneracy with respect to $\pm\Omega$ remains). The lowest- Ω orbitals from each spherical j -shell, which have wavefunctions with the highest probability of being close to the 3-axis of the nucleus, decrease in energy with prolate deformation and increase in energy

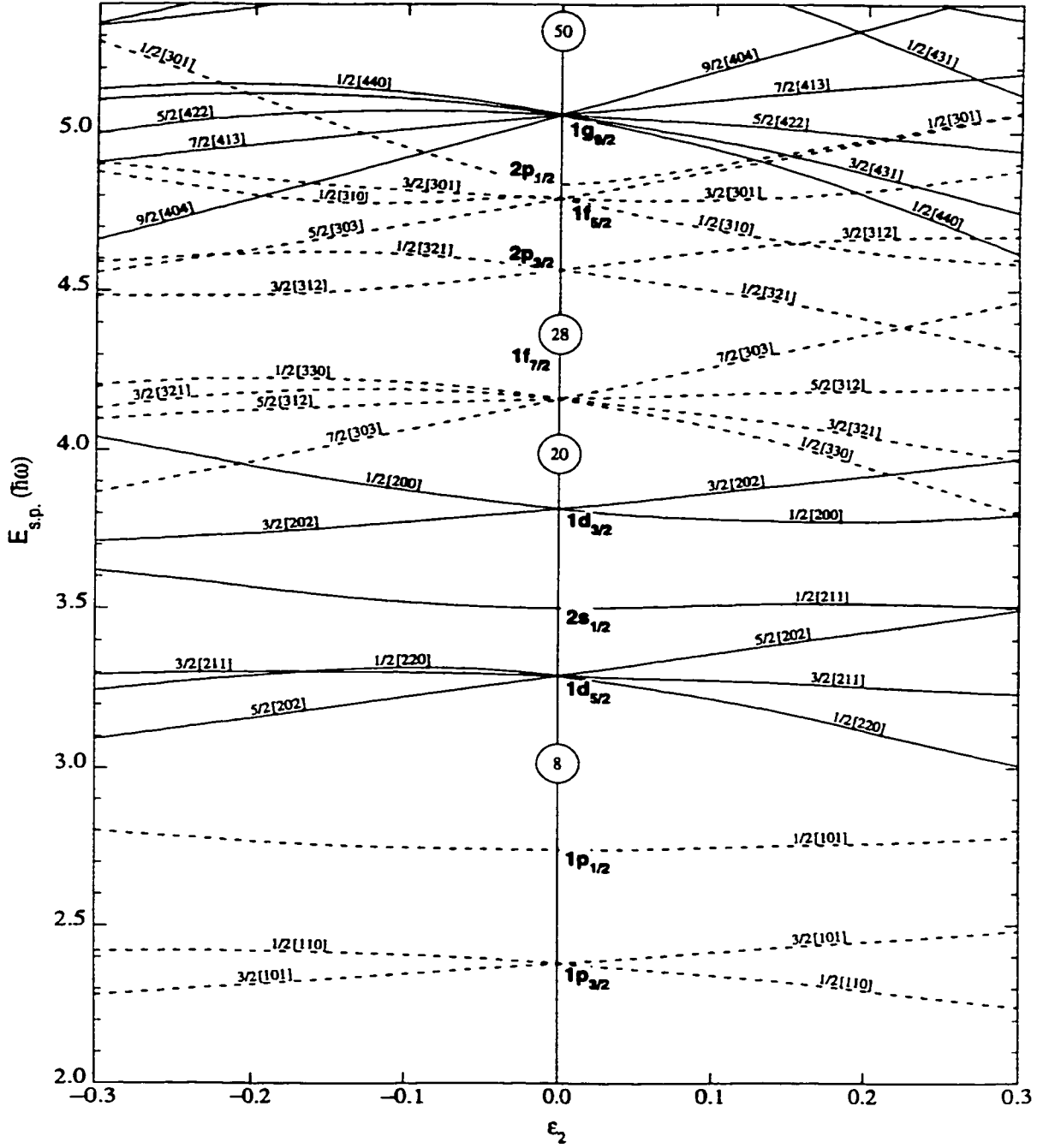


Figure 2.4: Nilsson diagram for $N, Z \leq 50$ and $|\varepsilon_2| \leq 0.3$, $\varepsilon_4 = 0$. Solid (dashed) lines represent positive (negative) parity, and the orbitals are labeled by their asymptotic Nilsson quantum numbers $\Omega[N, n_3, \Lambda]$ (see text for details). From [Fir 96].

with oblate deformation. The opposite is true of the highest- Ω orbitals. Another important feature of the Nilsson diagram is that, with increasing deformation, orbitals from different spherical j -shells with the same Ω^π may approach each other. These levels, which have the same good quantum numbers and can therefore never cross, become increasingly mixed and repel each other, exchanging principal wavefunction components in the process so that far from the interaction region their wavefunctions appear as if they had actually crossed. Such an interaction between the $\frac{1}{2}^+[211]$ and $\frac{1}{2}^+[200]$ orbitals[†] can be seen in Fig. 2.4.

Although j is not a good quantum number in a deformed potential, certain Nilsson orbitals do remain almost pure eigenstates of j^2 . For example, the spherical $1g_{9/2}$ level is lowered by the strong spin-orbit interaction and the $\frac{1}{2}^+[440]$ orbital decreases further in energy with prolate deformation. Although there are several nearby $\Omega = \frac{1}{2}$ orbitals originating from the spherical $1f - 2p$ shell, these orbitals have negative parity and therefore do not mix with the $\frac{1}{2}^+[440]$ orbital. This unnatural parity “intruder” orbital thus retains almost pure $j = \frac{9}{2}$ character out to considerable deformation. Similarly, the highest- Ω orbital from each N -shell cannot mix with any nearby levels because they all have smaller Ω values. High- Ω “extruder” orbitals, such as the $\frac{7}{2}^-[303]$ orbital in Fig. 2.4, thus also retain almost pure j values. As will be discussed in Chapters 5–7, the $\frac{1}{2}^+[440]$ and $\frac{7}{2}^-[303]$ orbitals play a dominant role in determining the structure of deformed bands in the $A \sim 60$ ($N, Z \approx 30$) mass region. Since these orbitals retain their spherical j -shell parentage to a high degree of accuracy, it is appropriate, and convenient, to simply label configurations in this region by their numbers of “ $f_{7/2}$ ” holes and “ $g_{9/2}$ ” particles, as was introduced schematically in Fig. 1.10.

[†]The asymptotic Nilsson quantum numbers labeling these strongly mixed orbitals should, of course, be treated with considerable caution in the interaction region.

2.2.2 The Deformed Woods-Saxon Potential

Although the Nilsson model is undoubtedly one of the most widely used and successful models of nuclear structure, it does suffer from a number of deficiencies. Among these are (i) the oscillator potential is not finite at large radii, which leads to an incorrect description of the tails of the wavefunctions, and (ii) the $\vec{l}^2 - \langle \vec{l}^2 \rangle_N$ term introduced to flatten the oscillator potential in the interior of the nucleus is artificial and has undesirable side-effects, among which are overestimates of moments of inertia in the Nilsson model [Ben 89]. These deficiencies of the Nilsson model may be removed by replacing the deformed oscillator potential (and the $\vec{l}^2 - \langle \vec{l}^2 \rangle_N$ term) with a more realistic form of the deformed nuclear potential. One commonly used form is the deformed Woods-Saxon potential [Dud 81]

$$V(r, \theta, \phi) = -V_0 \left[1 + \exp \left(\frac{r - R(\theta, \phi)}{a(\theta, \phi)} \right) \right]^{-1} \quad (2.31)$$

which generalizes the spherical Woods-Saxon potential of Eq. 1.8.

The single-particle energy levels of this potential are shown as a function of the quadrupole deformation parameter β_2 in Fig. 2.5. Also indicated in this figure are the particle numbers at which gaps appear in the energy levels. Of particular relevance to this thesis is the large shell gap at $N, Z = 30$ for $\beta_2 \approx 0.4$ - 0.6 , which stabilizes superdeformed shapes in the $A \sim 60$ mass region.

The price paid for the more realistic treatment of the nuclear potential in the deformed Woods-Saxon model is an added complexity of the numerical calculations and resulting wavefunctions compared to the relatively simple and transparent oscillator wavefunctions of the Nilsson model. For a detailed discussion and comparison of the relative merits of the Nilsson and deformed Woods-Saxon shell-model potentials, the reader is referred to [Ben 89].

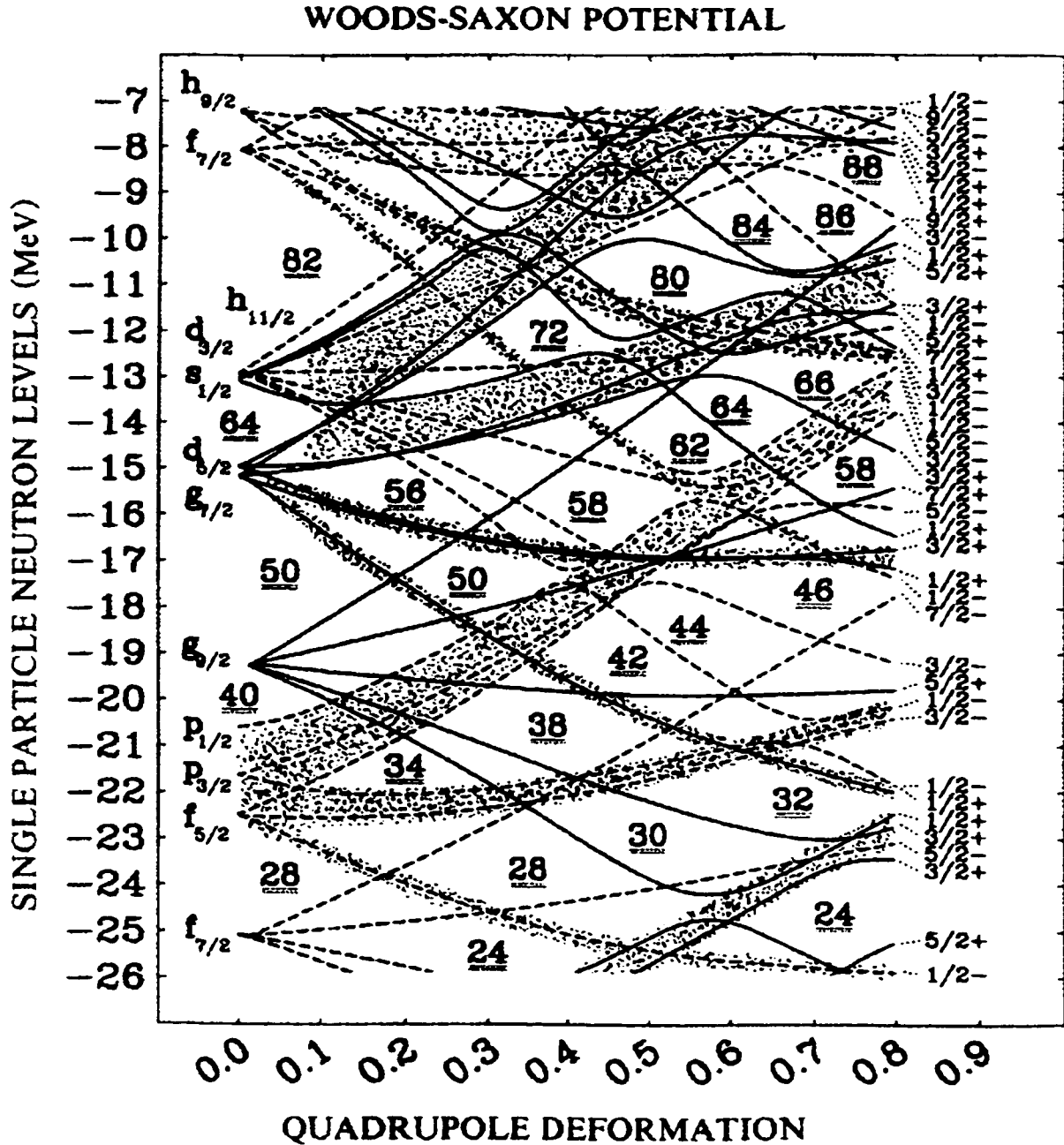


Figure 2.5: Single-particle energy levels of the Woods-Saxon potential as a function of the quadrupole deformation parameter β_2 . Particle numbers at the shell gaps between regions of higher level density (shaded) are indicated. Ω^π is given for each orbital on the right side of the figure. The large shell gap at $\beta_2 \approx 0.4-0.6$ for particle number 30 plays a dominant role in stabilizing superdeformed shapes in the $A \sim 60$ mass region. From [Dud 87].

2.2.3 Strutinsky Shell Correction

Although the Nilsson and Woods-Saxon shell model potentials are able to reproduce the correct shell closures (magic numbers) and are very successful in describing nuclear properties which involve only nucleons in the vicinity of the Fermi surface, they do not correctly describe bulk nuclear properties such as total binding energies which depend on all of the nucleons. This deficiency of the shell model potentials is related to the fact that, on average, they do not reproduce the correct density of levels. On the other hand, the liquid drop model of the nucleus is very successful in describing bulk nuclear properties which have a smooth dependence on the nucleon numbers, but has no means of accounting for quantum shell effects and the stability of deformed nuclei. In order to combine the qualities, and eliminate the deficiencies, of the shell and liquid drop models, Strutinsky [Str 67, Str 68] proposed a method in which the total nuclear energy is expressed as the sum of a smooth liquid drop energy E_{LD} and a quantum shell correction energy δE_{shell} :

$$E_{tot} = E_{LD} + \delta E_{shell}. \quad (2.32)$$

In the Strutinsky method, the shell correction is taken as the difference between the actual shell model energy E_{shell} and its smooth average behaviour $\langle E_{shell} \rangle$:

$$\delta E_{shell} = E_{shell} - \langle E_{shell} \rangle. \quad (2.33)$$

Considering neutrons (for protons simply replace N with Z), the shell energy is the sum of the energies of the N occupied shell-model orbitals:

$$E_{shell} = \sum_{i=1}^N \epsilon_i. \quad (2.34)$$

Defining the density of states $g(\epsilon)$, which takes the form of a series of delta functions

$$g(\epsilon) = \sum_i \delta(\epsilon - \epsilon_i), \quad (2.35)$$

the shell energy may be recast in the form

$$E_{shell} = \int^{\lambda} \epsilon g(\epsilon) d\epsilon, \quad (2.36)$$

where the Fermi surface λ lies between the last occupied orbital (ϵ_N) and the first unoccupied orbital (ϵ_{N+1}).

In order to calculate the average behaviour of the shell energy, a smooth density of states $\tilde{g}(\epsilon)$ is defined by

$$\tilde{g}(\epsilon) = \sum_i S(\epsilon - \epsilon_i), \quad (2.37)$$

where the smoothing function $S(\epsilon - \epsilon_i)$ replaces the δ -function of Eq. 2.35 and is usually taken as the product of a Gaussian, with a width $\gamma \approx \hbar\omega_0$ characteristic of the separation of major groups of shell model energy levels, and a Laguerre polynomial which stabilizes the shell correction energy with respect to changes in γ [RS 80]. A new Fermi surface $\tilde{\lambda}$ is imposed by particle number conservation

$$N = \int^{\tilde{\lambda}} \tilde{g}(\epsilon) d\epsilon \quad (2.38)$$

and the smooth part of the shell model energy is then given by

$$\langle E_{shell} \rangle = \int^{\tilde{\lambda}} \epsilon \tilde{g}(\epsilon) d\epsilon. \quad (2.39)$$

As discussed in Section 1.3.2, the shell correction approach was first employed by Strutinsky to explain the fission isomers in actinide nuclei. With the extension of this method to include the angular momentum dependence of the level density [And 76], calculations of the Nilsson-Strutinsky type also provide a powerful, and relatively straightforward, method of describing the high-spin properties of nuclei. Calculations of this type will form the theoretical basis for interpreting the experimental results presented in Chapters 5–7.

2.2.4 Other Mean Field Methods

The shell model potentials discussed in the previous sections by no means encompass the full spectrum of contemporary nuclear mean field theory. Two other approaches, the Hartree-Fock and relativistic mean field methods, are briefly mentioned here.

The Hartree-Fock (HF) method provides a self-consistent microscopic approach to the nuclear mean field. Starting with an effective interaction (often of the density-dependent Skyrme type [Sky 59]) and a set of trial wavefunctions (often taken as the eigenfunctions of a Nilsson or Woods-Saxon potential), the HF equations (see [RS 80] Chapter 5) are solved to obtain final wavefunctions which self-consistently reproduce the nuclear potential. Although this requires the computationally complex solution of a nonlinear eigenvalue problem, the HF method avoids the incorrect average level densities and internal inconsistencies of the phenomenological one-body potentials, for which the final wavefunctions do not necessarily reproduce the *a priori* chosen form of the potential. Combined with the cranking model (Section 2.3) and pairing correlations (Section 2.4), the HF method has provided a powerful tool for high-spin nuclear structure calculations throughout the chart of the nuclides, ranging from ^{24}Mg [Bon 87] to SD bands in the $A \sim 190$ mass region [Hee 98].

The relativistic mean field (RMF) approach is similar to the self-consistent HF method, but includes relativistic effects by treating the nucleons as Dirac particles with effective interactions resulting from the exchange of σ , ω , and ρ mesons (see [GM 96] Chapter 7). This theory has also been extended to the rotating frame [Koe 89], and cranked RMF (CRMF) calculations have been successfully employed in a systematic description of SD bands in the $A \sim 150$ mass region [Afa 96a]. CRMF calculations have recently been performed for ^{62}Zn and ^{60}Zn [Afa 98], and these calculations will be compared with the experimental results presented in Chapters 6 and 7.

2.3 The Cranking Model

In the previous section, the effects of deformation on the single-nucleon energy levels were discussed. In this section, we consider the effects of rotation on these energy levels. This is accomplished through the use of the cranking model, originally introduced by Inglis [Ing 54, Ing 56], which transforms the Hamiltonian to the body-fixed intrinsic frame of the rotating nucleus.

2.3.1 The Cranking Hamiltonian

For a deformed nucleus rotating with angular velocity ω , the single-particle potential V , as viewed from the laboratory coordinate system r, θ, φ (defined with respect to the rotation axis), has the time-dependent form

$$V(\vec{r}, t) = V(r, \theta, \varphi - \omega t, 0), \quad (2.40)$$

where $V(\vec{r}, 0)$ is the potential at time $t = 0$. The corresponding single-particle Hamiltonian is therefore also time dependent:

$$h(t) = -\frac{\hbar^2}{2m} \nabla^2 + V(\vec{r}, t). \quad (2.41)$$

This time dependence can, however, be eliminated through the unitary transformation

$$h^0 = U h(t) U^{-1}, \quad (2.42)$$

where

$$U = e^{i\omega t j_z / \hbar} \quad (2.43)$$

produces a rotation of angle ωt about the x -axis (the rotation axis) and transforms the single-particle wavefunctions to the intrinsic frame of the rotating nucleus

$$\phi^\omega = U \phi. \quad (2.44)$$

The laboratory-frame single-particle Schrödinger equation has the form

$$h(t)\phi = i\hbar \frac{\partial \phi}{\partial t}. \quad (2.45)$$

Applying the transformation U and making use of $U^{-1}U = 1$ we obtain

$$Uh(t)U^{-1}U\phi = i\hbar U \frac{\partial \phi}{\partial t} \quad (2.46)$$

$$h^0 \phi^\omega = i\hbar U \frac{\partial \phi}{\partial t}. \quad (2.47)$$

From Eqs. 2.44 and 2.43 we have

$$\frac{\partial \phi^\omega}{\partial t} = \frac{\partial U}{\partial t} \phi + U \frac{\partial \phi}{\partial t} \quad (2.48)$$

$$= \frac{i\omega j_x}{\hbar} \phi^\omega + U \frac{\partial \phi}{\partial t}. \quad (2.49)$$

Finally, substituting Eq. 2.49 in Eq. 2.47 we obtain

$$(h^0 - \omega j_x) \phi^\omega = i\hbar \frac{\partial \phi^\omega}{\partial t} \quad (2.50)$$

$$h^\omega \phi^\omega = i\hbar \frac{\partial \phi^\omega}{\partial t}, \quad (2.51)$$

where $h^\omega = h^0 - \omega j_x$ is the single-particle Routhian operator and represents the Hamiltonian in the rotating reference frame where Coriolis and centrifugal potentials (the $-\omega j_x$ term) modify the time-independent single-particle Hamiltonian h^0 . Summing over the A nucleons we obtain the total Routhian operator

$$\mathcal{R}^\omega = H^0 - \omega J_x, \quad (2.52)$$

where

$$J_x = \sum_{i=1}^A j_x^{(i)}. \quad (2.53)$$

2.3.2 Signature

As was discussed in Section 2.1.3, the Coriolis interaction mixes single-particle states which differ in Ω by ± 1 . At finite rotational frequency, Ω is therefore no longer a good quantum number. The single-particle Routhian operator h^ω is, however, invariant with respect to the rotation of 180° about the x -axis produced by the operator

$$R_x = e^{-i\pi J_x}. \quad (2.54)$$

The single-particle states may therefore be classified according to their symmetry with respect to R_x [Ben 79]

$$R_x \phi_\alpha^\omega = e^{-i\pi\alpha} \phi_\alpha^\omega \quad (2.55)$$

where, for single-particle states, the signature α takes on the values $\pm \frac{1}{2}$. Defined in this way, the signature is an additive quantum number, so that the total signature of a system of A nucleons is simply the sum of the α values of the A occupied orbitals

$$\alpha_{tot} = \sum_{i=1}^A \alpha_i \bmod 2, \quad (2.56)$$

where the modulo 2 reflects the fact that $\exp(-i\pi\alpha) = \exp(-i\pi(\alpha + 2n))$ for any integer n . The total signature, henceforth simply denoted by α , is related to the angular momenta in the $\Delta I = 2$ sequence of states in the rotational band built on a particular configuration by

$$\alpha = I \bmod 2. \quad (2.57)$$

For example, in an even- A nucleus, rotational bands with $\alpha = 0$ have the spins $I = 0, 2, 4, \dots$, whereas $I = 1, 3, 5, \dots$ for $\alpha = +1$ bands. In an odd- A nucleus, the corresponding values are $I = \frac{1}{2}, \frac{5}{2}, \frac{9}{2}, \dots$ for $\alpha = +\frac{1}{2}$, and $I = \frac{3}{2}, \frac{7}{2}, \frac{11}{2}, \dots$ for $\alpha = -\frac{1}{2}$.

In addition to signature, the only other good quantum number that can be used to label the single-particle states in the cranking model is their parity π .

2.3.3 Routhians

The solutions to the single-particle cranking equations

$$h^\omega \phi^\omega = e^\omega \phi^\omega, \quad h^\omega = h^0 - \omega j_x, \quad (2.58)$$

define a set of single-particle energies e^ω in the rotating system, referred to as Routhians. As an illustrative example, the single-proton Routhians near the Fermi surface in ^{60}Zn , calculated at a deformation $\beta_2 = 0.3$, $\beta_4 = 0.0$, $\gamma = 0^\circ$, are shown in Fig. 2.6. At zero rotational frequency, the energy levels are simply those of the deformed mean field potential (labeled in Fig. 2.6 by N_k , the k th lowest level from the N th oscillator shell) and the two signatures of each level are degenerate. At finite rotational frequencies, the Coriolis interaction breaks the degeneracy of the two signatures. As noted in Section 2.1.3, the Coriolis interaction contributes a diagonal term to the energy eigenvalue only for $\Omega = \frac{1}{2}$ orbitals, and it is therefore only for these levels that the Routhians have non-zero slope at $\omega = 0$ (cf. the 4_1 level in Fig. 2.6 which corresponds to the $\frac{1}{2}^+[440]$ Nilsson state). These orbitals have their angular momentum nearly parallel or antiparallel to the rotation axis, and the $-\omega j_x$ term in Eq. 2.58 strongly favours the aligned state over the antialigned state. The signature of this favoured state is related to the j -shell from which the orbital evolved by

$$\alpha_{fav} = j \bmod 2 \quad (2.59)$$

and from Eq. 2.58 we see that the slope of the Routhian is given by

$$\frac{de^\omega}{d\omega} = -\langle j_x \rangle. \quad (2.60)$$

The decrease in energy of aligned states resulting from the Coriolis interaction can lead to a situation where energy levels originating from high- N , high- j , low- Ω orbitals, which have already been lowered in energy by deformation, rapidly approach

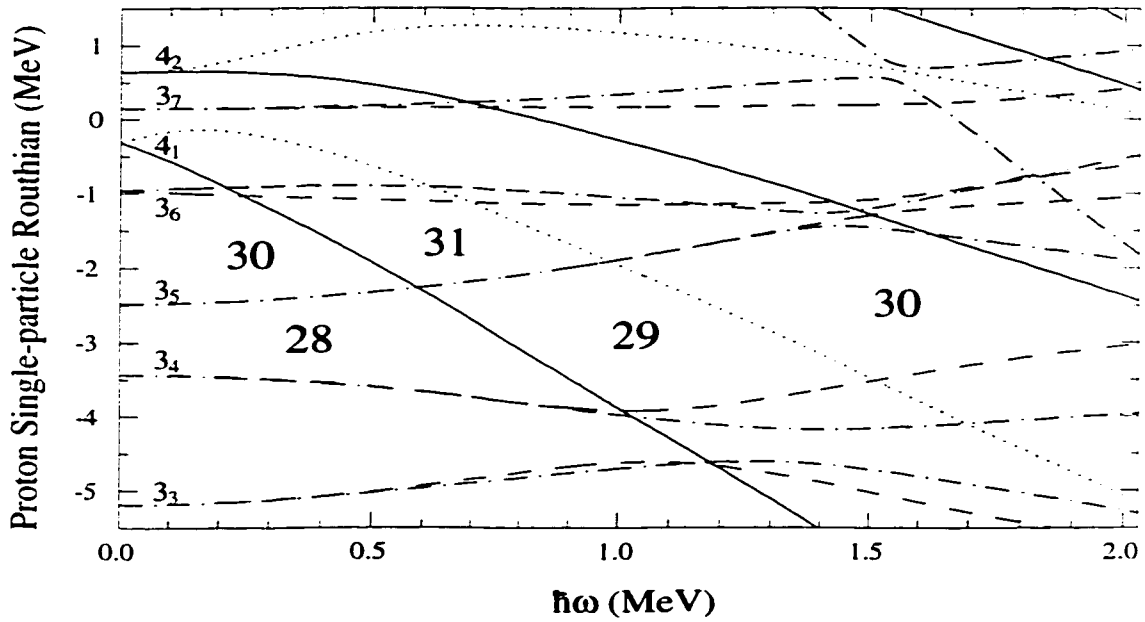


Figure 2.6: Single-proton energy levels as a function of rotational frequency $\hbar\omega$ calculated for ^{60}Zn at a deformation $\beta_2 = 0.3$, $\beta_4 = 0.0$, $\gamma = 0^\circ$. Different line types represent different combinations of parity π and signature α : $(\pi, \alpha) = (+, +\frac{1}{2})$ solid, $(+, -\frac{1}{2})$ dotted, $(-, +\frac{1}{2})$ dashed, and $(-, -\frac{1}{2})$ dot-dashed. At low frequency the orbitals are labeled by N_k , indicating the k th lowest state from the N th oscillator shell. Particle numbers are indicated in a few of the gaps.

the Fermi surface with increasing rotational frequency. An example of this is clearly seen in Fig. 2.6, where for $Z = 30$ and $\beta_2 = 0.3$ the positive signature of the 4_1 level (originating from the $g_{9/2}$ shell) crosses the Fermi surface at $\hbar\omega \approx 0.6$ MeV. For rotational frequencies above this crossing, the lowest energy state of the nucleus corresponds to having a particle in this 4_1 orbital and a hole in one of the signatures of the 3_5 level. As has already been mentioned, the occupation of $N = 4$ orbitals with increasing deformation and rotational frequency plays an important role in the structure of deformed and superdeformed rotational bands in the $A \sim 60$ mass region.

With increasing rotational frequency, the signature-split Routhians arising from the $\Omega = \frac{1}{2}$ levels approach, and mix with, levels of the same α and π , transferring their signature splitting to the $\Omega \neq \frac{1}{2}$ orbitals in the process. Since signature and

parity are the only good quantum numbers, Routhians with the same α and π can never cross and a number of “bounces” between Routhians with the same α and π are clearly seen in Fig. 2.6. Similar to the exchange of Nilsson wavefunctions discussed in Section 2.2.1 (where Ω and π were the relevant quantum numbers), the single-particle wavefunctions are also interchanged during such “virtual” crossings of the Routhians.

Because the Coriolis interaction only mixes wavefunction components that differ in Ω by ± 1 , and because all of the signature splittings ultimately originate from the $\Omega = \frac{1}{2}$ orbitals, the signature splitting of Routhians evolving from high- Ω orbitals may be viewed as the result of a successive series of Coriolis mixings through which the wavefunctions gradually acquire $\Omega - 1, \Omega - 2, \dots, \frac{1}{2}$ components. For high- Ω orbitals, the two signatures may thus remain degenerate out to relatively high rotational frequency, as is seen for the 3_5 level (corresponding to the $\frac{7}{2}^- [303]$ Nilsson orbital) in Fig. 2.6. If an odd particle occupies such a high- Ω orbital, the pair of rotational bands in the nucleus corresponding to the odd particle in one or the other of the signatures, referred to as signature partner bands, will be degenerate. This leads to the interesting situation where the energies of the electric quadrupole ($E2$) γ rays emitted in the decay of the $\Delta I = 2$ rotational sequences of these two bands are interleaved, $E_\gamma(I + 1 \rightarrow I - 1)$ in one band being the average of $E_\gamma(I + 2 \rightarrow I)$ and $E_\gamma(I \rightarrow I - 2)$ in the other band, and magnetic dipole ($M1$) “cross-over” transitions between the signature partners may also be observed. The observation of such a characteristic pattern of γ -ray transitions provides strong evidence that the bands are built on a configuration involving an odd particle in a signature-degenerate orbital. The reverse argument may also be applied in certain situations. If a rotational band is observed without a signature partner, it is unlikely that its single-particle configuration involves an odd particle in such an orbital.

2.3.4 Shell Correction and Configurations

In the cranking model, the total spin $I = I_x$ and energy E_{shell} in the laboratory frame are calculated from the single-particle energies e^ω and expectation values of j_x :

$$I = \sum_{occ} \langle \phi_i^\omega | j_x | \phi_i^\omega \rangle, \quad E_{shell} = \sum_{occ} \langle \phi_i^\omega | h^0 | \phi_i^\omega \rangle = \left(\sum_{occ} e_i^\omega \right) + \omega I, \quad (2.61)$$

where the sums are taken over the occupied (i.e. lowest energy) orbitals for both protons and neutrons. Not surprisingly, the cranked shell model, like its deformed shell model parent, does not properly reproduce average level densities and total energies. The Strutinsky shell correction method discussed in Section 2.2.3 is thus generalized to the case of finite rotational frequencies [And 76]

$$\delta E_{shell}(\vec{\varepsilon}, I) = E_{shell}(\vec{\varepsilon}, I) - \langle E_{shell}(\vec{\varepsilon}, I) \rangle, \quad (2.62)$$

where $\vec{\varepsilon}$ denotes the complete set of deformation parameters, $(\varepsilon_2, \varepsilon_4, \gamma)$ for example. and the Strutinsky smoothed sum $\langle E_{shell} \rangle$ is calculated from the Routhians at the same deformation and spin as E_{shell} . The total energy of the nucleus is then given by

$$E_{tot}(\vec{\varepsilon}, I) = E_{RLD}(\vec{\varepsilon}, I) + \delta E_{shell}(\vec{\varepsilon}, I), \quad (2.63)$$

where the rotating liquid drop energy E_{RLD} takes the form

$$E_{RLD}(\vec{\varepsilon}, I) = E_0 + E_{Coul}(\vec{\varepsilon}, I) + E_{surf}(\vec{\varepsilon}, I) + \frac{\hbar^2}{2\mathcal{J}(\vec{\varepsilon}, I)} I^2, \quad (2.64)$$

and the Coulomb energy, surface energy, and moment of inertia (usually taken as the rigid body value for high-spin studies) are explicitly deformation dependent.

The results of such calculations at a fixed spin I are often displayed as a potential energy surface (PES) showing a contour plot of E_{tot} in the (ε_2, γ) plane with the energy minimized with respect to ε_4 at each point. Inspection of such PES plots calculated at various spins, provides valuable information about changes in the nuclear

shape with increasing angular momentum, and extensive libraries of these plots have been calculated for nuclei throughout the chart of the nuclides [Åbe 82, WD 92].

Although PES calculations provide a valuable qualitative tool for high-spin nuclear structure studies, they suffer from a number of deficiencies when quantitative comparisons between theory and experiment are desired. Firstly, although it is straightforward to generate separate PES plots for the four combinations of α and π (since these good quantum numbers are easily identified in cranking calculations), the PES represents the low-energy envelope of all single-particle configurations of a given symmetry and it is not always possible to follow the evolution of a specific configuration when it is no longer yrast. Furthermore, in the semi-classical cranking model the rotational frequency ω is the natural independent parameter and virtual crossings of Routhians with the same α and π occur at a given value of ω . In the real nucleus, however, distinct configurations of the same symmetry interact at a given value of the total angular momentum I , not necessarily corresponding to the same cranking frequency for the two configurations. As discussed in detail in [Ben 85], this can lead to serious problems with the cranking description of the yrast line when an aligned high- j intruder orbital undergoes a virtual crossing near the Fermi surface and the sudden jump in angular momentum associated with the occupation of this orbital leads to I becoming a multivalued function of ω . It can, however, be noted that Routhians with different symmetries are free to pass smoothly through each other and no difficulties in describing the various yrast lines occur at such real crossings.

Noting that the characteristics of the wavefunctions are exchanged over a small range of ω when Routhians originating from different N -shells undergo abrupt virtual crossings, the idea of the configuration-dependent cranking approach [Ben 85, Naz 85] is to remove these virtual crossings and replace them with real crossings. In

this approach, the total numbers of neutron and proton oscillator quanta N_ν and N_π are treated as good quantum numbers that can be used to identify distinct configurations. More recently, this configuration concept has been extended to include the highest- j orbitals within a given N -shell, which often retain distinct wavefunctions and may be smoothly interpolated through virtual crossings by following the orbitals from a given shell with the largest expectation values of $\langle j^2 \rangle$ [Rag 95, Afa 95, Afa 96b]. This removal of virtual crossings in the cranking model is illustrated in Fig. 2.7, where single-proton Routhians for ^{62}Zn are shown. In the upper panel, the virtual crossings between the strongly downsloping $N = 5$ Routhian (dot-dashed line) and the $N = 3$ Routhians have been removed. In the lower panel of this figure, the high- j Routhians arising from the $f_{7/2}$ shell have also been identified and their virtual crossing with the other $N = 3$ orbitals have been removed. It is in this sense of smoothly interpolated Routhians with distinct high- j wavefunctions, combined with the rather pure j values of the Nilsson intruder and extruder orbitals discussed in Sections 2.2.1, that the different configurations in the $A \sim 60$ mass region can be identified and labeled by their numbers of “ $f_{7/2}$ ” holes and “ $g_{9/2}$ ” particles.

With configurations labeled by their N -shell and high- j content, in addition to α and π , it becomes straightforward within the cranking model to simultaneously perform shell correction calculations for a large number of distinct configurations. At each spin value and for each configuration separately, the nuclear energy can be minimized with respect to the deformation parameters and it is thus possible to follow the smooth evolution of each configuration in both energy and deformation, even in regions where it is no longer yrast. It is primarily with calculations performed by this method, referred to as the configuration-dependent shell-correction approach, that the experimental results presented in this thesis will be compared.

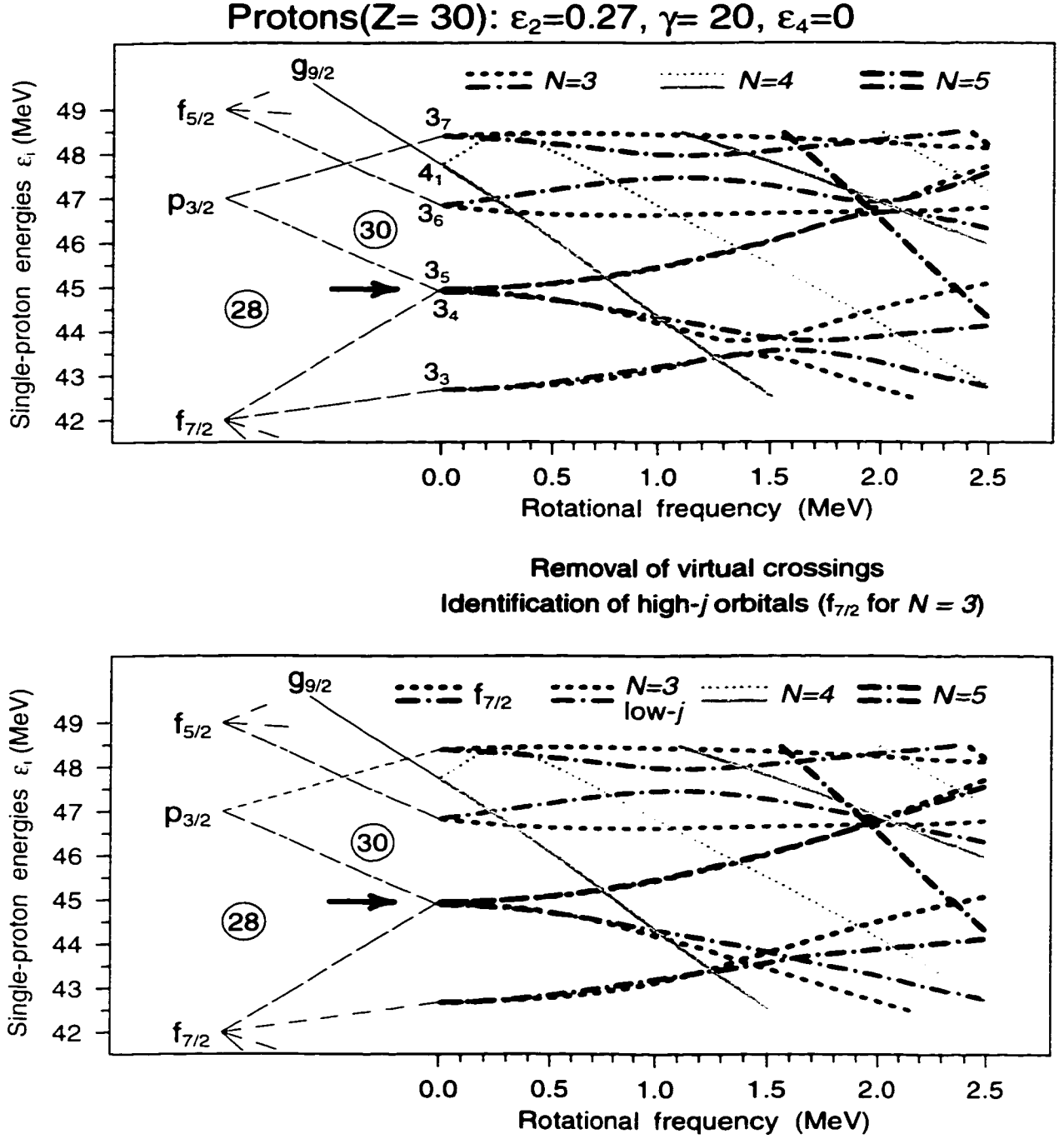


Figure 2.7: Single-proton Routhians calculated for ^{62}Zn at a deformation $\varepsilon_2 = 0.27$, $\varepsilon_4 = 0.0$, $\gamma = 20^\circ$. Different line types represent different combinations of parity π and signature α , as defined in Fig. 2.6. The lower panel illustrates the removal of virtual crossings between the high- j ($f_{7/2}$) and low- j $N=3$ orbitals [Rag 97].

2.4 Pairing

In the discussion of shell-model orbitals presented so far, the residual interactions (Eq. 1.5) between the valence nucleons have been largely ignored. These residual interactions do, however, have important effects on the structure of the nucleus.

As an example, consider a pair of like nucleons occupying a single j -shell outside a doubly-magic spherical core. Antisymmetrization of the wavefunction for this pair allows their angular momenta to couple to the values $I = 0, 2, 4, \dots, (2j - 1)$. In the independent-particle shell model all of these states are degenerate and there is no mechanism to account for the experimental fact that all even-even nuclei have $I^\pi = 0^+$ ground states. This can, however, be understood if a short-range attractive interaction between the valence nucleons is included in the nuclear Hamiltonian. If the two nucleons occupy “time-reversed” orbitals with magnetic substate quantum numbers $+m$ and $-m$, semi-classically corresponding to orbiting the nucleus in the same plane but in opposite directions, their wavefunctions will have a very large spatial overlap. A short-range attractive residual interaction will thus favour this configuration, which gives $I^\pi = 0^+$, over configurations where the $|m|$ values for the nucleons are different and the overlap of the wavefunctions is smaller. In an even-even nucleus, all of the nucleons “pair off” in this fashion and the ground state is therefore always $I^\pi = 0^+$, as observed.

In the case of a pair of non-identical nucleons occupying a j -shell all spin values between 0 and $2j$ are allowed and favoured configurations with large spatial overlaps occur both for time-reversed orbits (giving $I = 0$ or 1 depending on the orientation of the neutron and proton intrinsic spins) and time-symmetric orbits (giving $I = 2j$). Such neutron-proton pairings are particularly important in odd-odd $N = Z$ nuclei, where the odd particles occupy equivalent orbitals (see [Rud 96], for example).

2.4.1 The Pairing Interaction

In the study of heavy and intermediate-mass nuclei, the short-range residual interactions between valence nucleons are often described by an idealized pairing interaction H_{pair} . For the case of two identical nucleons coupling to spin I and a set of j -shells j_i , this pairing interaction is defined by the matrix elements [BM 75]

$$\langle j_1 j_2, I | H_{pair} | j_3 j_4, I' \rangle = -G \left(j_1 + \frac{1}{2} \right)^{\frac{1}{2}} \left(j_3 + \frac{1}{2} \right)^{\frac{1}{2}} \delta_{j_1 j_2} \delta_{j_3 j_4} \delta_{I,0} \delta_{I',0} \quad (2.65)$$

where, because of the Coulomb repulsion between protons, the pairing strength G is adjusted separately for protons and neutrons (typical values are $G_p \approx 17A^{-1}$ MeV and $G_n \approx 25A^{-1}$ MeV [GM 96]). The diagonal terms (all j_i equal) in Eq 2.65 lower the energy of the $I^\pi = 0^+$ state by $G(j + 1/2)$, where the factor $(j + 1/2)$ is the number of pairs of magnetic substates coupling to spin 0. It is also important to note that the pairing interaction has nondiagonal terms of the form $\langle (j)^2, 0 | H_{pair} | (j')^2, 0 \rangle$ that “scatter” pairs between different j -shells. These terms build up correlations that further depress the energy of the ground state, which is formed by a coherent superposition of states with pairs occupying different j -shells. In the presence of pairing, the orbitals are therefore characterized by fractional occupation numbers, as opposed to the independent-particle model in which a particular orbital either is occupied or is not occupied.

In direct analogy with the pairing of electrons with opposite linear momenta in the BCS theory of superconductivity [BCS 57], the pairing of nucleons with opposite angular momenta in nuclei [BMP 58], creates a pairing gap Δ . In nuclei this gap is simply the odd-even binding energy difference and global fits to nuclear masses indicate that its average dependence on A is well described by [BM 69]

$$\Delta = \frac{12}{\sqrt{A}} \text{ MeV}. \quad (2.66)$$

In the presence of this pairing gap, the shell-model notion of independent particles is replaced by Bogolyubov quasiparticles [Bog 58], which are noninteracting linear combinations of single-particle states, with excitation energies E_k related to Δ , the Fermi energy λ , and the single-particle energies ϵ_k by

$$E_k = \sqrt{(\epsilon_k - \lambda)^2 + \Delta^2}. \quad (2.67)$$

The breaking of a pair in an even-even nucleus, which corresponds to a 2 quasiparticle state, thus requires an energy $E_{k_1} + E_{k_2} \geq 2\Delta$, and only collective excitations are found in even-even nuclei below this 2Δ energy gap.

2.4.2 Backbending

Pairing correlations can have important effects on the rotational behaviour of the nucleus. In particular, the “backbending” phenomenon [Joh 72] can be explained as the result of pair breaking by the Coriolis force in a rotating nucleus [Ste 72]. As an example, consider a pair of $i_{13/2}$ neutrons in the deformed rare-earth nucleus ^{168}Hf . If this pair is broken, the angular momenta of the two neutrons can be aligned with the rotation axis. This angular momentum, however, is gained at the cost of the pairing energy 2Δ , so that at zero rotational frequency the band built on the aligned configuration (referred to as the s-band) is highly excited relative to the ground band (g-band) built on the paired configuration. However, with increasing rotational frequency the Coriolis force favours the aligned configuration and, as shown in Fig. 2.8(a), at a certain crossing frequency ($\hbar\omega_c \approx 0.26$ MeV in this case) the energy gained from the Coriolis interaction in the aligned band overcomes the pairing energy in the ground band. It then becomes energetically favourable for the nucleus to gain angular momentum by breaking the pair and aligning their spins with the rotation axis, rather than rotating more rapidly in the paired configuration.

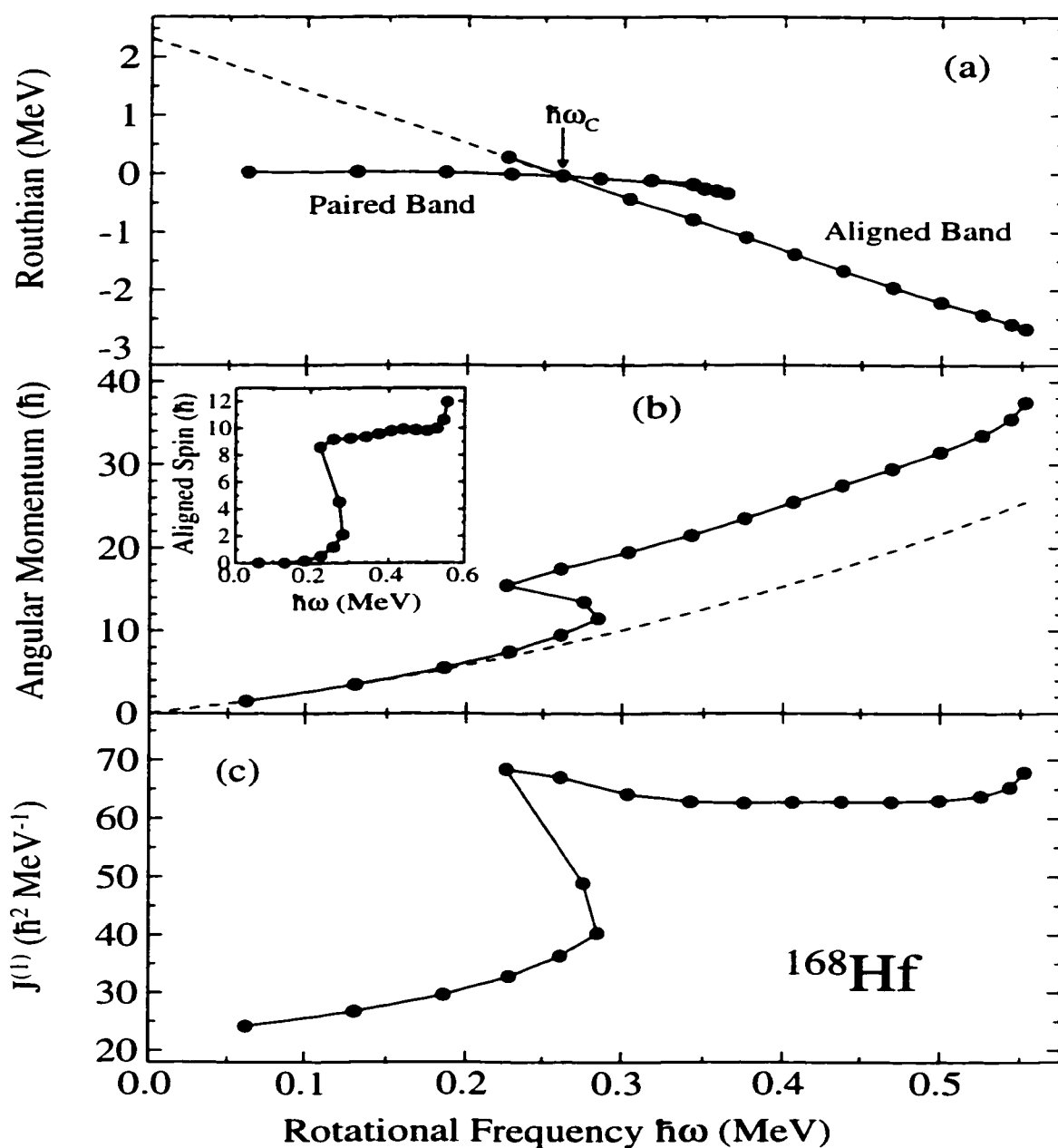


Figure 2.8: “Backbending” plots for ^{168}Hf . In (a) the experimental Routhian for the aligned s-band is shown with the paired g-band taken as the reference. The crossing frequency $\hbar\omega \approx 0.26$ MeV is indicated and an extrapolation of the s-band to zero frequency provides an estimate of the pairing gap $2\Delta \sim 2.3$ MeV. In (b) the angular momentum for the yrast cascade is shown and the difference between the data and the smooth extrapolation of the g-band (dashed curve) defines the aligned spin (shown in the inset). Panel (c) shows the backbend in the $\mathcal{J}^{(1)}$ moment of inertia at the crossing frequency. Data from [Bec 87].

The effect of this Coriolis-induced alignment is clearly seen in Fig. 2.8(b) where a large jump in angular momentum occurs at the crossing frequency. The aligned spin Δi of the broken neutron pair can be determined by subtracting the smooth extrapolation of the g-band (dashed line) from the experimental data. As shown in the inset of Fig. 2.8(b), these two particles contribute $\sim 10\hbar$ to the angular momentum of the s-band, in good agreement with theoretical expectations for the alignment of a pair of $i_{13/2}$ neutrons in this mass region [Ben 79].

As shown in Fig. 2.8(c), a “backbend” in $\mathcal{J}^{(1)}$ also occurs at the crossing frequency. Although such rapid changes in the moment of inertia are characteristic of the alignment process, how dramatic the effect is depends on the strength of the interaction between the aligned and paired bands [BFM 86]. If the interaction is weak, the alignment occurs abruptly at the crossing frequency and a strong backbend is observed. On the other hand, if there is strong mixing of the aligned and paired bands, the alignment process takes place over an extended spin range (a “gradual” alignment) and only a gentle upbend in the moment of inertia may be observed.

As the rotational frequency increases further, the Coriolis force breaks and aligns additional pairs of nucleons (a second upbend in ^{168}Hf , interpreted as the alignment of a pair of $h_{11/2}$ or $i_{13/2}$ protons [Cha 83], can be seen in Fig. 2.8 at $\hbar\omega \approx 0.55$ MeV). Eventually these broken pairs block the orbitals near the Fermi surface required to generate the pairing correlations and the pairing gap is expected to disappear at high rotational frequency [Mot 60]. For this reason, and because it greatly simplifies computations, pairing correlations are often neglected in theoretical calculations for high-spin states. It should, however, be clear from the present discussion that these calculations cannot be expected to reproduce the details of nuclear structure at low spin, where pairing is certainly important.

2.5 Band Termination

A major theme in nuclear structure physics, and one with which we have been concerned throughout this chapter, is the interplay between collective and single-particle degrees of freedom. Perhaps there is no better example of this interplay than the loss of collectivity associated with the termination of a rotational band.

The termination of rotational bands in nuclei is intimately related to the finite size of the nuclear system. For a macroscopic object, additional angular momentum can always be generated by increasing the rotational frequency until the forces binding the object can no longer support the rapid rotation and the body breaks apart. The nucleus, however, is a finite quantum system and its total angular momentum must ultimately be associated with a sum of contributions from individual nucleons. For any particular band, corresponding to a fixed intrinsic configuration, there is therefore a limit to the available spin which is simply given by aligning the angular momenta of all the contributing nucleons along one axis, remembering to obey the Pauli principle. For rotational bands in heavy nuclei, a large number of valence particles are usually involved and the terminating states, which may be at spins well above the fission cut-off, are generally not observed. However, in light and intermediate-mass nuclei, and in certain special cases in heavier nuclei, the effects of band termination may be directly observed.

A classic example of band termination occurs in the light nucleus ^{20}Ne [Rag 81]. With only 2 valence protons and 2 valence neutrons in the $d_{5/2}$ orbital outside a doubly-magic ^{16}O core, the maximum spin available in the ground-state band of this nucleus is $(\frac{5}{2} + \frac{3}{2})_{\pi} + (\frac{5}{2} + \frac{3}{2})_{\nu} = 8\hbar$, and this terminating state was studied in detail more than 25 years ago [Hau 72, Ale 72]. More recently, considerable attention has been focused on the study of similar band terminations in $N \approx Z$ nuclei in the $A \sim 50$ mass

region, where the maximum spin available to the valence particles in pure $1f_{7/2}$ -shell configurations is $I_{max} \leq 16\hbar$ and terminating states have now been identified in several of these nuclei [Cam 96, Len 96, Len 97, OLe 97, Cam 98, Sve 98c]. In heavy nuclei, band terminations were first predicted [Ben 83] and observed [Bak 85, Ste 85, Tjo 85] in nuclei around ^{158}Er . In these nuclei, the maximal alignment of ~ 10 – 12 valence particles outside a ^{146}Gd core leads to particularly favoured terminating states at $I \sim 35$ – $50\hbar$ [Rag 85, Rag 86]. However, as shown schematically in the upper panel of Fig. 2.9(a), these configurations rapidly move away from the yrast line below their “favoured” terminations, and it is therefore not possible to follow their evolution over an extended spin range prior to termination.

2.5.1 Smooth Termination

Recently, a new form of band termination has been identified in ^{109}Sb [Jan 95, Rag 95, Fos 94] and several neighbouring nuclei (see Fig. 4 in [Jan 97]). In these nuclei, proton excitations across the $Z = 50$ shell gap lead to well developed collective rotational bands, yet the number of valence particles and holes (~ 10 – 15) remains small enough that these bands terminate at experimentally observable spins ($I \sim 40\hbar$). Unlike the terminations in nuclei around ^{158}Er , where the full alignment of the valence particles leads to an energetically favoured state, in the nuclei around ^{109}Sb the last few spin units, which are obtained primarily from the alignment of the valence holes, are energetically very costly [Rag 95, Afa 95]. As shown in Fig. 2.9(b), the successively higher energy cost of building spin in these bands is reflected in moments of inertia which decrease with increasing spin. These bands are, however, yrast or near-yrast over a wide spin range prior to termination and, as shown in the lower panel of Fig. 2.9(a), can absorb the high cost of their “unfavoured” terminations while remaining close to the yrast line. These structures can therefore often be followed over extended spin

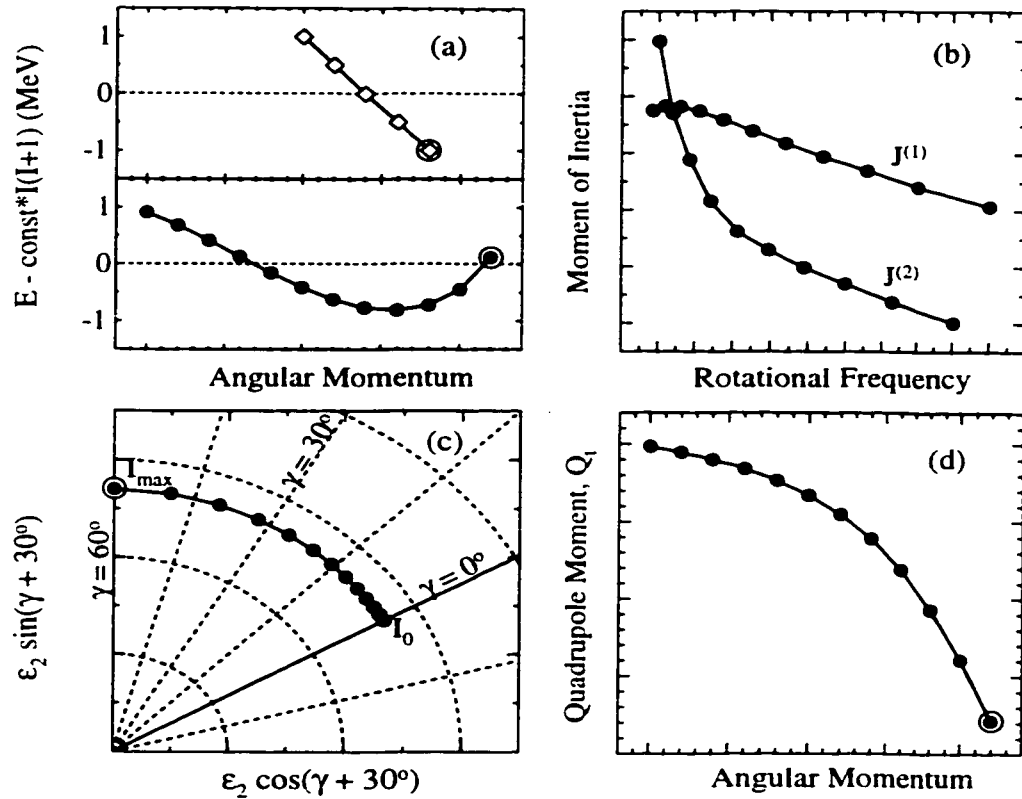


Figure 2.9: Schematic diagrams illustrating smooth band termination. (a) Energy relative to an $I(I + 1)$ reference for a favoured termination (upper panel) and for a smoothly terminating band (lower panel). Terminating states are indicated by large open circles. (b) Decreases in the kinematic $\mathcal{J}^{(1)}$ and, particularly, the dynamic $\mathcal{J}^{(2)}$ moments of inertia. (c) Shape trajectory in the ϵ_2, γ plane, starting from prolate ($\gamma = 0^\circ$), gradually becoming triaxial, and finally terminating in an oblate ($\gamma = 60^\circ$) state at $I = I_{\text{max}}$. (d) The loss of collectivity associated with smooth band termination leads to a decreasing transition quadrupole moment Q_t with increasing spin.

ranges up to their terminating states, and such smoothly terminating bands offer a unique opportunity to observe the gradual evolution of a fixed nuclear configuration from collective rotation to a noncollective terminating state.

The proton-rich $A \sim 60$ mass region is, in many ways, similar to the region around ^{109}Sb , with the $Z = 28$ shell gap and the ^{56}Ni core of the former replacing the $Z = 50$ shell gap and ^{100}Sn core of the latter. In Chapter 5, the first observation of the terminating states of rotational bands in the $A \sim 60$ mass region will be discussed.

2.5.2 Shape Changes and Collectivity

In the theoretical interpretation of smoothly terminating bands, the nucleus is predicted to undergo a gradual shape change with increasing angular momentum, as shown in Fig. 2.9(c). At relatively low spin the nucleus is prolate ($\gamma = 0^\circ$) and rotates collectively about an axis perpendicular to its symmetry axis. However, with increasing spin the valence nucleons gradually align their angular momenta with the rotation axis and the nucleus becomes triaxial. Finally, in the terminating state all of the single-particle angular momenta are maximally aligned and, semi-classically, all of the valence nucleons can be viewed as orbiting in the equatorial plane. The nuclear shape is thus oblate ($\gamma = 60^\circ$) and, as mentioned previously, collective rotation is forbidden. The nucleus is therefore predicted to undergo a smooth evolution from collective rotation to a non-collective state.

In order to obtain a quantitative description of this gradual loss of collectivity, we note that the collective transition quadrupole moment[†] Q_t for a triaxial rotor is related to γ and the intrinsic electric quadrupole moment Q_{20} by [BM 75]:

$$Q_t = Q_{20} \frac{\cos(\gamma + 30^\circ)}{\cos(30^\circ)}. \quad (2.68)$$

Thus, as shown in Fig. 2.9(d), the transition quadrupole moment in a smoothly terminating band is predicted to decrease as γ increases with spin and should approach zero at the noncollective $\gamma = 60^\circ$ terminating state (which should decay with a strength characteristic of a single-particle transition). The first experimental confirmation of this predicted loss of collectivity associated with smooth band termination [Sve 98a][‡] represents one of the highlights of this thesis and will be discussed in Chapter 5.

[†]See Appendix A for a discussion of electromagnetic transitions in nuclei.

[‡]Concurrent with this work, Q_t measurements approaching the terminating states of bands in ^{108}Sn and ^{109}Sb have also confirmed this predicted loss of collectivity [Wad 98].

Chapter 3

Gamma-Ray Spectroscopy

Analysis of the γ rays emitted in the decay of excited nuclear states provides one of the most sensitive experimental methods for studying the structure of nuclei. In this chapter, γ -ray detector systems and data analysis techniques are discussed.

3.1 Gamma-Ray Detection

3.1.1 Interactions of Gamma Rays with Matter

Gamma rays are detected through their electromagnetic interactions within a detector. There are three types of such interactions which contribute significantly to the detection of γ rays: the photoelectric effect, Compton scattering, and pair production. In the photoelectric effect, a γ ray is absorbed in the process of ionizing an atom of the detector material, the difference between the energy of the γ ray and the binding energy of the electron appearing as the kinetic energy of the emitted photoelectron. In the Compton scattering process, a γ ray again ionizes an atom of the detector material and transfers energy to a recoil electron. However, the γ ray, of initial energy E_γ , is not absorbed but scatters through an angle θ and emerges with a reduced energy E'_γ . Assuming that the binding and kinetic energies of the electron

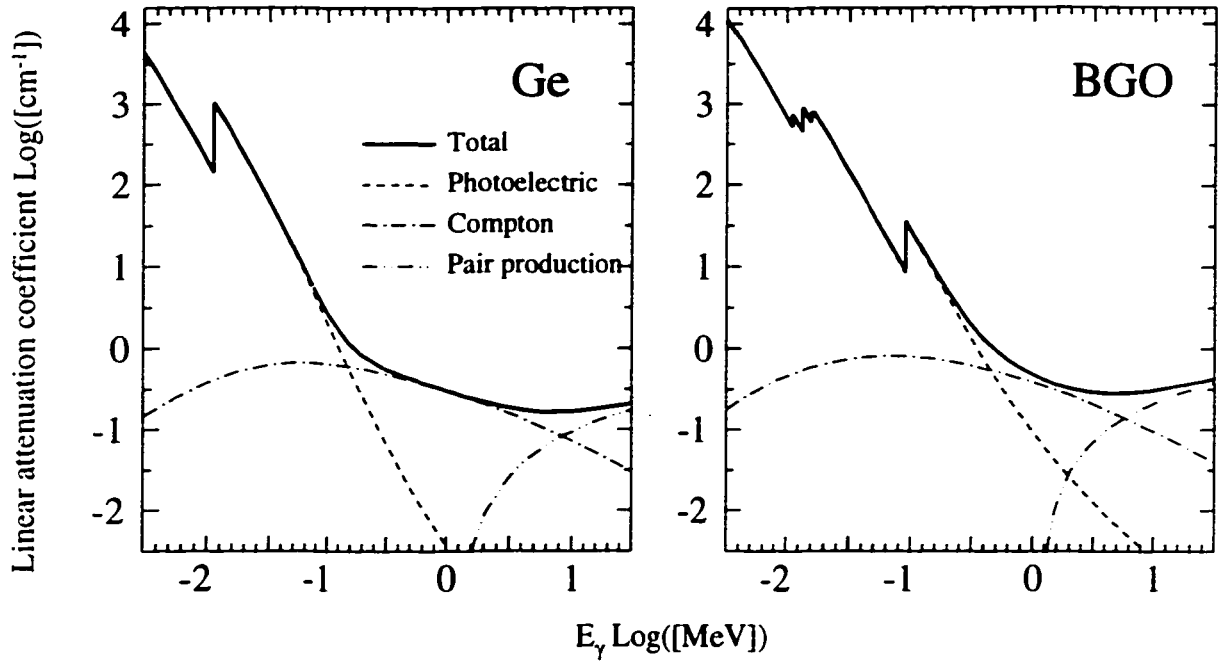


Figure 3.1: Total, photoelectric, Compton scattering, and pair production linear attenuation coefficients for germanium (Ge) and bismuth germanate (BGO) [BH 87].

before the scattering are negligible compared to E_γ , E'_γ is given by

$$E'_\gamma = E_\gamma \left[1 + \frac{E_\gamma}{m_e c^2} (1 - \cos \theta) \right]^{-1} \quad (3.1)$$

where $m_e c^2 = 511$ keV is the rest energy of the electron. Finally, if the energy of a γ ray is greater than twice the electron rest energy, the interaction between the γ ray and the electric field of a nucleus[†] can lead to a pair production event in which the γ ray is absorbed and an electron-positron pair is created. The positron, after slowing, will annihilate with an atomic electron producing two 511 keV γ rays. These γ rays may then also interact by Compton scattering or photoelectric absorption.

The cross sections for these interactions depend strongly on the energy of the γ ray and the properties of the detector material. Figure 3.1 shows the total

[†]Pair production can also occur in the field of an atomic electron, but for detector materials with $Z \gg 1$ this cross section is negligible compared to pair production in the nuclear field.

linear attenuation coefficient, and its photoelectric, Compton, and pair production components, for the two detector materials used in this work, germanium Ge and bismuth germanate $\text{Bi}_4\text{Ge}_3\text{O}_{12}$ (commonly referred to as BGO). For relatively low-energy γ rays, the photoelectric cross section, which decreases roughly as $E_\gamma^{-3.5}$ [Kno 89] but has large jumps when the γ -ray energy is sufficient to overcome the binding energy of the K, L, M, \dots electron shells, dominates the γ -ray interactions. The photoelectric cross section also depends strongly on the atomic number of the detector material, increasing as Z^n , where n depends on the γ -ray energy but is typically between 4 and 5 [Kno 89]. The Compton scattering cross section increases linearly with the density of electrons in the detector material and has the rather gentle energy dependence shown in Fig. 3.1. The pair production cross section, which increase with atomic number roughly as Z^2 [Kno 89], rises sharply with γ -ray energy above the 1.022 MeV threshold and for intermediate and high- Z detector materials typically becomes dominant at γ -ray energies of 5–10 MeV. Based on these cross sections, it is clear that maximum γ -ray detection efficiency will be obtained with high- Z , high-density materials.

3.1.2 Gamma-Ray Detectors

The end result in all of the γ -ray interactions discussed above is the production of energetic electrons (and positrons in the case of pair production). These electrons (and positrons) scatter from, and transfer energy to, other electrons, exciting them from the valence to the conduction band of the detector material and thereby producing a large number of electron-hole pairs. The number of electron-hole pairs produced is proportional (within statistical fluctuations) to the energy deposited in the detector. If the γ ray is completely absorbed in the detector, a measurement of the number of these pairs thus yields a measure of the γ -ray energy. Different detector types are based on different methods of measuring this number of electron-hole pairs.

In a scintillator, the primary detector is optically coupled to either a photomultiplier (PM) tube or a photodiode, in which a secondary electric signal is produced by the light emitted when the electrons and holes in the primary detector recombine. The main scintillator employed in this work is BGO, which has both a high density (7.3 g/cm^3) and a large atomic number ($Z = 83$) for its bismuth component. The resulting high γ -ray detection efficiency of BGO makes it ideal for use in Compton suppressors (see Section 3.1.3) and γ -ray sum-energy calorimeters (see Section 3.2.1). However, the poor energy resolution of scintillator detectors ($\sim 100 \text{ keV}$ at $E_\gamma = 1 \text{ MeV}$ for BGO) makes them of little use for detailed spectroscopic studies.

Semiconductor detectors made from single crystals of hyper-pure (HP) germanium or silicon provide the experimentalist with the excellent energy resolution ($\sim 2 \text{ keV}$ at $E_\gamma = 1 \text{ MeV}$ for typical large-volume HPGe detectors) necessary for detailed spectroscopy. These detectors are operated as massive diodes, with almost the entire crystal being depleted of charge carriers by the application of a large (several kV) reverse-bias voltage. The electron-hole pairs created when a γ ray interacts in the depletion region are rapidly swept away by the strong electric field across the detector and directly form a signal with a magnitude proportional to the energy deposited in the crystal. Although semiconductor detectors made from silicon ($Z = 14$) are often used for low-energy photons, the higher efficiency of germanium ($Z = 32$) has made HPGe detectors the modern standard for discrete-line γ -ray spectroscopy and these detectors have been used throughout this work. One disadvantage of germanium is that its relatively small band gap ($\approx 0.7 \text{ eV}$) leads to a high leakage current from thermally activated electron-hole pairs. In order to minimize the detector noise associated with this leakage current, bulky cryostats are required to maintain the detectors at liquid nitrogen temperature.

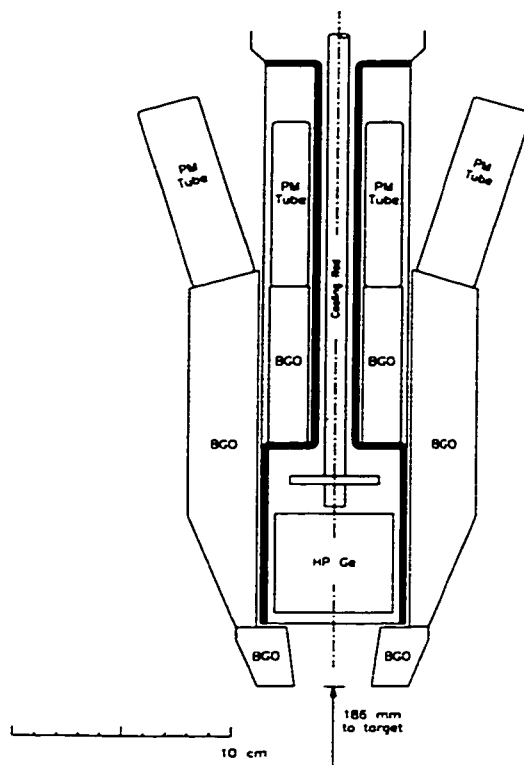


Figure 3.2: Schematic diagram of one of the HPGe detectors of the 8π Spectrometer and its BGO Compton suppression shield. Adapted from [Tar 83].

3.1.3 Compton Suppression

The majority of γ rays emitted in heavy-ion fusion-evaporation reactions have energies in the range of a few hundred keV to a few MeV, where the dominant interaction in a Ge detector is Compton scattering (see Fig. 3.1). Following a primary Compton event, the scattered γ ray may again Compton scatter and may eventually undergo photoelectric absorption. In such “photopeak” events, the detector signal provides a true measure of the γ -ray energy. However, even with large-volume Ge detectors, the majority (typically $\gtrsim 75\%$ at $E_\gamma \approx 1$ MeV) of Compton-scattered γ rays escape from the detector after depositing only a fraction of their energy. The detector signal then does not represent the full energy of the incident γ ray, and these events contribute

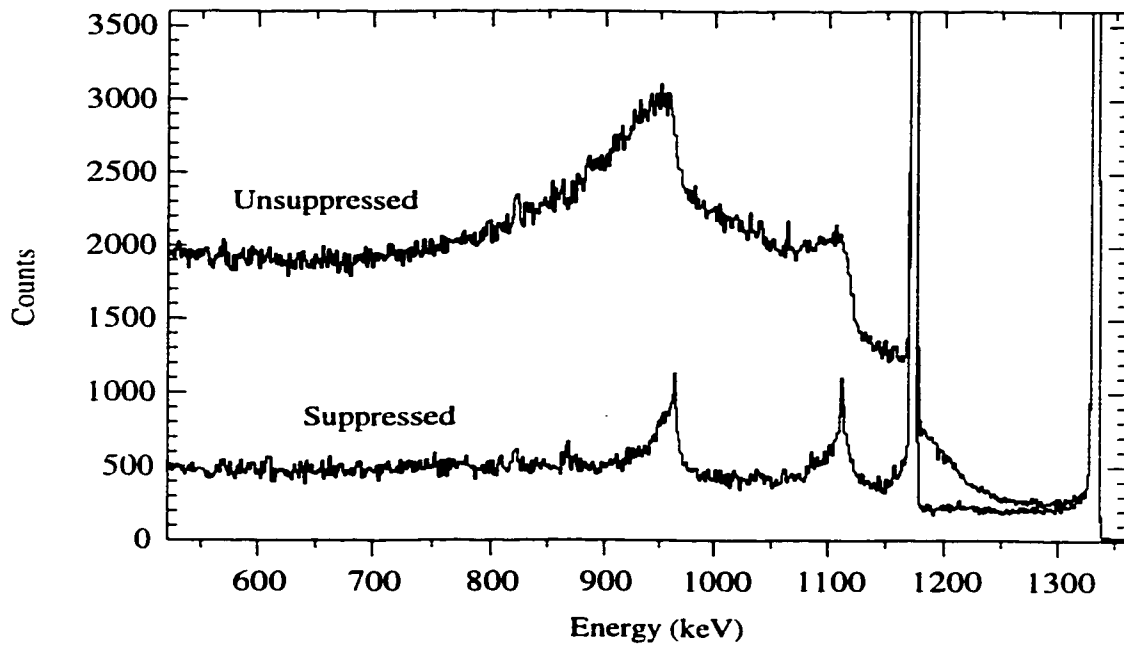


Figure 3.3: γ -ray spectra from a ^{60}Co source taken with one of the Gammasphere HPGGe detectors with and without the BGO Compton suppression shield enabled. The spectra are normalized to equal photopeak areas. The photopeak-to-total ratio increases from 0.24 in the unsuppressed spectrum to 0.57 in the suppressed spectrum.

an undesirable background to the γ -ray spectrum.

In order to reduce the Compton background, it has become standard to surround Ge detectors with BGO suppression shields, as shown in Fig. 3.2. The Ge detector and its BGO shield are operated in anticoincidence so that when a γ ray scatters from the Ge crystal and interacts in the surrounding BGO the signal from the suppression shield is used to veto the Ge signal. If only the Ge detector fires, it is assumed that the γ ray deposited its entire energy in the detector and the Ge signal is then taken as a valid measure of the γ -ray energy. Since the veto signal from the suppression shield does not require high energy resolution, the high efficiency of BGO makes it ideal for this purpose. Although Compton suppression is never 100% efficient, the substantial improvement in the photopeak-to-total (P/T) ratio obtained with a Compton suppressed Ge detector is clearly illustrated in Fig. 3.3.

3.1.4 Calibration

After shaping and amplification, the electrical pulse arising from a γ -ray interaction in a Ge detector is converted to a digital channel number proportional to the pulse height by an analogue to digital converter (ADC). The two basic quantities that can be determined from a spectrum of the ADC pulse heights are the γ -ray energies (from the channel numbers at which the peaks occur) and relative intensities (from the areas of the peaks). In order to extract these quantities, the detector response must be calibrated for both energy and relative efficiency. These calibrations are performed before and/or after each experiment by recording γ -ray spectra from sources with accurately known γ -ray transition energies and relative intensities.

The γ -ray energy can be expressed as a polynomial in the channel number n

$$E_\gamma = a + bn + cn^2 + \dots \quad (3.2)$$

where the constants a, b, c, \dots are determined by fitting Eq. 3.2 to the measured centroids and the accepted energies of γ rays from a source such as ^{152}Eu , which has several intense γ rays between 122 keV and 1408 keV. The $A \sim 60$ nuclei studied in this work have many high-energy transitions above 1.4 MeV and energy calibrations were therefore also performed with a ^{56}Co source, which emits intense γ rays with energies up to 3451 keV. An example of an energy calibration from one of the Gammasphere experiments discussed in this thesis is shown in Fig. 3.4. Although an ideal ADC response would be linear with $a = c = \dots = 0$ and b set to some value chosen by the experimenter ($\frac{2}{3}$ keV/channel for the data shown in Fig. 3.4), detailed energy calibrations usually reveal non-negligible values for both the offset a and the quadratic c parameters. As shown in the inset of Fig. 3.4, it is essential to include these terms in order to obtain accurate energy measurements, particularly for

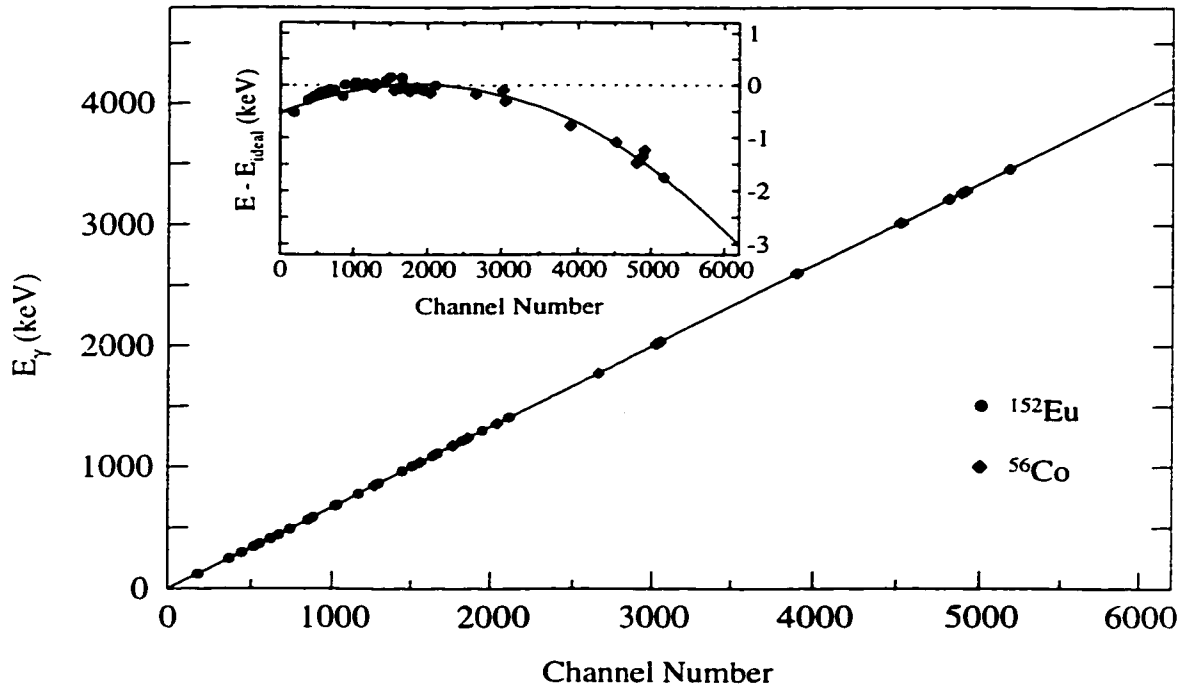


Figure 3.4: Energy calibration for the GSFMA9 Gammasphere experiment performed with ^{152}Eu and ^{56}Co γ -ray sources. The inset shows the difference between the actual energy calibration and an ideal ADC response with $b = \frac{2}{3}$ keV/channel and $a = c = 0$.

high-energy γ rays.

The relative photopeak efficiency ϵ of a Ge detector for γ rays of various energies is modeled by the function [Rad 95a]

$$\ln(\epsilon) = \left[(A + Bx + Cx^2)^{-G} + (D + Ey + Fy^2)^{-G} \right]^{-1/G} \quad (3.3)$$

where

$$x = \ln\left(\frac{E_\gamma}{100 \text{ keV}}\right), \quad y = \ln\left(\frac{E_\gamma}{1000 \text{ keV}}\right). \quad (3.4)$$

The constants A , B , and C describe the low-energy efficiency of the detector, determined primarily by the absorption of γ -rays in materials (auxiliary detectors, scattering chamber, detector housing, etc.) in front of the detector, D , E , and F describe the decrease in photopeak efficiency for high-energy γ rays, and the parameter G determines the smooth transition between these two limits. While ^{152}Eu and ^{56}Co sources

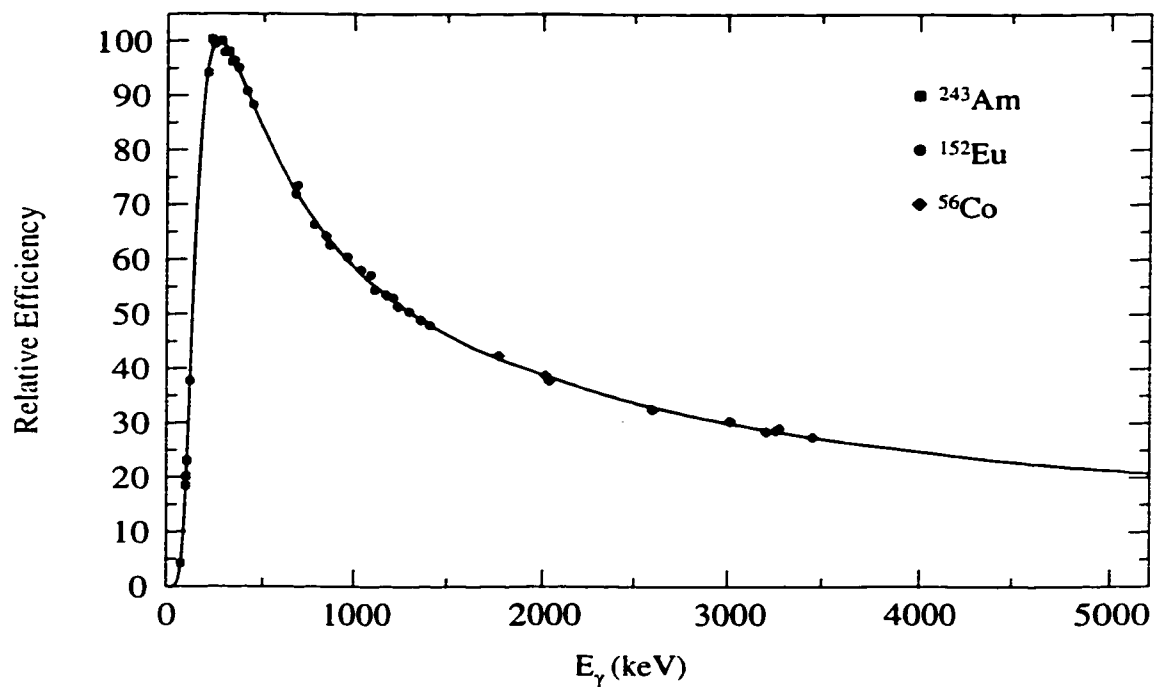


Figure 3.5: Efficiency calibration for the GSFMA9 Gammasphere experiment performed with ^{243}Am , ^{152}Eu , and ^{56}Co γ -ray sources placed inside the Microball charged-particle detector array. The data from the three sources have been empirically normalized in regions where their energies overlap and all of the data have been normalized to a relative efficiency of 100 at $E_\gamma = 265$ keV.

provide a good measure of the relative efficiency at intermediate and high energies, they do not provide enough data points to accurately determine the low-energy “roll-over” in the efficiency. For this purpose, a source such as ^{243}Am with a number of intense low-energy transitions is used. A relative efficiency calibration performed with ^{243}Am , ^{152}Eu , and ^{56}Co sources for one of the Gammasphere experiments discussed in this thesis is shown in Fig. 3.5. It is also important to note that, for efficiency calibrations, the γ -ray sources must be placed at the target position, inside auxiliary systems such as charged-particle detectors, so that the scattering and absorption of γ rays during the calibration reflects the actual experimental conditions.

3.2 Detector Arrays

Modern γ -ray spectroscopy is performed with large multi-detector arrays that subtend close to the full 4π solid angle around the target. In this section, two such detector systems, the 8π Spectrometer and the Gammasphere array, are discussed.

3.2.1 The 8π Spectrometer

The Canadian 8π Spectrometer [Tar 83] is regarded as the best of the “second-generation” γ -ray detector arrays. It consists of a 72-element BGO inner ball and 20 HPGe detectors, each with a BGO Compton suppression shield (see Fig. 3.2). A photograph of one hemisphere of the 8π Spectrometer is shown in Fig. 3.6.

The BGO ball, which has an inner radius of ~ 11 cm, a thickness of ~ 7 cm, and subtends 95% of the solid angle, is formed by tiling the sphere with 60 hexagonal and 12 pentagonal detectors[†]. On an event-by-event basis, the BGO ball detects, with high efficiency, a γ -ray sum energy H and multiplicity K , which can be used to select events of interest (see Chapter 4). The “flash” of γ -rays detected in the BGO ball also provides the time reference and hardware trigger for an event.

The 20 HPGe detectors, and their suppression shields, are located outside the BGO ball, with the front faces of the Ge crystals 22 cm from the target. They are arranged in four rings of five detectors at angles of 37° , 79° , 101° , and 143° relative to the beam axis and view the target through hexagonal holes in the inner ball (see Fig. 3.6), each of which subtends a solid angle of 0.25%. Events are recorded when a minimum number (usually 2) of the HPGe detectors are not suppressed by their Compton shields and fire in prompt coincidence with a trigger from the BGO ball with K exceeding a threshold value chosen by the experimenter.

[†]Two of the pentagons are often removed, one to allow the beam to enter the ball and, if the beam is dumped outside the array, one to allow it to exit.

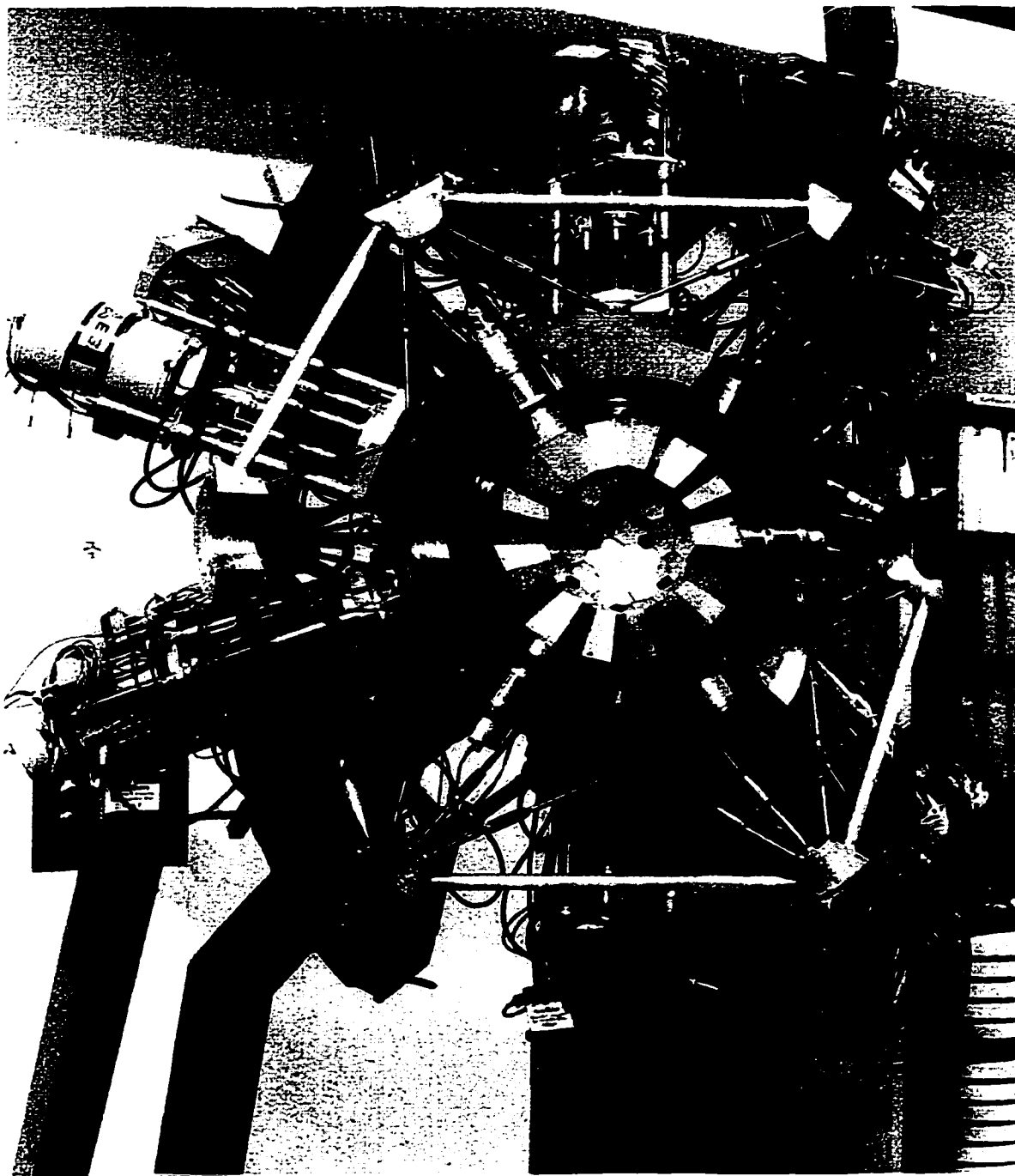


Figure 3.6: One hemisphere of the 8π Spectrometer. Eight of the hexagonal holes in the BGO inner ball through which the HPGe detectors view a target placed at the center of the ball are visible. The beam would enter from the left.



Figure 3.7: A portion of the Gammasphere array.

3.2.2 Gammasphere

The Gammasphere array [DD 88, Lee 90] is a “third-generation” γ -ray spectrometer designed to detect high-fold[†] γ -ray coincidences with high efficiency. It consists of a maximum of 110 large-volume HPGe detectors within hexagonal BGO Compton suppression shields packed in a near- 4π geometry around the target. These detectors are situated in 17 rings with angles ranging from 17.3° to 162.7° relative to the beam axis and the front faces of the Ge crystals are 25 cm from the target location. A portion of the Gammasphere array is shown in Fig. 3.7.

Unlike the 8π spectrometer, Gammasphere does not have an inner ball. Hevimet[‡]

[†]“Fold” refers to the number of γ rays from a particular event detected in coincidence.

[‡]A tantalum-nickel-copper alloy with a density of $\approx 19 \text{ g/cm}^3$ [Dev 96].

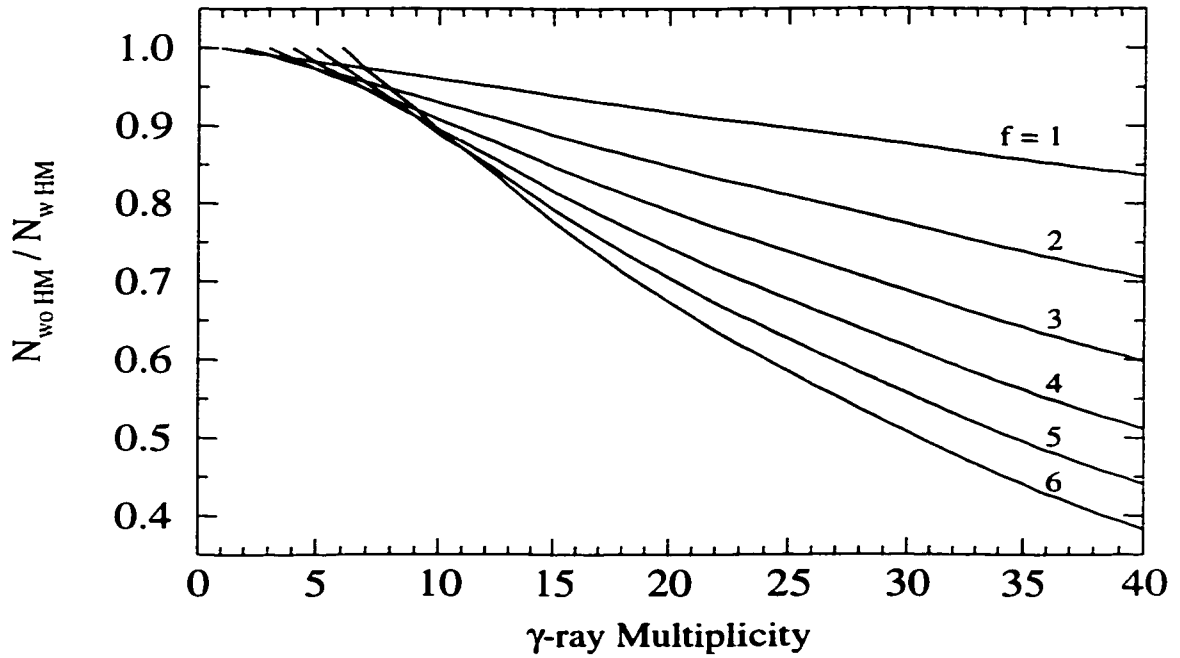


Figure 3.8: Monte Carlo simulation of the loss of statistics associated with removing the Hevimet collimators from Gammasphere. For each fold f , the statistics have been calculated by unpacking all higher f' -fold coincidences into $\binom{f'}{f}$ events. The lines represent the ratio of the number N_{woHM} of such events recorded without the collimators to the number N_{wHM} recorded with the collimators.

shields are therefore usually placed in front of the Compton suppressors in order to prevent the false rejection of good HPGe photopeak events resulting from a second γ ray directly hitting the Compton suppressor. In this mode of operation, however, almost half of the solid angle is viewed by absorbing material and poor H and K responses are obtained. If the Hevimet collimators are removed, Gammasphere becomes a 4π γ -ray detector, with roughly half of the solid angle viewed by the HPGe crystals and half viewed directly by the BGO suppression shields. Although good H and K resolution is then obtained [Dev 96], photopeak efficiency is clearly lost to the abovementioned false vetos. The results of a Monte Carlo simulation of the loss of statistics associated with removing the Hevimets is shown in Fig. 3.8. For high γ -ray multiplicities and high-fold coincidences (the usual case in high-spin studies of

heavy nuclei), the loss of statistics can be severe ($\gtrsim 50\%$) and the Hevimets are rarely removed. In the $A \sim 60$ mass region, however, high-spin events correspond to γ -ray multiplicities of ~ 10 –15 and 2 or 3 fold coincidences are typically analyzed. The loss of statistics (~ 10 –20%) is then acceptable and is, in fact, greatly outweighed by the improved channel selection made possible by the H and K information (see Chapter 4). Therefore, the Hevimet collimators were removed in all of the Gammasphere experiments performed during this work.

3.2.3 Efficiency, Resolution, and Sensitivity

The photopeak efficiency ϵ of a single HPGe detector for γ rays of a particular energy is largely determined by the size and geometry of the detector. In order to achieve high detection efficiencies, large-volume detectors are clearly desirable. The number N of these detectors available for an array is then, to a large extent, determined by monetary constraints. In designing an array, an important question that arises is what distance from the target the detectors should be placed or, equivalently, what solid angle Ω should be viewed by each detector. The total photopeak efficiency of the array for a single γ ray is given by $N\epsilon\Omega$ and is maximized by packing the detectors close to the target so that $N\Omega \approx 4\pi$. There are, however, several problems with this design philosophy. Among these are (i) degradation of the P/T ratio if enough space is not left for sufficiently thick Compton suppression shields, (ii) degradation of both P/T and ϵ resulting from two or more γ rays hitting the same detector, and, as discussed below, (iii) degradation of the γ -ray energy resolution.

A nucleus produced in a fusion-evaporation reaction typically recoils at a velocity v that is a few percent of the speed of light c . A γ ray, with energy E_γ in the rest frame of the nucleus, emitted at an angle θ relative to recoil direction is therefore

detected with a Doppler-shifted energy

$$E'_\gamma = \frac{E_\gamma \sqrt{1 - \beta^2}}{1 - \beta \cos \theta}, \quad (3.5)$$

where $\beta = v/c$. The width, or resolution, ΔE_γ of a γ -ray peak receives contributions from Doppler-broadening effects due to variations in β and θ , as well as the intrinsic resolution ΔE_{int} of the HPGe detector, and, to first order, is given by

$$\Delta E_\gamma = \left[(\Delta E_{int})^2 + (E_\gamma \cos \theta \Delta \beta)^2 + (E_\gamma \beta \sin \theta \Delta \theta)^2 \right]^{\frac{1}{2}}. \quad (3.6)$$

The variations $\Delta \beta$ and $\Delta \theta$ in Eq. 3.6 arise primarily from three sources; the “kick” given to the nucleus by the evaporated particles, the finite thickness of the target, and the opening angles of the Ge detectors. Here we consider the latter two of these, while the contribution of particle evaporation will be discussed in Section 4.2.5.

Both the beam ions and the recoil nuclei lose energy as they pass through the target (see Section 3.4.2). The nuclei produced in reactions at different locations within the target therefore emerge with different velocities[†]. As shown in Fig. 3.9, this velocity spread can dominate the γ -ray energy resolution for detectors close to the beam axis. For this reason, thin targets, or stacks thereof, are used in experiments where good energy resolution is a primary concern. For detectors at large angles relative to the beam axis, the γ -ray energy resolution is often dominated by the Doppler broadening associated with the finite opening angles of the Ge detectors. Improved resolution can be achieved, while retaining the high photopeak efficiency of a large-volume detector, by segmenting the detector (either physically or electronically) so as to obtain a better measure of the angle at which the γ ray is emitted. This technique, in electronic form, is used for the Gammasphere detectors [Mac 94] located

[†]Multiple scattering in the target also leads to a distribution of recoil angles, but this effect is small for the high recoil velocities and relatively low- Z targets and recoils involved in this work.

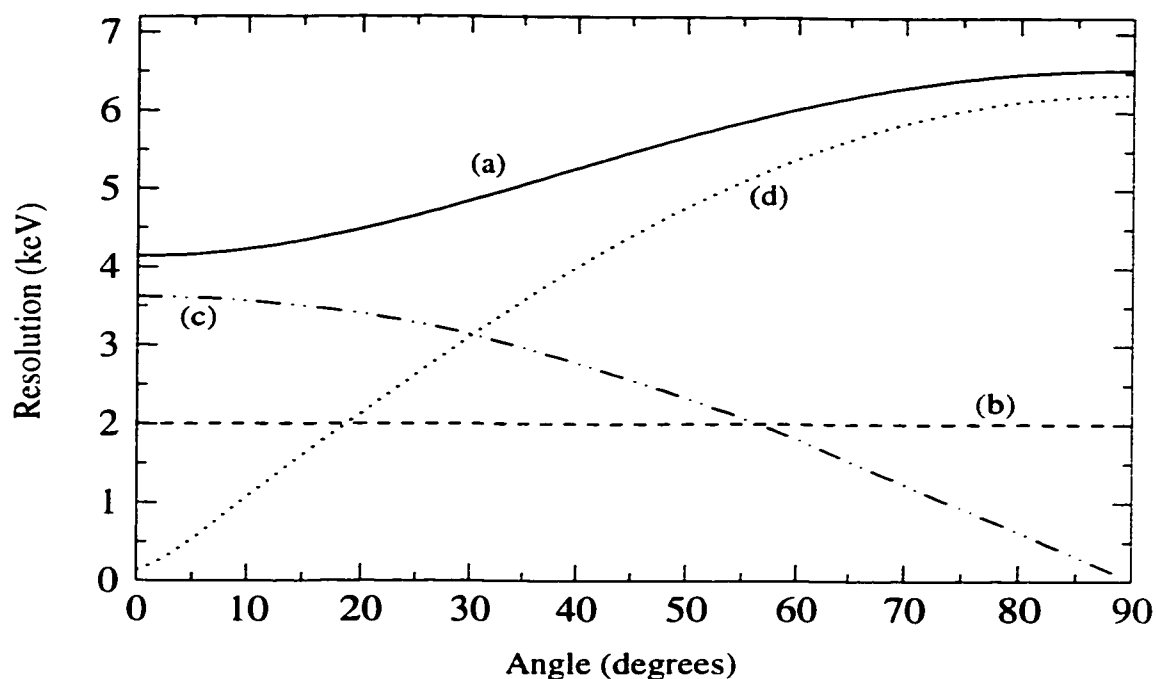


Figure 3.9: (a) The resolution for a 1 MeV γ ray from the reaction of 125-MeV ^{28}Si on ^{40}Ca as a function of the angle of the detector relative to the beam axis. Contributions from (b) the intrinsic resolution of the Ge detector (taken as 2 keV), (c) the velocity spread of the recoils due to the finite thickness of the target ($500 \mu\text{g}/\text{cm}^2$), and (d) the finite opening angle of the Ge detector (taken as 15°) are included, but not the contribution from particle evaporation (see Section 4.2.5).

at angles between 58.3° and 129.9° . Ultimately, however, a balance must be struck in the design of an array between good energy resolution, which favours detectors with small opening angles, and high efficiency, which favours detectors close to the target.

The ultimate design goal for a detector array is to achieve the highest possible sensitivity, which may be defined as the reciprocal of the weakest decay branch that can be resolved. As discussed in the detailed analysis of Radford [Rad 93], the sensitivity achieved by an array in a particular coincidence fold f depends both on the quantity of data recorded, which is proportional to the f -fold efficiency $(N\epsilon\Omega)^f$, and on the quality of this data, which is related to R^f where R describes the increase in the peak-to-background ratio per fold and is proportional to $(P/T)/\Delta E_\gamma$. For low-

fold coincidences, an enormous number of events can be recorded but the sensitivity will remain low because of the poor peak-to-background ratio. For very high-fold coincidences, excellent peak-to-background may be achieved but the sensitivity will be limited by poor statistics. At some intermediate fold, the statistical and background limits will be approximately equal and maximum sensitivity will be achieved.

The 8π Spectrometer is characterized by high quality γ - γ coincidence data but, with $N\epsilon\Omega \approx 0.008$, records limited statistics for $f > 2$. With the possible exception of searches for long rotational cascades where combinatorics may favour a triples analysis [Hac 95a], the maximum sensitivity is therefore almost always achieved in fold 2. Gammasphere, on the other hand, detects high-fold events with high efficiency ($N\epsilon\Omega \approx 0.11$ for the full array), and in Radford's [Rad 93] archetypical $A \sim 150$ high-spin experiment achieves maximum sensitivity in fold 4, increasing to fold 5 for the analysis of long rotational cascades [Hac 95a]. The experiments performed in this work, however, differ in a number of essential features from this "standard" experiment. In the $A \sim 60$ mass region, the γ -ray transition energies are relatively high and the γ -ray multiplicities are relatively low. These effects decrease the probability of detecting high-fold events and the statistical limit is encountered at lower fold than in studies of heavier nuclei. Furthermore, the powerful channel selection techniques discussed in Chapter 4 greatly enhance the peak-to-background ratio for weak reaction channels without any recourse to γ -ray coincidences, thereby reducing the low-fold background limit. Both of these effects reduce the fold at which the statistical and background limits are approximately equal and the experience gained during this work indicates that Gammasphere achieves maximum sensitivity in this mass region in fold 2 or 3. For this reason, all of the detailed spectroscopy carried out during this work was performed with either γ - γ or γ - γ - γ coincidences.

3.3 Coincidence Spectroscopy

The cascade of γ rays emitted in any particular event corresponds to one of many possible decay pathways between levels of the nucleus. If two or more of these γ rays are detected in each event, the sets of γ rays which appear in coincidence with each other can be determined and the decay pathways and level structure of the nucleus can be deduced. The techniques of coincidence spectroscopy are best illustrated by the example of the γ - γ matrix.

3.3.1 The $\gamma - \gamma$ Coincidence Matrix

Consider an event in which two γ rays, with energies $E_{\gamma 1}$ and $E_{\gamma 2}$, are detected in coincidence. This information can be efficiently stored by incrementing the bin labeled by $(E_{\gamma 1}, E_{\gamma 2})^\dagger$ in a two-dimensional histogram, referred to as a coincidence matrix. The peaks that appear in this matrix after a large number of these events have been detected define the coincidence relationships between pairs of γ -ray transition energies in the nucleus. Figure 3.10 shows a simple example of such a matrix for a few of the low-spin transitions in the ^{62}Zn decay scheme. Many of these transitions are in coincidence with each other and peaks appear in the γ - γ matrix for all such pairs. Note, however, that certain transitions do not appear in coincidence. The 7^- state, for example, decays by the emission of either a 557 keV or a 1197 keV γ ray. These two transitions are never observed in the same event and no peak appears in the matrix at the location (557,1197). Similarly, the 1604 keV and 1521 keV transitions occur in parallel decay pathways and are never observed in coincidence. It is also worth noting that in this particular decay scheme there are two different γ rays with the same energy (557 keV). In ^{62}Zn , these two γ rays are in coincidence and the peak

[†]The order of the γ rays is arbitrary and it is often convenient to symmetrize the matrix explicitly by incrementing both the bin at $(E_{\gamma 1}, E_{\gamma 2})$ and the bin at $(E_{\gamma 2}, E_{\gamma 1})$.

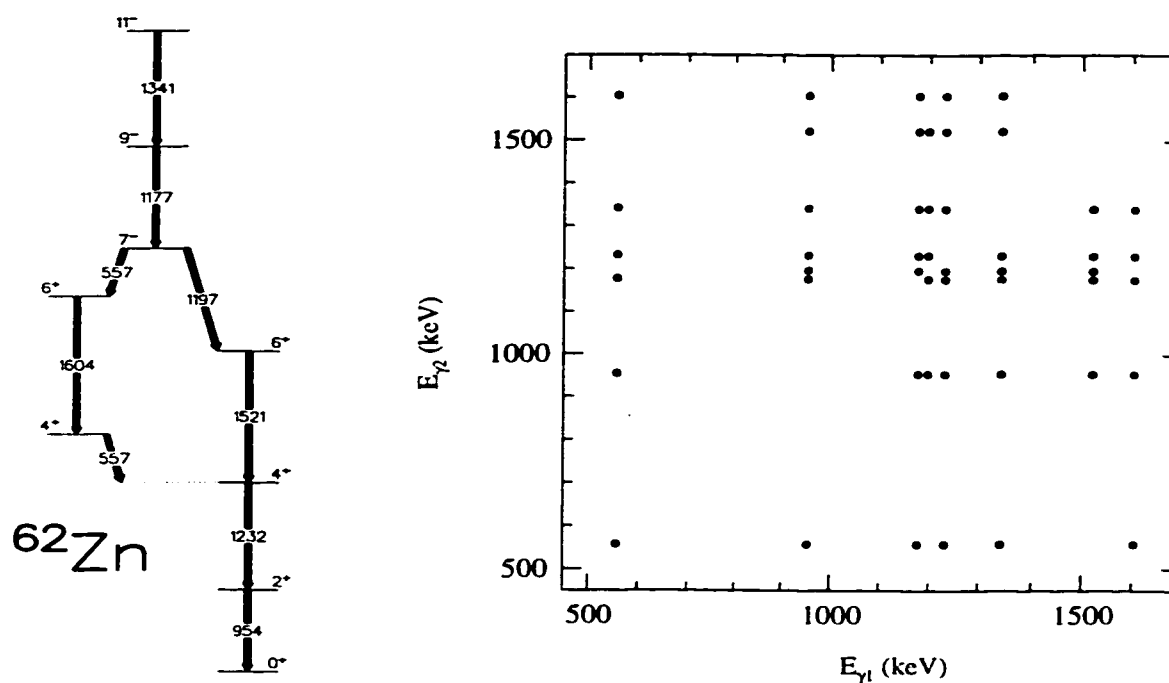


Figure 3.10: A simple example of $\gamma - \gamma$ coincidences. A few of the low-lying levels and γ -ray transitions in ^{62}Zn are shown on the left. The corresponding coincidence peaks are indicated by circles in the matrix shown on the right.

in the matrix at $E_{\gamma 1} = E_{\gamma 2} = 557$ keV makes it clear that this transition is actually a doublet. In general, however, this need not be the case and doublets often lead to serious difficulties in constructing a decay scheme.

The discussion above involved the relatively simple task of mapping a known decay scheme onto a set of peaks in a coincidence matrix. The considerably more formidable task faced by the experimentalist is to reverse this process and determine the level structure of a nucleus from measured γ -ray coincidences. The decay schemes of nuclei produced in fusion reactions may involve hundreds of discrete transitions and it therefore becomes necessary to investigate the coincidence relationships between thousands of pairs of γ rays. The entire spectrum of γ rays in coincidence with a particular transition of interest can be obtained by selecting a narrow range of channels, referred to as a gate, across the peak of interest on one axis of the matrix

and projecting the thin slice of the matrix that satisfies this gating condition onto the other axis. This gated spectrum will, however, include peaks from both the γ rays in real coincidence with the transition of interest and from those in coincidence with the smooth background of Compton-scattered and continuum γ rays on which the transition of interest sits. These latter peaks can be removed by subtracting a properly normalized fraction of a background spectrum[†] from each gated spectrum. Examples of such gated spectra for several of the low-spin transitions in ^{62}Zn are shown in Fig. 3.11. In accordance with the partial decay scheme shown in Fig. 3.10, the spectra gated on the 954 keV and 1177 keV transitions contain peaks from all of the other γ rays, the spectrum gated on the 557 keV doublet reveals the strong coincidence between the two 557 keV transitions but does not include peaks at 1197 or 1521 keV, and the spectrum gated on the 1197 keV transition has a large peak at 1521 keV but no peaks at 557 or 1604 keV. It is largely through deductive reasoning based on the analysis of large numbers of gated spectra such as these that the experimenter unravels the decay scheme of the nucleus.

One aspect of the data analysis that can be effectively automated is the search for rotational bands. As shown in Fig. 3.12, the decay of a rotational band with transition energies $E_\gamma = E_{\gamma 0} + n\Delta E_\gamma$ (n being an integer) leads to a regular grid of coincidence peaks in the γ - γ matrix. For real bands, the γ -ray spacing ΔE_γ is never perfectly constant and it is useful to define a parameter $\Delta^2 E_\gamma$ that describes the change in ΔE_γ per transition. A particular set of parameters $(E_{\gamma 0}, \Delta E_\gamma, \Delta^2 E_\gamma)$ (and higher order terms if necessary) then defines the N γ -ray energies in a “candidate” band and the $\binom{N}{2}$ independent locations in the matrix at which peaks would occur for this band. A figure of merit (FOM) can be assigned to this candidate by checking

[†]The spectrum in coincidence with the smooth background can be obtained by gating on nearby channels in which no peaks occur.

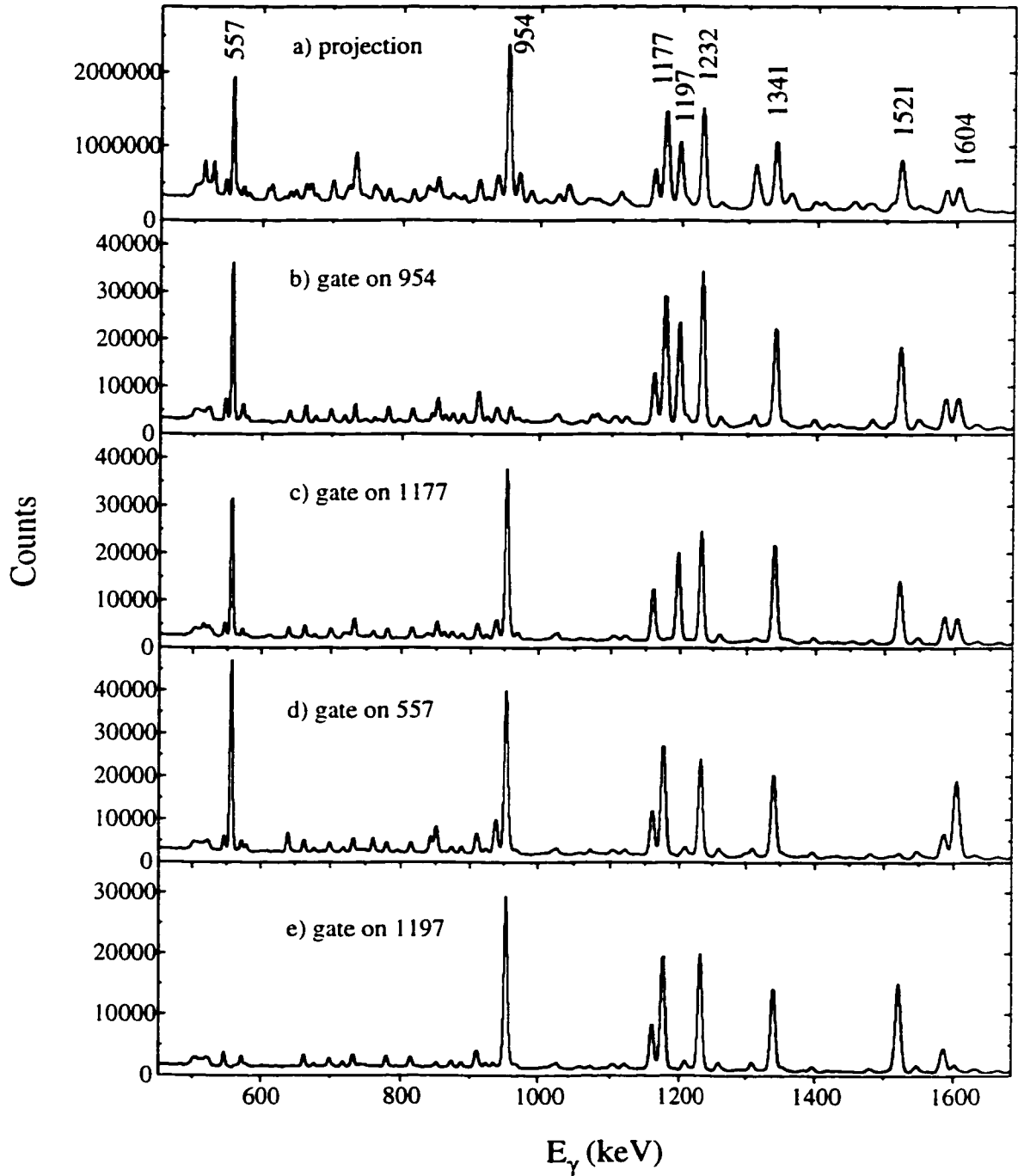


Figure 3.11: The (a) total spectrum of γ rays from events selected for ^{62}Zn and the γ -spectra obtained by gating on the (b) 954, (c) 1177, (d) 557, and (e) 1197 keV transitions. Note that the 557 keV transition is a “self-coincident” doublet.

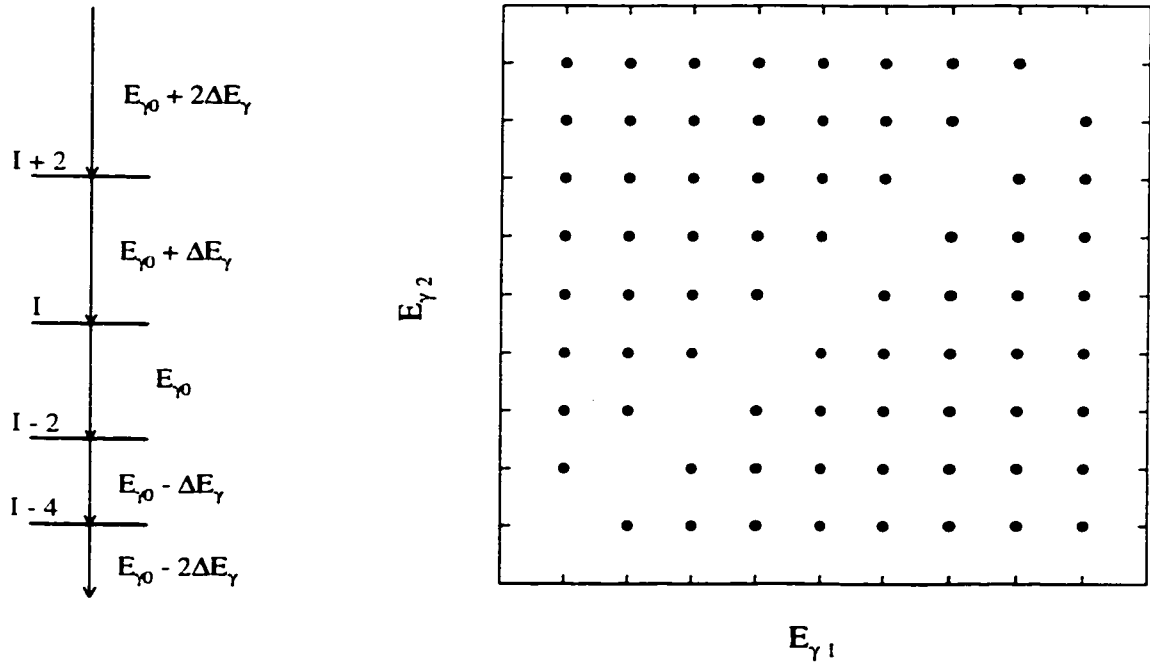


Figure 3.12: The regular grid of coincidence peaks (circles) in a γ - γ matrix resulting from the decay of a rotational band with transition energies $E_\gamma = E_{\gamma 0} + n\Delta E_\gamma$.

the intensity that appears in the predicted locations in the matrix and the regularity of this intensity. If the complete background in the matrix is subtracted [Pal 85] and the intensity is summed over elliptical gates (with axis lengths defined by the γ -ray energy resolution) centered at every $(E_{\gamma 1}, E_{\gamma 2})$ location in the matrix, such an intensity check is reduced to reading $\binom{N}{2}$ values from the matrix. The prepared matrix can be held in memory and millions of candidate bands which completely span all reasonable values of the parameters N , $E_{\gamma 0}$, ΔE_γ , and $\Delta^2 E_\gamma$ can be investigated in a matter of minutes. A two-dimensional display [Rod 98] of the calculated FOM as a function of $E_{\gamma 0}$ and ΔE_γ (for fixed N and $\Delta^2 E_\gamma$) will reveal peaks for those parameters which describe real rotational bands in the data set and inspection of a small number of these 2D histograms (for various N and $\Delta^2 E_\gamma$) provides a rapid and efficient means to identify these bands.

3.3.2 Higher Folds

The concepts of the γ - γ matrix can, in principle, be generalized to the case of an n -dimensional histogram in which bins are labeled by $(E_{\gamma 1}, E_{\gamma 2}, \dots, E_{\gamma n})$ and one-dimensional spectra can be generated by gating on $(n - 1)$ γ rays of interest. In practice, this approach rapidly becomes limited by the size of such histograms. Three-dimensional coincidence cubes are relatively simple to handle and standard software packages have been developed to facilitate their analysis [Rad 95a]. Through the use of sophisticated data compression algorithms, it has also recently become possible to analyze 4-fold coincidences in this manner [Rad 98]. For $n > 4$, however, the storage of an n -dimensional histogram becomes impractical[†] and it is more efficient to store such data as a list of events with their associated γ -ray energies.

Since third-generation arrays often achieve maximum sensitivity for folds $\gtrsim 4$, considerable effort has been devoted to the development of techniques to analyze such data. These include methods to store and rapidly set gates on list-mode data [Fli 92], high-fold background subtraction algorithms [Cro 95, Hac 95a, Rad 95b], the use of n -dimensional ellipsoidal gates [Cro 95, Wil 97], grid-search techniques appropriate for list-mode data [Has 94], and methods to increment spectra which avoid the non-statistical “spikes” associated with the combinatorics of setting n -fold gates on $(n + 2)$ or higher fold data [Bea 95]. However, as noted in Section 3.2.3, in the $A \sim 60$ mass region maximum sensitivity is usually achieved in fold 2 or 3 and the analysis performed during this work has thus been carried out with the standard techniques of γ - γ matrices and γ - γ - γ cubes. For a detailed discussion of high-fold data analysis the reader is therefore referred to the literature cited above.

[†]Symmetrization allows all of the information to be stored in a fraction $\frac{1}{n!}$ of such a histogram. Nevertheless, even $\frac{1}{120}$ of a 5-dimensional histogram with 1024 channels per side and 2 bytes per bin would require more than 10,000 GBy of storage space.

3.3.3 Spins and Parities

The measurement of γ -ray transition energies and the construction of a decay scheme by the techniques of coincidence spectroscopy establish the energies of the nuclear levels. It is also important to determine the spins and parities of these levels and such measurements require a knowledge of the γ -ray multiplicities.

For high-spin states populated in heavy-ion fusion-evaporation reactions, the angular momentum vector of the nucleus will lie approximately in the plane perpendicular to the beam axis. In the presence of such nuclear alignment, the relative yield $W(\theta)$ for a γ ray carrying angular momentum λ will be a function of the angle θ with respect to the beam axis and can be expressed as

$$W(\theta) = 1 + a_2 P_2(\cos \theta) + a_4 P_4(\cos \theta) + \dots, \quad (3.7)$$

where the P_l are the Legendre polynomials and only terms with $l \leq 2\lambda$ contribute. The coefficients a_2, a_4, \dots depend on λ and on the change ΔI in the nuclear spin and their measurement can therefore be used to determine the relative spins of the two states involved in the transition. The angular distributions[†] for dipole ($\lambda = 1$) and quadrupole ($\lambda = 2$) transitions from high-spin states[‡] are shown (for $\Delta I \leq 0$ [§]) in Fig. 3.13. It is clear from this figure that precise angular distribution measurements are required to define λ and ΔI uniquely; $\Delta I = 0$ dipole and $\Delta I = \pm 2$ quadrupole transitions, for example, have similar angular distributions. It should also be noted that the angular distributions for mixed $M1/E2$ transitions depend on the mixing

[†]These angular distributions are strictly valid only for γ -ray singles measurements. The coincident detection of charged particles and other γ rays leads to more complicated angular correlations. These correlation effects are, however, removed if the other transitions are detected at all angles with equal efficiency. The “ordinary” angular distributions are therefore also approximately valid in coincidence experiments with near- 4π detector arrays like Gammasphere and the Microball.

[‡]For a given λ and ΔI , the a_2, a_4, \dots also depend on the spin of the initial nuclear state. They do, however, asymptote to fixed values for high-spin states (see [Yam 67] for tables).

[§]For high-spin states, the transitions with $\pm\Delta I$ have similar angular distributions.

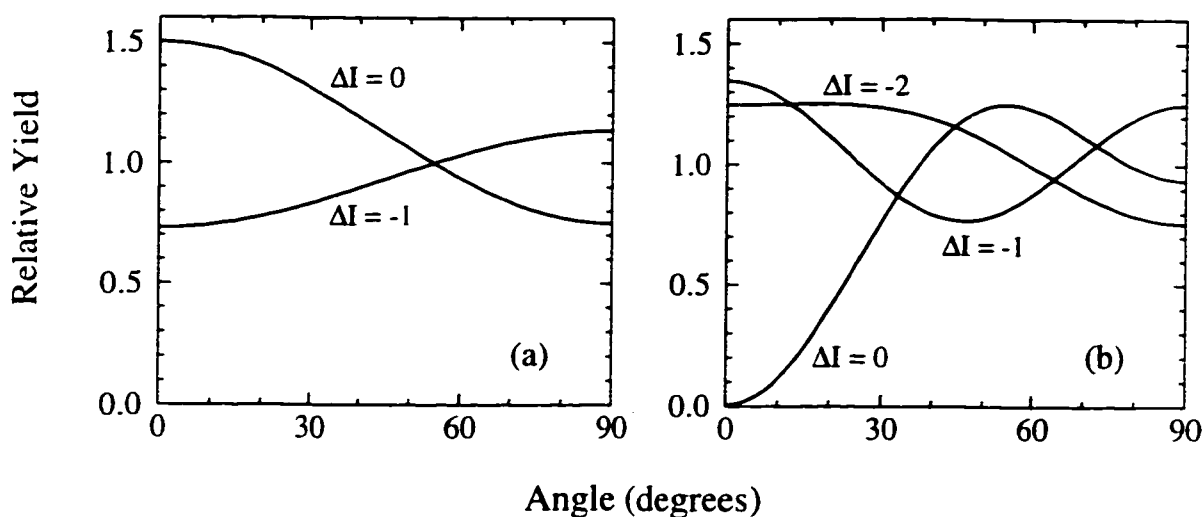


Figure 3.13: Angular distributions relative to the beam axis for (a) dipole and (b) quadrupole transitions appropriate for high-spin states. Full alignment is assumed.

ratio δ (see [MS 74]) and, for particular δ and ΔI values, can effectively mimic any of the angular distributions shown in Fig. 3.13. Even relatively simple angular distribution measurements can, however, be used to rule out certain λ and ΔI values and can readily distinguish between the two most common cases in high-spin studies, namely stretched dipole ($I \rightarrow I - 1$) and stretched quadrupole ($I \rightarrow I - 2$) transitions.

If a γ ray is identified as a quadrupole, it is usually safe to assume that it has $E2$ character (see Appendix A) and, therefore, that the initial and final levels have the same parity. For dipoles, however, both $E1$ and $M1$ transitions are common. Although these γ rays can, in principle, be distinguished by the angular dependence of their Compton scatterings [FH 59], the types of detectors used in this work have little sensitivity to this effect [Sch 98] and definite parity assignments are therefore not always possible in high-spin studies such as the ones presented here. It should, however, be noted that, when there are many more γ rays than levels, it is often possible to determine parities reliably by the simple (and usually valid) assumption that all observed transitions are either $E1$, $M1$, or $E2$ (see Appendix A).

3.4 Lifetime Measurements

Although spin, parity, and excitation energy measurements provide much detailed nuclear-structure information, more sensitive tests of theoretical models are often obtained from the transition matrix elements deduced from lifetime measurements. In this section, the Doppler shift attenuation method (DSAM) of measuring nuclear lifetimes is discussed.

3.4.1 The Doppler Shift Attenuation Method

The γ -decay lifetimes of excited nuclear states are, in general, short compared to the time resolution (typically nanoseconds) of standard γ -ray detectors. The lifetimes of these states can therefore not be determined by direct time measurements. However, as noted in Sec 3.2.3, the nuclei produced in heavy-ion fusion reactions recoil with substantial velocities. Measurements of the associated γ -ray Doppler shifts can be used to determine the recoil velocity of the nucleus at the time when the γ rays were emitted. In order to translate these velocity measurements into lifetime measurements it is, of course, necessary that the nuclear recoil velocity change measurably on a time scale similar to the lifetimes of interest.

In a standard DSAM experiment, the thin target in which fusion reactions occur is evaporated on a backing material (often Au or Ta) thick enough ($10\text{--}20\text{ mg/cm}^2$) to stop the recoiling nuclei. If the lifetime of a state is of the same order as the stopping time (a few picoseconds), energy measurements for a γ ray emitted in the decay of this state will reveal a Doppler-broadened peak resulting from γ -ray emission at recoil velocities ranging from zero to the full velocity at which the nuclei are produced in the reaction. The shape of such a Doppler-broadened peak can be used to determine the lifetime of the emitting state (see [Bra 98], for example).

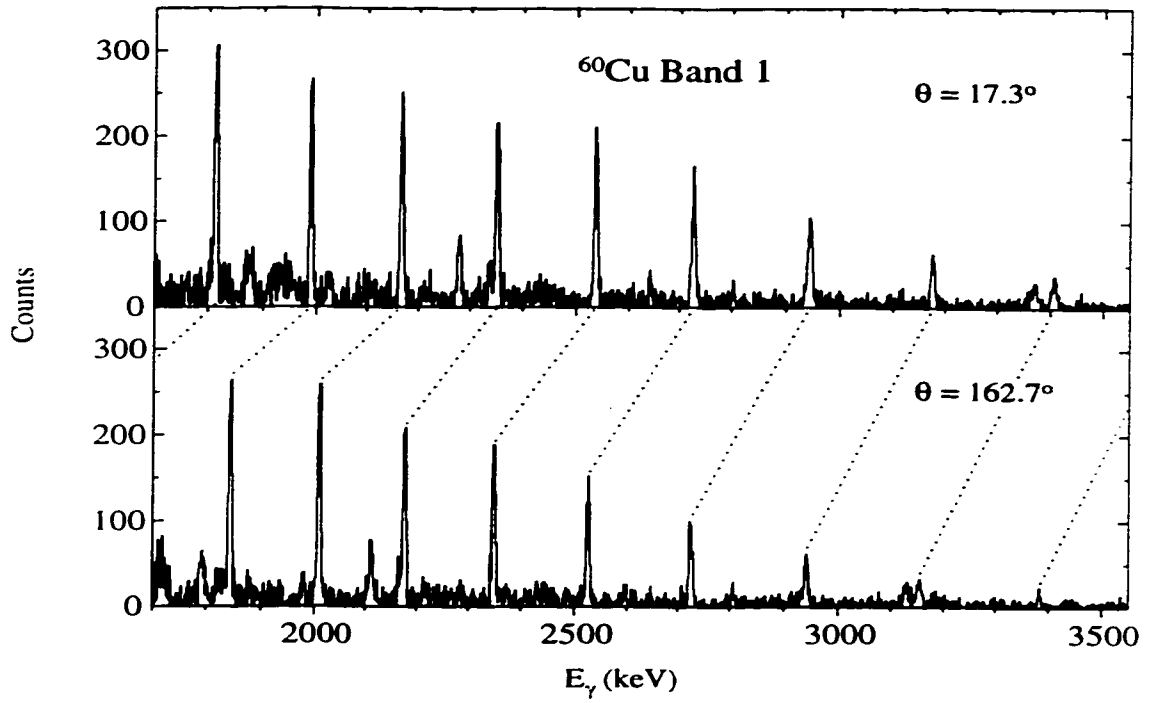


Figure 3.14: Forward ring ($\theta = 17.3^\circ$) and backward ring ($\theta = 162.7^\circ$) γ -ray spectra for Band 1 in ^{60}Cu identified in the GS112 Gammasphere experiment. The dashed lines connect the same γ -ray peak in the two spectra and the splitting of these peaks determines the mean velocity of the recoiling nucleus at the time the γ -ray is emitted.

If the lifetimes of individual states populated in a cascade of decays are short compared to the stopping time, as is often the case for high-spin rotational bands, the Doppler broadening of the individual γ rays may not be resolved in the Ge detectors. The cumulative time delay associated with the cascade does, however, lead to successively slower mean recoil velocities with decreasing spin. If the centroid energy of a Doppler shifted γ ray is measured to be E_f at a forward angle θ relative to the beam axis and E_b at the corresponding backward angle $180^\circ - \theta$, Eq. 3.5 can be used to determine the mean recoil velocity associated with this transition,

$$\frac{v}{c} = \frac{E_f - E_b}{(E_f + E_b) \cos \theta}, \quad (3.8)$$

which is often expressed as a fraction $F = v/v_0$ of the initial velocity v_0 of the recoils

produced in the reaction. An example of such forward-backward centroid shifts is shown in Fig. 3.14 for the fast transitions in one of the rotational bands in ^{60}Cu .

For the $E2$ γ -ray decays in a rotational band, the mean lifetime τ of a state with spin I and angular momentum projection K on the nuclear symmetry axis is given by (see Appendix A)

$$\tau^{-1} = 1.219 Q_t^2 E_\gamma^5 |\langle IK20|(I-2)K \rangle|^2 \text{ ps}^{-1}, \quad (3.9)$$

where the transition quadrupole moment Q_t is in units of eb and E_γ is in MeV. Assuming a constant Q_t value[†] and a model for the time delay associated with the feeding of the band (see Section 3.4.3), Eq. 3.9 can be used to model the decay of the band and to calculate a mean decay time for each state[‡]. Given a knowledge of the slowing down process for the recoils (see Section 3.4.2), these mean decay times can be converted to mean recoil velocities, and the Q_t for the band can thus be deduced from a fit to the measured F values for the γ -ray transitions. An example of calculated F values for a hypothetical rotational band with $Q_t = 2.0$ eb and perfectly regular transition energies is shown in Fig. 3.15. The fractional shifts calculated for this band assuming $Q_t = 1.0$ eb and 3.0 eb are also shown to illustrate the degree of sensitivity to Q_t that can be achieved from such Doppler shift measurements.

One important feature of collective rotational bands in $A \sim 60$ nuclei is that their relatively high γ -ray transition energies lead to very short state lifetimes. As an example, a band in ^{60}Zn with a deformation $\beta_2 = 0.45$ would have a quadrupole moment of 2.63 eb (Eq. 2.7). Assuming the rigid body value $14.5 \hbar^2 \text{MeV}^{-1}$ for the moment of inertia (Eq. 2.5), the $I = 30$ state in such a band is predicted to decay by

[†]See Chapter 5 for a discussion of a model in which Q_t is allowed to vary throughout the band.

[‡]Although this requires I and K values for the states in the band, which are often not known, for the usual case of large I and small K , $|\langle IK20|(I-2)K \rangle|^2$ asymptotes to the constant value $\frac{3}{8}$ (see Eq. A.10) and is relatively insensitive to typical uncertainties (a few \hbar) in I and K .

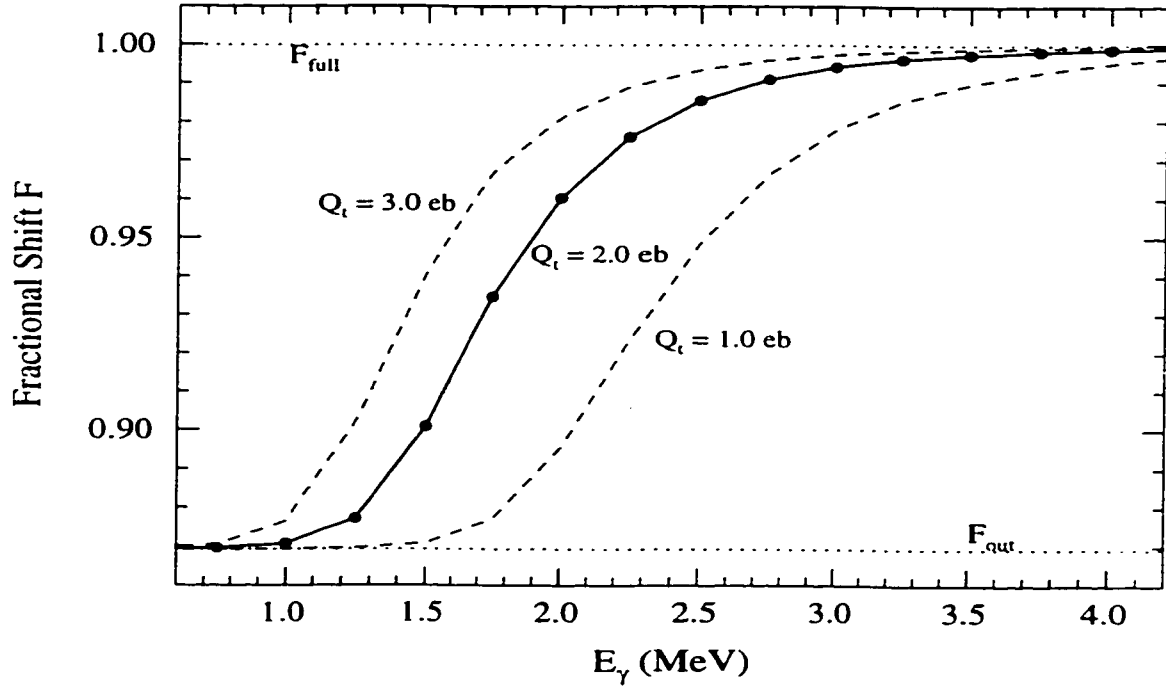


Figure 3.15: An example of fractional Doppler shifts calculated for a hypothetical band with $Q_t = 2.0$ eb and perfectly regular γ -ray transition energies. The stopping powers are calculated for a ^{60}Zn nucleus with an initial recoil velocity $v/c = 0.04$ at the center of a $500\mu\text{g}/\text{cm}^2$ ^{40}Ca target and fast side feeding is assumed (see Section 3.4.3). The calculated F curves for the same band with $Q_t = 1.0$ and 3.0 eb are also shown. F_{out} represents the fractional Doppler shift upon exiting the thin target.

a 4.08 MeV γ ray (Eq. 2.11) with a mean lifetime of only 0.3 fs (Eq. 3.9). At lower spins the γ -ray energies decrease and the lifetimes increase, but even the $I = 10$ state in such a band is predicted to have a lifetime of only 90 fs. Typical recoil velocities in the fusion reactions used to populate high-spin states in $A \sim 60$ nuclei are $\sim 0.04c$ and at these velocities the average time taken for the recoils to escape from the thin (few μm thick) target is on the order of 100 fs. The majority of the γ -ray decay in these bands thus occurs while the recoils remain in the thin target and target backings are of little use for high-spin studies in this mass region. Lifetime measurements can, however, still be performed by the thin-target DSAM method [Ced 95], where the necessary slowing of the recoils is that which occurs in the target itself.

3.4.2 Stopping Powers

In order to make a comparison with experimentally measured Doppler shifts, the mean decay time calculated for each transition in a band must be converted to a mean velocity. A knowledge of the slowing down process for the recoils is therefore required. The initial velocity v_0 of the recoils can be calculated from the fusion reaction kinematics and their subsequent deceleration resulting from collisions with electrons and nuclei in the target can be expressed as

$$\frac{dv}{dt} = \frac{\rho}{m} \frac{dE}{dx}, \quad (3.10)$$

where m is the recoil ion mass, ρ is the target density, and the stopping powers dE/dx , with units of MeV/(mg/cm²), have been tabulated for a large number of recoil ions, recoil energies, and target materials. In this work, the heavy-ion (HI) electronic stopping powers of Northcliffe and Schilling (NS) [NS 70] have been scaled by the ratio of the Ziegler and Chu (ZC) [ZC 74] alpha-particle stopping powers to those of NS at a common recoil energy per nucleon,

$$\left(\frac{dE}{dx}\right)_{HI}^{better} = \left(\frac{dE}{dx}\right)_{HI}^{NS} \left[\left(\frac{dE}{dx}\right)_{\alpha}^{ZC} / \left(\frac{dE}{dx}\right)_{\alpha}^{NS} \right]. \quad (3.11)$$

As discussed by Sie *et al.* [Sie 77], the “better” stopping powers thus obtained combine the advantages of the experimentally determined effective charges for heavy ions used by NS with the atomic shell effects on the stopping powers included in the ZC tables.

For DSAM experiments in which the recoils are stopped in a backed target, it is also necessary to account for changes in the energies and directions of the recoils due to scatterings from nuclei in the target [Bla 66]. However, for the thin-target experiments performed in this work, the recoil velocities are always greater than $\sim 0.03c$. At these velocities the nuclear stopping is negligible [Bla 66] compared to the uncertainties (typically 10–15%) associated with the much larger electronic stopping powers

and, therefore, no attempt has been made to include the nuclear stopping. The evaporation of particles from the compound system does, however, have significant effects on the recoil energies and directions for the relatively light nuclei discussed in this thesis. All of the γ -ray data sets used to perform lifetime measurements in this work have been taken in coincidence with the detection of charged evaporation particles (see Section 4.2). Charged particles emitted forward relative to the beam axis receive an energy “boost” from the nuclear recoil and are detected with higher efficiency than the lower-energy particles emitted at backward angles. Events in which the particles go forward, and hence the recoils are slowed, are thus preferentially detected and this bias in the initial velocity distribution of the recoils can be significant, particularly for channels involving alpha-particle evaporation. In order to account for this bias, the distribution of initial recoil energies and directions for the events that make up the experimental data set for each reaction channel can be calculated from the measured energies and directions of the *detected* charged particles.

For a particular initial recoil energy and direction, the velocity of the nucleus can be calculated as a function of time by numerically integrating Eq. 3.10 with the energy-dependent stopping powers of Eq. 3.11. The mean recoil velocity as a function of time can then be obtained by averaging over the experimentally determined distribution of initial recoil energies and directions resulting from the particle evaporation. It is also important to further average over reactions occurring at different locations in the target, for which the recoils penetrate different target thicknesses before escaping into vacuum and the compound systems have different initial velocities due to the decrease in effective beam energy as the projectile ions lose energy in the target. The numerical function relating recoil velocity to time thus obtained can then be used to convert calculated decay times to mean recoil velocities.

3.4.3 Side Feeding

The mean time at which a particular state in a rotational band decays depends not only on the lifetime of this state and the time delay associated with its feeding by transitions higher in the cascade (both of which can be calculated from Eq. 3.9), but also on the time delay associated with the side feeding of intensity into the band by unobserved transitions. Although the intensity of the side feeding into each state in the band can be determined from the intensity profile of the in-band transitions, the time history of this feeding is not known and must be modeled. For collective rotational bands, a standard procedure is to assume that the feeding occurs by rotational cascades characterized by a moment of inertia equal to that of the band of interest and a side-feeding transition quadrupole moment Q_{sf} . The time delay associated with the side feeding can then be adjusted by varying Q_{sf} and the number of transitions n_{sf} in the feeding cascades.

In certain cases where very precise DSAM measurements have been made for long rotational cascades, it has been possible to extract values of n_{sf} and Q_{sf} , as well as the in-band Q_t , from fits to the experimental data. For SD bands in $^{148,149}\text{Gd}$ and ^{152}Dy [Sav 96], fast side feeding with $Q_{sf} \approx Q_t$ and $n_{sf} = 1-3$ is observed, while the feeding of SD bands in $^{192,194}\text{Hg}$ [Moo 97] and ^{142}Sm [Hac 98] is found to be considerably slower, with $n_{sf} \approx 5$ and Q_{sf} substantially smaller than Q_t . For the $A \sim 60$ SD bands discussed in this thesis, it is clear from the Doppler-shift measurements that the feeding is very fast, and the Q_t values extracted for these bands are quite insensitive to the exact details of the side-feeding model (see Chapters 6 and 7). For the ND bands in this region, however, the choice of side-feeding parameters is less clear. The sensitivity of Q_t values deduced for these bands to assumptions regarding their feeding will be discussed in more detail in Chapter 5.

Chapter 4

Channel Selection

Different nuclei are populated in a heavy-ion fusion-evaporation reaction depending on the number and type of particles evaporated from the compound system. In analyzing the decay of any one of these nuclei, the γ rays from competing reaction channels constitute an undesirable background. An improved peak-to-background ratio in the γ -ray data, and hence a higher sensitivity to weak decay pathways in the nucleus of interest, can be achieved through the use of auxiliary detector systems that identify, or help to identify, the nucleus populated in each event. This chapter focuses on a number of such channel selection methods, including the development and testing of a new technique designed to meet the particularly severe channel selection requirements of high-spin studies in the $A \sim 60$ mass region.

4.1 Gamma-Ray Multiplicity and Sum Energy

One method of channel selection, particularly suited to high-spin studies of heavy and intermediate-mass nuclei, is based on measurements of the γ -ray multiplicity and sum energy emitted in each event. This method of channel selection relies on the different excitation energy and angular momentum entry distributions for nuclei populated following the evaporation of different numbers of particles.

4.1.1 Entry Distributions

The channel dependence of the excitation energy and spin entry distributions is best illustrated by the example of a fusion reaction leading to a heavy compound nucleus relatively close to the valley of stability. In such reactions, denoted generically as (HI, xn) reactions, the high Coulomb barrier in the compound system hinders the evaporation of charged particles and the final nucleus produced is determined by the number of evaporated neutrons.

The results of a statistical-model calculation [Hil 79] for an example of such a reaction, namely $^{124}\text{Sn}(^{40}\text{Ar}, xn)^{164-x}\text{Er}$ at $E(^{40}\text{Ar}) = 147$ MeV, are shown in Fig. 4.1. The upper panel of this figure shows the angular momentum distribution for the compound system resulting from reactions with different impact parameters. The central panel indicates the calculated regions of the yrast diagram populated following the evaporation of 1, 2, ..., 5 neutrons from the compound system. Shaded areas represent entry regions that are calculated to decay by γ -ray emission rather than the evaporation of another neutron. The corresponding angular momentum and excitation energy entry distributions for the $3n$, $4n$, and $5n$ channels are shown in the lower and left panels, respectively. In this reaction, most events are calculated to result in the evaporation of 4 neutrons. It is only for the highest angular momentum events that the evaporation of 3 neutrons leaves the nucleus close enough to the yrast line to prevent the emission of another neutron. Conversely, it is primarily for the low-spin events that there is sufficient excitation energy between the compound system and the yrast line for the evaporation of 5 neutrons. Although the details of particle evaporation will depend on the particular reaction, the decreases in the average entry spin and excitation energy with increasing particle multiplicity shown in Fig. 4.1 are a generic feature of fusion-evaporation reactions.

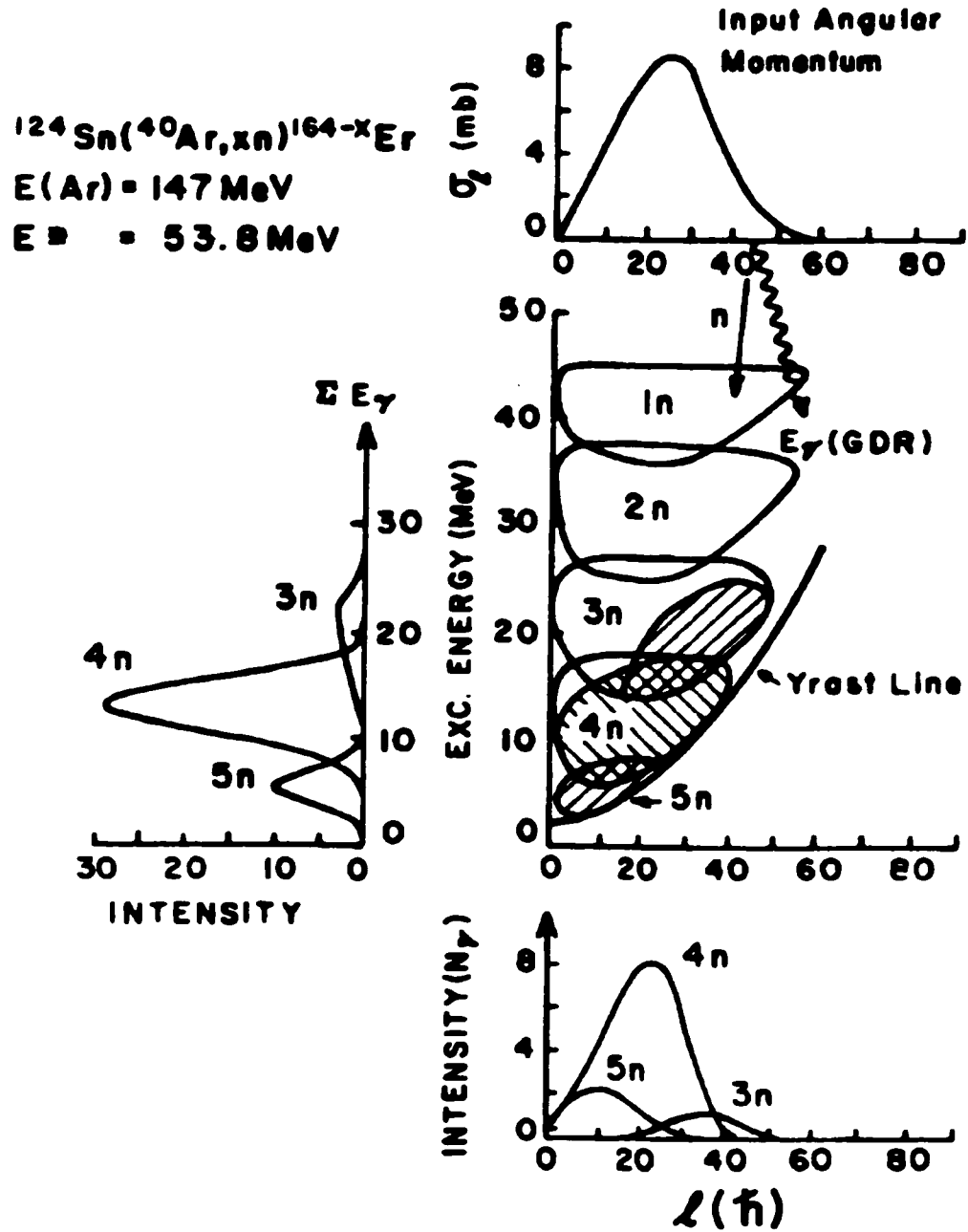


Figure 4.1: Statistical-model calculation for the reaction $^{124}\text{Sn}(^{40}\text{Ar}, xn)^{164-x}\text{Er}$ at $E(^{40}\text{Ar}) = 147 \text{ MeV}$. The compound nucleus is formed at an excitation energy of 53.8 MeV and with the angular momentum distribution shown in the top panel. The central panel shows the region of the yrast diagram populated after each neutron is evaporated, with shaded areas indicating entry regions that decay by γ -ray emission. The resulting angular momentum and excitation energy entry distributions for the 3n, 4n, and 5n channels are shown in the bottom and left panels. From [Hil 79].

4.1.2 H and K Gating

The entry distributions shown in Fig. 4.1 suggest a method of selecting events from different reaction channels. The total detected γ -ray energy H is, following correction for detection efficiency, a measure of the entry excitation energy and the detected γ -ray multiplicity K is roughly proportional to the entry spin. Gating on various values of H and K is thus approximately equivalent to gating on different entry regions in the yrast diagram and will preferentially select events with different particle multiplicities.

The channel selectivity provided by H and K gating is illustrated in Fig. 4.2 with data from the reaction $^{100}\text{Mo}(^{36}\text{S}, xn)^{136-x}\text{Ce}$ at $E(^{36}\text{S}) = 150$ MeV taken with the 8π Spectrometer. The K and H distributions obtained by gating on strong γ rays from the $3n$, $4n$, and $5n$ channels are shown in panels (a) and (b), respectively. The total γ -ray spectrum subject only to the $K > 7$ hardware trigger condition is shown in panel (c) and indicates that the $4n$ channel is dominant in this reaction, with smaller cross sections for the $3n$ and $5n$ channels. As shown in panel (d), it is possible to enhance the $3n$ channel in the γ -ray data by selecting only those events with large values of K and/or H . Requiring $K > 21$ and $H > 32$ MeV, for example, increases the fraction of events in the γ -ray spectrum belonging to the $3n$ channel by a factor of 4.2. This enhancement does, however, come at the expense of 67% of the statistics for this channel. In choosing the most appropriate H and K gates, a balance must therefore be struck between channel selectivity and this loss of statistics.

It should also be noted that high-resolution H and K measurements are useful not only for channel selection, but also for studying the fusion-evaporation process itself. Given a detailed knowledge of the detector response, measured H and K values can be converted to entry excitation energy and spin values. By gating on discrete γ rays from various reaction channels and from various decay pathways within a

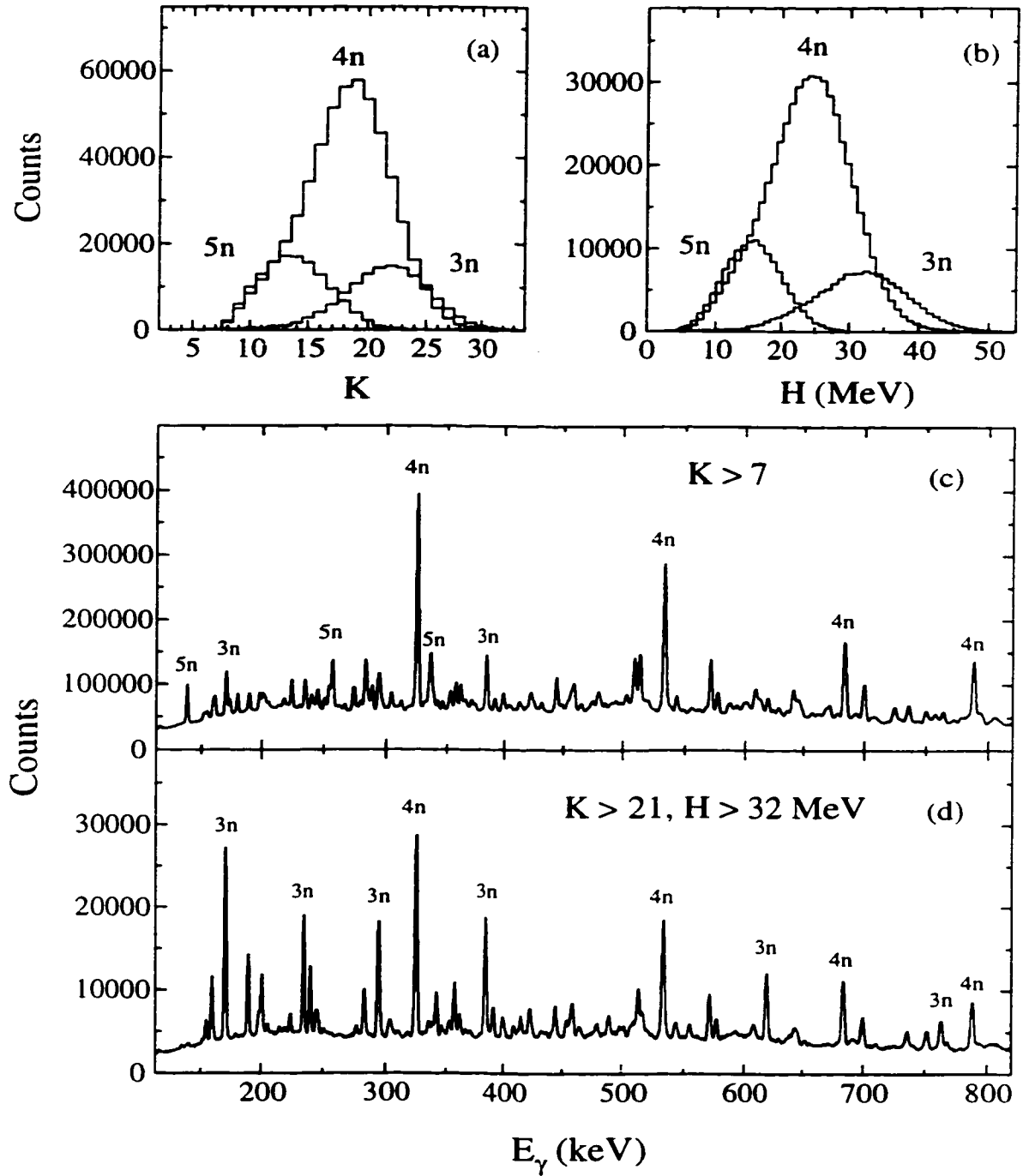


Figure 4.2: Data from the reaction $^{100}\text{Mo}(^{36}\text{S}, xn)^{136-x}\text{Ce}$ at $E(^{36}\text{S}) = 150$ MeV taken with the 8π Spectrometer. The (a) K and (b) H distributions gated on γ rays from the 3n, 4n, and 5n channels. The lower half of the figure shows the γ -ray spectra obtained requiring (c) only the $K > 7$ hardware trigger and (d) $K > 21$ and $H > 32$ MeV. A number of the γ rays are labeled by the channel to which they belong.

given nucleus, it is possible to determine the region of the yrast diagram that feeds particular states. Such measurements have been used, for example, to study the population mechanism for superdeformed bands [Lau 92, Kho 93, Wil 98].

4.1.3 The $A \sim 60$ Mass Region

Channel selection requirements in the proton-rich $A \sim 60$ mass region are considerably more severe than in the (HI, xn) reactions discussed in the previous sections. The $N = Z$ compound systems studied in this work have a substantial proton excess relative to stable nuclei and the proton separation energies (~ 5 MeV) in these systems are much smaller than the neutron separation energies (~ 15 MeV). Proton evaporation removes much less binding energy from the system and is favoured by the statistical weight of the exponential increase in level density with excitation energy in the daughter nucleus. Charged particles do have to overcome the Coulomb barrier, but this barrier is relatively low for the light nuclei studied here and provides little hindrance to charged-particle evaporation.

Although charged-particle evaporation tends to dominate in the $A \sim 60$ mass region, the combination of the two effects mentioned above leads to a general competition between proton, alpha-particle, and neutron evaporation and, therefore, to a fragmentation of the total fusion cross section into a large number of exit channels. In a typical high-spin reaction in this region, 3–5 particles are evaporated from the compound system. In a (HI, xn) reaction, this leads to only 3 exit channels. However, for the more general case of a $(\text{HI}, x\alpha y p z n)$ reaction, there are 46 different channels with $x + y + z = 3\text{--}5$. Although not all of these channels are populated with significant cross sections, it is common in the $A \sim 60$ mass region to observe 20 or more channels with measurable intensity. This fragmentation of the fusion cross section is illustrated in Fig. 4.3 for the reaction of 125-MeV ^{28}Si on ^{40}Ca . It is possible to select

4.2 Charged-Particle Detection

The principles of charged-particle detection are similar to those of γ -ray detection and both scintillator and semiconductor detectors are also used for charged particles. Because of their large cross sections for Coulomb scattering with electrons in the detector, charged particles are much more easily detected than γ rays. However, the detection of charged particles is complicated by the requirement that the particles not only be detected, but also identified. This requirement, and other aspects of charged-particle detection, are discussed in the following sections.

4.2.1 Detector Arrays

Like the large γ -ray detectors with which they are associated, modern charged-particle detection systems consist of multi-detector arrays that subtend almost the full 4π solid angle around the target. These detectors are placed inside the central vacuum chamber of the γ -ray spectrometer and detect the evaporated charged particles, while the majority of the γ rays pass through the particle detector and undergo interactions in the surrounding γ -ray detectors. A photograph of the Microball charged-particle detector array inside the scattering chamber of Gammasphere is shown in Fig. 4.4.

Although charged-particle detectors can, in principle, be designed with almost 100% detection efficiency, the design of charged-particle detectors for use in conjunction with large γ -ray spectrometers is constrained by a number of requirements. Obviously, the size of the charged-particle detector is limited by the dimensions of the inner chamber of the γ -ray detector. Scattering and absorption of γ rays in the charged-particle detector will inevitably degrade both the efficiency and peak-to-total ratio of the γ -ray array. In order to minimize these effects, the charged-particle detectors should be kept to the minimum thickness capable of stopping evaporated

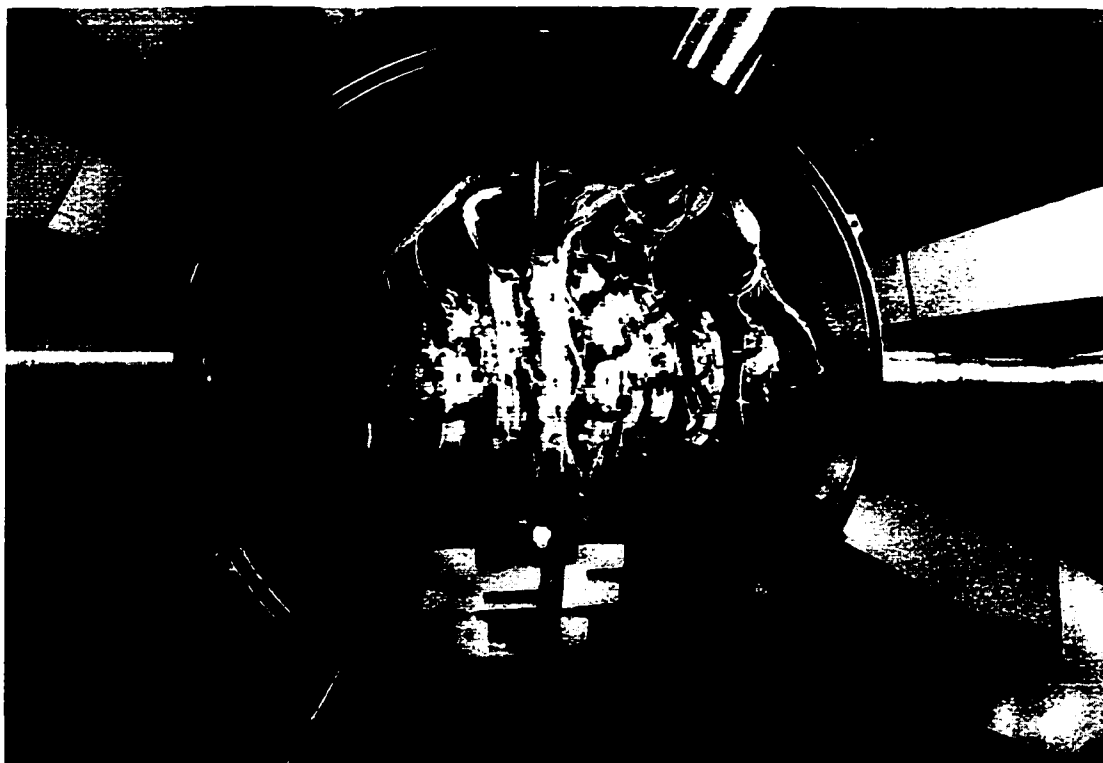


Figure 4.4: A photograph of the Microball charged-particle detector inside the scattering chamber of Gammasphere. The beam enters from the left. From [Sar 96].

protons, and the associated support structure should be made of the lowest- Z materials possible (usually plastic and aluminum). The charged-particle array should have sufficient segmentation to avoid multiple hits in any detector in events with high particle multiplicities and should be capable of running at the same event rates as the γ -ray detector. As will be discussed in Sections 4.2.2 and 4.2.3, excellent particle identification capabilities and reasonable energy resolution are also required.

Two charged-particle detectors designed to satisfy the above criteria have been used in this work; the Miniball array [Gal 92] used in conjunction with the 8π Spectrometer and the Microball array [Sar 96] used with Gammasphere. Both of these detectors are based on arrays of thallium-doped cesium iodide CsI(Tl) scintillators coupled to large-area photodiodes. The Miniball consists of 44 of these scintillators.

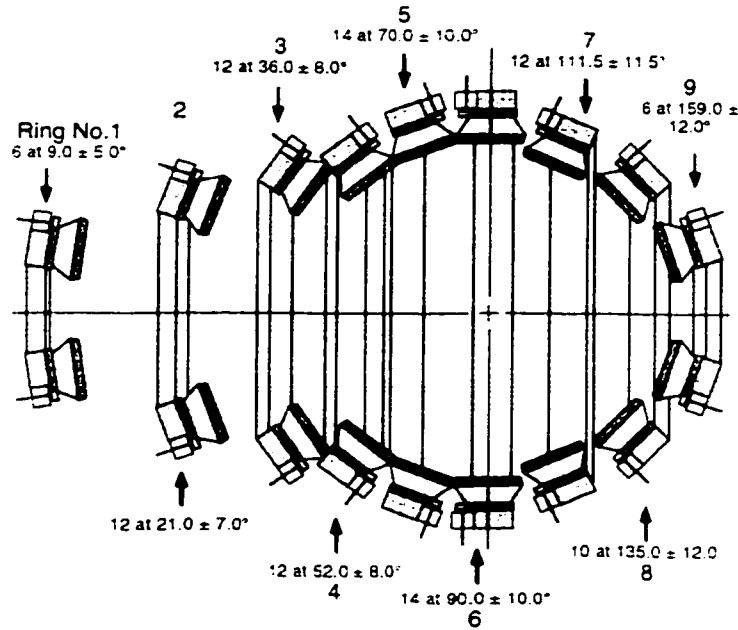


Figure 4.5: Schematic diagram showing a cross section of the Microball. The beam enters from the right and the target position is marked by the +. The number of detectors and angular spread of each ring is indicated. From [Sar 96].

each 5 mm thick and with its front face 4.1 cm from the target location. These detectors are close packed and subtend 94% of the 4π solid angle. The Microball consists of 95 CsI(Tl) scintillators with thickness varying from 2.7 mm (forward detectors) to 1.1 mm (backward detectors). These detectors are arranged in 9 rings and subtend 96.5% of the solid angle. As shown in Fig. 4.5, these rings are located at different distances from the target, ranging from 4.5 cm for ring 7 ($\theta = 111.5^\circ$) to 11 cm for ring 1 ($\theta = 9.0^\circ$), and the detectors from neighbouring rings overlap slightly in order to prevent solid-angle loss to dead spaces at the detector edges. Both the Miniball and the Microball have increased segmentation at forward angles where kinematic focusing of the charged particles leads to higher count rates. The preamplifiers and associated electronics for both arrays are located outside the γ -ray detector in order to minimize the amount of material inside the scattering chamber.

4.2.2 Charged-Particle Identification

Charged-particle identification with CsI(Tl) detectors is accomplished by pulse-shape discrimination. The scintillation in a CsI(Tl) crystal has two components; a fast component with a $\sim 0.7 \mu\text{s}$ decay time and a $7 \mu\text{s}$ slow component [Sar 96]. For a given particle energy, the division of the light output between these two components depends on the density of ionization in the crystal. The higher ionization density produced by alpha particles leads to a larger fraction of the light in the fast component compared to the lower ionization density produced by protons[†].

Two independent pulse-shape discrimination techniques are commonly used with CsI(Tl) scintillators. In the first method, the pulse from the photodiode preamplifier is differentiated to obtain a bipolar signal. The zero-crossing time (ZCT) of this signal depends on the shape of the pulse, occurring earlier for the more densely ionizing alpha particles than for protons. Recording the time interval T between this ZCT and a fixed time reference[‡] thus allows the particle to be identified. An example of this method is shown in Fig. 4.6, where the data from one of the Microball detectors from the reaction of 125-MeV ^{28}Si on ^{40}Ca is plotted in a two-dimensional histogram of time versus particle energy. A clear separation of the alpha particles and protons is seen in this figure. This method is also used to identify particles with the Miniball.

The energy E of the charged particle is determined by integrating the preamplifier signal over a time window around the peak of the pulse. With the Microball detectors, a second method of pulse-shape discrimination is accomplished by also in-

[†]The fast component arises from the recombination of weakly bound electron-hole pairs called excitons, while the slow component arises from the recombination of free electrons and holes. With increasing ionization density, the concentration of electrons and holes increases and more excitons are formed, resulting in a larger fraction of the scintillation appearing in the fast component [Leo 87].

[‡]With the Miniball this time reference is provided by the “flash” of γ rays detected in the BGO ball of the 8π Spectrometer, while for the Microball it is derived from the next cycle of the radio frequency (RF) from either the 88-Inch Cyclotron at Lawrence Berkeley National Laboratory or the ATLAS Linac at Argonne National Laboratory.

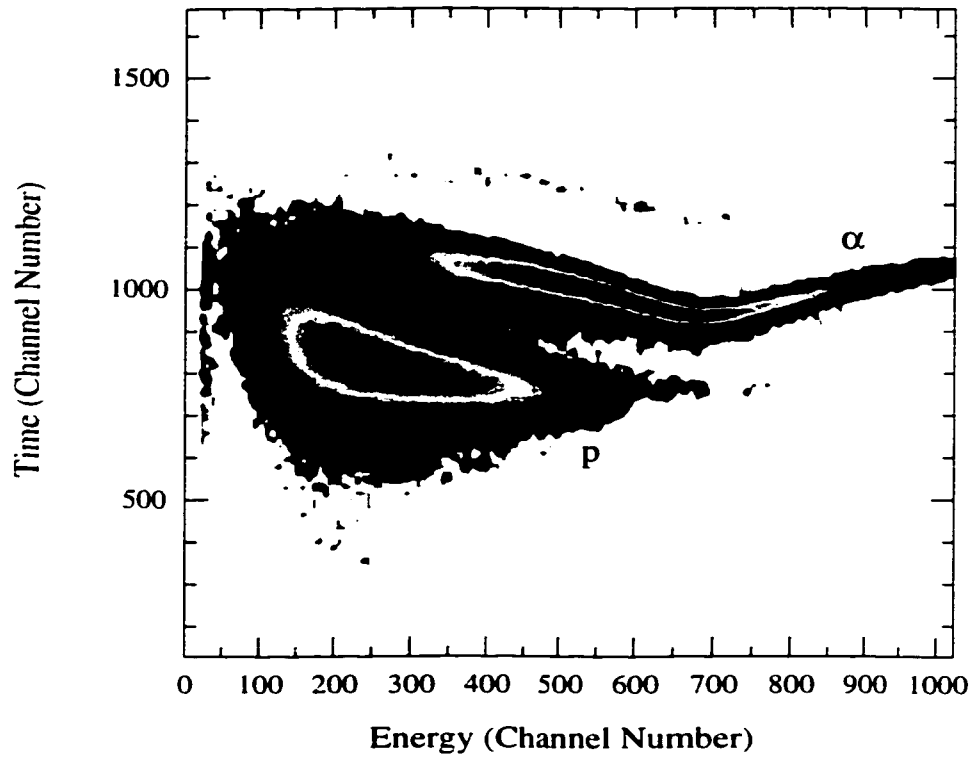


Figure 4.6: A two-dimensional histogram of time versus energy for one of the Microball detectors showing the separation of protons and alpha particles. Note that the time interval is started by the Microball zero-crossing time and stopped by the next pulse of the Cyclotron RF so that the alpha particles, with earlier zero crossings, appear with larger time intervals. The data are from the reaction of 125-MeV ^{28}Si on ^{40}Ca and Microball detector #16, at an angle of 21° relative to the beam axis.

tegrating this signal over a narrow time window on the tail of the pulse to obtain a second energy E_{slow} . The ratio of these energies $R = E/E_{slow}$ depends on the shape of the pulse and can also be used to identify the particles. This method is illustrated in Fig. 4.7, where data from the same reaction and Microball detector as in Fig. 4.6 is plotted in a two-dimensional histogram of E_{slow} versus E . The protons and alpha particles are again clearly separated, with the larger fraction of the light in the slow scintillation component for the protons giving a larger value of E_{slow} for a given E .

The best particle identification with the Microball is obtained by combining the two methods discussed above. The time interval and energy ratio are first lin-

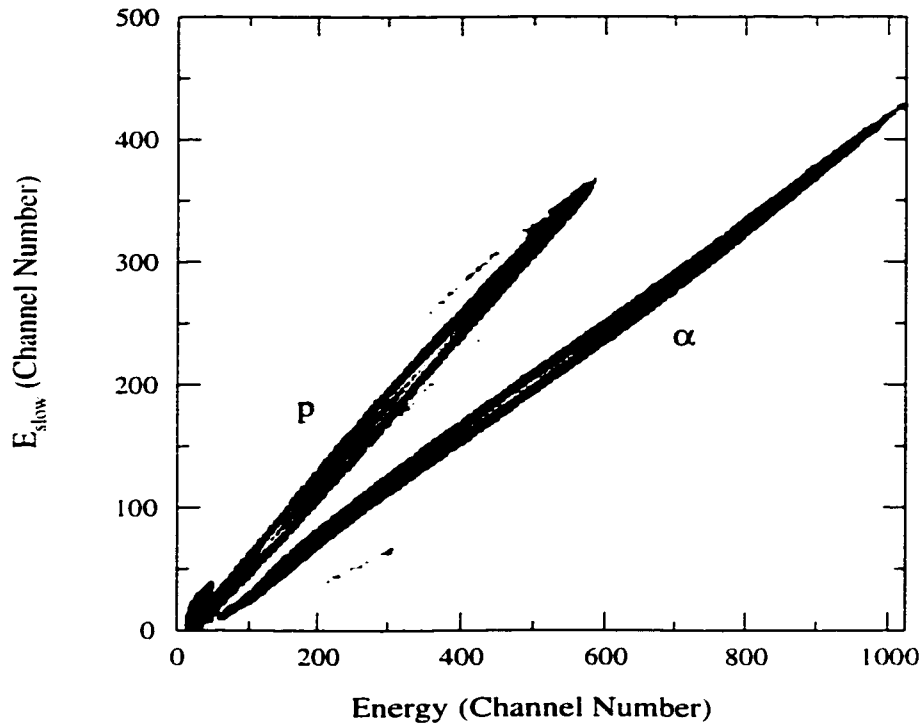


Figure 4.7: A two-dimensional histogram of E_{slow} versus energy for one of the Microball detectors showing the separation of protons and alpha particles. The highest-energy protons punch through the detector and produce the “backbend” at the top of the proton branch. The data are from the reaction of 125-MeV ^{28}Si on ^{40}Ca and Microball detector #16, at an angle of 21° relative to the beam axis.

earized with respect to the particle energy and then plotted in a two-dimensional histogram of R versus T . Such a plot is shown in Fig. 4.8 for the same data as shown in Figs. 4.6 and 4.7. This figure illustrates the very clean separation of alpha particles and protons that can be achieved by this method. It should be noted that the data in all of Figs. 4.6, 4.7, and 4.8 were taken with a detector at a forward angle ($\theta = 21^\circ$) relative to the beam axis, where the particles receive an energy “boost” from the recoil of the nucleus. For the lower-energy particles at backward angles, the separation of protons and alpha particles by both the time and energy-ratio methods is less pronounced. However, by combining these two methods, as in Fig. 4.8, good particle identification can be achieved even for the detectors at $\theta = 159^\circ$.

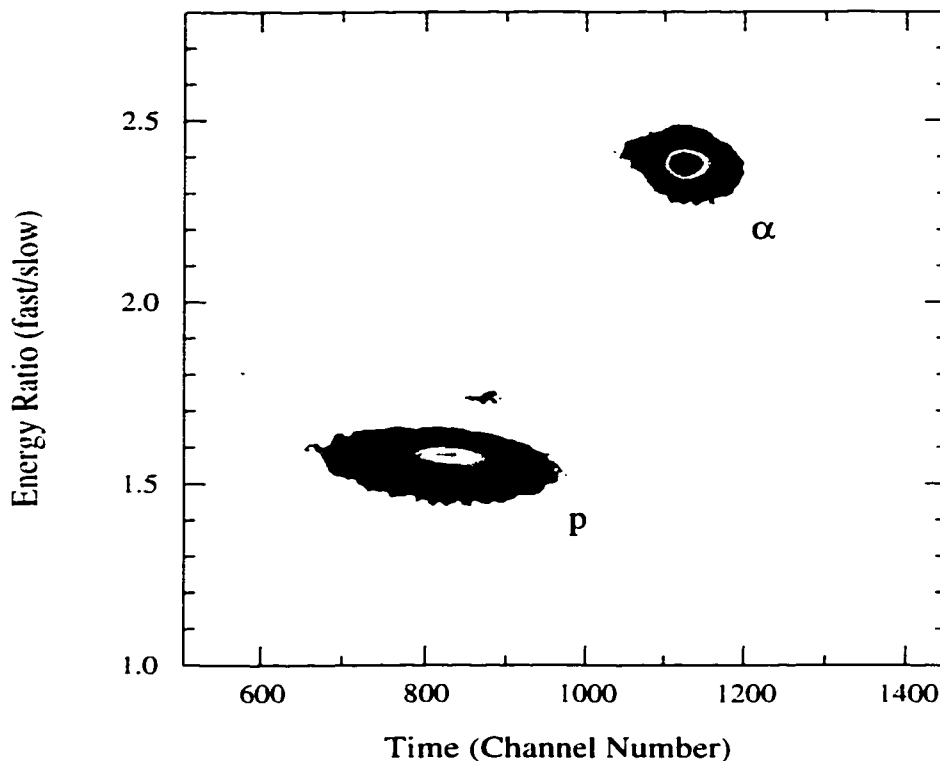


Figure 4.8: A two-dimensional histogram of the energy ratio $R = E/E_{slow}$ versus time for one of the Microball detectors showing the very clean separation of protons and alpha particles that can be achieved by combining these two methods of pulse-shape discrimination. The data are the same as those plotted in Figs. 4.6 and 4.7, with both R and T linearized with respect to the particle energy.

4.2.3 Energy Calibration

The total energy channel selection method (see Section 4.3) and the event-by-event reconstruction of reaction kinematics (see Section 4.2.5) require a knowledge of the charged-particle energies. It is therefore necessary to calibrate the energy response of the CsI(Tl) detectors. These calibrations are performed either before or after an experiment by scattering beams of protons and alpha particles with known energies.

For the proton energies relevant to fusion-evaporation reactions, the light output of CsI(Tl) increases linearly with the energy deposited in the detector [Sar 96].

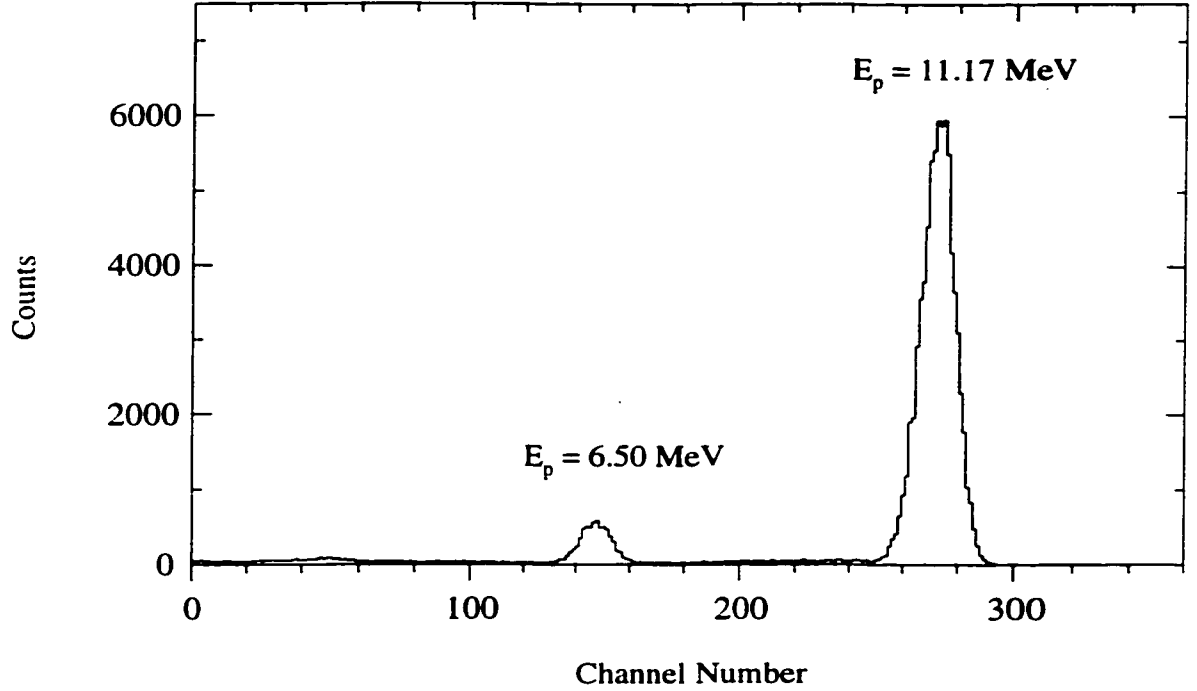


Figure 4.9: Proton energy calibration obtained by scattering 11.87 MeV protons from a ^{12}C target. The elastic $E_p = 11.17$ MeV and inelastic $E_p = 6.50$ MeV energies have been corrected for both the scattering kinematics and the energy loss of the protons in the detector absorbers. The data are from Microball detector #16, at $\theta = 21^\circ$.

The proton energy E_p is thus expressed in terms of the ADC channel number n as

$$E_p = d(n - n_0), \quad (4.1)$$

where the gain d and ADC pedestal n_0 (i.e. channel number for zero energy) for each detector can be determined from two calibration points. A convenient method of obtaining these two calibration points simultaneously is to scatter protons from ^{12}C , which gives both an elastically scattered proton peak and an inelastic peak in which the 2^+ state of ^{12}C at 4.439 MeV is excited[†]. An example of such a calibration for one of the Microball detectors obtained by scattering 11.87 MeV protons from a

[†]The inelastic peak is generally not observed for protons scattered into the most forward ring of detectors. In order to obtain a second calibration point for these detectors, a second proton beam energy is used. This provides at least three calibration points for the other detectors, and these data confirm the linear response of the CsI(Tl) light output for protons.

100 $\mu\text{g}/\text{cm}^2$ ^{12}C target is shown in Fig. 4.9. The energies of the protons are reduced slightly from 11.87 MeV and 11.87 - 4.439 MeV by the scattering kinematics. A more important correction, however, is the energy loss of the protons in the absorbers that are placed in front of the detectors to stop scattered beam particles in an actual experiment. This energy loss is a nonlinear function of the proton energy and thus Eq. 4.1 applies only to the “post-absorber” energies deposited in the detector and not to the incident proton energies. One must calculate the energy losses in the absorbers from the known absorber thicknesses and tabulated proton stopping powers [NS 70]. These corrected energies and the measured centroids of the elastic and inelastic scattering peaks then determine the d and n_0 parameters in Eq. 4.1. In an actual experiment, it is the pre-absorber proton energies not the post-absorber energies that are of interest. The post-absorber energy corresponding to each channel number must therefore be transformed to an incident proton energy by calculating the energy that was lost in the absorber. The final proton energy calibration thus obtained is a nonlinear function of the channel number and is most conveniently stored as a large “look-up” table that contains the incident proton energy corresponding to each channel number for each detector.

The alpha-particle energy calibration is somewhat more complicated. The high ionization density produced by alphas is known to lead to a quenching of the CsI(Tl) scintillation and to a nonlinear light output for low-energy alpha particles [Str 90]. A convenient empirical parametrization of this response is obtained by expressing the alpha energy as the sum of a linear and a logarithmic term,

$$E_\alpha = a(n - n_0) + b \ln[1 + c(n - n_0)], \quad (4.2)$$

where a , b , and c are parameters and the ADC pedestal n_0 is fixed, for each detector, by the proton calibration. Figure 4.10 shows alpha particle calibration data for one

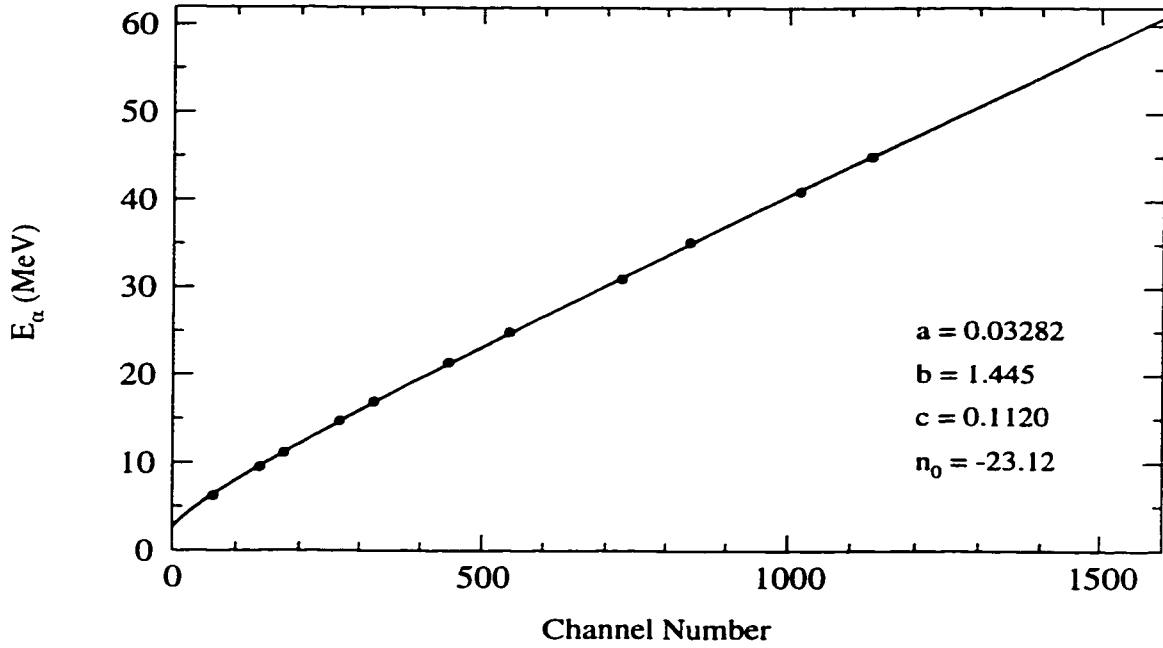


Figure 4.10: Alpha-particle energy calibration obtained by scattering alphas from a ^{232}Th target at 11 beam energies between 12.23 and 47.30 MeV. The alpha energies have been corrected for both scattering kinematics and energy losses in the detector absorbers. The data are from Microball detector #16 ($\theta = 21^\circ$) and the calibration parameters for this detector obtained by fitting Eq. 4.2 to the data are indicated.

of the Microball detectors obtained by scattering alphas from a $800 \mu\text{g}/\text{cm}^2$ ^{232}Th target at 11 beam energies between 12.23 and 47.30 MeV[†]. The alpha-particle energies shown in this figure have been corrected for both the scattering kinematics and the energy losses in the absorbers. The low-energy nonlinearity of the CsI(Tl) response is clearly seen in Fig. 4.10 and is observed to be well described by Eq. 4.2. As with the proton calibrations, the post-absorber alpha-particle energy calibrations obtained by fitting Eq. 4.2 to the data for each detector must be numerically transformed to the corresponding incident alpha-particle energies and stored in a look-up table.

[†]An additional beam energy, 10.29 MeV, as well as the 5.812 MeV alphas from a ^{249}Cf source were also used in this calibration for the backward detectors. However, these low-energy alphas do not penetrate the thicker absorbers on the forward detectors.

4.2.4 Efficiency and Particle Gating

Although both the Miniball and Microball arrays cover $\approx 95\%$ of the 4π solid angle, the proton and alpha detection efficiencies, ϵ_p and ϵ_α , achieved in experiments are reduced by a number of factors. Among these are (i) pile-up and summing losses in reactions with high charged-particle multiplicities, (ii) kinematic focusing of the particles out the beam exit hole, (iii) energy thresholds below which the particles are either stopped in the absorbers or are not cleanly identified by pulse-shape discrimination, and (iv) in the case of the Miniball, where the detectors do not overlap, solid angle losses to detector frames and dead areas at the detector edges. Because of differences in particle multiplicities and energy spectra, the exact values of ϵ_p and ϵ_α depend on the reaction and even on the channel within a given reaction. For a given channel, however, it is straightforward to determine these efficiencies by measuring the intensities of γ rays from this channel in the various particle-gated spectra. For the reactions discussed in this work, typical values obtained are $\epsilon_p \approx 0.55$ and $\epsilon_\alpha \approx 0.45$ for the Miniball and $\epsilon_p \approx 0.80$ and $\epsilon_\alpha \approx 0.70$ for the Microball.

There are two problems associated with these imperfect particle-detection efficiencies. Firstly, the reduction in background resulting from charged-particle gating is achieved at the expense of statistics for the selected channel. For example, the efficiency of selecting the $4p$ channel by requiring the detection of 4 protons is ϵ_p^4 , i.e. $\approx 10\%$ for the Miniball and $\approx 40\%$ for the Microball. The second problem is encountered when analyzing low particle multiplicity channels. Because of the imperfect particle-detection efficiencies, low particle multiplicity gated data sets are contaminated by events from higher particle multiplicity channels in which some of the particles escape detection. For example, the data in coincidence with the detection of 3 protons will contain not only real $3p$ events, but also $4p$, $\alpha 3p$, and $3pn$ events

where the additional particle was not detected. If the low particle multiplicity channel of interest is weakly populated, this “leak-through” from higher particle multiplicity channels can completely dominate the γ -ray spectra and charged-particle gating fails to provide the desired channel selectivity.

The merits and limitations of channel selection by charged-particle gating are illustrated in Fig. 4.11 with data from the reaction of 80-MeV ^{24}Mg on ^{40}Ca . The total γ -ray spectrum from this reaction shown in panel (a) contains γ rays from more than a dozen different nuclei. Panel (c) shows the spectrum in coincidence with the detection of 4 protons. In this relatively low-energy reaction, there is no significant cross section for 5-particle channels and thus no leak-through into the 4p spectrum from higher particle multiplicity channels. The spectrum shown in Fig. 4.11(c) is thus almost 100% events from the real 4p channel (^{60}Ni). Although the loss of statistics associated with requiring the detection of 4 protons is clear, so is the substantial improvement in the peak-to-background relative to the total spectrum. The problems associated with leak-through are illustrated in panel (b), where the γ -ray spectrum in coincidence with the detection of 3 protons is shown. The similarity of this spectrum and the total γ -ray spectrum results from the fact that the $3p$, $4p$, $\alpha 3p$, and $3pn$ channels are all among the most strongly populated in this reaction. Because of the imperfect particle-detection efficiencies, all of these channels appear in the 3p-gated spectrum as well as the total spectrum. In this case, the improvement in peak-to-background resulting from charged-particle gating is minimal.

The loss of statistics associated with charged-particle gating can only be reduced by designing an array with a higher efficiency[†]. The problems associated with

[†]Higher particle-detection efficiencies can also be obtained by reducing the beam current so as to reduce the pile-up losses. However, statistics are then lost because of the lower event rate and it is up to the discretion of the experimenter to choose a beam current which balances these two effects.

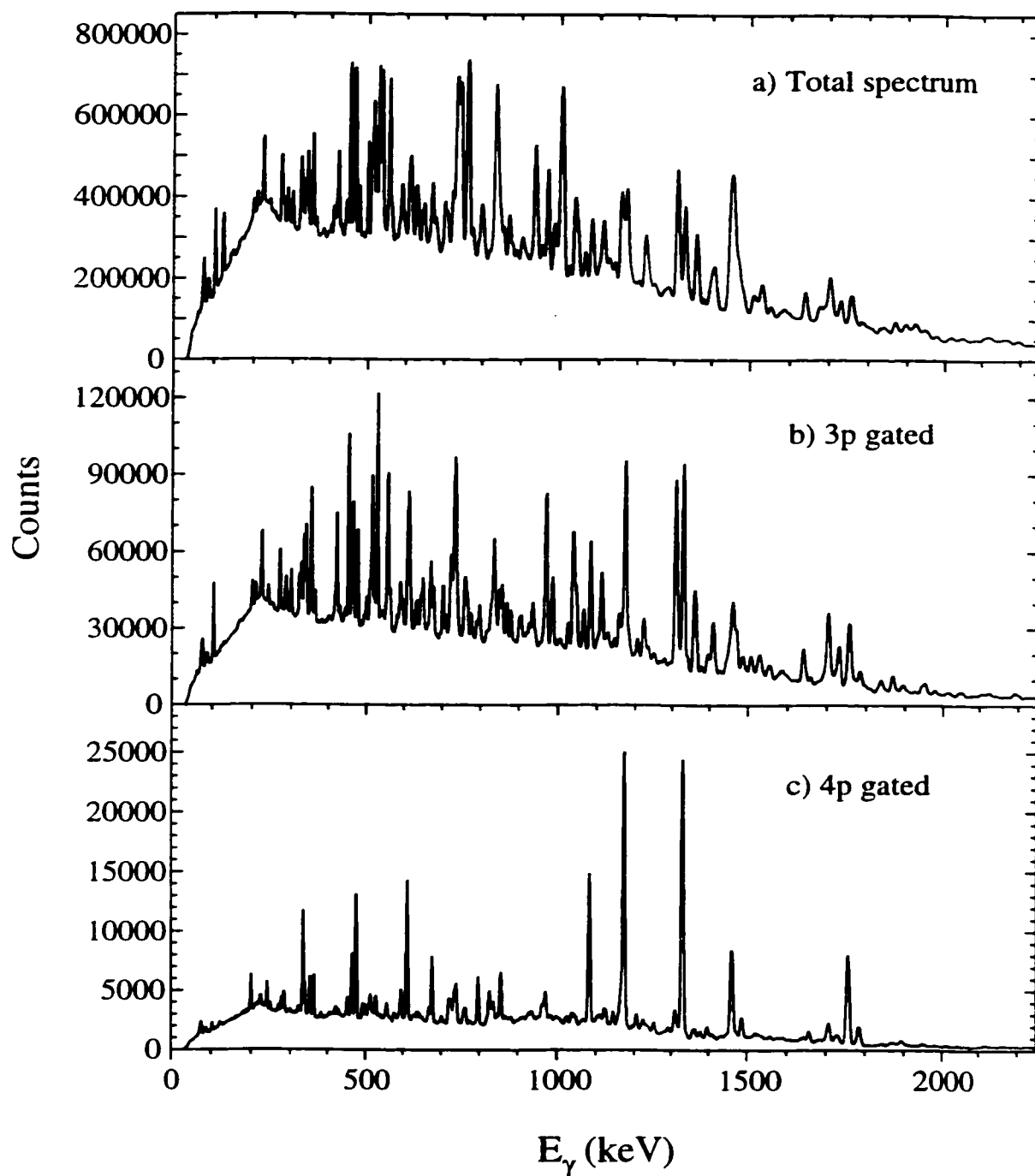


Figure 4.11: The (a) total γ -ray spectrum from the reaction of 80-MeV ^{24}Mg on ^{40}Ca and the spectra in coincidence with the detection of (b) 3 protons and (c) 4 protons. The data were taken with the 8π Spectrometer and the Miniball array.

leak-through can, however, be largely overcome by combining charged-particle detection with total particle and γ -ray energy measurements. This technique was developed as part of this work and will be discussed in Section 4.3.

4.2.5 Kinematic Reconstruction

The degradation of γ -ray energy resolution resulting from the finite target thickness and the opening angles of the Ge detectors was discussed in Section 3.2.3. For the relatively light nuclei studied in this work, however, the largest contribution to the widths of the γ -ray peaks is usually associated with the spread in the nuclear recoil velocities and angles resulting from the “kick” given to the nucleus by the evaporated particles. This loss of resolution can be largely recovered by detecting the charged particles and reconstructing the kinematics of each event [Nyb 92, Sew 94].

The initial recoil momentum of the compound system is known from the kinematics of the beam–target collision. If the charged particles are detected, their emission angles are determined by the detectors they hit (to within the opening angle of the detector) and, as discussed in Section 4.2.3, their energies can be measured. The momenta of the charged particles are therefore determined and it is simply a matter of linear momentum conservation to calculate the momentum vector of the residual nucleus for each event. The energy of each detected γ ray can then be Doppler-shift corrected by applying Eq. 3.5, but with the actual recoil velocity calculated for the event rather than an average recoil velocity, and the angle to each Ge detector taken relative to the calculated recoil direction rather than the beam axis.

The substantial improvement in γ -ray energy resolution that can be achieved by this method is illustrated in Fig. 4.12. Both panels of this figure show the same data for band 1 in ^{60}Cu populated in the reaction $^{40}\text{Ca}(^{29}\text{Si}, 2\alpha p)^{60}\text{Cu}$ at $E(^{29}\text{Si}) = 130$ MeV. The spectrum in (a) is obtained with only an average Doppler-shift correction, while

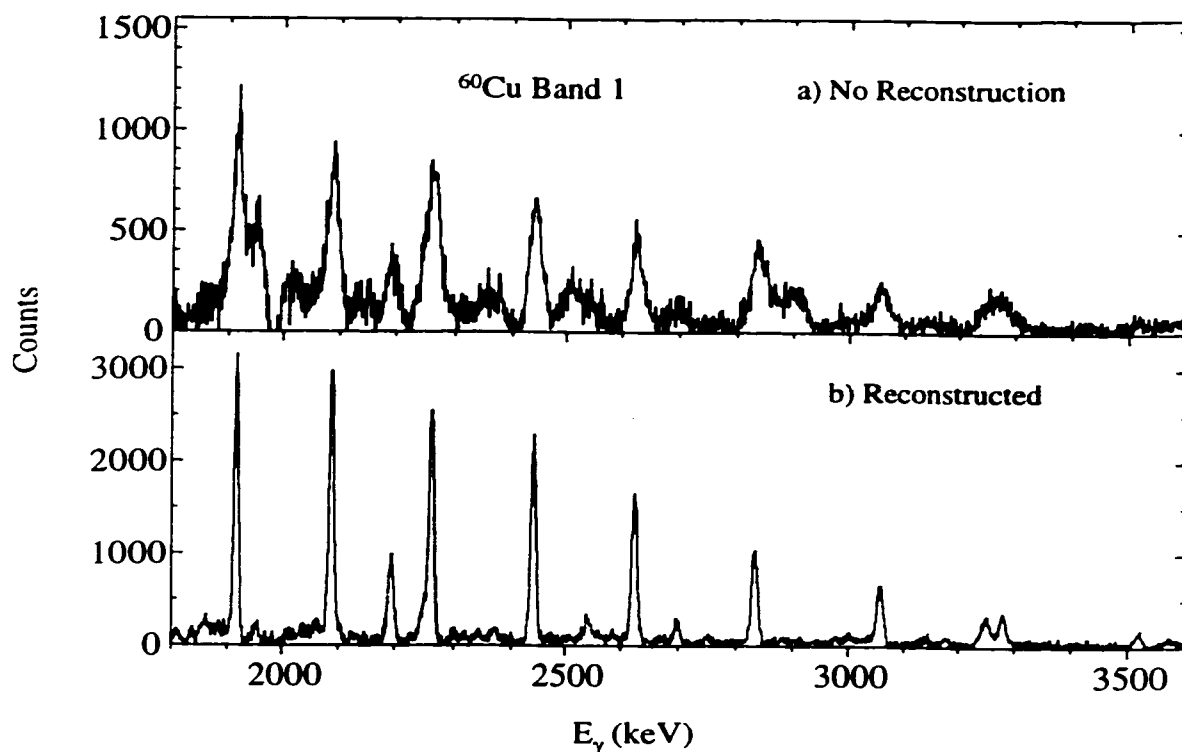


Figure 4.12: The γ -ray spectra of band 1 in ^{60}Cu populated in the reaction $^{40}\text{Ca}(^{29}\text{Si}, 2\alpha p)^{60}\text{Cu}$ at $E(^{29}\text{Si}) = 130$ MeV obtained with (a) an average Doppler-shift correction and (b) event-by-event kinematic reconstruction. The FWHM of the 2441 keV transition, for example, improves from 26.3 keV in (a) to 10.2 keV in (b). Both spectra have been generated by summing gates of one FWHM on all transitions in the band. This implies wider gates in (a) than in (b) and hence additional contamination in the former spectrum.

that in (b) is obtained with event-by-event kinematic reconstruction. The reconstruction technique improves the resolution by a factor of approximately 2.5 in this case. It should also be noted that this improvement in peak-to-background scales as the power of the fold in which the analysis is performed, representing a factor 6.25 improvement for γ - γ coincidences, 15.6 for γ -ray triples, 39 for quadruples, etc.. The kinematic reconstruction made possible by charged-particle detection thus represents a significant gain in sensitivity in high-spin studies of light nuclei and all of the γ -ray spectroscopy performed during this work has made use of this technique.

4.3 Total Energy Channel Selection

The total energy channel selection method [Sve 97a, Sve 97b] was developed in order to overcome the “leak-through” problem associated with imperfect particle-detection efficiencies (see Section 4.2.4). The method is based on the measurement of the total charged-particle and γ -ray energies emitted in heavy-ion fusion reactions and is applicable to all reactions in which charged-particle evaporation from the compound system dominates. This technique has played a significant role in the success of the spectroscopic studies presented in Chapters 5, 6, and 7 and will therefore be discussed in some detail in the following sections.

4.3.1 The Total Energy Method

The total energy method is based on the requirement of energy conservation in reactions where the total energy of all emitted radiations can be measured. In order to distinguish events from different channels in which different particles are emitted, but the same charged particles are detected, we consider the total energy available in the center of mass (CM) system for a particular reaction channel,

$$E_{CM} = T_{CM} + Q, \quad (4.3)$$

where T_{CM} is the center of mass kinetic energy of the beam–target collision (the same for all channels) and Q is the Q -value for the specific channel of interest. This total energy is subsequently emitted as the sum of the kinetic energies of the evaporated particles T_{part} and the total γ -ray energy H_γ emitted by the final nucleus,

$$E_{CM} = T_{part} + H_\gamma. \quad (4.4)$$

It should be noted that T_{part} includes not only the CM energies of the evaporated particles, but also the CM recoil kinetic energy of the nucleus.

If T_{part} and H_γ are measured on an event-by-event basis, each event can be entered into a two-dimensional histogram, referred to as a total energy plane (TEP), where the x -coordinate of the event is H_γ and the y -coordinate is T_{part} . If the small decrease in beam energy through the target is neglected for the moment, E_{CM} is a constant for a given reaction channel and thus Eq. 4.4 constrains all events from this channel to lie on a line of constant total energy in the TEP (i.e. a line with slope equal to negative one and x and y intercepts equal to E_{CM}).

For channel-selection purposes, we are concerned with events in which one or more particles escape detection. As an example, consider a 3-proton particle-gated data set. As noted above, the real $3p$ events must all lie on a line of constant energy in the TEP. Now, consider a $4p$ event that appears in the $3p$ -gated data because one of the protons was not detected. The total energy detected for such an event will differ from that detected for real $3p$ events for two reasons. First, the Q -value for the $4p$ channel is more negative than that for the $3p$ channel, the difference simply being the binding energy of the fourth proton. Therefore, there is less total CM energy available in the $4p$ channel. Second, the kinetic energy of the proton that was not detected is missing from the sum in Eq. 4.4. These two effects add constructively and allow $4p$ events in which one proton is not detected to be distinguished from real $3p$ events. Similar arguments apply to the $\alpha 3p$ and $3pn$ events in the $3p$ -gated data. This is illustrated in Fig. 4.13, where a “theoretical” TEP for a $3p$ -gated data set is shown. The real $3p$ events lie on a line of constant total energy and are separated from the $4p$, $\alpha 3p$, and $3pn$ events with less total detected energy. These latter events will be spread over a region of the TEP by the energy distributions of the missed particles. Given a TEP plot like that shown in Fig. 4.13, the channel selection achieved by charged-particle gating alone can be greatly improved by setting

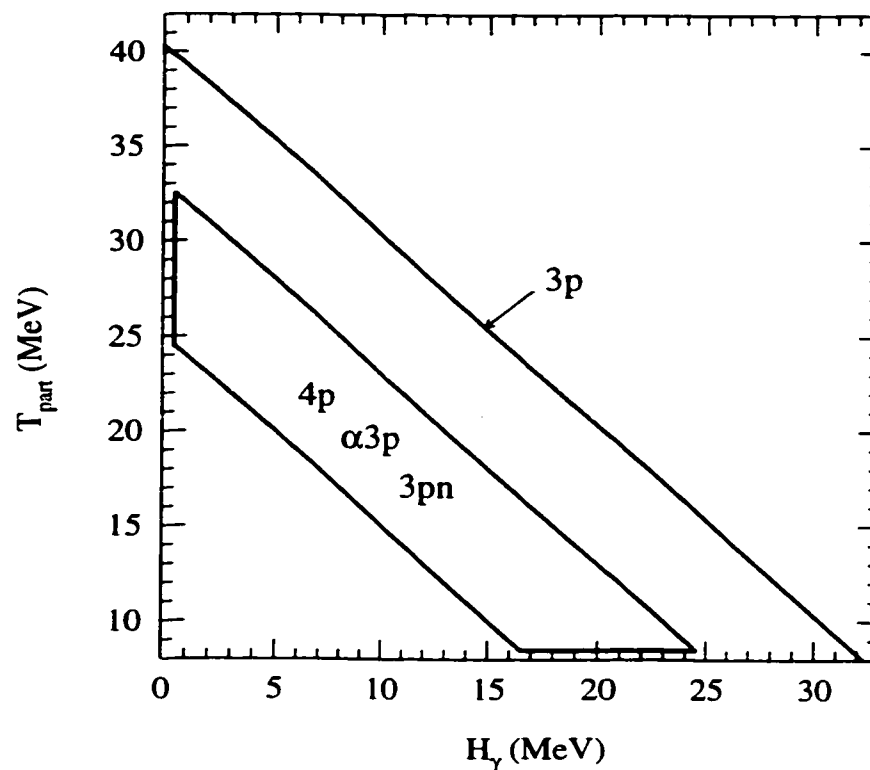


Figure 4.13: “Theoretical” total energy plane for a 3-proton gated data set. The real $3p$ events lie on a line of constant energy and have considerably larger total detected energy than events from the contaminating 4-particle channels.

a two-dimensional gate that selects the real $3p$ events and eliminates the background from the higher particle multiplicity channels that have leaked through because of the imperfect particle detection efficiencies.

An important point should be made to distinguish the total energy method from other combined channel selection methods that have been used in conjunction with charged-particle detection. Given the $3p$ -gated data set discussed above, the real $3p$ events can be preferentially selected simply by setting gates on high H and K values, without making any use of the particle kinetic energies. Alternatively, since the average particle kinetic energy is higher for events from lower particle multiplicity channels, the real $3p$ events can be preferentially selected by taking only events in

which high-energy protons are detected[†], and this method has also been used by a number of authors (e.g. [Bal 89, Gal 92]). For a given channel, however, there are distributions in H , K , and the particle kinetic energies resulting from the statistical nature of the evaporation process and the distributions from channels differing in particle multiplicity by one overlap substantially (see Figs. 4.1 and 4.2). Gating on such distributions always involves a compromise between channel selectivity and loss of statistics. Recall that in Fig. 4.2 an improvement in the fraction of $3n$ events in the γ -ray spectrum by a factor of 4.2 involved the loss of 67% of the events for this channel. The total energy method, however, involves gating on a fixed value (the total energy), not a distribution. The ability to select a channel of interest is therefore determined by the resolution of the total energy measurements, not by the physics of the evaporation process. Since these measurements can often be made with substantially better resolution than the separation in total energy of neighbouring channels, the total energy method can simultaneously provide much higher channel selectivity than the methods mentioned above *and* retain the vast majority of the statistics for the selected channel.

[†]The H and K gating method is usually superior because it selects the highest-spin events, while gating on high-energy particles selects the lowest-spin events from the channel of interest.

4.3.2 Implementation: $8\pi + \text{Miniball}$

The total energy channel selection method was initially tested in an experiment performed with the 8π Spectrometer and the Miniball charged-particle detector array. A 1–2 particle nA beam of 80-MeV ^{24}Mg ions provided by the TASSC facility at the Chalk River Laboratories was directed onto a self-supporting $460 \mu\text{g}/\text{cm}^2$ calcium target, isotopically enriched to 99.8% in ^{40}Ca . In two days of beam time, 4.7×10^8 events were recorded in which at least one γ ray was detected in an HPGe detector, a least three γ rays were detected in the BGO ball, and at least one particle was detected in the Miniball array. Although the results presented below were thus obtained with HPGe γ -ray singles, the total energy method is independent of the fold of the γ -ray data and the generalizations to higher-fold coincidences are straightforward.

The 8π Spectrometer measures the total γ -ray energy for each event with high ($\approx 72\%$) efficiency. The Miniball array measures the energies and directions of the charged evaporation particles in the laboratory frame. Since the initial recoil velocity of the compound system is known from the reaction kinematics, this information allows the CM energies of the charged particles and the CM recoil energy of the nucleus to be calculated. The $8\pi + \text{Miniball}$ system thus provides event-by-event measurements of both H_γ and T_{part} and the total energy channel selection method can be implemented. As noted above, the selectivity of this method is determined by the experimental resolution of the total energy measurements. An example of the total energy response of the $8\pi + \text{Miniball}$ system is presented in Fig. 4.14, where a spectrum of the sum of H_γ and T_{part} is shown for events in which 4 protons were detected. The mean total energy available in the $4p$ channel is 35.5 MeV and the hatched bar of width 2.0 MeV shown in Fig. 4.14 represents the expected range of total energies available in this channel resulting from the decrease in beam energy through

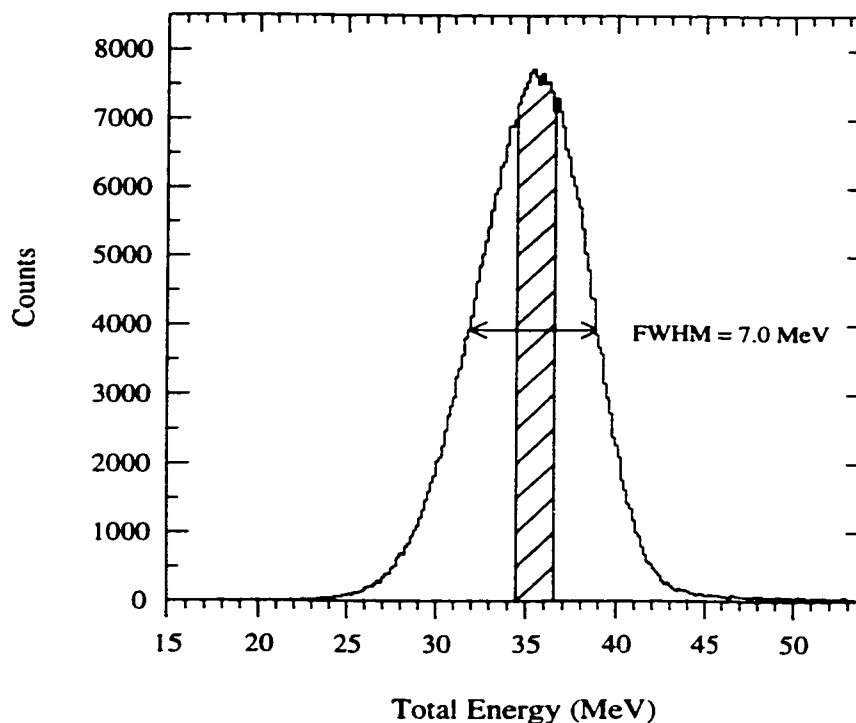


Figure 4.14: Total energy measurement for the $4p$ channel from the reaction of 80-MeV ^{24}Mg on ^{40}Ca . The hatched bar represents the calculated range of total energies available in this channel resulting from the decrease in beam energy through the target. In addition to the detection of 4 protons, a sum of gates has been set on discrete γ rays from the $4p$ channel in order to eliminate contamination from pile-up events and leak-through from 5-particle channels.

the target. The remainder of the 7.0 MeV FWHM represents the experimental total energy resolution. This resolution involves contributions from a number of sources, among which are the intrinsic resolutions of the particle and γ -ray detectors, event-to-event variations in the fraction of the total γ -ray energy that is actually detected, and uncertainties in the CM particle kinetic energies resulting from the finite opening angles of the charged-particle detectors. It should be noted that typical total energy separations for one-particle leak-through channels in this mass region are 10–20 MeV. The total energy response shown in Fig. 4.14 is therefore usually sufficient to resolve the channel of interest from these leak-through channels.

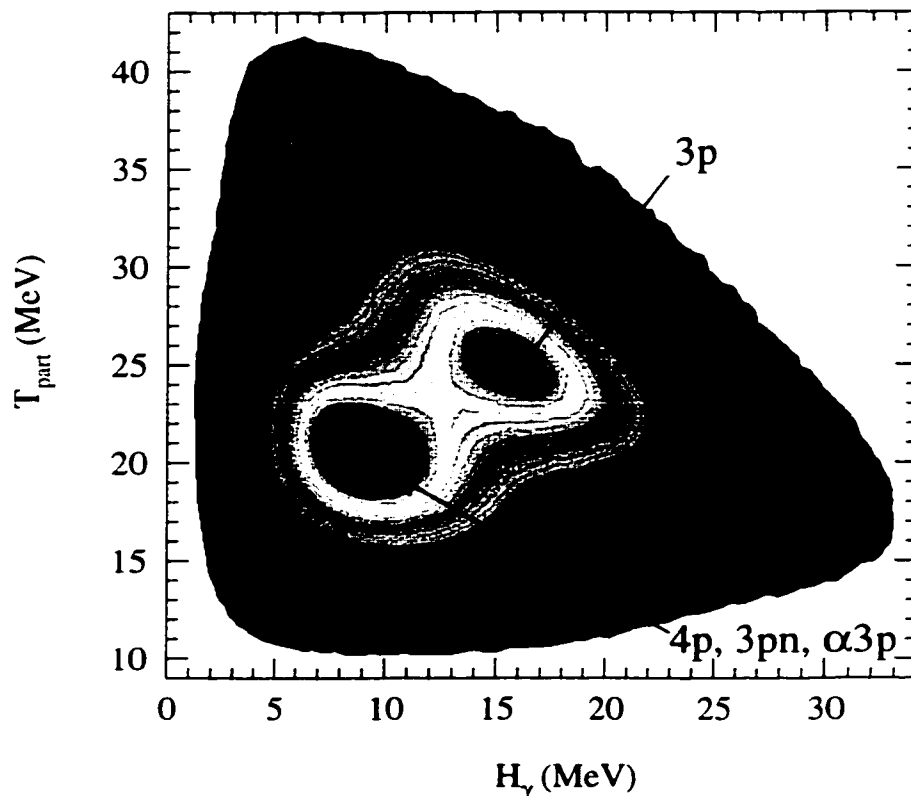


Figure 4.15: TEP histogram for all events in which 3 protons were detected. The real $3p$ events with the larger total detected energy are cleanly separated from events from the contaminating 4-particle channels.

The problems associated with $4p$, $\alpha 3p$, and $3pn$ events in the 3-proton gated data were discussed in Section 4.2.4. In Fig. 4.15, the TEP for the $3p$ -gated data is shown. As expected from the discussion of Section 4.3, the real $3p$ events have considerably larger total detected energy than the $4p$, $\alpha 3p$, and $3pn$ events and the TEP method is seen to provide a clean separation of the $3p$ channel from the contaminating 4-particle channels. The exact positions of the $3p$, $4p$, $\alpha 3p$, and $3pn$ events in Fig. 4.15 can be determined by entering the $3p$ -gated data into a cube in which the x - and y -coordinates of the event are again H_γ and T_{part} , and the z -coordinate is the energy of a discrete γ ray detected in a Ge detector. Gates can then be set on discrete γ rays and the TEP for the channel to which the γ ray belongs projected from the

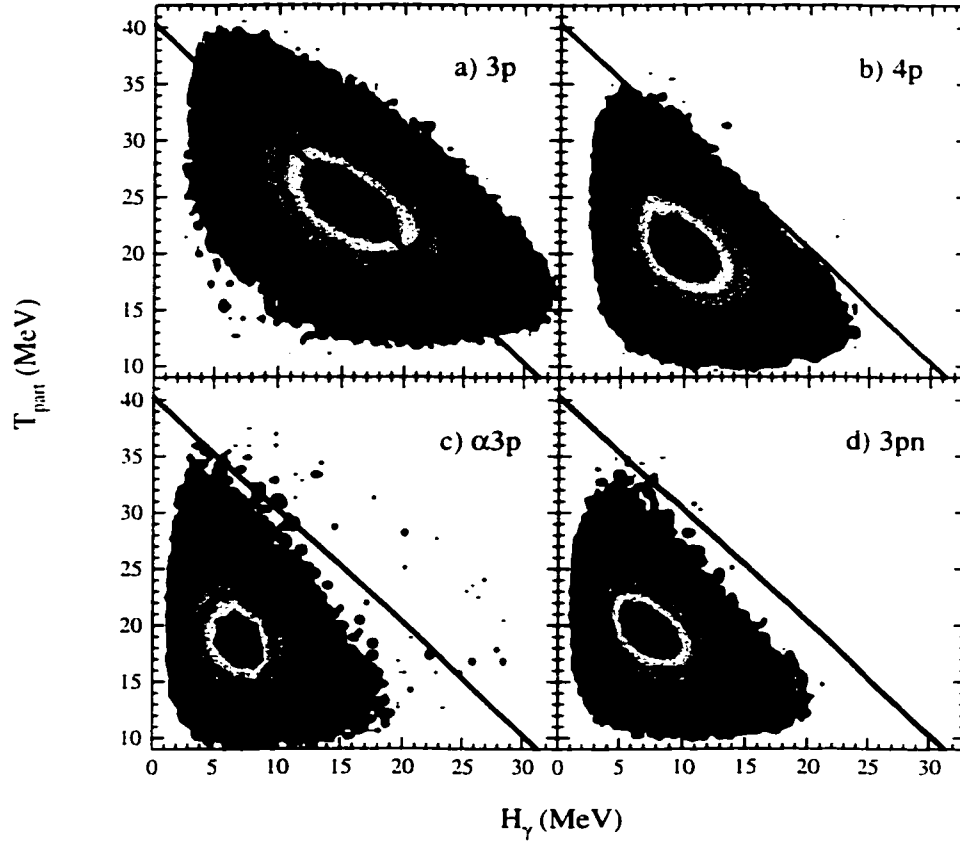


Figure 4.16: TEPs from the $3p$ -gated data obtained by gating on discrete γ rays from the (a) $3p$ (^{61}Cu), (b) $4p$ (^{60}Ni), (c) $\alpha 3p$ (^{57}Co), and (d) $3pn$ (^{60}Cu) channels. The line of constant total energy available in the $3p$ channel is shown for reference.

cube. Total energy planes produced in this manner are shown for gates on γ rays from the $3p$ (^{61}Cu), $4p$ (^{60}Ni), $\alpha 3p$ (^{57}Co), and $3pn$ (^{60}Cu) channels in Figs. 4.16 (a), (b), (c), and (d), respectively. For reference, the calculated line of constant total energy, $E_{CM} = 40.3$ MeV, expected for $3p$ events at the center of the target is shown in each panel. The real $3p$ events lie along this line, while the total energies detected for the 4-particle channels are considerably smaller. The $4p$ events are well removed from the $3p$ constant energy line and, because of the large kinetic energy of the missed alpha particle and the large neutron binding energy, the separation is even more complete for the $\alpha 3p$ and $3pn$ channels.

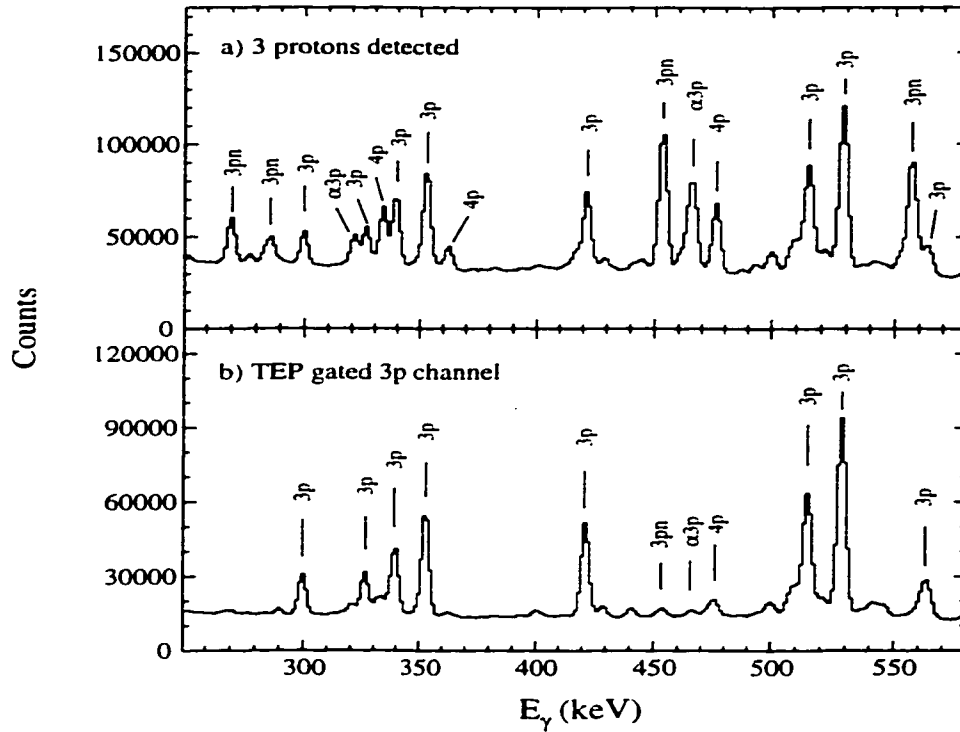


Figure 4.17: A portion of the γ -ray spectrum obtained by (a) gating on 3 detected protons and (b) setting a gate on the real $3p$ region of the $3p$ -gated TEP (Fig. 4.15).

In order to select the $3p$ channel, a two-dimension gate[†] can be set in the TEP of Fig. 4.15 which includes the majority of real $3p$ events but little contamination from the 4-particle channels. In Fig. 4.17 the γ -ray spectra obtained by (a) gating on 3 detected protons and (b) setting a gate on the real $3p$ events in the TEP are compared. Spectrum (b) contains 90% of the real $3p$ events from spectrum (a), but only 14% of the $4p$ events and less than 4% of the $\alpha 3p$ and $3pn$ events. While real $3p$ events constitute only 53% of the 3-proton gated spectrum, the TEP-gated spectrum is 95% $3p$ events. The TEP technique is thus seen to provide a powerful method of improving channel selection with little loss of statistics for the selected channel.

[†]Alternatively, a one-dimension gate on the total energy, i.e. the sum of H_γ and T_{part} , can be used. This is equivalent to setting gates consisting of diagonal lines in the TEP. However, the two-dimensional gating method is more versatile in that the gating lines need not be diagonal and different TEP regions for the channel of interest, e.g. high H_γ , can be easily selected.

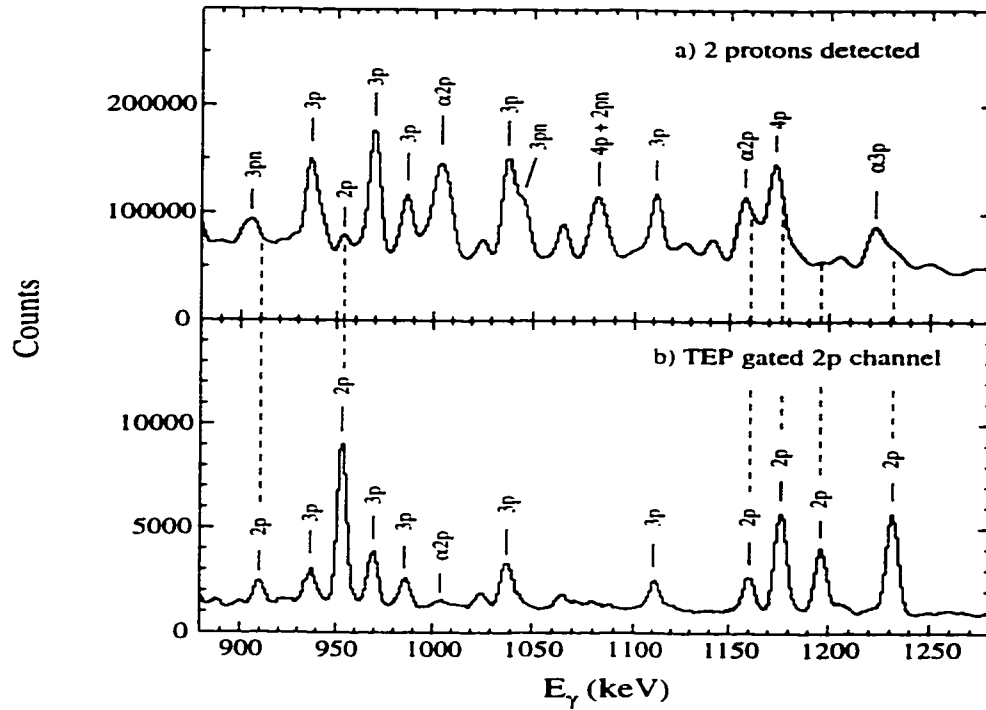


Figure 4.18: A portion of the γ -ray spectrum obtained by (a) gating on 2 detected protons and (b) applying the TEP gate shown in Fig. 4.19 to the $2p$ -gated data.

In the above discussion, the $3p$ -gated data, in which all of the relevant channels were strongly populated, has been used to illustrate the effectiveness of the total energy method. The real power of the method, however, is in the selection of weakly populated low particle multiplicity channels. In the reaction discussed here, for example, the $2p$ channel leading to ^{62}Zn represented only $\sim 0.3\%$ of the total fusion cross section. A portion of the γ -ray spectrum in coincidence with the detection of 2 protons is shown in Fig. 4.18 (a). Because of the weak population of the $2p$ channel and the imperfect particle detection efficiencies, this spectrum is completely dominated by leak-through from the more strongly populated $4p$, $\alpha 3p$, $\alpha 2pn$, $2\alpha 2p$, $3pn$, $3p$, $\alpha 2p$, and $2pn$ channels. Of the γ rays in ^{62}Zn , only the $2^+ \rightarrow 0^+$ transition at 954 keV is visible in the $2p$ -gated data and this peak is an order of magnitude smaller than those from the contaminating channels.

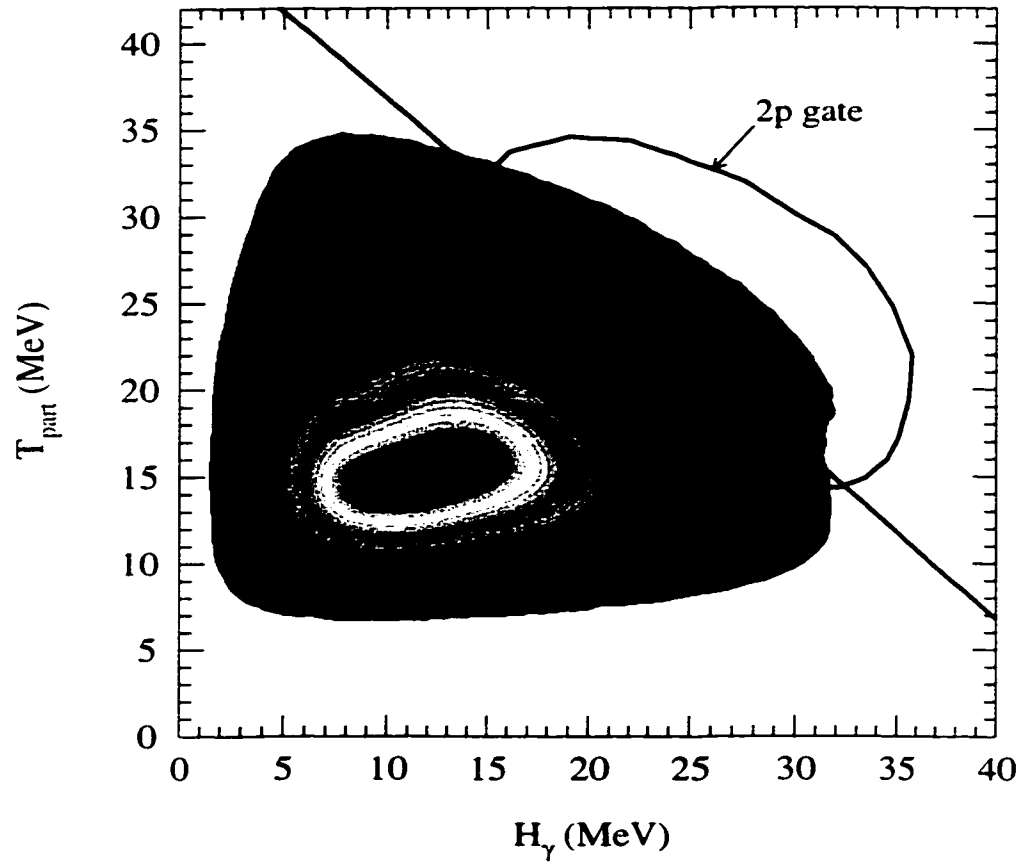


Figure 4.19: TEP histogram for all events in which 2 protons were detected. The high-energy “bulge” is produced by events from the weakly populated $2p$ channel.

In Fig. 4.19 the TEP for all events in which 2 protons were detected is shown. Although the $2p$ channel is sufficiently weak compared to the contaminating leak-through channels that it does not show up as a peak in this TEP, the calculated line of constant energy for the $2p$ channel focuses attention on the high-energy “bulge” in the TEP that is produced by the real $2p$ events. Setting the gate shown in Fig. 4.19, the γ -ray spectrum shown in Fig. 4.18 (b) is obtained. This spectrum is now dominated by real $2p$ events. The TEP gate improves the fraction of real $2p$ events in the γ -ray spectrum by a factor of 46 and the clean γ -ray gates required for a detailed spectroscopic study of this weakly-populated channel are now clearly available.

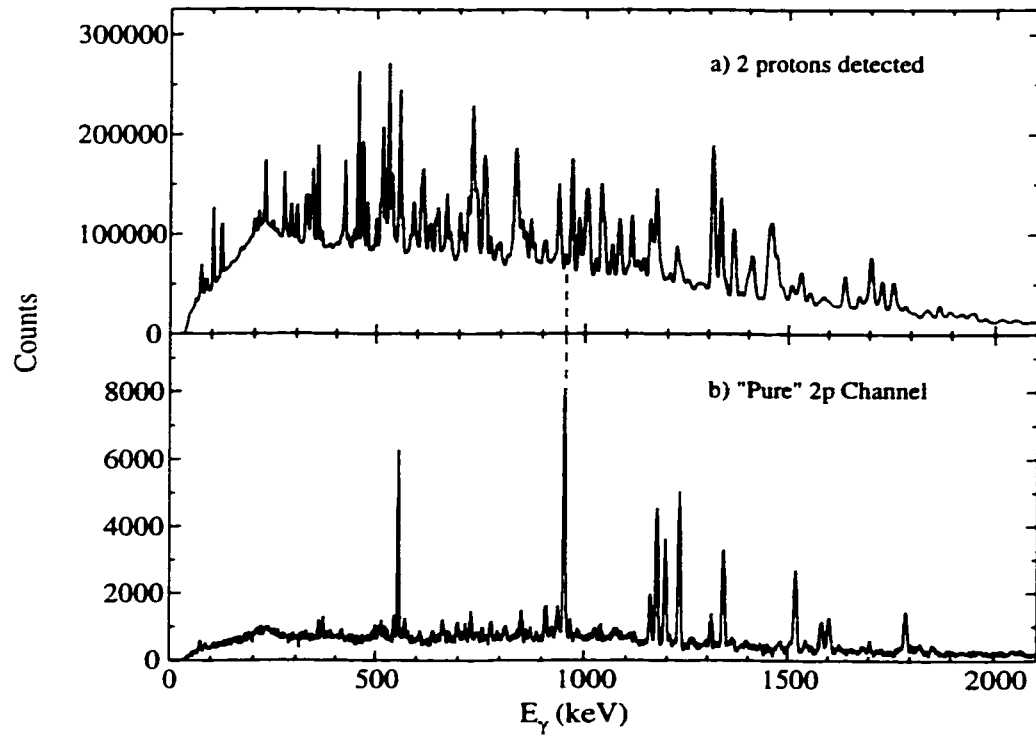


Figure 4.20: Comparison of (a) the γ -ray spectrum in coincidence with the detection of 2 protons and (b) a “pure” $2p$ channel (^{62}Zn) spectrum obtained by applying the TEP gate shown in Fig. 4.19 and subtracting remaining contaminants.

Because of the width of the total energy response (see Fig. 4.14), a small number of events from the higher particle multiplicity channels leak-through the TEP gate. These remaining contaminants can subsequently be removed by subtracting higher particle multiplicity gated spectra. For example, the small contaminating peaks remaining in Fig. 4.18 (b) are primarily from the $3p$ channel (^{61}Cu). In Fig. 4.20, the spectrum in coincidence with the detection of 2 protons is compared with a “pure” ^{62}Zn spectrum obtained by subtracting a properly normalized portion of the $3p$ -gated spectrum from the TEP-gated $2p$ spectrum of Fig. 4.18 (b). All of the γ rays visible in Fig. 4.20 (b) belong to ^{62}Zn , while the dashed vertical line above the 954-keV $2^+ \rightarrow 0^+$ transition shows the small contribution the real $2p$ channel makes in Fig. 4.20 (a). It should be noted that care must be taken in the subtraction procedure used to produce

“pure” spectra like that shown in Fig. 4.20 (b). The events involved in the subtraction must be treated in a manner identical to the events that form the contamination in the original data. In preparing the $3p$ -gated spectrum to subtract from the $2p$ TEP-gated spectrum, the detection of three protons is simply used to tag the events. One of the protons (chosen at random) is then intentionally ignored in the remainder of the analysis, including the kinematic reconstruction. These tagged events are subjected to all of the same gating conditions used to create the TEP-gated $2p$ spectrum and should thus be statistically equivalent to the $3p$ events that appear in this spectrum because a proton was missed in the experiment. A normalized fraction of this $3p$ spectrum can then be subtracted from the TEP-gated $2p$ spectrum to yield a “pure” $2p$ spectrum like that shown in Fig. 4.20 (b).

One can, of course, attempt to make a “pure” spectrum without any recourse to the TEP method by subtracting properly normalized fractions of all the higher particle multiplicity channels that contribute to the leak-through contamination. In situations where the channel of interest is not too weak compared to the contamination being subtracted, this method can be quite effective (see [Cam 96, Rud 96], for example). However, subtraction of the small contaminating peaks remaining following TEP gating is a superior method. Firstly, the success of subtraction relies on the statistical equivalence of the “tagged” events from the higher particle multiplicity gated data and the leak-through events that one is attempting to remove. If the channel of interest is weakly populated and contaminants dominate the spectrum (as in the $2p$ example above), the statistical fluctuations in the spectrum remaining after subtraction will overwhelm the signal from the desired channel. Subtracting only the small contaminating peaks remaining after TEP gating, however, greatly reduces the statistical fluctuations in the “pure” spectrum. Secondly, usually signifi-

cant amounts of only one contaminating channel leak-through the TEP gate (the $3p$ contaminant in the $2p$ example above). The subtraction of only a single spectrum is therefore required. Subtraction without TEP gating, however, requires the proper normalization of many higher particle multiplicity spectra ($4p$, $\alpha 3p$, $2\alpha 2p$, $3p$, and $\alpha 2p$ in our example). Thirdly, channels differing only by neutron evaporation cannot be separated by subtracting charged-particle gated spectra. In the reaction discussed here, the cross section for the $2pn$ channel is ~ 10 times larger than that for the $2p$ channel. A “pure” $2p$ channel spectrum produced by subtraction without TEP gating is therefore dominated by $2pn$ rather than real $2p$ events. The $2p$ TEP gate, however, cleanly rejects the $2pn$ events and the “pure” $2p$ spectrum shown in Fig. 4.20 (b) contains no measurable contamination from the $2pn$ channel.

The examples discussed above have involved the selection of channels involving only charged-particle evaporation. These channels always represent the highest total energy component of their respective TEPs and can therefore be cleanly and efficiently selected by the TEP method. For channels involving neutron evaporation, the method is less effective and requires subtraction. Nonetheless, the TEP method can still make a significant contribution to the selection of these channels. For example, the $3pn$ channel can be selected from the events in which 3 protons are detected by setting a gate in the TEP around the region containing the $3pn$ events (Fig. 4.16(d)). Although this gate contains contamination from the $4p$ and $\alpha 3p$ leak-through channels, it eliminates the real $3p$ events. The $4p$ and $\alpha 3p$ events can then be subtracted using the higher particle multiplicity gated data. A “pure” $3pn$ (^{60}Cu) spectrum obtained in this manner is compared with a “pure” $3p$ (^{61}Cu) spectrum in Fig. 4.21. It is clear that the two spectra shown in this figure are completely different and, as noted above, such a separation of channels differing only by neutron evaporation cannot be

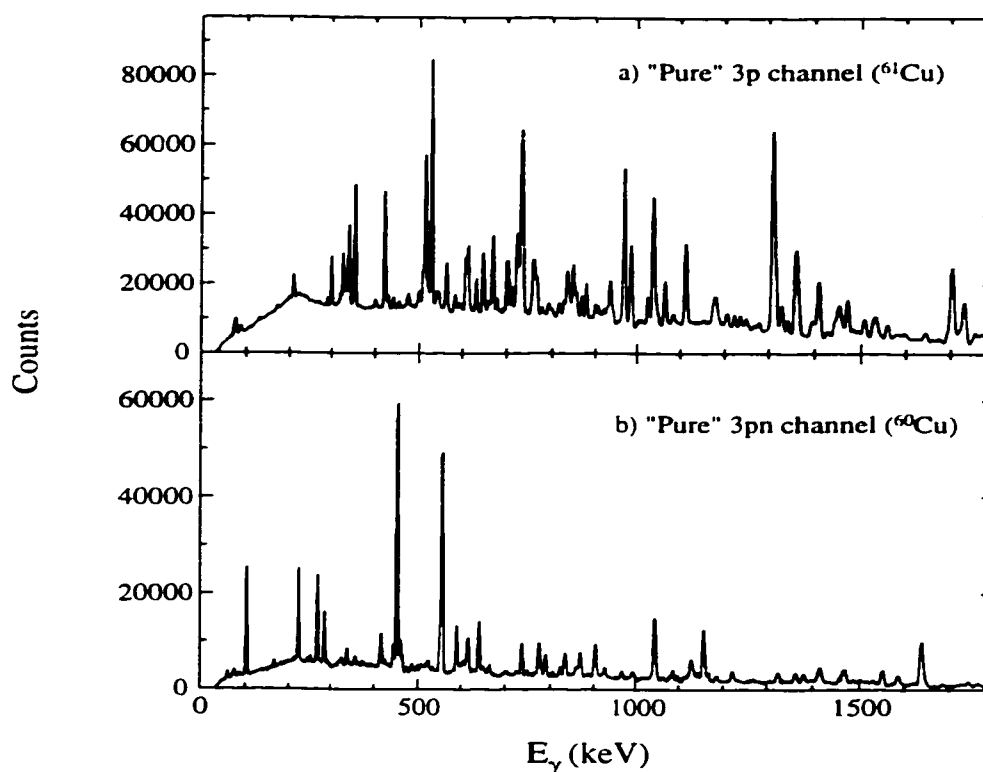


Figure 4.21: “Pure” γ -ray spectra for the (a) $3p$ and (b) $3pn$ channels obtained by applying TEP gates to the $3p$ -gated data and subtracting remaining contaminants.

accomplished by straight subtraction of charged-particle gated spectra.

The results presented in this section clearly demonstrate that the channel selectivity required for high-spin studies of proton-rich $A \sim 60$ nuclei can be achieved by combining charged-particle detection with the total energy method. In fact, this technique often allows the experimenter to analyze data containing only γ rays from the channel of interest, a luxury that is seldom possible even in reactions in which a small number of different nuclei are produced. For channels populated with relatively large cross sections, this leads to an improved peak-to-background ratio and to a higher sensitivity to weak decay pathways, while for very weak reaction channels the combination of high efficiency and high selectivity provided by this method is essential to the success of detailed spectroscopic studies.

4.3.3 Implementation: Gammasphere + Microball

Although the total energy channel selection method was specifically designed to take advantage of the excellent total energy resolution of the 8π Spectrometer + Miniball system, it is applicable in any situation where a 4π charged-particle detector array with reasonable energy and angular resolution is combined with a 4π γ -ray spectrometer capable of event-by-event H_γ measurements. In particular, these criteria are met by the combination of the Microball charged-particle detector and Gammasphere operated without the Hevimet collimators (see Section 3.2), and the total energy channel selection method has been successfully employed with this system in all of the spectroscopic studies presented in Chapters 5–7.

As noted in Section 4.3.1, the selectivity and efficiency of the total energy method are determined by the total energy resolution of the detection system. The spectrum of total energies measured with Gammasphere and the Microball for events in which 4 protons were detected from the reaction of 134-MeV ^{32}S on ^{40}Ca is shown in Fig. 4.22. The hatched bar of width 2.7 MeV centered at 49.7 MeV represents the expected range of total energies available in this channel due to energy loss of the beam through the $500\text{ }\mu\text{g}/\text{cm}^2$ target. The remainder of the 9.0 MeV FWHM represents the total energy resolution of Gammasphere and the Microball. Comparing this with the FWHM of 7.0 MeV at a total energy of 35.5 ± 1.0 MeV shown for the 8π Spectrometer and Miniball array in Fig. 4.14, it can be seen that the fractional width of the total energy response is effectively equivalent for these two detection systems.

It should be noted that an *a priori* knowledge of the H_γ efficiency of Gammasphere was not available and, in fact, this efficiency will vary considerably between experiments depending on the number of HPGe detectors used. This efficiency can, however, be determined from the experimental data by making use of the energy

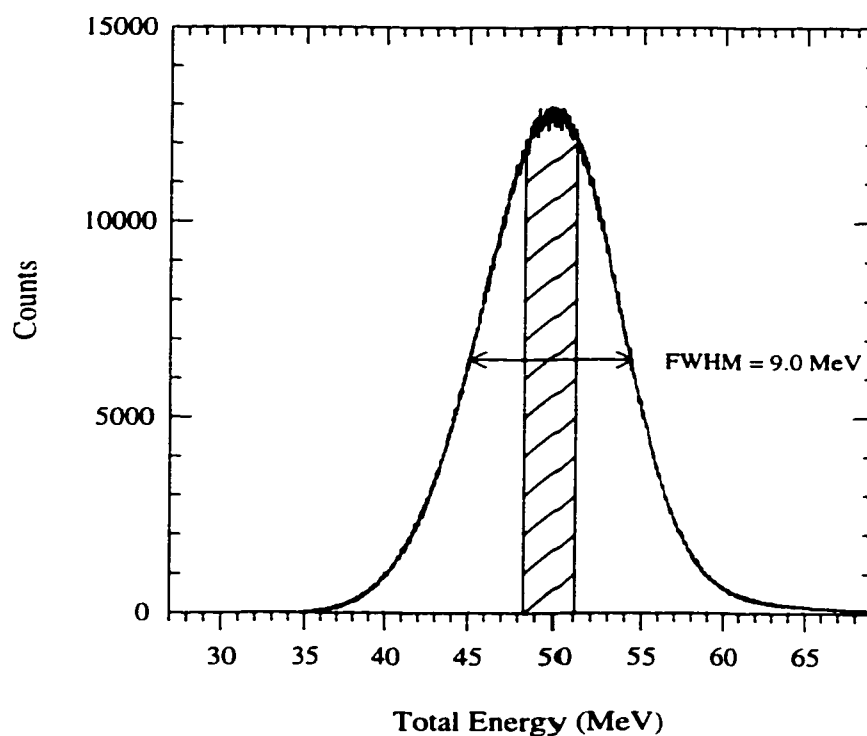


Figure 4.22: Total energy measurement for the $4p$ channel from the reaction of 134 MeV ^{32}S on ^{40}Ca . The hatched bar represents the calculated range of total energies available in this channel resulting from the decrease in beam energy through the target. Four protons have been detected and the real $4p$ events have been selected by gating on discrete γ rays from ^{68}Ge .

calibration for the Microball and the known total energy available in each reaction channel. For the experiment discussed above, in which 101 HPGe detectors were used, the H_γ efficiency of Gammasphere was measured to be 70% by the requirement that the centroid of the $4p$ -gated total energy peak shown in Fig. 4.22 occur at the known available energy of 49.7 MeV. It should also be noted that event-to-event fluctuations in this efficiency resulting from the missing solid angle in the detector array make a substantial contribution to the width of the total energy response, and the 6–7% increase in H_γ efficiency that could be achieved if the full 110 HPGe detectors were used would lead to a significant improvement in the total energy resolution of the Gammasphere + Microball system.

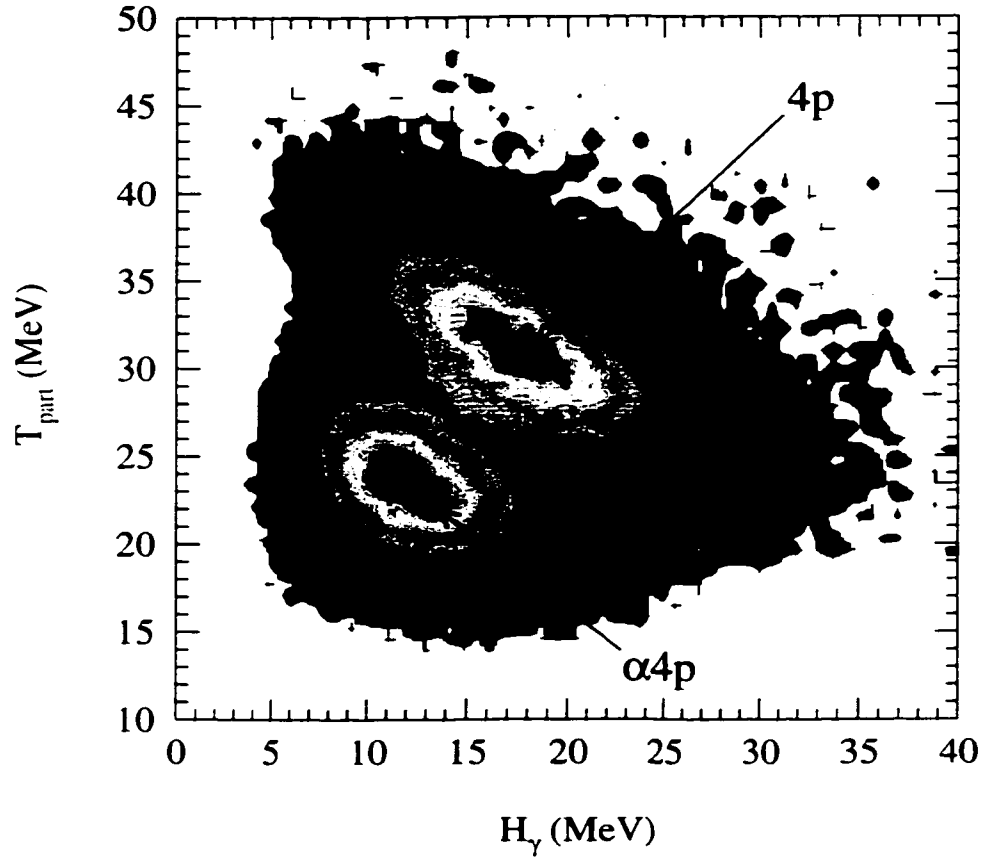


Figure 4.23: Total energy plane for events from the reaction of 134-MeV ^{32}S on ^{40}Ca in which 4 protons were detected. A gate has been set on a 1315-keV γ ray, which is a strong transition in both the $4p$ and $\alpha 4p$ channels.

As noted above, the total energy resolution achieved with Gammasphere and the Microball is similar to that achieved with the 8π and Miniball and is certainly sufficient to identify and remove leak-through events in charged-particle gated data. This is clearly illustrated in Fig. 4.23, where the TEP for events in which 4 protons were detected from the reaction of 134-MeV ^{32}S on ^{40}Ca is shown. This TEP has also been gated by a 1315-keV γ ray, which occurs in both the real $4p$ channel (^{68}Ge) and the leak-through $\alpha 4p$ channel (^{64}Zn). This gate leaves the $4p$ and $\alpha 4p$ channels with roughly equal intensity in Fig. 4.23 and highlights the very clean separation of these events achieved by the total energy method.

4.4 Other Channel Selection Methods

4.4.1 Neutron Detection

The selection of channels involving neutron evaporation by the TEP method was briefly discussed in the previous section. Although this method has the advantage of high efficiency and, as shown in Fig. 4.21, can cleanly separate channels differing by neutron evaporation, the TEP method does require subtraction. For weak reaction channels, this method will ultimately be limited by the statistical fluctuations associated with the subtraction process and it is desirable to avoid this problem by detecting the evaporated neutrons. Neutron detection is, however, considerably more difficult than charged-particle detection and is achieved with both a lower efficiency and a higher penalty to the γ -ray detection efficiency.

Neutrons, as neutral particles, do not undergo electromagnetic interactions in a detector. The fast neutrons produced in fusion-evaporation reactions are thus usually detected by the electromagnetic interactions of the recoil protons produced when the neutrons undergo nuclear scatterings in a hydrogen-rich scintillator material. The cross sections for such scatterings are, however, relatively low and neutron detection is inefficient. The neutron detectors must also be relatively large and it is necessary to remove some of the γ -ray detectors, resulting in decreased γ -ray detection efficiency and a degradation of the H_γ response. For example, 15 of the Gammasphere HPGe detectors at forward angles were replaced with liquid-scintillator neutron detectors in one of the experiments performed during this work. In the reaction of 125-MeV ^{28}Si on ^{40}Ca , a $\sim 5\%$ neutron detection efficiency was achieved and the γ -ray efficiency was reduced to 82% of its original value. It is important to note that this loss of γ -ray efficiency scales as the power of the coincidence fold, representing a reduction to 55% of the original triples efficiency, for example. The combination of the low neutron

detection efficiency and this loss of γ -ray efficiency leads to a severe price in statistics associated with neutron detection. Experience gained from this experiment indicates that, in this mass region, the higher efficiency of the TEP method yields superior quality data for neutron evaporation channels populated with cross sections greater than ~ 1 mb. For channels populated with less than $\sim 0.1\%$ of the total fusion cross section, however, the higher selectivity of neutron detection becomes essential (see [Rud 97], for example).

4.4.2 Recoil Detection

The channel selection methods discussed thus far have involved methods of identifying the number and type of evaporated particles. An alternative approach is to detect and identify the recoiling nucleus. A number of large electromagnetic recoil separators, including the Daresbury Recoil Separator (DRS) [Jam 88], the Argonne Fragment Mass Analyzer (FMA) [Dav 92], and the Oak Ridge Recoil Mass Spectrometer (RMS) [Col 92], have been built for this purpose. In general, these separators consist of a series of strong electric and magnetic fields which separate the recoiling nuclei from beam ions and determine the mass of the recoils by dispersing them on a position-sensitive focal-plane detector according to the ratio of their mass A to charge state Q . To identify the recoil nucleus, it is also necessary to determine its atomic number Z . For relatively light nuclei, this is often accomplished by making use of the Z -dependence of the recoil energy losses in a segmented ionization chamber. The sensitivity of this method, however, depends strongly on the reaction kinematics. For inverse-kinematic reactions (i.e. the beam ions heavier than the target ions), the high recoil velocities both focus the recoiling nuclei into the separator and provide good Z resolution in the ionization chamber (see [Cam 90, Enn 91], for example). For lower recoil velocities, both the efficiency and resolution decrease.

This method of channel selection, in conjunction with charged-particle detection and H and K measurements, was used in the 134-MeV ^{32}S on ^{40}Ca Gammasphere + Microball + FMA experiment performed during this work. The discussion in this thesis, however, focuses on the results obtained for ^{60}Zn in this experiment. For this nucleus, which was populated via the 3α evaporation channel, the broad recoil cone led to a very low ($\sim 0.1\%$) recoil detection efficiency. This channel was therefore selected and studied by the more efficient charged-particle detection + TEP method.

Although not used in this work, a discussion of channel selection is not complete without briefly mentioning a very powerful method of recoil identification that has recently gained considerable attention in the study of proton-rich nuclei with charged-particle unstable ground and/or isomeric states. In the recoil decay tagging (RDT) method [Pau 95], the recoiling nuclei are implanted in a double-sided silicon strip detector (DSSD) which detects both the arrival of the recoil and its subsequent charged-particle decay. The combination of gating on the discrete energy of the emitted charged particle and requiring the decay to be correlated with the implantation in both space (determined by the pixel of the DSSD) and time (on the order of the charged-particle decay half-life) provides an extremely sensitive means of identifying the recoil ion. Clearly, this method only applies to the study of nuclei which decay by charged-particle emission. In this realm of applicability, however, this technique undoubtedly provides the most sensitive channel selection of any method currently used in conjunction with large γ -ray detectors and has enabled γ -ray spectroscopy to be performed for nuclei populated with cross sections of only a few hundreds, or even tens, of nanobarns. For a detailed discussion of this powerful technique, and the study of proton radioactivity in general, the reader is referred to the recent review article by Woods and Davids [WD 97] and references cited therein.

Chapter 5

Smooth Band Termination in ^{62}Zn

The observation of two sets of strongly coupled rotational bands in ^{62}Zn [Sve 98a] is discussed in this chapter. The terminating states of these bands have been identified and lifetime measurements indicate that the transition quadrupole moments in these bands decrease as termination is approached. These results represent the first observation of the terminating states of rotational bands in the $A \sim 60$ mass region and confirm the predicted loss of collectivity associated with smooth band termination.

5.1 Motivation

Previous spectroscopic studies of proton-rich $A \sim 60$ nuclei with small γ -ray detector systems were limited to the noncollective spherical states that dominate the low-spin structures of nuclei in this mass region. In 1995, just prior to the start of this work, a first experiment to probe the high-spin structure of $A \sim 60$ nuclei using a 4π charged-particle detector (the Miniball) in conjunction with a modern 4π γ -ray detector array (the 8π Spectrometer) was performed by Galindo-Uribarri *et al.* at the Chalk River Laboratories. This experiment led to the discovery of a pair of strongly coupled rotational bands in ^{64}Zn that were interpreted as being built on a proton excitation across the $Z = 28$ spherical shell gap from the $f_{7/2}$ to the $g_{9/2}$ orbital [Gal 98]. This

exciting discovery of well-developed collective rotation in such a light nucleus formed a large part of the initial motivation for the research presented in this thesis. The total energy channel selection method discussed in the previous chapter was developed with the specific goal of increasing the sensitivity of high-spin studies in this mass region and, employing this technique, two sets of strongly coupled rotational bands were identified in ^{62}Zn in the data from the same experiment in which ^{64}Zn had been studied. These rotational bands in ^{62}Zn form the subject of the present chapter.

Smoothly terminating rotational bands were first identified [Jan 95] and interpreted [Rag 95] in $A \sim 110$ nuclei with a relatively small number of valence particles outside doubly-magic ^{100}Sn . Similar to these bands, the rotational bands in ^{62}Zn and ^{64}Zn , with a small number of valence particles outside doubly-magic ^{56}Ni , showed the rapidly decreasing dynamic moment of inertia characteristic of smooth band termination (see Fig. 2.9). In fact, it was clear from the limited spin content of the valence particles and holes in these light nuclei that these bands were being observed almost to their terminating states. However, in neither ^{62}Zn nor ^{64}Zn were the high-energy transitions identified that decay out of these bands and link them to the remainder of the level scheme. Definite spin, parity, and excitation energy assignments were therefore not possible. Even more crucial to understanding these smoothly terminating bands, both in the $A \sim 60$ and $A \sim 110$ mass regions, was the predicted loss of collectivity inherent in their theoretical description (see Section 2.5.2). Although many such bands had been identified in nuclei around ^{109}Sb (see Fig. 4 in [Jan 97]), the lifetime measurements close to termination necessary to test this prediction had not been possible. Similarly, insufficient statistics were recorded in the original 8π + Miniball experiment to perform such measurements for the terminating bands in ^{62}Zn and ^{64}Zn .

The possibility of testing the predicted loss of collectivity in smoothly terminating bands motivated a second experiment to study high-spin states in ^{62}Zn performed with Gammasphere and the Microball charged-particle detector array. As will be discussed in the following sections, this experiment led to the extension of the ^{62}Zn bands to their terminating states and to the observation of transitions linking these bands to the remainder of the decay scheme. Most significantly, lifetime measurements were possible all the way to the terminating states, and these measurements have confirmed the predicted loss of collectivity associated with the phenomenon of smooth band termination [Sve 98a][†].

5.2 Experiments

As noted above, ^{62}Zn was studied in two experiments. In both experiments, high-spin states in ^{62}Zn were populated via the $^{40}\text{Ca}(^{28}\text{Si},\alpha 2p)^{62}\text{Zn}$ reaction. In the first experiment, a $430\text{ }\mu\text{g}/\text{cm}^2$ target of natural calcium (96.9% ^{40}Ca) was bombarded by a beam of 115-MeV ^{28}Si ions provided by the TASCC facility at the Chalk River Laboratories. Gamma rays were detected with the 8π Spectrometer and charged particles were detected with the Miniball array. The hardware event trigger required at least 2 clean HPGe detectors to fire in prompt coincidence with at least 3 elements of the BGO ball and 1.8×10^8 such events were recorded during the experiment.

In the second experiment, a $500\text{ }\mu\text{g}/\text{cm}^2$ target isotopically enriched to 99.9% in ^{40}Ca was bombarded by a 125-MeV ^{28}Si beam provided by the 88-Inch Cyclotron at Lawrence Berkeley National Laboratory. The detection system consisted of the Gammasphere array, comprising 83 HPGe detectors with the Hevimet collimators

[†]As noted in Section 2.5, lifetime measurements approaching the terminating states of bands in ^{108}Sn and ^{109}Sb [Wad 98] performed concurrent with this work have also confirmed the loss of collectivity associated with smooth band termination.

removed to allow γ -ray multiplicity and sum-energy measurements, the Microball charged-particle detector array, and 15 liquid scintillator neutron detectors[†] located at forward angles ($\theta \leq 37.4^\circ$) relative to the beam axis. The event trigger required at least 3 clean HPGe detectors or at least 2 HPGe detectors and a neutron detector to fire in prompt coincidence. A total of 2.7×10^9 such events were recorded during the experiment, 2.5×10^9 of which involved at least 3 HPGe detectors.

Based on measured γ -ray yields, the $\alpha 2p$ evaporation channel leading to ^{62}Zn was estimated to represent $\sim 16\%$ and $\sim 10\%$ of the total fusion cross section in the first and second experiments, respectively. In each case, this channel was cleanly selected by applying the total energy channel selection method to events in which an alpha particle and two protons were detected. As discussed in Section 4.2.5, the detected charged particles were also used to perform event-by-event reconstruction of the reaction kinematics in order to improve the γ -ray energy resolution. The total γ -ray spectra of the selected events from each experiment are shown in Fig. 5.1. In each of these spectra, $\sim 95\%$ of the events are associated with ^{62}Zn . Note, however, the factor of ~ 25 increase in statistics in the second experiment. It should also be noted that, because of the larger volume of the Gammasphere HPGe detectors, the gain in γ -ray photopeak efficiency relative to the 8π experiment increases with γ -ray energy and the improved efficiency for high-energy γ -rays in the second experiment was crucial in identifying the high-energy transitions both at the tops of the terminating bands and at the bottoms of these bands where they decay to spherical states.

[†]The neutrons detectors were used in this experiment to study weak reactions channels involving neutron evaporation, such as the αpn channel leading to the odd-odd $N = Z$ nucleus ^{62}Ga [Sko 98]. Obviously, they were not used in the analysis of the pure charged-particle channel leading to ^{62}Zn .

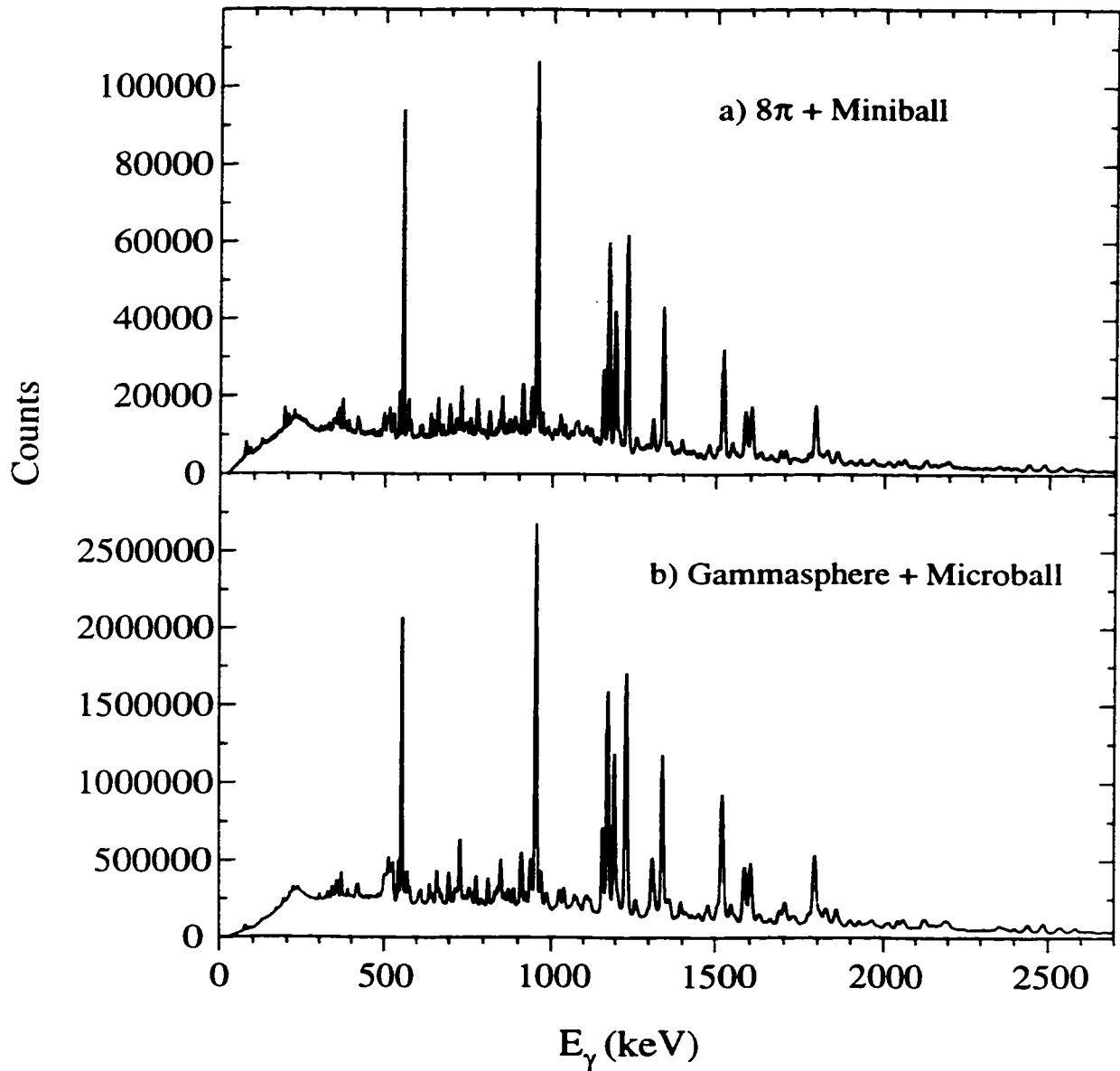


Figure 5.1: The total γ -ray spectra selected for ^{62}Zn from (a) the 8π + Miniball experiment and (b) the Gammasphere + Microball. In each case, ^{62}Zn has been cleanly selected by requiring the detection of an alpha particle and two protons and applying the total energy channel selection technique. In both spectra, $\sim 95\%$ of the events belong to ^{62}Zn . Note, however, the factor of ~ 25 increase in statistics in the latter experiment.

5.3 Results: Rotational Bands in ^{62}Zn

A partial decay scheme for ^{62}Zn from the present work is shown in Fig. 5.2. The spin assignments are based on directional correlations from oriented state (DCO) ratios [War 91] from the 8π data, and angular distribution measurements from the Gammasphere data. The parity assignments are based on these angular distributions, the large number of interconnections between the levels in this decay scheme, and the assumption that all transitions with lifetimes short enough to be observed in these thin-target experiments are of $E1$, $M1$, or $E2$ character (see Appendix A). Many of the low-lying levels up to the yrast 11^- state were previously known [Bru 76, Mul 79, War 81] and, concurrent with this work, a number of the noncollective spherical states up to the yrast 17^- level were also identified by Furutaka *et al.* [Fur 97]. In this discussion, we focus on the properties of the two sets of strongly coupled rotational bands, labeled bands 1 and 2 in Fig. 5.2, that were first identified in the $8\pi + \text{Miniball}$ experiment and extended to higher spin and linked to the remainder of the ^{62}Zn decay scheme in the Gammasphere + Microball experiment.

The γ -ray spectra from the Gammasphere experiment obtained by summing the spectra in coincidence with all clean gates set on the $M1$ and $E2$ transitions in bands 1 and 2 are shown in Figs. 5.3 (a) and (b), respectively. The energies and relative intensities of the γ -rays in these bands, as measured in the Gammasphere experiment, are given in Tables 5.1 and 5.2. The insets in Fig. 5.3 present the high-energy regions of the γ -ray spectra and clearly show both the transitions at the tops of the bands (diamonds) and the decay-out transitions from the bottoms of the bands (squares). These two types of high-energy transitions can be easily distinguished by inspection, the peaks being broader for the decay-out transitions. This difference in the peak widths occurs because these spectra have been Doppler-shift corrected

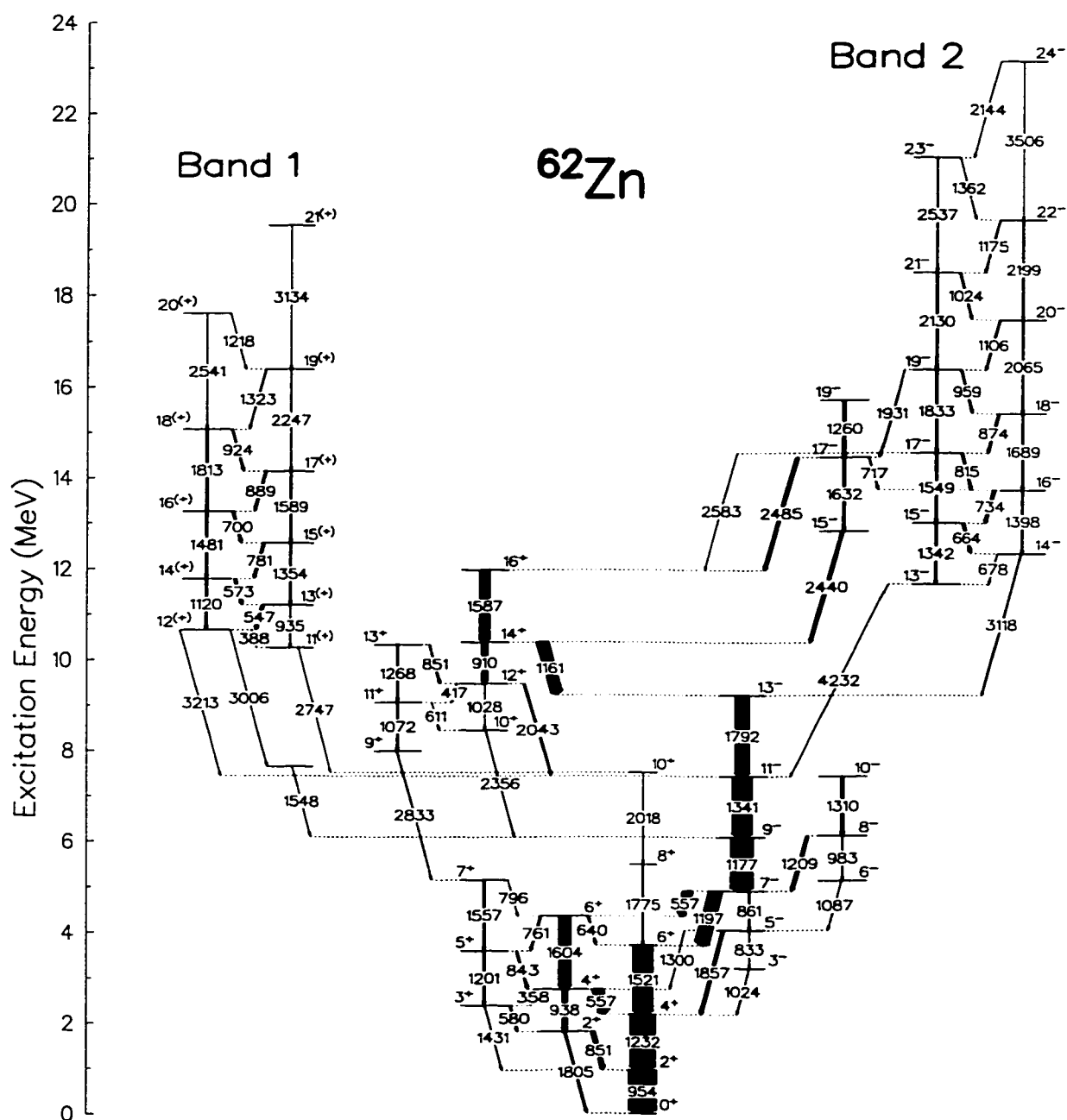


Figure 5.2: Partial level scheme of ^{62}Zn from the present work. The transition energies are given to the nearest keV.

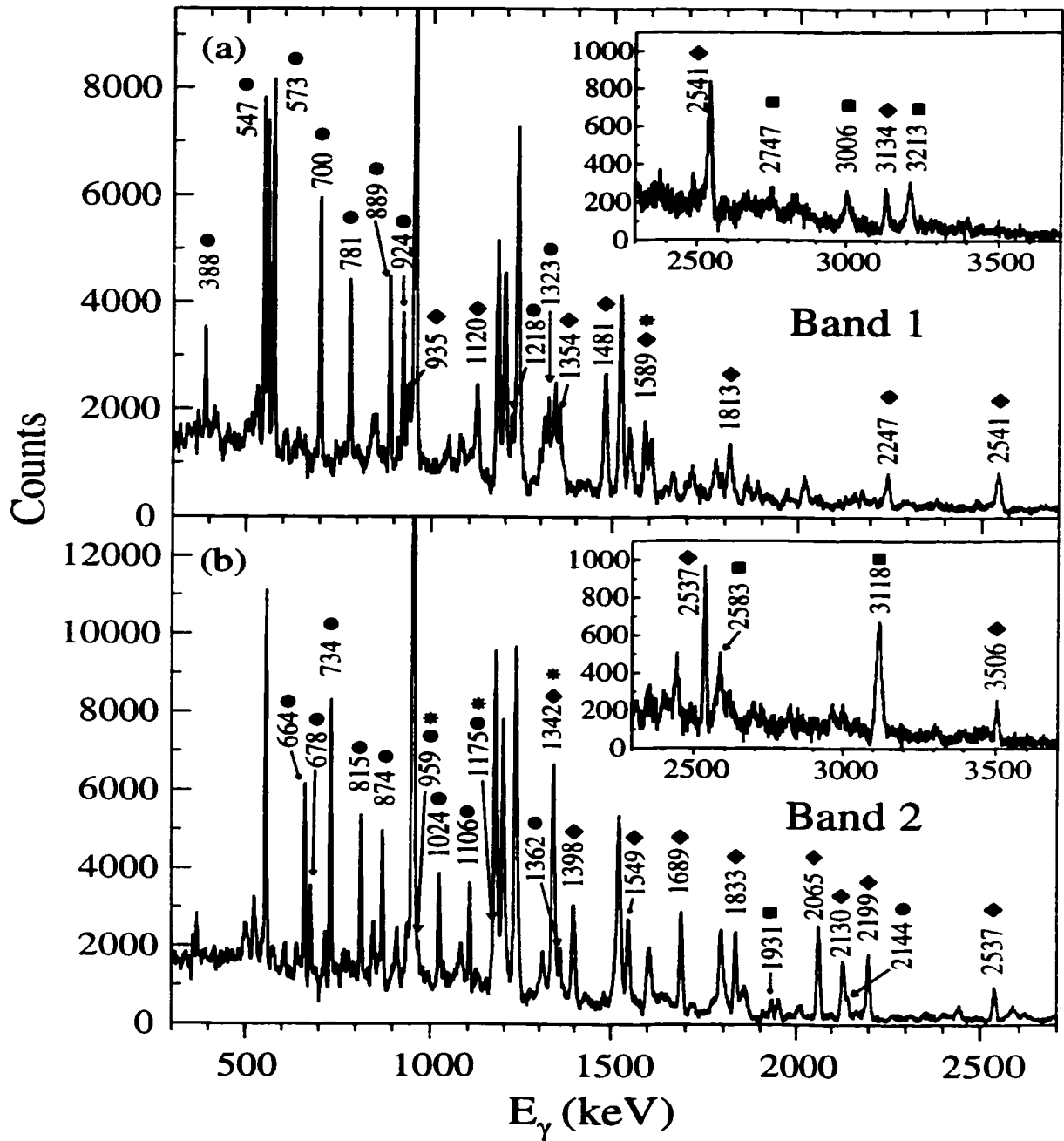


Figure 5.3: γ -ray spectra generated by summing coincidence gates set on the transitions in (a) band 1 and (b) band 2. The energies of the in-band E2 (diamonds) and M1 (circles) transitions and the linking transitions (squares) are given to the nearest keV. Asterisks denote contaminated transitions that were not included in the gates.

I_i^π	I_f^π	E_γ (keV)	Intensity (%)
12(+)	11(+)	388.3 (3)	1.2 (1)
13(+)	11(+)	935.5 (5)	1.2 (1)
13(+)	12(+)	546.9 (3)	5.0 (3)
14(+)	12(+)	1119.8 (4)	3.2 (2)
14(+)	13(+)	573.1 (3)	5.0 (3)
15(+)	13(+)	1353.8 (5)	2.8 (2)
15(+)	14(+)	780.6 (3)	4.1 (3)
16(+)	14(+)	1481.2 (4)	4.8 (3)
16(+)	15(+)	699.6 (3)	4.2 (3)
17(+)	15(+)	1589.0 (6)	2.7 (2)
17(+)	16(+)	888.7 (3)	3.4 (2)
18(+)	16(+)	1813.0 (5)	3.2 (2)
18(+)	17(+)	924.1 (4)	2.4 (2)
19(+)	17(+)	2246.7 (8)	1.6 (2)
19(+)	18(+)	1323.3 (6)	1.5 (2)
20(+)	18(+)	2541.4 (9)	1.8 (2)
20(+)	19(+)	1217.5 (7)	0.6 (1)
21(+)	19(+)	3134.7 (12)	0.6 (1)

Table 5.1: Energies and intensities relative to the ^{62}Zn channel of γ -ray transitions in band 1, as measured in the Gammasphere experiment.

for the velocity of the recoiling nuclei immediately following particle evaporation, which is approximately the velocity when the γ rays from the highest-spin states are emitted. During the time in which the remainder of the transitions in these bands occur, the recoiling nuclei slow down in the target. The Doppler-shift correction in Fig. 5.3 is therefore not optimal for the decay-out transitions, and these peaks are noticeably wider than those of the high-spin transitions. One can, of course, reverse this situation and sharpen the decay-out peaks by applying a Doppler-shift correction appropriate to the recoil velocity after the nuclei have escaped from the thin target. Coincidence matrices with each of these Doppler-shift corrections, as well as several intermediate cases, were constructed during the analysis in order to obtain the best

I_i^π	I_f^π	E_γ (keV)	Intensity (%)
14 ⁻	13 ⁻	677.7 (4)	2.0 (2)
15 ⁻	13 ⁻	1342.0 (10)	4.1 (10)
15 ⁻	14 ⁻	663.6 (3)	4.3 (3)
16 ⁻	14 ⁻	1397.6 (4)	3.8 (3)
16 ⁻	15 ⁻	733.6 (3)	5.0 (4)
17 ⁻	15 ⁻	1549.3 (5)	3.4 (3)
17 ⁻	16 ⁻	815.0 (3)	3.7 (3)
18 ⁻	16 ⁻	1689.2 (5)	4.5 (3)
18 ⁻	17 ⁻	873.7 (3)	3.5 (3)
19 ⁻	17 ⁻	1833.1 (5)	3.7 (3)
19 ⁻	18 ⁻	959.0 (8)	3.0 (8)
20 ⁻	18 ⁻	2065.4 (6)	5.0 (4)
20 ⁻	19 ⁻	1105.9 (4)	2.4 (2)
21 ⁻	19 ⁻	2130.3 (8)	3.5 (4)
21 ⁻	20 ⁻	1024.3 (4)	2.0 (2)
22 ⁻	20 ⁻	2199.5 (7)	4.0 (3)
22 ⁻	21 ⁻	1174.6 (12)	1.6 (8)
23 ⁻	21 ⁻	2537.4 (9)	2.7 (3)
23 ⁻	22 ⁻	1362.3 (7)	1.5 (2)
24 ⁻	22 ⁻	3505.7 (14)	1.0 (2)
24 ⁻	23 ⁻	2143.8 (12)	0.4 (1)

Table 5.2: Energies and intensities relative to the ^{62}Zn channel of γ -ray transitions in band 2, as measured in the Gammasphere experiment.

γ -ray energy resolution at various points during the decay of these bands.

As shown in Fig. 5.2, band 2 in ^{62}Zn is linked to the noncollective spherical states not only by the high-energy transitions that decay out of the bottom of the band, but also by several interconnecting transitions near the middle of the band. These latter transitions occur because an “accidental degeneracy” of the 17⁻ state in the band with another 17⁻ level leads to a substantial mixing of the wavefunctions for these two states. Together with the decay-out transitions at the bottom of the band, the multiple interconnections of band 2 with high-spin spherical states provides definite spin and parity assignments for the levels in this band. For band 1, however,

the decay-out transitions were only sufficient to establish the spins of the levels. The tentative positive parity assignment for this band indicated in Fig. 5.2 and Table 5.2 is based on the assumption that the 3213-keV linking transition, which has an angular distribution consistent with a pure stretched dipole transition, is of $E1$ rather than $M1$ character. This parity assignment is also strongly favoured by the theoretical calculations for ^{62}Zn discussed in the following section.

5.4 Interpretation

In order to assign single-particle configurations to the bands in ^{62}Zn , theoretical calculations were carried out by I. Ragnarsson and A.V. Afanasjev [Rag 97] employing the configuration-dependent shell-correction approach (see Section 2.3.4) with the cranked Nilsson potential (parameters from [Ben 85]). Pairing correlations were not included in these calculations, and the results should therefore be considered realistic only for high-spin states. The calculated energies of favoured configurations in ^{62}Zn are compared with the experimental results in Fig. 5.4. It is interesting to note how a series of single-particle excitations are required to generate increasing amounts of available angular momentum in this nucleus with only two valence protons and four valence neutrons outside doubly-magic ^{56}Ni . As shown in Fig. 5.4, the maximum attainable spin is $I_{\max}^{\pi} = 10^{+}$ with all of the valence particles in the $f_{5/2}$ and $p_{3/2}$ orbitals, 13^{-} with a neutron excited to the $g_{9/2}$ orbital, 16^{+} with also a proton excited to the $g_{9/2}$ orbital, 19^{-} if a second neutron is excited to $g_{9/2}$ or 21^{+} if a proton hole is made in the $f_{7/2}$ orbital below the $Z = 28$ shell gap, and finally, before superdeformed bands become yrast (see Chapter 6), 24^{-} with both the latter excitations. As can be seen in Fig. 5.4, all of the bands corresponding to these favoured single-particle configurations have their counterparts in the experimental spectrum.

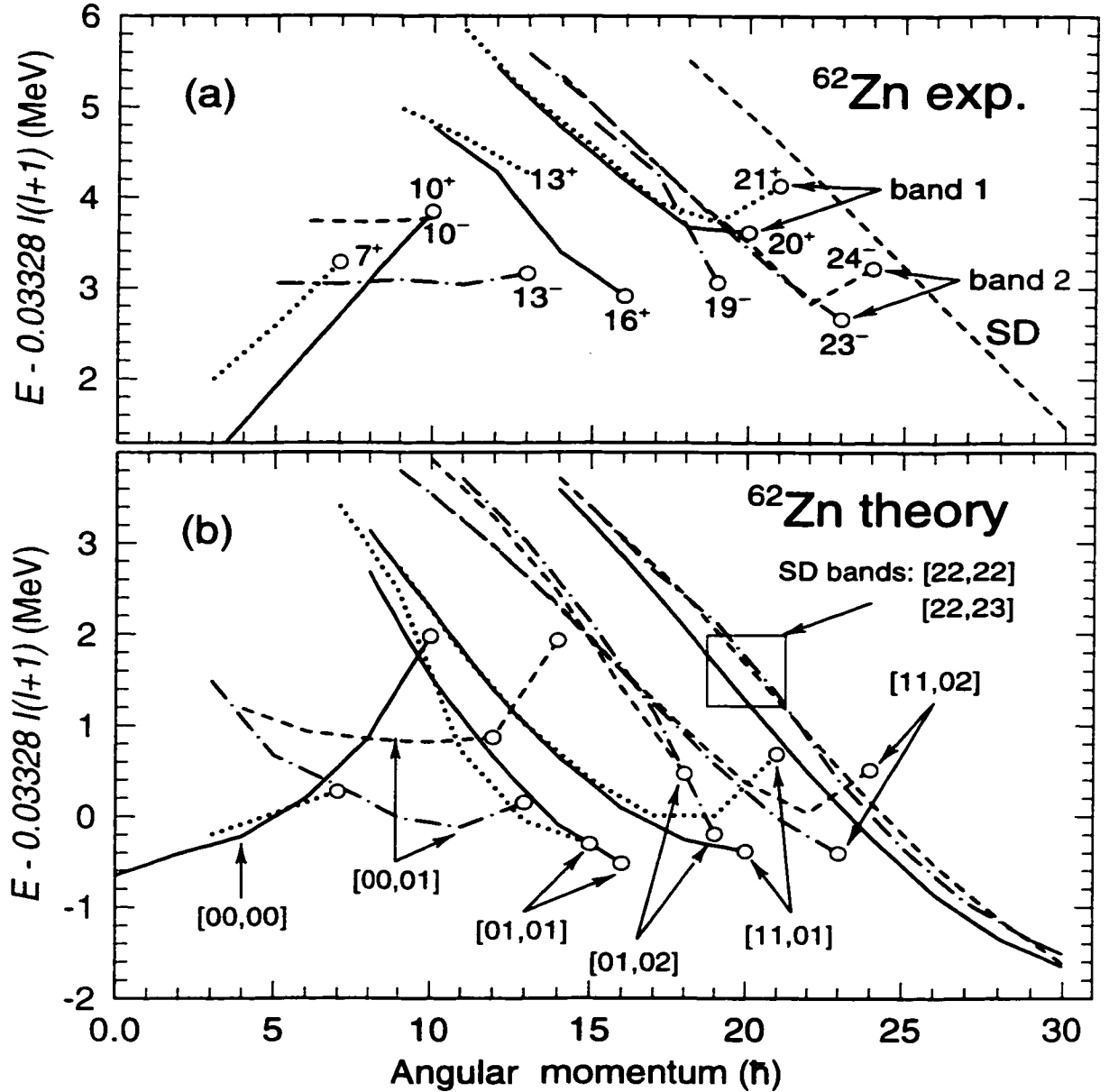


Figure 5.4: Energies of states in ^{62}Zn relative to an $I(I+1)$ reference from (a) experiment and (b) theory [Rag 97]. The parity π and signature α of each configuration is given by the line type: $(\pi, \alpha) = (+, 0)$ solid line, $(+, 1)$ dotted line, $(-, 0)$ dashed line, and $(-, 1)$ dot-dashed line. Terminating states are shown by open circles. The highest spin state observed in each configuration is labeled in (a). In (b) the short-hand configuration notation $[p_1 p_2, n_1 n_2]$ is used where $p_1(n_1)$ is the number of proton (neutron) $f_{7/2}$ holes, $p_2(n_2)$ is the number of proton (neutron) $g_{9/2}$ particles, and the ^{62}Zn ground-state valence configuration is $[00, 00] \equiv \pi[f_{5/2} p_{3/2}]^2 \otimes \nu[f_{5/2} p_{3/2}]^4$.

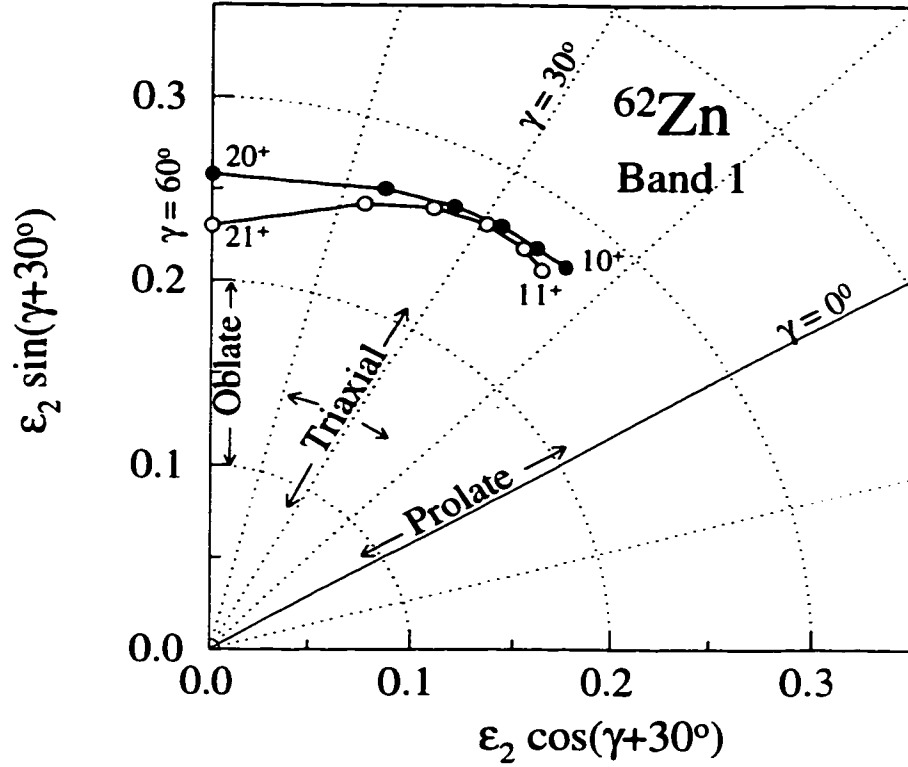


Figure 5.5: Calculated shape trajectory in the (ϵ_2, γ) plane as a function of spin for band 1 in ^{62}Zn . Closed (open) symbols are used for the $\alpha = 0$ ($\alpha = +1$) signature.

Of special interest to the discussion here are the last two configurations mentioned above, which have a single proton hole in the $f_{7/2}$ shell. Both the proton hole in the high- Ω , $f_{7/2}$ extruder orbital and the proton and neutron(s) in the low- Ω , $g_{9/2}$ intruder orbital favour a considerable nuclear deformation (see Figs. 5.5 and 5.6) and these configurations are predicted to lead to collective rotational bands. The proton single-particle Routhians for ^{62}Zn calculated at a deformation ($\epsilon_2 = 0.27, \gamma = 20^\circ$) appropriate for intermediate-spin states in these bands were shown in Fig. 2.7. It can be seen in this figure that the two signatures of the $\Omega = \frac{7}{2}$, $f_{7/2}$ orbital (labeled 3_5 in Fig. 2.7) remain degenerate up to high rotational frequencies. A single proton hole in this orbital is therefore expected to lead to a pair of signature-degenerate bands, as observed for the two sets of strongly coupled bands in ^{62}Zn . It should be

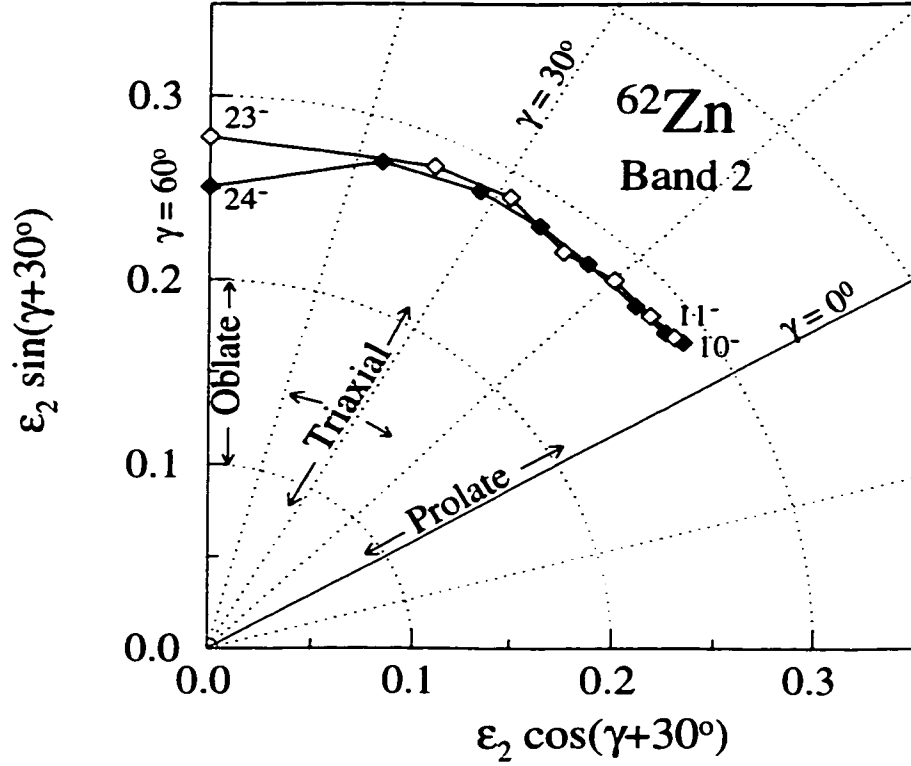


Figure 5.6: Calculated shape trajectory in the (ϵ_2, γ) plane as a function of spin for band 2 in ^{62}Zn . Closed (open) symbols are used for the $\alpha = 0$ ($\alpha = +1$) signature.

noted that even the signature splitting observed at the highest-spin states in bands 1 and 2 (Fig. 5.4 (a)) is accurately reproduced in the calculations (Fig. 5.4 (b)), where it results from the greater energy required to fully align the $\alpha = +\frac{1}{2}$ signature of the $f_{7/2}$ proton hole compared to the $\alpha = -\frac{1}{2}$ signature of this hole at the oblate deformation ($\epsilon_2 \sim 0.25, \gamma = 60^\circ$) appropriate for the terminating states of these bands [Rag 97]. Based on the excellent agreement between these calculations and the experimental results, the high- j valence configurations $\pi[(f_{7/2})^{-1}(g_{9/2})^1] \otimes \nu(g_{9/2})^1$ and $\pi[(f_{7/2})^{-1}(g_{9/2})^1] \otimes \nu(g_{9/2})^2$ (or $[11,01]$ and $[11,02]$ in the shorthand notation of Fig. 5.4) are assigned to bands 1 and 2 in ^{62}Zn . The maximum possible spin in these configurations is 21^+ for band 1 and 24^- for band 2. It is therefore concluded that these bands have been observed up to their terminating states.

As in the case of the terminating bands in $A \sim 110$ nuclei, bands 1 and 2 in ^{62}Zn are examples of smoothly terminating rotational bands which are observed over an extended spin range prior to their termination. As shown in Figs. 5.5 and 5.6, the nucleus is calculated to be triaxial at intermediate spins and to change shape gradually, terminating in a noncollective oblate state in which the angular momenta of all the valence particles and holes are maximally aligned along one axis. It is also interesting to note that, unlike the terminating bands in the $A \sim 110$ mass region where the nucleus is predicted to lose quadrupole deformation as termination is approached [Afa 95], in the ^{62}Zn bands the nucleus is calculated to remain well deformed ($\varepsilon_2 \sim 0.23\text{--}0.29$) over the entire spin range. The predicted loss of collectivity as termination is approached in the ^{62}Zn bands is therefore associated entirely with the γ degree of freedom (see Eq. 2.68), whereas in the $A \sim 110$ bands it results from a combination of increasing γ and decreasing ε_2 .

5.5 Evidence for a Loss of Collectivity

As noted in Section 5.1, the loss of collectivity inherent in the theoretical interpretation of smoothly terminating rotational bands had not been tested prior to this work. The relatively low spins at which the ^{62}Zn bands terminate, however, offered the opportunity to perform the lifetime measurements necessary to test this prediction.

Despite the predicted loss of collectivity in the ^{62}Zn bands, the high γ -ray transition energies lead to state lifetimes that are short compared to the average time taken for the recoils to escape from the thin target. These bands thus decay almost entirely while the recoiling nuclei are slowing down in the target and their transition quadrupole moments can be measured by the thin-target Doppler-shift attenuation method discussed in Section 3.4.1. The measured fractions F of the full Doppler shift

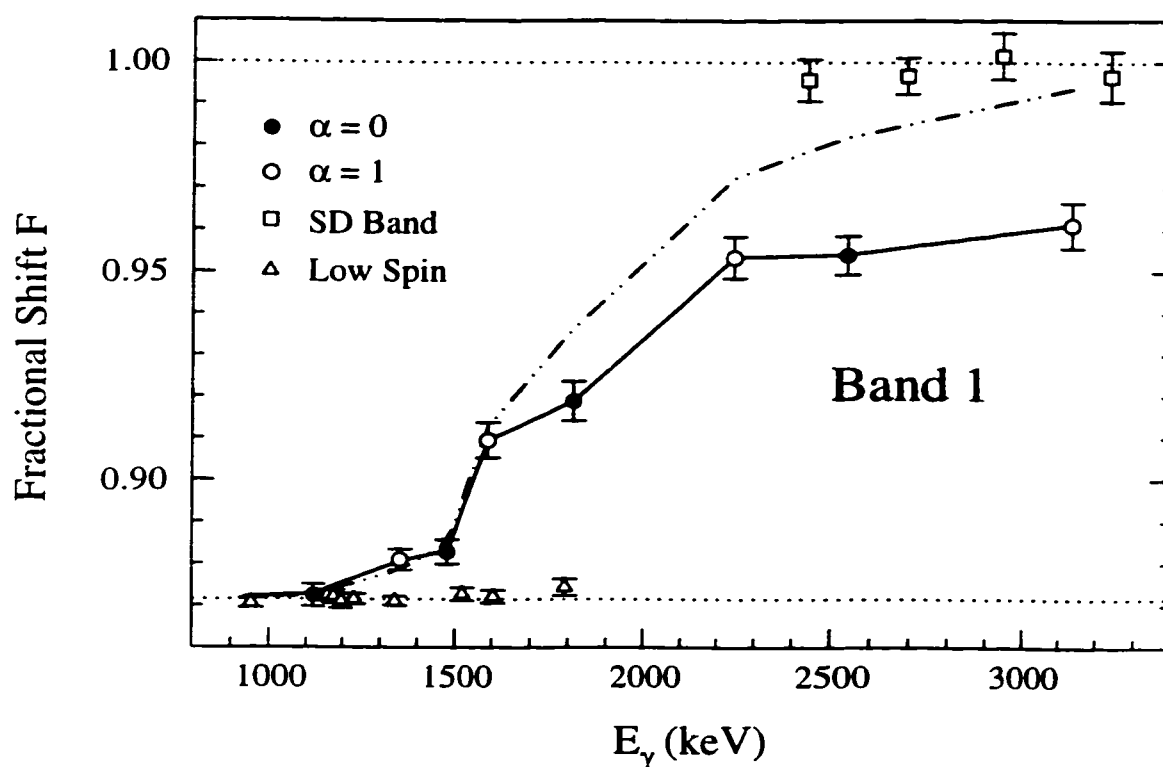


Figure 5.7: Fractional Doppler shifts F for transitions in the $\alpha = 0$ (solid circles) and $\alpha = +1$ (open circles) signatures of band 1. Also shown are the F values for transitions at the top of the ^{62}Zn SD band (squares) and from low-spin spherical states in ^{62}Zn (triangles). The dotted lines at $F = 1.00$ and $F = 0.872$ represent the full shift and the constant shift for decays outside the thin target, respectively. The dot-dashed line is a fit to the low-spin members of band 1 assuming a constant in-band Q_t and the solid line is a “fit” allowing Q_t to vary freely within the band.

for the transitions in bands 1 and 2 are shown in Figs. 5.7 and 5.8, respectively. It should be noted that the mean decay time is a property of the initial state and, in these strongly coupled bands, the F value is the same for the $E2$ and the $M1$ transition from a particular level. Although the F values in Figs. 5.7 and 5.8 are plotted against the energy of the $E2$ in-band transition, they are actually the weighted averages of measurements for the $E2$ and the $M1$ transitions. These figures show that bands 1 and 2 do indeed decay on the same time scale (of order 100 fs) as the time taken by the recoiling nuclei to leave the target, while the low-spin transitions between the

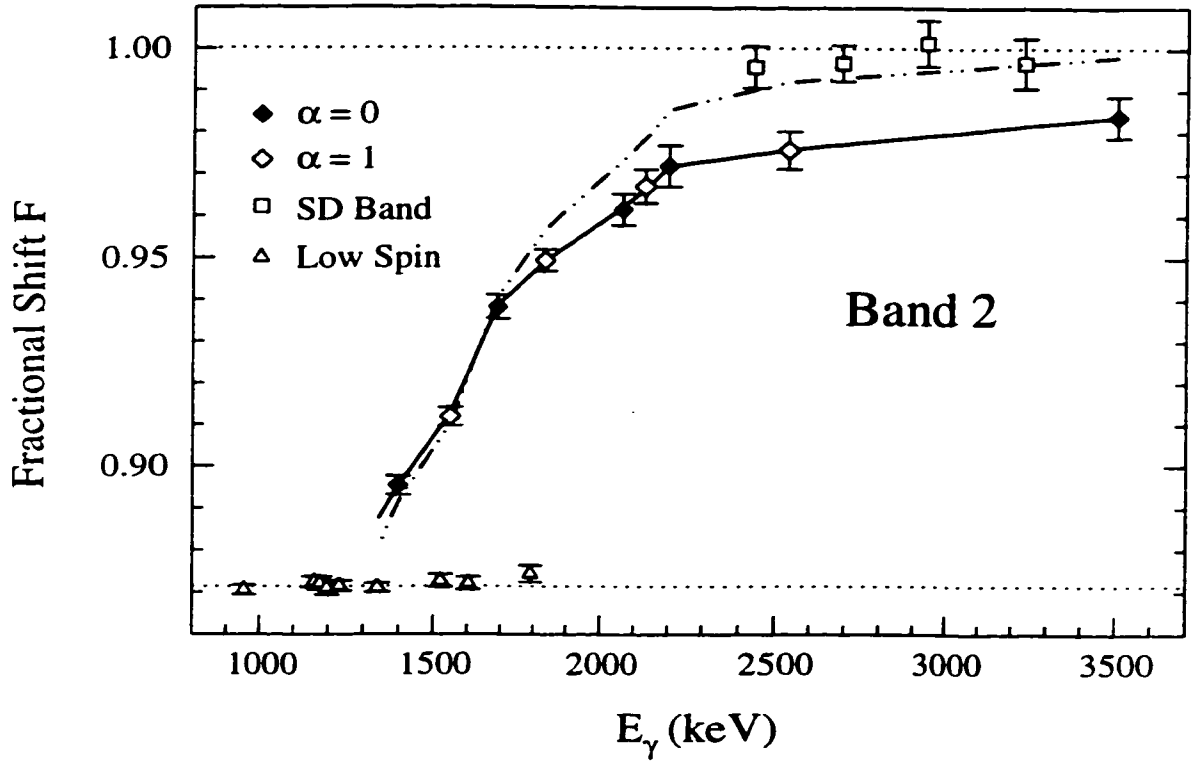


Figure 5.8: The same as Fig. 5.7, but for the $\alpha = 0$ (solid diamonds) and $\alpha = +1$ (open diamonds) signatures of band 2.

spherical states in ^{62}Zn occur after the recoils have escaped from the thin target and have the constant shift $F = 0.872$. It is also important to note that the average unattenuated recoil velocity, which defines $F = 1.00$ and has been calculated from the reaction kinematics, the stopping powers for the beam ions in the target, and the experimental bias in the initial velocity distribution resulting from charged-particle detection (see Section 3.4.1), is confirmed by the F values measured for the very fast transitions at the top of the ^{62}Zn SD band (see Chapter 6).

To extract Q_t values for bands 1 and 2 from the Doppler-shift measurements shown in Figs. 5.7 and 5.8, the slowing down of the recoiling nuclei in the target was modeled with the electronic stopping powers of Northcliffe and Schilling [NS 70] scaled by the Ziegler and Chu [ZC 74] stopping powers for ^4He , as suggested by

Sie *et al.* [Sie 77] and discussed in Section 3.4.2. The γ decays in both signatures of the bands were modeled together using the experimental transition energies and $E2/M1$ branching ratios given in Tables 5.1 and 5.2. The unobserved side feeding into each state was modeled by a single $E2$ transition with $Q_t = 1.0$ eb, an energy 0.5 MeV greater than the subsequent in-band transition, and an intensity to match the measured intensity profile of the band. This side-feeding model was chosen to produce plausible mean time delays associated with the feeding of these bands. Clearly, there is an uncertainty involved in this model and the consequences of this assumed side-feeding structure on the extracted Q_t values for these bands will be discussed below.

As discussed in Section 3.4.1, the transition quadrupole moment in a high-spin rotational band is usually assumed to be constant and the value of Q_t is extracted from a fit to the measured fractional Doppler shifts. Best fits to the low-spin members of bands 1 and 2 under the assumption of constant in-band Q_t values are shown by the dot-dashed lines in Fig. 5.7 ($Q_t = 0.80$ eb) and Fig. 5.8 ($Q_t = 1.12$ eb). These constant- Q_t fits clearly do not reproduce the high-spin F values in these bands: they predict significantly larger F values, i.e. shorter lifetimes, than are measured at the tops of the bands. Alternatively, one can attempt to fit the high-spin transitions with constant Q_t values. However, such fits predict substantially longer lifetimes, i.e. smaller F values, than are measured at the bottoms of the bands. Within the decay model discussed above, no reasonable fit to all of the measured F values for either band can be obtained with a constant Q_t value.

To fit all of the measured Doppler shifts, the Q_t value was allowed to vary freely for each transition. This model contains one free parameter per data point, and the “fitting” procedure reduces to an extraction of the Q_t value for each transition that exactly reproduces the measured F value (solid lines in Figs. 5.7 and 5.8). The Q_t

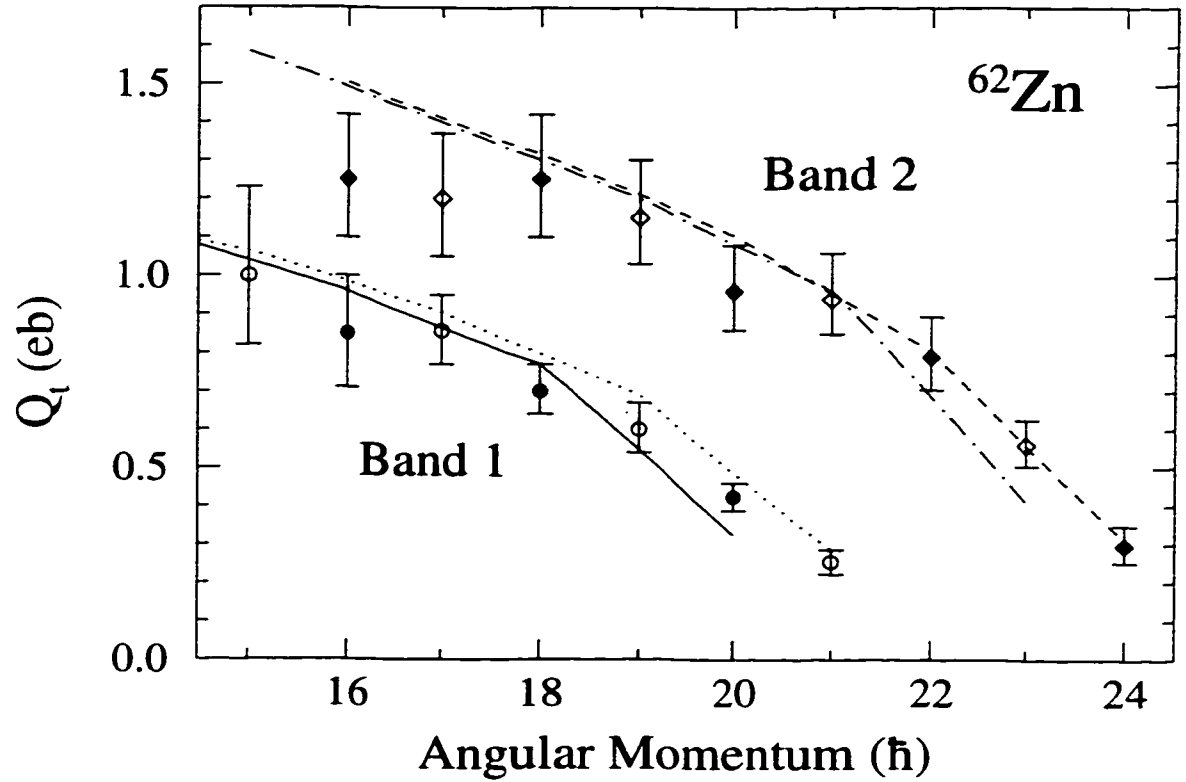


Figure 5.9: The Q_t values for bands 1 and 2 in ^{62}Zn as a function of the spin of the initial state. The data points represent the values extracted from the fits to the fractional Doppler-shift measurements shown in Figs. 5.7 and 5.8 and the lines represent the calculated Q_t values for these bands. Circles (diamonds) are used for band 1 (band 2) and closed (open) symbols denote signature $\alpha = 0$ ($\alpha = +1$). The different line types for the calculated Q_t values represent different combinations of parity and signature, as defined in Fig. 5.4.

values derived from this analysis are shown for both bands in Fig. 5.9. These Q_t values decrease as the terminating states are approached and reach values corresponding to noncollective transition strengths of approximately one Weisskopf unit ($Q_t \approx 0.2 \text{ eb}$) at the highest angular momenta. The lines in Fig. 5.9 are the theoretical Q_t values for these bands. The calculated Q_t for the $I \rightarrow I - 2$ transition has been taken as the average of the Q_t values for the I and $I - 2$ states obtained from Eq. 2.68 and the calculated equilibrium deformations for these states. Although these calculations do not account for the imperfect overlap of the shape wavefunctions for the initial and

final states, and should thus be treated with caution close to termination where the shape change per transition is large [Afa 95], the general decreases in Q_t which they predict are in excellent agreement with the experimental results.

It should be noted that the uncertainties in the Q_t values shown in Fig. 5.9 represent only the statistical uncertainties in the Doppler-shift measurements. These Q_t uncertainties increase with decreasing spin because of the covariance between the in-band Q_t values. For the highest-spin transition, the indicated Q_t uncertainty arises from the uncertainty in the F value for only this transition. For lower-spin transitions, the Q_t uncertainties include contributions from both the uncertainty in the F value for the transition of interest and those for higher-lying transitions. This “top-down” compounding of the uncertainties in the F measurements leads to increasing Q_t uncertainties with decreasing spin. The 10-15% uncertainties in the stopping powers are not included in Fig. 5.9. To first order, however, variations in the stopping powers shift all of the experimental Q_t values together and do not alter the conclusion that these Q_t values decrease with increasing spin. Similarly, there are uncertainties at the 10% level in the theoretical Q_t values. For example, the calculated Q_t values depend on the square of the nuclear radius parameter r_0 , and variations of this parameter by $\pm 5\%$ from the value of 1.2 fm used in the calculations are certainly permissible. Such variations, however, also shift all of the Q_t values in the same direction and do not affect the calculated spin-dependence of these values. Given these experimental and theoretical uncertainties, it should be stressed that the important result shown in Fig. 5.9 is the decrease in the Q_t values as termination is approached, rather than the quantitative agreement between experiment and theory[†].

[†]It is worth noting that the model of the decay of these bands and the parameters of the theoretical calculations were chosen independently, and the quantitative agreement between theory and experiment shown in Fig. 5.9 was obtained without any *a posteriori* adjustment of parameters.

The one aspect of the decay model that does affect the spin-dependence of the deduced Q_t values is the assumed structure of the unobserved side feeding. To investigate the sensitivity of the extracted in-band Q_t values to the assumed side-feeding model, all of the side-feeding parameters, i.e. the side-feeding Q_t , the number of transitions in the side-feeding cascades, and the energies of these transitions, were varied. To a good approximation, only the mean time delay resulting from the combination of these three parameters is significant. Increasing the mean side-feeding times, for example, increases the Q_t values deduced for the high-spin states where the feeding occurs, but does not affect the Q_t values extracted for the lower-spin transitions. A factor of two increase in the feeding times, however, does not alter any of the high-spin Q_t values by an amount larger than the statistical uncertainties shown in Fig. 5.9.

An alternative approach to the side-feeding problem is to assume that the Q_t values in these bands are actually constant. The measured Doppler shifts are then fit by allowing the side-feeding Q_t to vary independently for each state. The result of this model is that the side-feeding times must *increase* with increasing spin. The competition between statistical $E1$ and collective $E2$ transitions in the γ decay following a fusion-evaporation reaction (see Fig. 1.5 and [Døs 95a]), however, leads to the general expectation that feeding times become systematically shorter with increasing spin, and it is unlikely that this situation would ever be reversed. It could be argued that the observed bands in ^{62}Zn are fed by higher-lying terminating bands and that the high-spin states are therefore fed more slowly. However, this argument amounts to using the predictions of the theoretical model of terminating bands to obtain the constant in-band Q_t values necessary to discredit this very model. Although some contribution from this effect to the low Q_t values deduced for the highest-spin states cannot be ruled out, a consistent interpretation of the Doppler

shift measurements for the bands in ^{62}Zn requires in-band Q_t values that decrease with increasing spin. This result represents the first experimental confirmation of the loss of collectivity associated with the smooth termination of rotational bands.

An additional result obtained from the lifetime measurements discussed above is related to the magnetic properties of the smoothly terminating bands in ^{62}Zn . The $B(M1)/B(E2)$ ratios in these bands, derived from the γ -ray transition energies and relative intensities[†] given in Tables 5.1 and 5.2, lie in the range of $\approx 10\text{--}15 (\mu_N/\text{eb})^2$ and, within the experimental uncertainties, are constant with spin. This constancy of the $B(M1)/B(E2)$ ratios implies that the $B(M1)$ values in these bands, shown in Fig. 5.10, decrease with spin in the same manner as the $B(E2)$ values.

The spin-dependence of the $B(M1)$ values in the ^{62}Zn bands shown in Fig. 5.10 is remarkably similar to that which has recently been measured for the magnetic-dipole bands in ^{198}Pb and ^{199}Pb [Cla 97]. In these “shears” bands, the Pb nucleus is thought to be weakly oblate ($\beta_2 \sim -0.1$) and the total spin arises largely from coupling the angular momenta of a small number of high- Ω , $h_{9/2}$ and $i_{13/2}$ protons and low- Ω , $i_{13/2}$ neutron holes. Near the bandhead, the angular momentum vector \vec{j}_π of the high- Ω protons is approximately parallel to the nuclear symmetry axis, while the angular momentum vector \vec{j}_ν of the low- Ω neutron holes is approximately perpendicular to it. The total spin vector $\vec{I} \approx \vec{j}_\pi + \vec{j}_\nu$ therefore lies along a tilted axis relative to the symmetry axis and the large component μ_\perp of the magnetic dipole moment perpendicular to \vec{I} gives rise to large $B(M1)$ values [DF 82]. Higher-spin

[†]In this analysis, the $\Delta I = 1$ transitions are assumed to be of pure $M1$ character. The energies of these cross-over transitions are approximately one half those of the in-band $E2$ transitions. Simply from the E_γ^5 factor in the $E2$ transition probability, one expects the $\Delta I = 1$ $E2$ branch to be $\sim \frac{1}{32}$ of the $\Delta I = 2$ branch. Since the $\Delta I = 1$ and $\Delta I = 2$ branches are of roughly equal intensity, this implies a few percent $E2$ contribution to the $\Delta I = 1$ branch. The small uncertainty in the deduced $B(M1)$ values resulting from the assumption of pure $M1$ transitions is thus not significant compared to the uncertainties in the experimental Q_t values (Fig. 5.9) used to calculate the $B(E2)$ values.

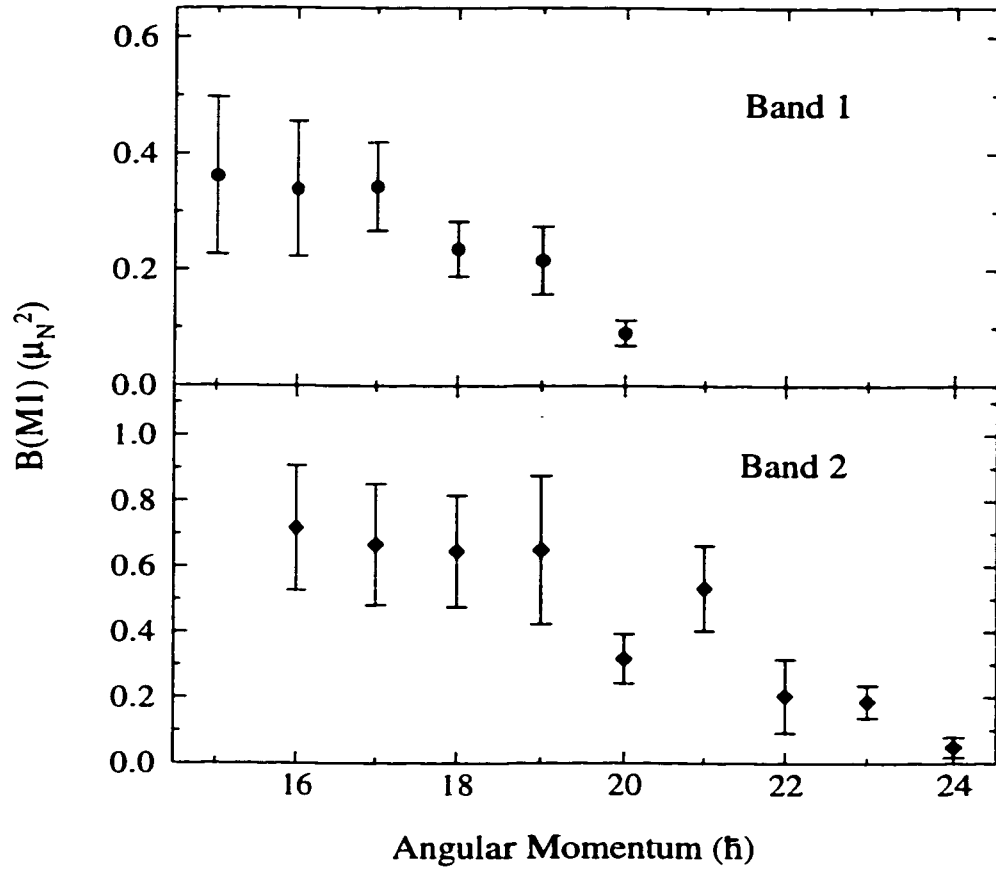


Figure 5.10: The $B(M1)$ values for bands 1 and 2 in ^{62}Zn as a function of the spin of the initial state. The $B(M1)$ values have been calculated from the Q_t values shown in Fig. 5.9 and the $B(M1)/B(E2)$ ratios derived from the γ -ray energies and intensities given in Tables 5.1 and 5.2.

states are generated by aligning \vec{j}_π and \vec{j}_ν along the tilted axis defined by \vec{I} , in a manner reminiscent of the closing of a pair of shears. This alignment decreases μ_\perp and both a semiclassical description of this mechanism [Mac 98] and full calculations within the tilted-axis cranking (TAC) model [Fra 93] reproduce the experimentally observed [Cla 97] decreases in the $B(M1)$ values with increasing spin.

It is interesting to note that, interchanging particles and holes, there are similarities between the single-particle configurations of the ^{62}Zn terminating bands and those of the shears bands in $^{198,199}\text{Pb}$. At relatively low spin in the ^{62}Zn bands, the

angular momentum of the low- Ω , $g_{9/2}$ neutron(s) should be roughly parallel to the rotation axis, while that of the high- Ω , $f_{7/2}$ proton hole should be roughly perpendicular to this axis. The angular momentum of the low- Ω , $g_{9/2}$ proton must also be considered, so the total proton and neutron angular momentum vectors will not be perpendicular near the bandhead. Nevertheless, there should be a substantial μ_{\perp} , and hence large $B(M1)$ values, at low spin. In the terminating state, all of the angular momenta of the particles and holes are maximally aligned with the total spin vector and μ_{\perp} should be small. Qualitatively, one then expects the $B(M1)$ values to decrease with spin, in accordance with the results shown in Fig. 5.10.

A quantitative description of the magnetic properties of the ^{62}Zn bands is more difficult. If the strong-coupling limit (see Section 2.1.3) is assumed and K is treated as a good quantum number, the $B(M1)$ values can be calculated in the model of Dönau and Frauendorf [DF 82]. However, the assumption of constant K is clearly not valid in these terminating bands where all of the single-particle angular momenta are gradually aligned with the “rotation” axis. The $B(M1)$ values could, in principle, be calculated within the TAC model. Unlike the shears bands, however, the bands in ^{62}Zn have large, triaxial, and spin-dependent deformations and a substantial fraction of the total angular momentum, at least at low spin, is associated with collective rotation. These effects would have to be included in the TAC calculations and, to the author’s knowledge, no such calculations have yet been performed. A quantitative analysis of the magnetic properties of these bands is therefore considered beyond the scope of this thesis. The similar spin-dependences of the $B(M1)$ ’s measured for the $^{198,199}\text{Pb}$ shears bands and those for the bands in ^{62}Zn shown in Fig. 5.10 are, however, intriguing and a detailed investigation of the role of the shears mechanism in the $A \sim 60$ mass region is certainly an interesting topic for future research.

5.6 Summary

Two sets of signature-partner rotational bands with strong $M1$ crossover, as well as in-band $E2$, transitions have been identified in ^{62}Zn . Configuration-dependent cranked Nilsson-Strutinsky calculations have been performed for high-spin states in ^{62}Zn and the excellent agreement between these calculations and the experimental results has led to configuration assignments involving a proton particle-hole excitation across the $Z = 28$ shell gap from the $f_{7/2}$ to the $g_{9/2}$ orbital and the excitation of 1 (2) valence neutrons to the $g_{9/2}$ orbital for band 1 (2). With these assignments, it is concluded that the bands in ^{62}Zn have been observed up to the terminating states of their respective configurations. This represents the first observation of the terminating states of rotational bands in the $A \sim 60$ mass region.

Smoothly terminating rotational bands offer a unique opportunity to study the interplay between collective and single-particle degrees of freedom within a fixed nuclear configuration. In the ^{62}Zn bands, the nucleus is calculated to remain well deformed ($\epsilon_2 \sim 0.23\text{--}0.29$) over the entire spin range and to change shape gradually from triaxial at intermediate spins to an oblate terminating state in which all of the angular momenta of the valence particles and holes are maximally aligned along one axis. Thin-target Doppler-shift attenuation lifetime measurements for these bands have revealed transition quadrupole moments that decrease with increasing spin and reach noncollective values corresponding to transition strengths of approximately one Weisskopf unit at the terminating states. These measurements, together with recent lifetime measurements approaching the terminating states of bands in ^{108}Sn and ^{109}Sb [Wad 98], provide the first experimental confirmation of the loss of collectivity inherent in the theoretical description of smoothly terminating rotational bands.

Chapter 6

Superdeformation in ^{62}Zn

The observation of a superdeformed rotational band in ^{62}Zn [Sve 97c] is discussed in this chapter. This band consists of a cascade of six γ rays with a dynamic moment of inertia consistent with the expectation for a superdeformed shape. The large deformation and high collectivity of this band are confirmed by thin-target Doppler-shift attenuation lifetime measurements which yield a transition quadrupole moment $Q_t = 2.7_{-0.5}^{+0.7}$ eb, corresponding to a deformation $\beta_2 = 0.45_{-0.07}^{+0.10}$. The properties of this band are in excellent agreement with theoretical calculations which predict that superdeformed bands with deformations $\beta_2 = 0.41\text{--}0.53$ become yrast in ^{62}Zn for spins $I \gtrsim 24\hbar$. These results represent the first observation of superdeformation in the $A \sim 60$ mass region and establish a new region of superdeformation for nuclei with proton and neutron numbers $N, Z \approx 30$.

6.1 Motivation

As discussed in Section 1.3, the large moment of inertia associated with a highly-deformed nuclear shape can lead to a situation where, at high angular momentum, the decrease in rotational energy associated with deformation outweighs the corresponding increase in surface energy, and a highly-deformed shape becomes the lowest energy

state of the nucleus. For nuclei with certain particle numbers, superdeformation is also favoured by the large gaps that occur in the single-particle energy levels when the ratio of the nuclear axes is approximately 2 : 1. The combination of these macroscopic and microscopic effects stabilizes superdeformed nuclear shapes at high angular momentum, and many high-spin superdeformed rotational bands have been identified in $A \sim 190, 150, 130$, and 80 nuclei [Sin 96] with proton and neutron numbers in the vicinity of the SD shell gaps shown in Fig. 2.5.

Figure 2.5 also indicates that there is a large SD shell gap for particle number 30, and superdeformed bands in proton-rich $A \sim 60$ nuclei with $N \approx Z \approx 30$ were predicted almost a decade ago [Rag 90, She 91]. The study of superdeformed rotational bands in such light nuclei is of particular interest for a number of reasons. These nuclei are presently just at the limits of modern large-scale shell model calculations [Dea 97]. The observation of superdeformed bands in this mass region should, in the near future, provide an unprecedented opportunity to compare the most collective rotational states with both the mean-field cranking models of the nuclear intrinsic state and the microscopic laboratory-frame description of nuclear structure obtained from shell model calculations. Although mixing of high- j and low- j orbitals at large deformation and high rotational frequency [TA 81] prevents highly-deformed rotational bands from terminating in the sense of the normal deformed bands discussed in the previous chapter, the limited spin content of the single-particle configurations in the $A \sim 60$ mass region offers a unique possibility of investigating the loss of collectivity in the high-spin states of superdeformed bands. The valence protons and neutrons in these $N \approx Z$ nuclei occupy the same orbitals and neutron-proton, as well as the usual like-nucleon, pairing is expected to be important. As discussed in Section 2.4, isospin $T = 1$ pairs coupled to spin 0 are broken by the Coriolis force and have their

angular momenta aligned with the rotation axis at high rotational frequency. Isospin $T = 0$ neutron-proton pairs, however, can form with a neutron and proton in the same magnetic substate of the same orbital, i.e. with their angular momenta in the same, rather than opposite, directions. Such pairs are favoured, rather than broken, by the Coriolis interaction and the study of high-spin superdeformed bands in $N \approx Z$ nuclei may provide important information regarding the predicted onset of $T = 0$ neutron-proton pairing at high rotational frequency [Mül 82].

Despite the longstanding prediction of superdeformation in the proton-rich $A \sim 60$ mass region, and the motivation for studying highly collective rotational bands in light $N \approx Z$ nuclei discussed above, no such bands had been identified prior to this work. This was primarily due to the experimental difficulties associated with high-spin studies of these nuclei (see Section 1.4). The recent coupling of large γ -ray spectrometers and 4π charged-particle detector arrays, and the development of the experimental techniques discussed in Chapters 3 and 4, have largely overcome these difficulties. As discussed in the following sections, the first superdeformed band in the $A \sim 60$ mass region was identified in ^{62}Zn [Sve 97c] during this work.

6.2 Results: A Superdeformed Band in ^{62}Zn

The doubly-magic superdeformed configuration in the $A \sim 60$ mass region, corresponding to filling the single-particle energy levels up to the SD shell gaps at $N, Z = 30$, should be observed in the $N = Z$ nucleus ^{60}Zn . Although this doubly-magic SD band was, in fact, identified in this work (see Chapter 7), the study of $N = Z$ nuclei in this mass region is hindered by the small cross sections for populating these nuclei in fusion-evaporation reactions with stable beams and targets. The $N = Z + 2$ nucleus ^{62}Zn , however, can be populated at high-spin and with substan-

tial cross section in the reaction $^{40}\text{Ca}(^{28}\text{Si},\alpha 2p)^{62}\text{Zn}$ and, as a pure charged-particle evaporation channel, can be efficiently selected by the methods described in Chapter 4. This nucleus was therefore considered the best candidate for an initial search for superdeformation in the $A \sim 60$ mass region.

The search for superdeformation in ^{62}Zn formed a large part of the motivation for the 125-MeV ^{28}Si on ^{40}Ca Gammasphere + Microball experiment performed during this work. The details of this experiment have already been described in Section 5.2. The $\alpha 2p$ evaporation channel leading to ^{62}Zn represented $\sim 10\%$ of the total fusion cross section in this reaction and this channel was cleanly selected by applying the total energy method to events in which an alpha particle and two protons were detected in the Microball. The detected charged particles were also used to reconstruct the kinematics of each event to correct for the charged-particle induced Doppler broadening. As the lifetimes of high-spin SD states in the $A \sim 60$ mass region are expected to be very short (see below), the γ -ray coincidence data for the selected events were Doppler-shift corrected for the recoil velocity of the nucleus immediately following particle evaporation, thereby obtaining the best possible energy resolution for fast γ -ray transitions. These data were unfolded into a symmetrized matrix that contained 5.0×10^8 γ - γ coincidences, 95% of which were associated with ^{62}Zn (see Fig. 5.1), and this matrix was searched (see Section 3.3.1) for approximately regular rotational sequences characterized by moments of inertia in the range expected for $A \sim 60$ superdeformed bands. This search led to the identification of one candidate for a superdeformed band in ^{62}Zn consisting of a cascade of six mutually-coincident high-energy γ rays. As will be demonstrated below, these transitions are fed only by the highest excitation energy components of the ^{62}Zn entry distribution and do indeed represent the decay of high-spin superdeformed band.

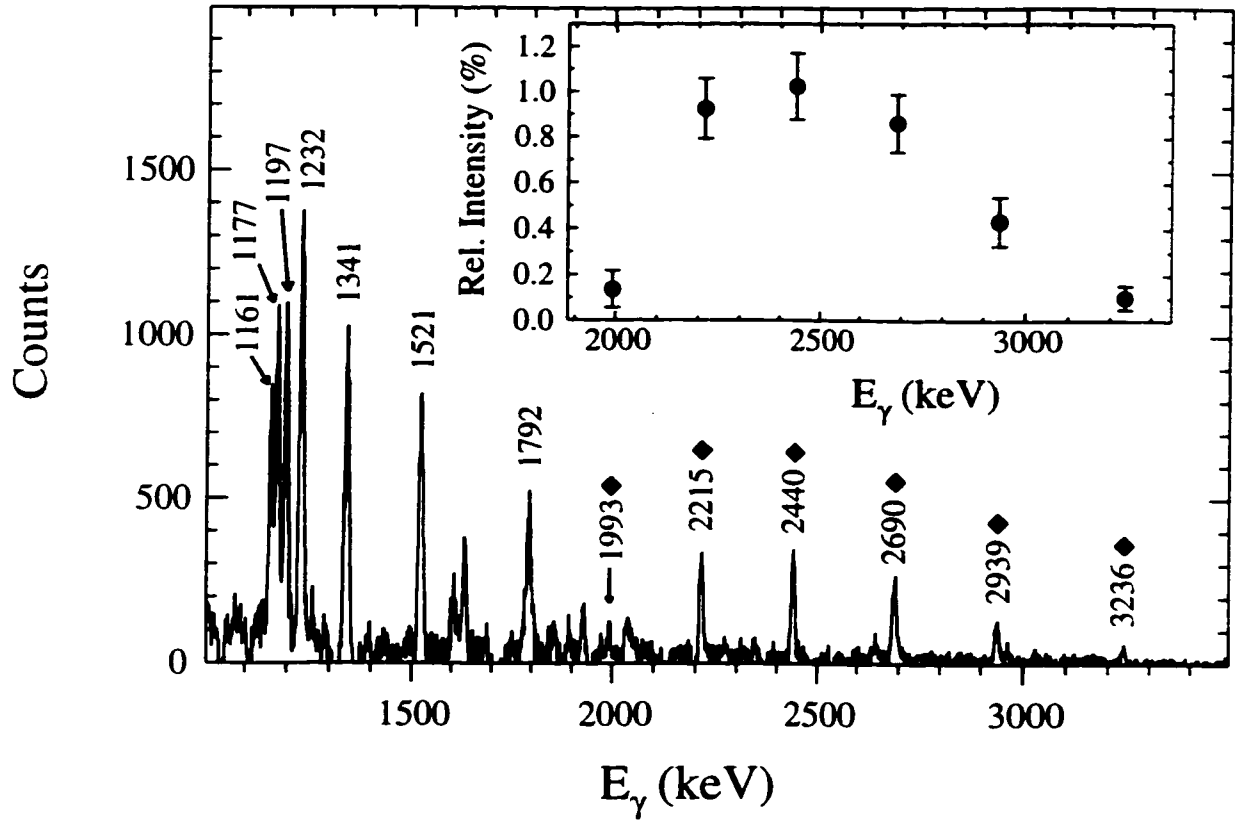


Figure 6.1: Gamma-ray spectrum generated by summing coincidence gates set on the transitions in the ^{62}Zn SD band (diamonds). The energies of the band members and of a number of other transitions in ^{62}Zn (see Fig. 5.2) are given to the nearest keV. The inset shows the intensity of the band relative to that of the ^{62}Zn channel.

The γ -ray spectrum obtained by summing coincidence gates set on the members of the ^{62}Zn superdeformed band is shown in Fig. 6.1, and the γ -ray transition energies and intensities relative to the ^{62}Zn channel are given in Table 6.1. The intensity profile of the SD band, which peaks at $\sim 1\%$ of the ^{62}Zn channel intensity (i.e. $\sim 0.1\%$ of the total fusion cross section), is also shown in the inset of Fig. 6.1. Despite the small cross section for populating this band, the combination of the clean selection of the ^{62}Zn channel and the fact that the γ rays in this band are at higher energy than most of the strong transitions between low-lying levels in ^{62}Zn provided a sufficiently high peak-to-background ratio that the mutual coincidence of the mem-

E_γ (keV)	Intensity (%)
1992.7 (12)	0.14 (7)
2215.3 (8)	0.93 (13)
2439.5 (9)	1.02 (15)
2689.7 (10)	0.86 (13)
2939.1 (12)	0.43 (11)
3235.6 (14)	0.10 (5)

Table 6.1: Energies and intensities relative to the ^{62}Zn channel of γ -ray transitions in the ^{62}Zn superdeformed band.

bers of this band could be established from the γ -ray spectra in coincidence with single gates set at the location of each transition. Only in the case of the weak 1993-keV transition at the bottom of the band, where the background from other transitions in ^{62}Zn is higher, was it necessary to sum gates on the higher band members to generate a statistically significant peak in the γ -ray spectrum. The coincidences of the band members were also confirmed by setting double gates on the γ rays in the SD band in a γ - γ - γ coincidence cube. However, because of the limited statistics for this band, and the absence of a significant gain in combinatorics with increasing fold for such short rotational structures, the statistical quality of the gated γ -ray spectra obtained by summing single gates in the coincidence matrix, as in Fig. 6.1, was actually superior to that obtained by summing double gates in the coincidence cube.

The high-spin nature of the ^{62}Zn SD band is confirmed by its coincidences with transitions between high-spin states in the ND level scheme, a number of which are labeled in Fig. 6.1. A conclusive linking of the SD band into the remainder of the decay scheme was, however, not possible. Therefore the parity and exact spins and energies of the SD states are not known. As shown in Fig. 6.2(a), an additional high-energy γ ray at 3986 keV, which is interpreted as a decay-out transition, was observed in coincidence with the band. This γ ray carries only $\sim 8\%$ of the intensity

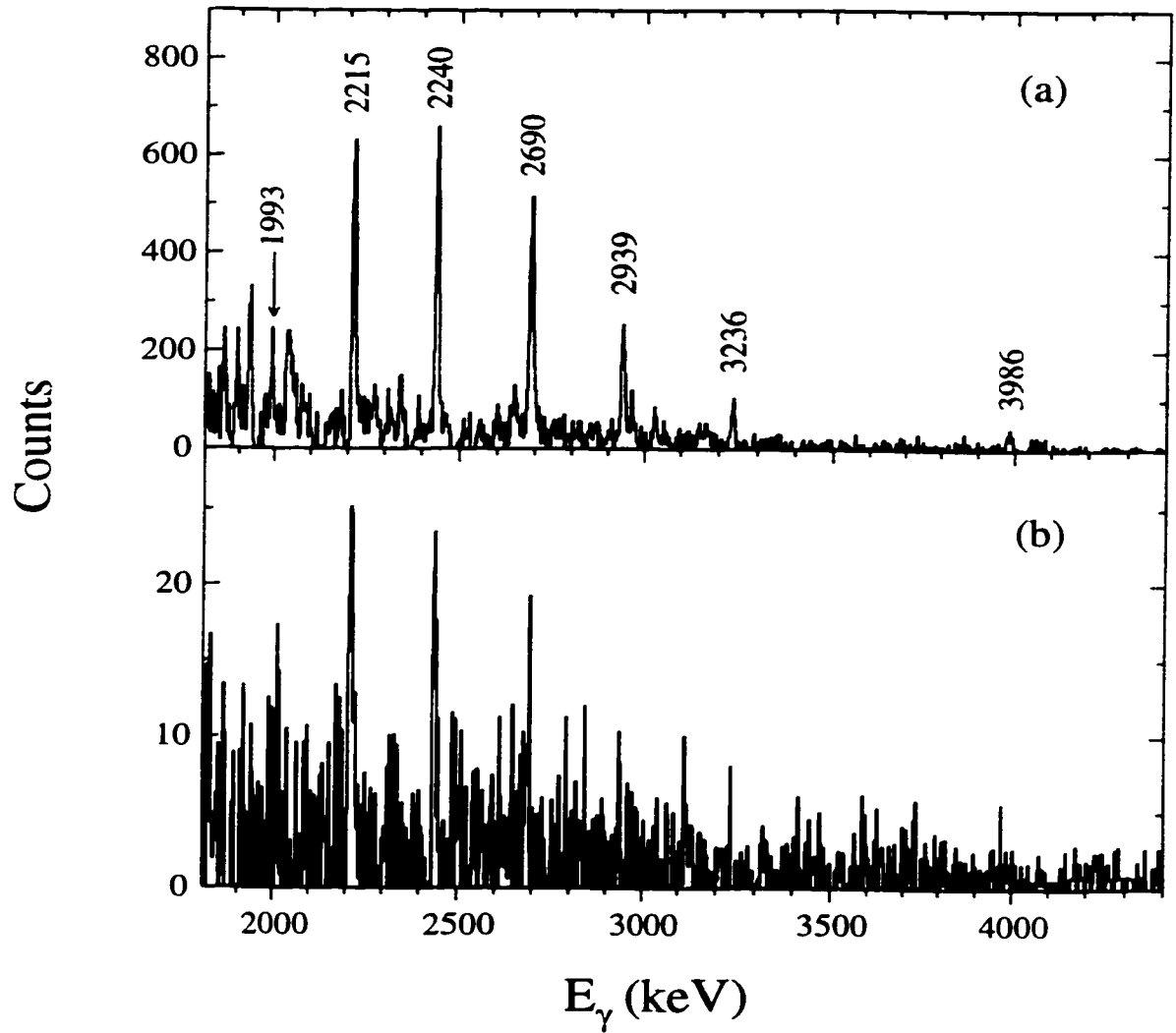


Figure 6.2: Gamma-ray spectra (a) in coincidence with a sum of gates on the members of the ^{62}Zn SD band, and (b) in coincidence with a gate set on the 3986-keV transition. The dispersion of these spectra is one half that of the spectrum shown in Fig. 6.1.

of the SD band, i.e. $\sim 0.008\%$ of the total fusion cross section. Nevertheless, the γ -ray spectrum in coincidence with a single gate set at 3986 keV in the ^{62}Zn matrix is sufficiently free of contamination to reveal the three strongest transitions in the SD band, as shown in Fig. 6.2(b). Based on the coincidences indicated in this spectrum, the 3986-keV transition is interpreted as a primary decay-out transition from the SD state fed by the 2215-keV in-band transition. The statistical quality of the spectrum

shown in Fig. 6.2(b), however, was not sufficient to determine conclusively the state fed by the 3986-keV γ ray, and it is possible that this transition feeds an intermediate level which subsequently decays to, or toward, the yrast states by a number of weaker transitions. No other discrete γ rays could be identified to account for the missing 92% of the decay-out intensity. This suggests that the decay of the ^{62}Zn SD band is fragmented over a large number of multistep pathways, as is typical of the decay-out of SD bands in heavier nuclei (see Section 1.3.3 and [Hen 94, Lop 96b], for example).

Although the SD band could not be linked into the remainder of the decay scheme, and definite spin, parity, and excitation energy assignments could therefore not be made, information regarding the spin and excitation energy of the band can be deduced by measuring the entry region in ^{62}Zn which feeds the SD band. The total center of mass energy of the evaporated particles T_{part} and the total γ -ray energy H_γ emitted by the final nucleus sum to a known constant value, the total center of mass energy E_{CM} (see Eq. 4.4). The entry excitation energy can therefore be determined by measuring either T_{part} or H_γ . For SD bands in heavy nuclei, H_γ measurements are used by necessity because the evaporated particles in the reactions used to populate these nuclei are primarily neutrons, which are usually not detected and are difficult to obtain accurate energy measurements for even if they were to be detected. One advantage of ^{62}Zn is that it is populated by a pure charged-particle channel and the entry excitation energy distribution can be determined with high resolution by measuring the charged-particle energies. Figure 6.3 compares the T_{part} distribution for events feeding the ^{62}Zn SD band (solid line) with the total T_{part} distribution for the ^{62}Zn channel (dashed line). These distributions were obtained by summing triple gates set on the γ rays in the SD band and on γ rays near the bottom of the ^{62}Zn decay scheme, respectively. The mean T_{part} of 28.8 MeV for events feeding

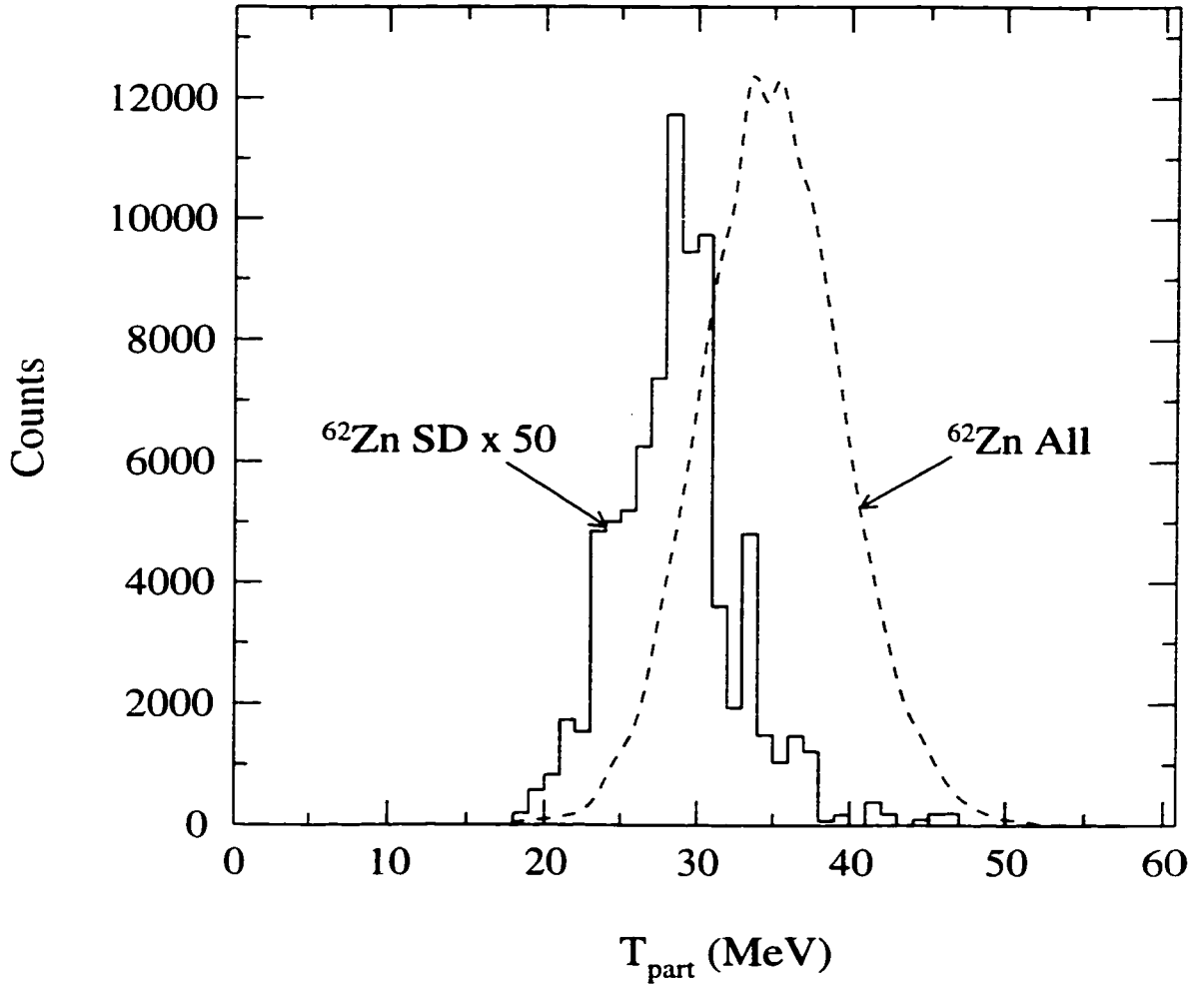


Figure 6.3: Spectra of the total center of mass particle kinetic energy T_{part} in coincidence with triple gates set on γ rays from the superdeformed band (solid line) and from low-spin states in ^{62}Zn (dashed line).

the band is 6.2 MeV below the average for the channel. The corresponding mean H_γ of 32.0 MeV for decays that pass through the band is therefore 6.2 MeV larger than the ^{62}Zn average. These spectra clearly show that the SD band is populated by only the highest excitation energy, and hence highest spin, components of the ^{62}Zn entry distribution. Based on the mean excitation energy of 32.0 MeV for events feeding the SD band, a decay-out energy of at least 3986 keV, the coincidences of the band with known transitions between high-spin ND states in the ^{62}Zn decay scheme.

the intensity profile of the band, and comparisons with theoretical calculations (see Section 6.3) which predict that SD bands become yrast in ^{62}Zn for spins $I \geq 24\hbar$, the observed transitions in the SD band are estimated to cover the spin range from $I = 18\hbar$ to $I = 30\hbar$, with an uncertainty of approximately $\pm 2\hbar$.

A definite conclusion regarding the deformation of the band in ^{62}Zn requires a measurement of its transition quadrupole moment. Because of the high collectivity and high transition energies in this band, the state lifetimes are very short (on the order of 1 fs) compared to the average time taken by the recoiling nuclei to leave the thin target (on the order of 100 fs). Very little attenuation of the recoil velocity occurs during the time in which the entire band decays, and an accurate Q_t measurement is thus difficult. The measured fractional Doppler shifts for the transitions in the SD band are shown in Fig. 6.4. The F values for the $\alpha = +1$ signature of ND band 1 and for low-spin transitions in ^{62}Zn , which decay with constant average shift $F = 0.872$ after the recoils have left the thin target, are also shown for comparison. All of the transitions in the SD band are observed with approximately the full Doppler shift, immediately implying the combination of fast side feeding and a large in-band Q_t .

In order to extract the transition quadrupole moment of the ^{62}Zn SD band from the Doppler-shift measurements shown in Fig. 6.4, the slowing of the recoils in the target was modeled with the Northcliffe and Schilling electronic stopping powers scaled by the ^4He stopping powers of Ziegler and Chu (as discussed in Section 3.4.2). The decay of the band was modeled assuming a constant in-band Q_t^\dagger , and the side feeding into each state was modeled by a single transition with the same lifetime as the precursor in-band state and an intensity to match the measured intensity profile of

[†]As will be discussed in Section 6.3, theoretical calculations for SD bands in ^{62}Zn predict that the transition quadrupole moment should increase with decreasing spin. However, the calculated variations in Q_t over the observed spin range are smaller than the uncertainty in the average Q_t value deduced from the present data, which are therefore not sensitive to such variations.

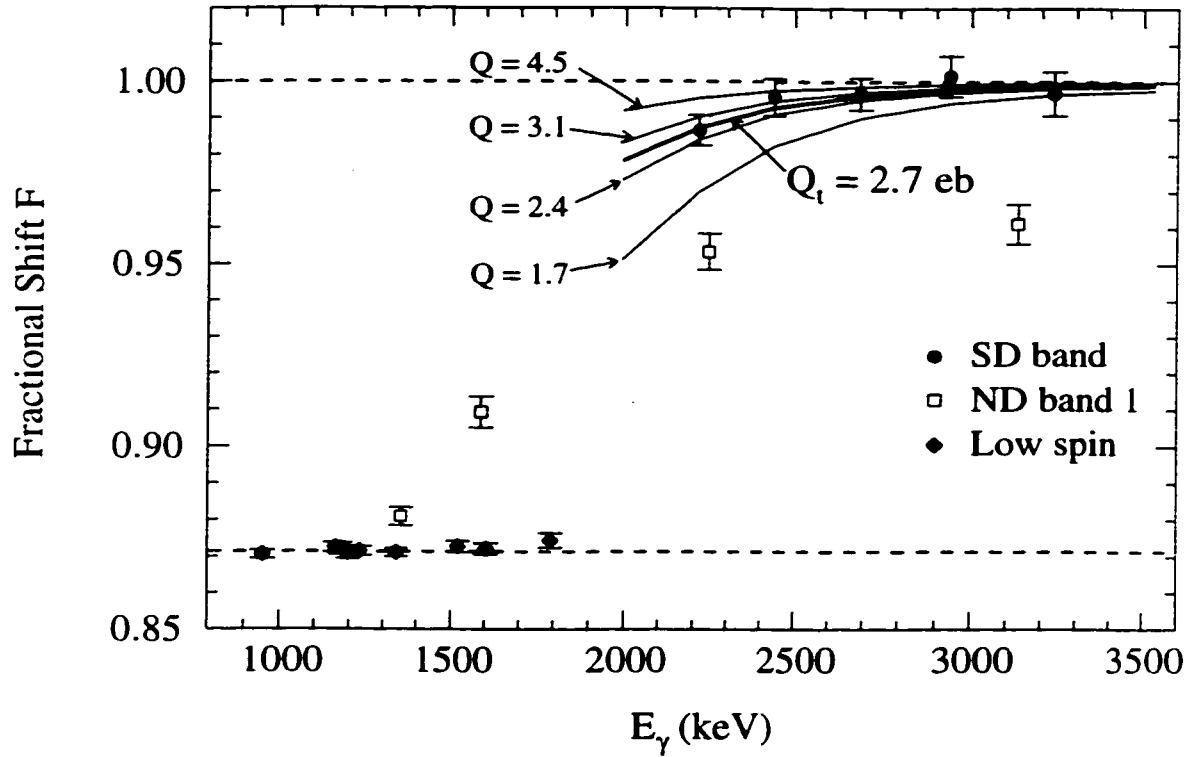


Figure 6.4: Fractional Doppler shifts F for transitions in the ^{62}Zn SD band (circles). The F values for transitions in the $\alpha = +1$ signature of ND band 1 (squares) and from low-spin spherical states (diamonds) in ^{62}Zn are also shown for reference. The dashed lines at $F = 1.00$ and 0.872 represent the full shift and the constant average shift for decays outside the thin target, respectively. Calculated F curves for various Q_t values are shown by solid lines. The SD band is best fit by $Q_t = 2.7^{+0.4}_{-0.3}$ eb.

the band. The fractional Doppler shifts calculated in this model for various values of Q_t are shown by the solid lines in Fig. 6.4. The SD band is best fit by $Q_t = 2.7^{+0.4}_{-0.3}$ eb. It should be noted that the upper limit on this Q_t value is determined entirely by the measured F value for the 2215-keV transition[†], and should thus be treated with caution. The measurements are, in fact, only 2.5 standard deviations from being consistent with an infinitely large value of Q_t . The lower limit on the extracted Q_t value, on the other hand, is determined by the measurements for all of the transitions and can therefore be treated with confidence.

[†]A measurement was not possible for the weak 1993-keV transition at the bottom of the band.

The side-feeding structure used in modeling the decay of this band is of the same form as that found to be appropriate in the feeding of SD bands in the $A \sim 150$ mass region [Sav 96]. As shown in Fig. 6.4, the F values for all of the transitions from states where intensity feeds into the SD band are consistent with the full Doppler shift $F = 1.00$. It is therefore clear that the feeding of this band is very fast, and any variation of the side-feeding model which allows the F values for the transitions at the top of the band to be fit is found to have little effect on the deduced value of Q_t . However, the uncertainties associated with the stopping powers are significant, and when combined with the statistical uncertainties in the measured F values yield a final in-band Q_t value of $2.7^{+0.7}_{-0.5}$ eb. Assuming an axially symmetric shape, the corresponding quadrupole deformation (Eq. 2.7) of the ^{62}Zn SD band is $\beta_2 = 0.45^{+0.10}_{-0.07}$.

The observation of the SD band in ^{62}Zn establishes a new region of high-spin superdeformation for nuclei with particle numbers $N, Z \approx 30$. The systematics of presently known regions of superdeformation are illustrated in Fig. 6.5, where the $\mathcal{J}^{(2)}$ values for the ^{62}Zn SD band, as well as those for SD bands characteristic of previously observed SD mass regions, are plotted versus rotational frequency. All of the $\mathcal{J}^{(2)}$ values have been divided by $A^{5/3}$ in order to remove the mass dependence of the moment of inertia (see Eq. 2.5). The dashed line in Fig. 6.5 represents the moment of inertia expected for a rigid rotor with deformation $\beta_2 = 0.5$. Although the $\mathcal{J}^{(2)}$ values for SD bands in different mass regions have different dependences on the rotational frequency (see Section 6.3 for a discussion of this dependence in ^{62}Zn), the magnitudes of these values are similar, suggesting similar deformations. Throughout the chart of the nuclides, from the uranium region with $A \sim 240$ to light Zn nuclei with $A \sim 60$, wherever there are calculated gaps in the single-particle energy levels for nuclear shapes with approximately 2 : 1 axis ratios, superdeformed bands are experimentally

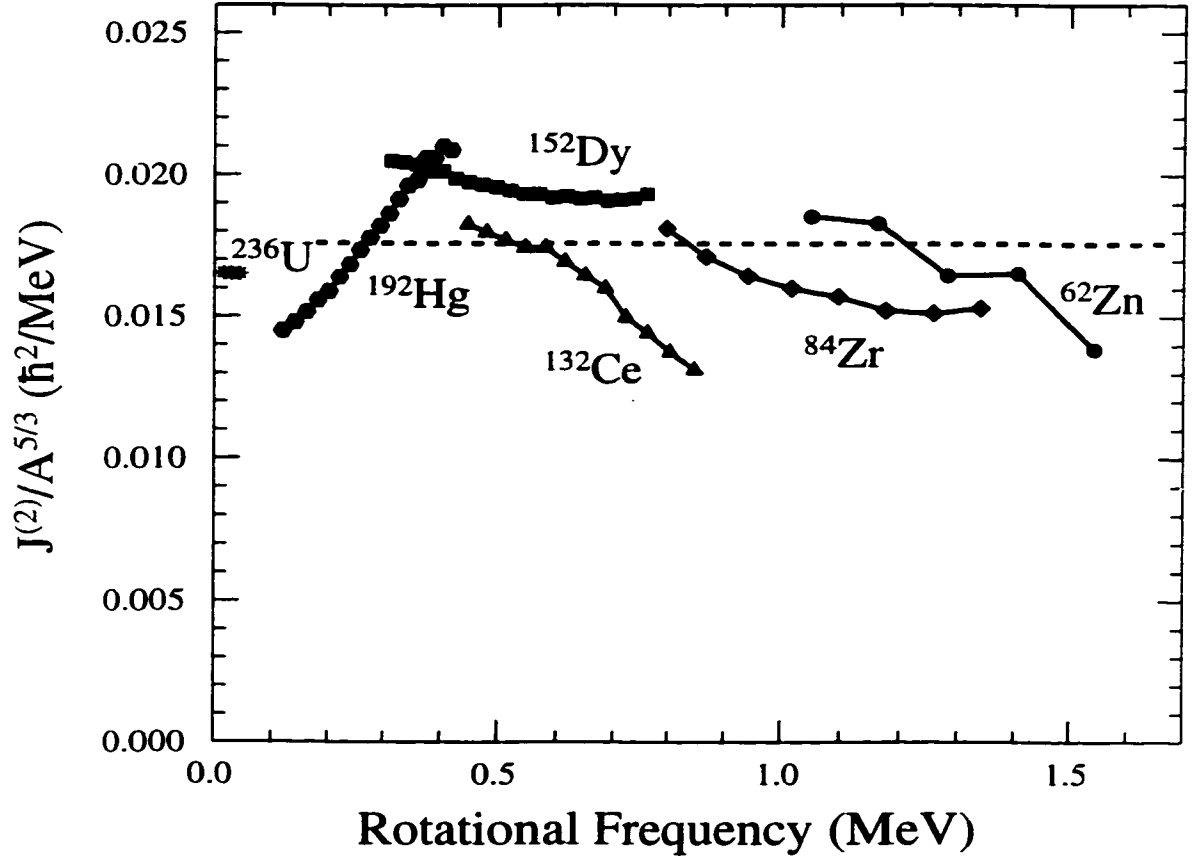


Figure 6.5: Dynamic moment of inertia $\mathcal{J}^{(2)}$ divided by $A^{5/3}$ versus rotational frequency for the ^{62}Zn SD band and for SD bands from other mass regions. The dashed line represents the moment of inertia of a rigid rotor with deformation $\beta_2 = 0.5$.

observed. It is also worth noting that Fig. 1.6 indicates a superdeformed shell gap for particle number 16, and both cranked Nilsson-Strutinsky [She 91] and cranked Hartree-Fock [Yam 98] calculations have predicted superdeformation in the $N = Z$ nucleus ^{32}S . Although high-spin studies of nuclei in the $A \sim 30$ mass region are faced by all of the experimental challenges that were discussed in the context of the proton-rich $A \sim 60$ mass region in Section 1.4, these studies are not, in author's opinion, beyond the reach of modern γ -ray and charged-particle detector arrays. The observation of high-spin superdeformation in these very light $N \approx Z$ nuclei would be of interest for the same reasons discussed for $A \sim 60$ nuclei in Section 6.1.

6.3 Interpretation

Theoretical calculations for superdeformed bands in ^{62}Zn [Rag 97] were carried out employing the configuration-dependent shell-correction approach with the cranked Nilsson potential at the same time as the calculations described in Section 5.4 for the terminating ND bands in ^{62}Zn . Representative high-spin potential energy surfaces from these calculations are shown in Fig. 6.6. For the $I^\pi = 20^-$ potential energy surface, the absolute energy minimum at $\varepsilon_2 \approx 0.27, \gamma \approx 30^\circ$ corresponds to band 2 discussed in Chapter 5. Note, however, that a well defined superdeformed second minimum exists at $\varepsilon_2 \approx 0.43, \gamma \approx 0^\circ$. At $I^\pi = 24^-$, band 2 in ^{62}Zn terminates on the oblate $\gamma = 60^\circ$ axis, and the prolate superdeformed minimum becomes yrast.

The calculated energies of the yrast superdeformed band for each of the four combinations of signature and parity are shown relative to an $I(I+1)$ reference in Fig. 6.7. For $I \gtrsim 24\hbar$, a number of superdeformed configurations with deformation in the range $\varepsilon_2 = 0.36\text{--}0.45$ ($\beta_2 = 0.41\text{--}0.53$), $\gamma = 0\text{--}15^\circ$ are calculated to lie close to the yrast line. In all of these superdeformed bands, the proton and neutron orbitals up to the $N, Z = 30$ SD shell gaps are filled, corresponding to the $f_{7/2}$ -hole, $g_{9/2}$ -particle configuration $[f_{7/2}]^{-2}[g_{9/2}]^2$ in both the proton and neutron subsystems, or $[22,22]$ in the shorthand configuration notation introduced in Section 5.4. Different SD bands in ^{62}Zn are formed depending on the orbitals occupied by the last two neutrons.

The different SD configurations in ^{62}Zn can be understood in terms of the single-particle Routhians shown in Fig. 6.8. These Routhians have been calculated at the deformation $\varepsilon_2 = 0.401, \gamma = 4.0^\circ, \varepsilon_4 = 0.067$ appropriate for the $[22,22]$ SD configuration, in which the last two neutrons occupy the two signatures of the low- j negative parity orbital labeled 3_5 in Fig. 6.8. The lower panel of this figure shows that, at this deformation, the positive signature of the 4_2 orbital arising from the $g_{9/2}$

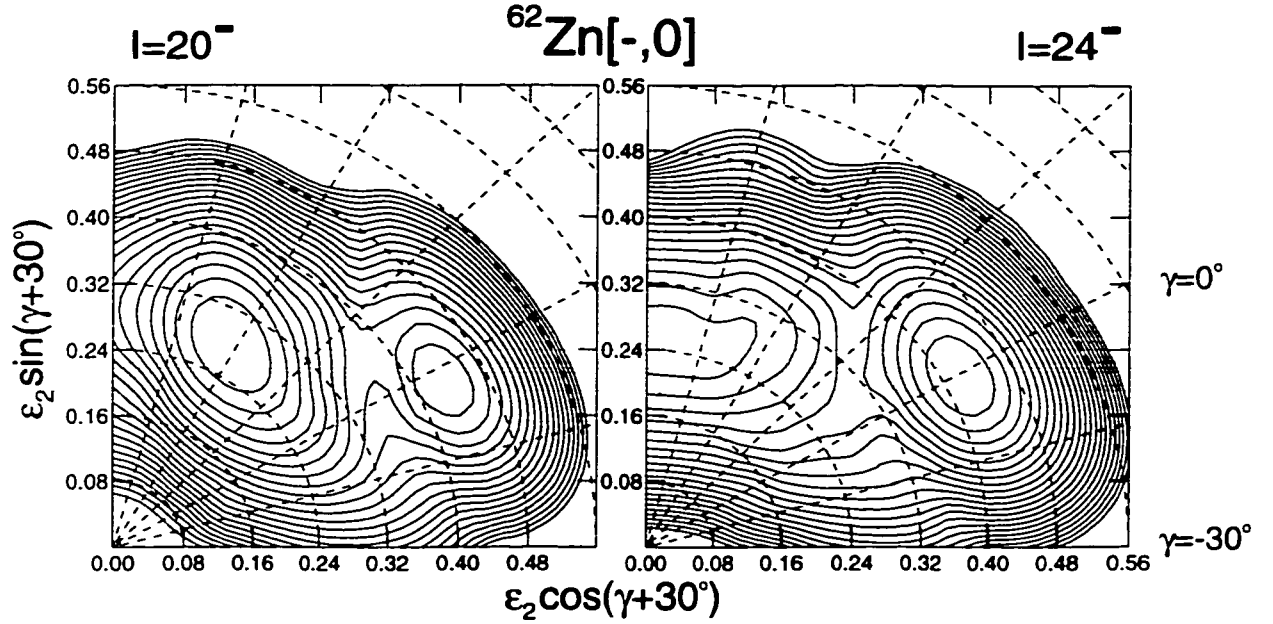


Figure 6.6: Calculated potential energy surfaces for ^{62}Zn at $I^\pi = 20^-$ (left) and $I^\pi = 24^-$ (right) [Rag 97]. Equipotential lines separated by 0.25 MeV are shown up to 5.5 MeV above the minima.

shell also lies close to the Fermi surface for $N = 32$. A pair of superdeformed bands with the $[22,23]$ configuration can thus be formed if a neutron occupies this orbital and one of the signatures of the 3_5 orbital is occupied by the other neutron. If the deformation is decreased relative to that used in Fig. 6.8, the 4_2 orbital moves away from the Fermi surface and the $\Omega = \frac{7}{2}$ extruder orbital (labeled 3_6) from the $f_{7/2}$ shell is lowered in energy. If one of the neutrons is placed in this high- Ω orbital, signature degenerate superdeformed bands with the $[22,12]$ configuration are expected. On the other hand, if the deformation is increased, the $N = 4$, $g_{9/2}$ intruder orbitals are lowered in energy and the negative signature of the 4_2 orbital can be brought to the Fermi surface, leading to a superdeformed band with the $[22,24]$ configuration. This band is not shown in Fig. 6.7 because it is calculated to lie at higher energy than the band built on the $[22,22]$ configuration, which has the same signature and parity.

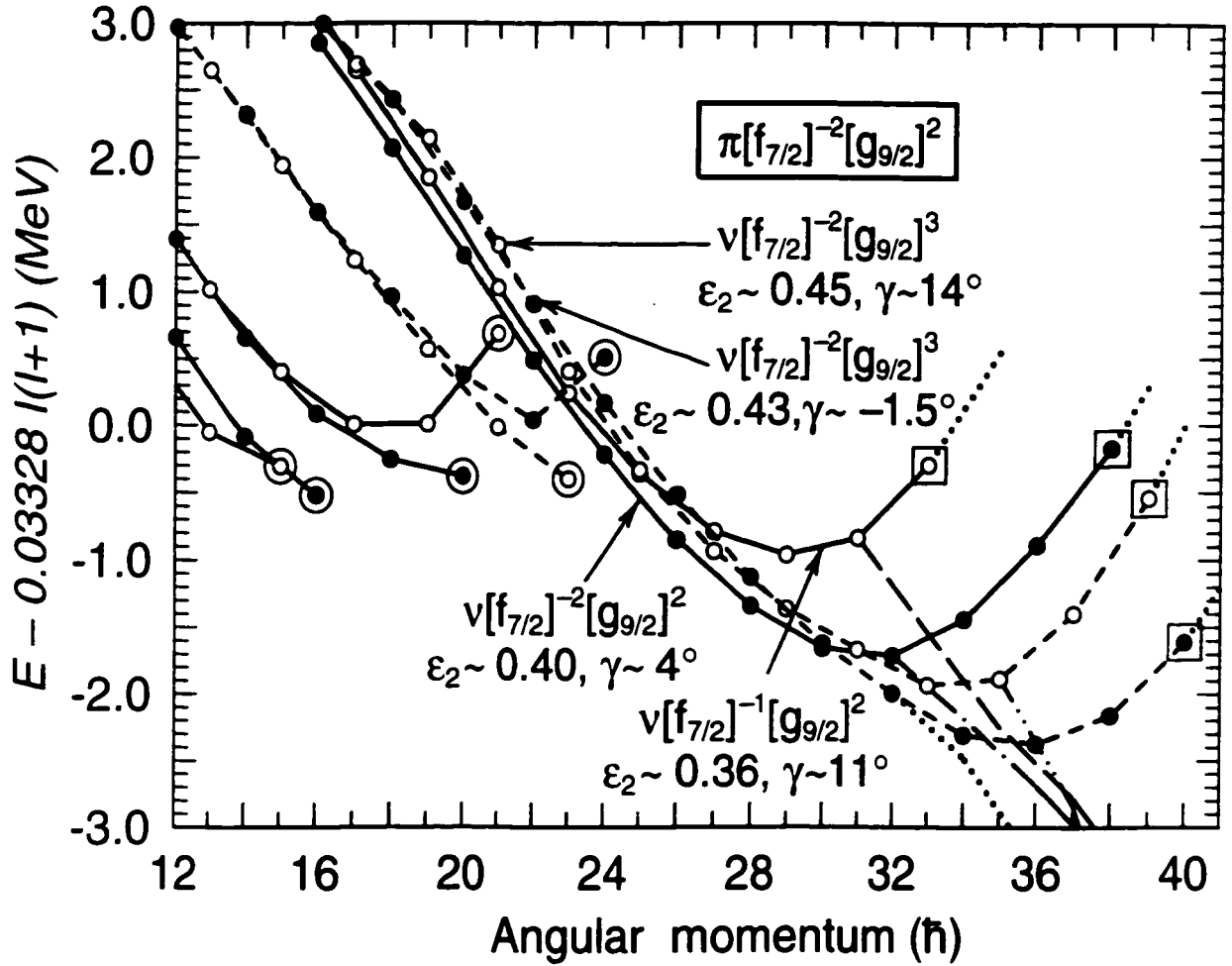


Figure 6.7: Energies of favoured collective configurations in ^{62}Zn relative to an $I(I+1)$ reference from the Nilsson-Strutinsky calculations [Rag 97]. The SD configurations are labeled by their proton and neutron $f_{7/2}$ holes and $g_{9/2}$ particles and by their equilibrium deformations at $I \approx 22 \hbar$. Solid (dashed) lines represent positive (negative) parity, and closed (open) symbols denote signature $\alpha = 0$ ($\alpha = +1$). Terminating ND states are circled. For $I \geq 30 \hbar$, the yrast lines for different combinations of parity and signature are shown by lines of different type without symbols. The states corresponding to the maximum spin available from the low-spin SD configurations are indicated by large open squares. Note that these states are collective and that the SD bands can be extended to higher spins, as indicated by the dotted lines.

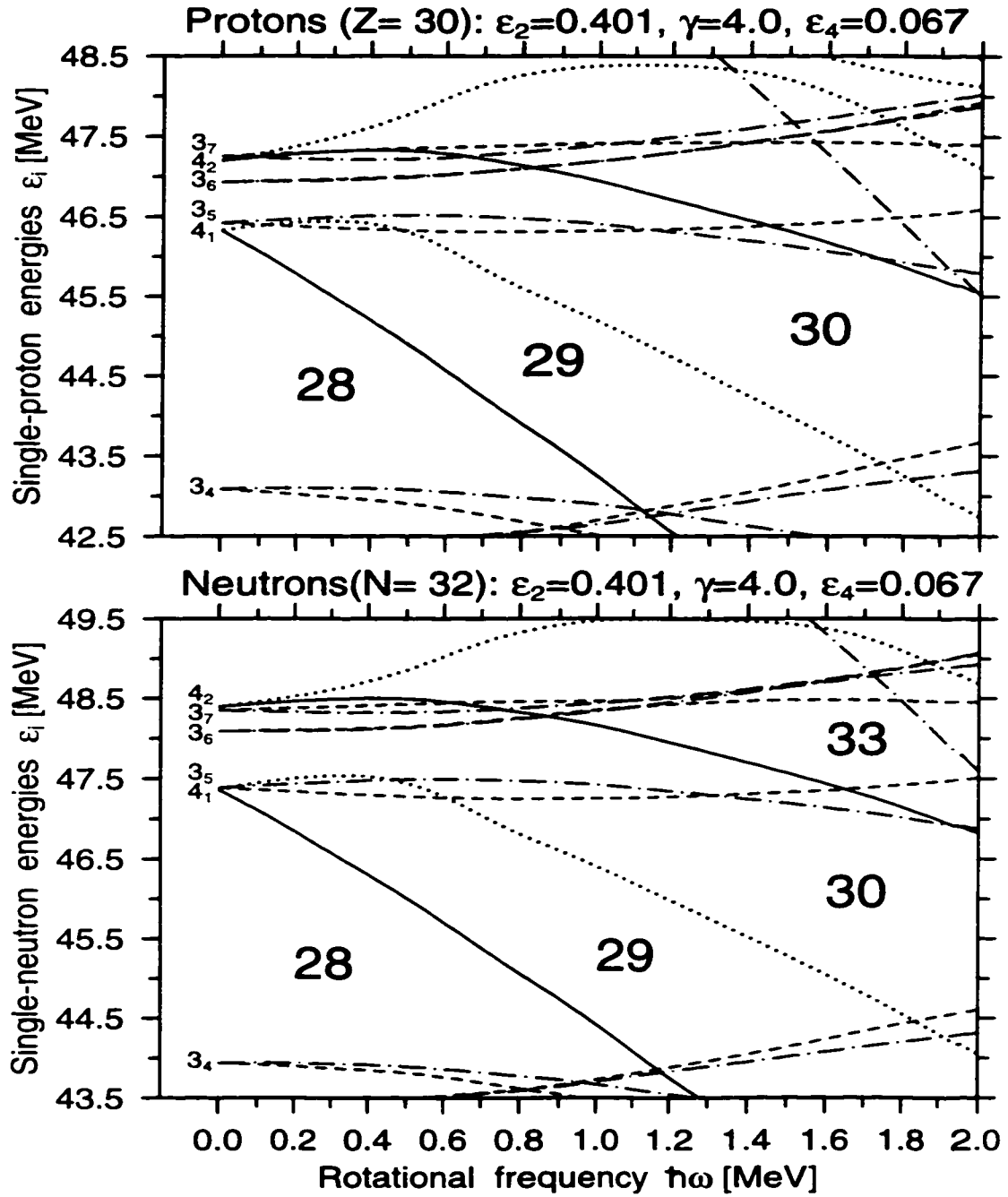


Figure 6.8: Single-proton (top) and single-neutron (bottom) Routhians for ^{62}Zn calculated at a deformation $\varepsilon_2 = 0.401$, $\gamma = 4^\circ$, $\varepsilon_4 = 0.067$. The orbitals are labeled at zero rotational frequency by N_k , the k th lowest orbital from the N th oscillator shell. The line types represent: $(\pi, \alpha) = (+, +1/2)$ solid, $(+, -1/2)$ dotted, $(-, +1/2)$ dashed, and $(-, -1/2)$ dot-dashed. The high- j orbitals have been identified and their virtual crossings with low- j orbitals removed, as discussed in Section 2.3.4.

Of the calculated SD bands in ^{62}Zn , the $[22,12]$ configurations are not likely candidates for the observed band. As noted above, a single $f_{7/2}$ neutron hole should lead to a pair of signature-degenerate bands. The absence of any evidence for a signature partner to the observed superdeformed band thus argues strongly against this configuration assignment. Furthermore, the Q_t values of 2.1–1.2 eb calculated for these bands in the relevant spin range ($I \sim 18\text{--}30\hbar$) are below the lower limit on the measured value. The measured Q_t value of $2.7^{+0.7}_{-0.5}$ eb is, however, in good agreement with the calculations for the $[22,2n]$ configurations with $n = 2\text{--}4$. In all of these bands, the Q_t values are predicted to decrease with increasing spin (see below). For $I \approx 18\hbar$ to $I \approx 30\hbar$, the calculated values cover the ranges from 2.7–2.1 eb for the $[22,22]$ configuration, 3.2–2.5 eb for the $[22,23]$ configurations, and 3.3–2.9 eb for the $[22,24]$ configuration. All of these values are consistent with the experimental measurement and, as the observed superdeformed band is not linked to the rest of the ^{62}Zn decay scheme, it is not possible to eliminate any of these configurations based on signature and parity considerations.

In addition to its transition quadrupole moment, the dynamic moment of inertia of the observed superdeformed band can be compared with theoretical calculations in order to help determine a configuration assignment. Recently, cranked Hartree-Fock calculations employing the SLy4 [Cha 95] parametrization of the Skyrme interaction have been performed for SD bands in ^{62}Zn by Dobaczewski *et al.* [Dob 98]. The $\mathcal{J}^{(2)}$ values from these calculations for the $[22,22]$, $[22,23]$, and $[22,24]$ configurations are compared with the experimental results in Fig. 6.9. In these calculations, the experimental $\mathcal{J}^{(2)}$ values are best fit by either the $[22,24]$ configuration or the $\alpha = +1$ signature of the $[22,23]$ configuration. The calculations for the $\alpha = 0$ signature of the $[22,23]$ configuration also reproduce the trend of the data reasonably well,

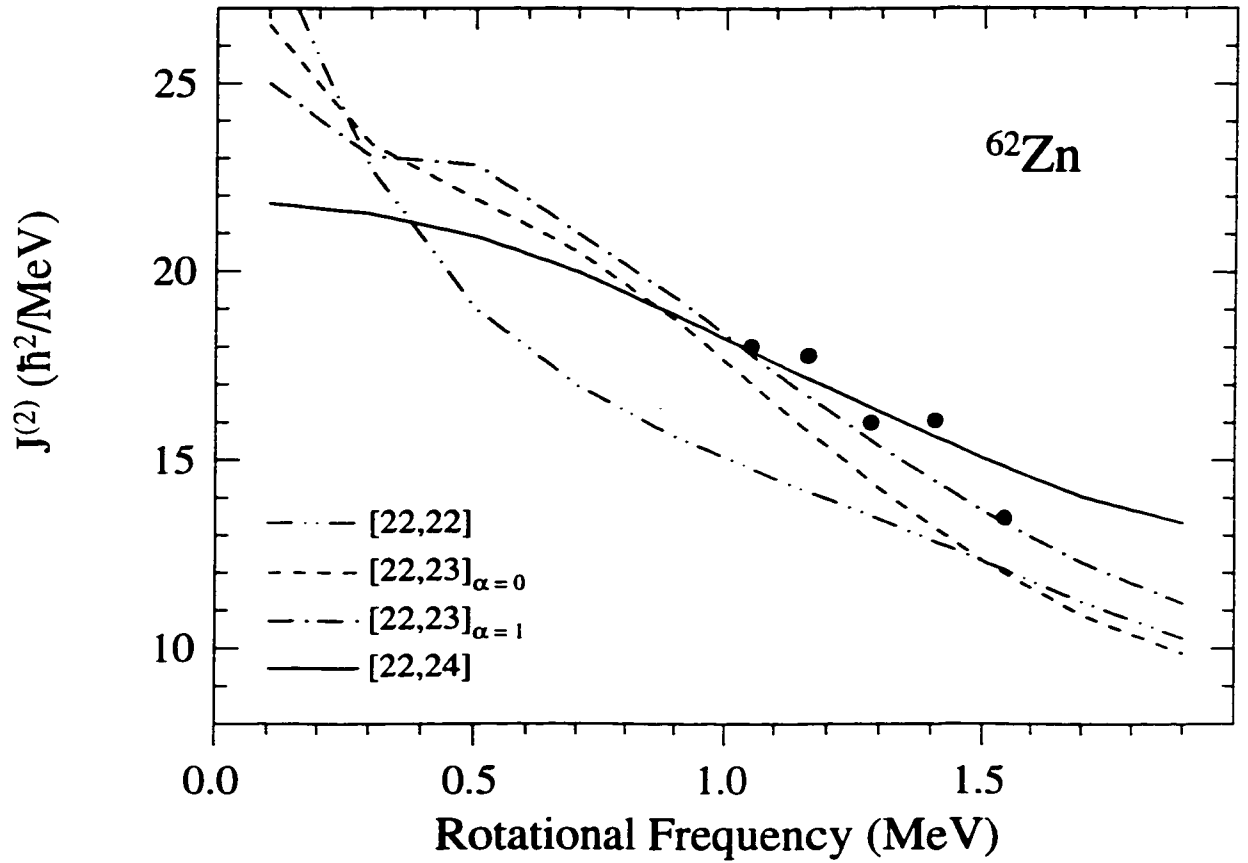


Figure 6.9: Comparison of the experimental $\mathcal{J}^{(2)}$ values (circles) for the SD band in ^{62}Zn with the results of cranked Hartree-Fock calculations [Dob 98] for the $[22,22]$, $[22,23]$, and $[22,24]$ configurations.

but the calculated $\mathcal{J}^{(2)}$ values for the $[22,22]$ configuration do not agree with those of the observed band. Calculations for SD bands in ^{62}Zn have also recently been performed by Afanasjev *et al.* [Afa 98] employing the cranked relativistic mean field (CRMF) formalism with various parametrizations of the RMF Lagrangian, namely the NL1 [Rei 86], NL3 [Lal 97], and NLSH [Sha 93] parameter sets. These calculations favour the assignment of the $[22,24]$ configuration to the observed SD band [Afa 98]. As shown in Fig. 6.10, the calculated $\mathcal{J}^{(2)}$ values for this configuration are in good agreement with the experimental measurements. The calculated $\mathcal{J}^{(1)}$ values for the $[22,24]$ configuration are also shown in this figure, and are in excellent agreement

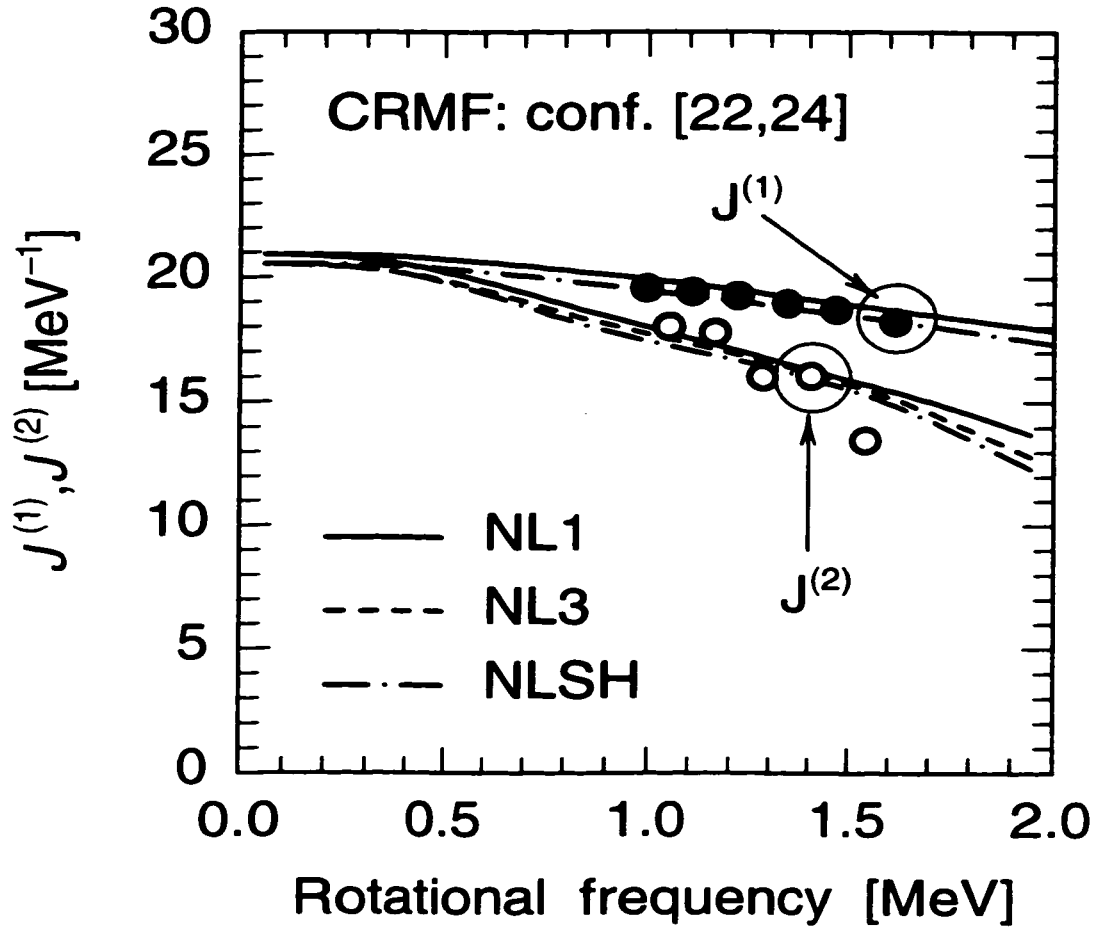


Figure 6.10: Comparison of the experimental $\mathcal{J}^{(2)}$ values (open circles) and $\mathcal{J}^{(1)}$ values (solid circles), assuming spins from $18\hbar$ to $30\hbar$ for the SD band in ^{62}Zn , with the results of cranked relativistic mean field calculations for the $[22,24]$ configuration. Different line types are used for different parametrizations of the RMF. From [Afa 98].

with the data if the estimated spins from $I = 18\hbar$ to $I = 30\hbar$ are adopted for the observed states in the SD band.

A consistent interpretation of the observed SD band in ^{62}Zn , based on comparisons with the cranked Nilsson-Strutinsky, Hartree-Fock, and relativistic mean field calculations, would seem to favour the $[22,24]$ configuration assignment. Given the uncertainties in the exact ordering and spacing of the energy levels above the $N = 30$ SD shell gap, however, an assignment to one of the $[22,23]$ configurations cannot be

ruled out at this time. The $\mathcal{J}^{(2)}$ values calculated with both the Hartree-Fock method and the CRMF method indicate that the [22,22] configuration is not a likely candidate for the observed SD band. Interestingly, this configuration is actually predicted to be yrast for spins between $24\hbar$ and $30\hbar$ in both the Nilsson-Strutinsky calculations (see Fig. 6.7) and the CRMF calculations [Afa 98]. As will be discussed in Chapter 7, linking transitions have been observed for the doubly-magic superdeformed band in ^{60}Zn . It is to be hoped that future high-spin studies of $A \sim 60$ nuclei will identify linking transitions for SD bands with valence particles outside the ^{60}Zn SD core. The firm configuration assignments resulting from such observations would provide important information about the single-particle energy levels in the vicinity of the $N, Z = 30$ SD shell gaps and help to refine the parametrizations of the mean field models used to describe high-spin rotational bands in this mass region.

As noted in Section 6.1, an interesting feature of superdeformation in the $A \sim 60$ mass region is that the single-particle configurations in these light nuclei have a relatively small total spin content. For example, the maximum possible spins that can be extracted from the orbitals occupied at low spin in the [22,22], [22,23], and [22,24] SD configurations in ^{62}Zn are $38\hbar$, $40\hbar$, and $40\hbar$, respectively. Although the mixing of low- j and high- j orbitals at large deformation and high rotational frequency prevents these bands from terminating in the sense of the normal deformed bands discussed in Chapter 5, the properties of the superdeformed bands in the $I = 30\text{--}40\hbar$ range are predicted to be strongly affected by the limited spin content of their single-particle configurations. The high energy cost of generating angular momentum in this spin range, relative to a rigid rotor, is indicated by the upswing in the energy curves for these bands shown in Fig. 6.7. The decreasing collectivity in these bands with increasing angular momentum is also reflected in the decreasing

transition quadrupole moments mentioned above. The predicted Q_t decreases in the superdeformed bands are, however, more gradual than those in the terminating bands discussed in Chapter 5. Even at the highest spins in the SD bands, the calculated Q_t values are sufficiently large that, when combined with the very high γ -ray transition energies at these spins, the predicted state lifetimes are in the sub-femtosecond range. As can be seen from the measured F values for the high-spin transitions in the ^{62}Zn SD band shown in Fig. 6.4, such short lifetimes are well beyond the resolution of present experimental techniques. It is therefore unlikely that it will be possible to test the predicted loss of collectivity in these superdeformed bands by direct lifetime measurements any time in the foreseeable future. The moments of inertia of these bands, however, can be determined, and they also reflect the high energy cost associated with building very high spin states in these configurations. Pairing correlations are expected to be negligible at high rotational frequencies (see Section 2.4), and one might therefore expect regular rotational bands characterized by a rigid-body moment of inertia. The $\mathcal{J}^{(2)}$ values in the $A \sim 60$ superdeformed bands, however, are calculated to lie well below the $\mathcal{J}^{(1)}$ values at high spin and to decrease rapidly with increasing rotational frequency, in agreement with the experimental observations for the SD band in ^{62}Zn (see Fig. 6.10). Although the effect is not as dramatic as in the terminating normal deformed bands, these decreasing $\mathcal{J}^{(2)}$ values reflect the increasing cost of generating angular momentum as the superdeformed band gradually exhausts the spin available from its single-particle configuration and, in the absence of direct lifetime measurements, can be regarded as the best available evidence for the predicted loss of collectivity in $A \sim 60$ superdeformed bands.

6.4 Summary

The first superdeformed band in the $A \sim 60$ mass region has been identified in ^{62}Zn . This band consists of a cascade of six γ rays covering an estimated spin range from $I = 18\hbar$ to $I = 30\hbar$. Thin-target Doppler-shift attenuation lifetime measurements for this band yield a transition quadrupole moment $Q_t = 2.7^{+0.7}_{-0.5}$ eb, corresponding to a deformation $\beta_2 = 0.45^{+0.10}_{-0.07}$ for an axially symmetric shape. Although a candidate for a decay out transition at 3986 keV was identified, the SD band could not be conclusively linked to the remainder of the ^{62}Zn decay scheme and definite spin, parity, and excitation energy assignments for the SD states were therefore not possible. Nonetheless, these results confirm the longstanding theoretical prediction of $A \sim 60$ superdeformation and establish a new region for the study of high-spin superdeformed bands in light nuclei with proton and neutron numbers $N, Z \approx 30$.

Cranking calculations employing the Nilsson-Strutinsky, Hartree-Fock, and relativistic mean field approaches predict that superdeformed bands with deformations $\beta_2 = 0.41\text{--}0.53$ become yrast in ^{62}Zn for $I \gtrsim 24\hbar$. Although the lack of exact spin and parity assignments for the observed band and the relatively large uncertainty in the measured Q_t value prevented a definite configuration assignment, comparisons with these calculations favour a single-particle configuration involving 2 $f_{7/2}$ proton holes, 2 $g_{9/2}$ protons, 2 $f_{7/2}$ neutron holes, and 4 (or possibly 3) $g_{9/2}$ neutrons. Future high-spin studies of $A \sim 60$ nuclei will hopefully identify linking transitions for yrast and excited superdeformed bands in nuclei with particles outside the doubly-magic ^{60}Zn SD core. The definite spin, parity, excitation energy, and configuration assignments resulting from such observations will provide crucial information about the, as yet unknown, single-particle energy levels at large deformation in this mass region.

Chapter 7

The Doubly-Magic Superdeformed Band in ^{60}Zn

The observation of the doubly-magic superdeformed band in the $N = Z$ nucleus ^{60}Zn [Sve 98b] is discussed in this chapter. This band consists of a cascade of eleven γ rays with a measured transition quadrupole moment $Q_t = 2.75 \pm 0.45$ eb, corresponding to a deformation $\beta_2 = 0.47 \pm 0.07$. Linking transitions connecting this band to the yrast line have been identified, and these transitions establish the spins, parity, and excitation energies of the superdeformed states from the $I^\pi = 8^+$ state at 9.621 MeV to the $I^\pi = 30^+$ state at an excitation energy of 33.90 MeV. The stretched- $E2$ character and relatively large $B(E2)$'s of these linking transitions indicate that the decay-out process for this superdeformed band differs substantially from that observed in heavier nuclei. Although theoretical calculations that do not include pairing are in good agreement with the high-spin properties of this band, a strong upbend in the dynamic moment of inertia at low rotational frequency indicates that pairing correlations are important in the low-spin superdeformed states.

7.1 Motivation

The doubly-magic superdeformed configuration in the $A \sim 60$ mass region, corresponding to filling the single-particle energy levels up to the large SD shell gaps at $N, Z = 30$, should be observed in the $N = Z$ nucleus ^{60}Zn . In addition to the motivation discussed in Section 6.1 for studying $A \sim 60$ superdeformation in general, the doubly-magic superdeformed band in ^{60}Zn is of particular interest for a number of reasons. Firstly, the observation of this band would establish the natural reference core relative to which single-particle configurations may be assigned to other SD bands in this mass region. Secondly, neutron-proton pairing is expected to be of particular importance in $N = Z$ nuclei, and the observation of superdeformation in ^{60}Zn would provide an ideal case to investigate the role of isospin $T = 0$ pairing at high rotational frequency. Finally, the doubly-magic superdeformed band in ^{60}Zn should be strongly favoured in energy. Indeed, cranked Nilsson-Strutinsky calculations (see Section 7.4) performed prior to the experimental investigations discussed here predicted that this band would become yrast at $I = 16 \hbar$, and by $I = 24 \hbar$ would be separated from excited states by a large (~ 2 MeV) energy gap. If ^{60}Zn were populated at high-spin, one would therefore expect that a substantial fraction of the channel intensity would feed this band, and that the SD band would be observed to relatively low spin before it decays to spherical states.

The observation of the ^{60}Zn SD band to low spin would provide two unique opportunities in the study of $A \sim 60$ superdeformation. Firstly, this band offers the best opportunity to obtain an accurate measurement of the transition quadrupole moment, and hence deformation, of a superdeformed band in the $A \sim 60$ mass region. As was discussed in Section 6.2 and can be seen in Fig. 6.4, the relatively large uncertainty in the measured Q_t of the ^{62}Zn SD band is primarily due to the very

short lifetimes of the high-spin superdeformed states, which do not permit a significant attenuation of the recoil velocity during the time in which the entire band decays. At lower spin, the γ -ray transition energies are lower and the state lifetimes are longer. Observing the ^{60}Zn SD band to low spin would thus result in a larger fractional change in the recoil velocity and a more accurate Q_t measurement than was possible for the SD band in ^{62}Zn . Secondly, the predicted low-spin decay of this band also makes it the best candidate to search for γ rays linking the superdeformed states to the remainder of the decay scheme. The identification of such linking transitions would permit definite spin, parity, and excitation energy assignments for the SD states, the first time such information would become available for any superdeformed band below the $A \sim 190$ mass region.

Motivated by these opportunities, experiments were carried out to search for superdeformation in the $N = Z$ nucleus ^{60}Zn . As will be discussed in the following sections, these experiments led to the identification of the doubly-magic SD band in this nucleus. An accurate transition quadrupole moment measurement was obtained and linking transitions that establish the spins, parity, and excitation energies of the SD states were identified. In addition, the stretched- $E2$ character and relatively large $B(E2)$ values of these linking transitions indicate that the decay-out mechanism for this band differs from that observed for SD bands in the $A \sim 190$ mass region.

7.2 Experiments

High-spin states in ^{60}Zn were studied with the Gammasphere array and the Microball charged-particle detector in two experiments. In the first experiment, a $500\text{ }\mu\text{g}/\text{cm}^2$ target isotopically enriched to 99.9% in ^{40}Ca was bombarded by a 125-MeV beam of ^{28}Si ions provided by the 88-Inch Cyclotron at Lawrence Berkeley National Laboratory, populating ^{60}Zn via the $^{40}\text{Ca}(^{28}\text{Si}, 2\alpha)^{60}\text{Zn}$ reaction. Gammasphere comprised 83 HPGe detectors in this experiment and 2.5×10^9 γ - γ - γ and higher-fold coincidence events were recorded. Additional details of this experiment, hereafter referred to as GS90, have already been given in Section 5.2.

In the second experiment, hereafter referred to as GSFMA9, a $500\text{ }\mu\text{g}/\text{cm}^2$ target of isotopically enriched ^{40}Ca (99.9%) was again used. In this experiment, thin ($100\text{ }\mu\text{g}/\text{cm}^2$) layers of ^{197}Au were flashed on both sides of the ^{40}Ca target in order to prevent oxidation of the calcium during the brief period that the target was exposed to air while being transferred from its inert gas storage cell to the Gammasphere vacuum chamber. This target was bombarded by a 134-MeV beam of ^{32}S ions provided by the ATLAS facility at Argonne National Laboratory, populating ^{60}Zn via the $^{40}\text{Ca}(^{32}\text{S}, 3\alpha)^{60}\text{Zn}$ reaction. In this experiment, Gammasphere comprised 101 HPGe detectors and, in addition to the detection of charged particles with the Microball, nuclei recoiling at approximately zero degrees relative to the beam axis were detected and identified with the Argonne Fragment Mass Analyzer (FMA). The mass-to-charge (A/q) ratios of these recoils were determined by dispersing them on a position-sensitive channel-plate detector at the FMA focal plane, and clean rejection of scattered beam ions and partial Z resolution for the recoiling nuclei were achieved by measuring their energy losses in a segmented ionization chamber located behind the channel-plate detector. In this chapter, we focus on the results obtained for ^{60}Zn

in this experiment. As was discussed in Section 4.4.2, the broad recoil cone for the ^{60}Zn nuclei resulting from the evaporation of three alpha particles led to a very low ($\sim 0.1\%$) recoil detection efficiency for this channel. The ^{60}Zn events were therefore selected and studied by the more efficient charged-particle detection plus total energy method, and additional details of the FMA setup and analysis of the recoil-gated data will therefore not be discussed here. The hardware pre-trigger condition in this experiment required at least 3 HPGe detectors to fire in coincidence, and the main trigger condition necessary before events were written to magnetic tape required clean signals from at least 4 HPGe detectors or at least 2 clean HPGe detectors to fire in coincidence with the detection of a recoil at the FMA focal plane. A total of 1.7×10^9 such events, $\sim 98\%$ of which involved at least 4 HPGe detectors, were recorded during the experiment.

High-spin spectroscopic studies of $N = Z$ nuclei in the $A \sim 60$ mass region are hindered by the small cross sections for populating these nuclei in heavy-ion fusion-evaporation reactions with stable beams and targets. Based on measured γ -ray yields, the pure alpha-particle evaporation channels leading to ^{60}Zn were estimated to represent only $\sim 0.1\%$ of the total fusion cross section in each of the experiments discussed here. A highly efficient and selective means of identifying the γ rays associated with these weak channels was therefore essential in these experiments. In both experiments, primary selection of ^{60}Zn events was accomplished by requiring the detection of all of the evaporated alpha particles in the Microball. As the center of mass recoil velocity given to the ^{60}Zn nuclei by the evaporated alpha particles is large, the improved γ -ray energy resolution achieved by using the detected alpha particles to reconstruct the kinematics of each event (see Section 4.2.5) was also crucial to the success of these studies. Because of the small cross sections for the

channels populating ^{60}Zn , the alpha-particle gated data sets from each experiment were dominated by leak-through events from much stronger channels ($2\alpha p$ and $2\alpha 2p$ in GS90, and $3\alpha p$ in GSFMA9) in which evaporated protons were not detected. In both experiments, the Hevimet collimators were removed from the Gammasphere HPGe detectors to provide event-by-event γ -ray multiplicity and sum-energy measurements, and these leak-through events were largely removed by the total energy channel selection method discussed in Section 4.3. As will be discussed in the following sections, the combination of the clean selection of the weak ^{60}Zn channel achieved by this method, and the very strong population of the doubly-magic superdeformed band ($60 \pm 4\%$ and $34 \pm 3\%$ of the ^{60}Zn channel intensity in the GS90 and GSFMA9 experiments, respectively) resulting from the large energy gap separating this band from other states at high spin (see Section 7.4), enabled the observation and detailed analysis of high-spin superdeformation in this $N = Z$ nucleus.

7.3 Results: Superdeformation in ^{60}Zn

The very clean selection of the weak ^{60}Zn channel achieved by detecting the evaporated alpha particles and applying the total energy method is illustrated in Fig. 7.1. This figure shows a portion of the *total* γ -ray spectrum for events from the GSFMA9 experiment in which three alpha particles were detected in the Microball. A total energy gate has been set to select the ^{60}Zn events, the detected alpha particles have been used to reconstruct the reaction kinematics for each event, and the γ rays have been Doppler-shift corrected for the full recoil velocity immediately following particle evaporation in order to obtain the best possible energy resolution for fast transitions. In addition to γ rays from two normal deformed rotational bands identified in ^{60}Zn , labeled by squares and diamonds in Fig. 7.1, transitions in the doubly-magic superdeformed band (circles) are clearly visible, in fact dominant, in this region of the γ -ray spectrum without making any use of γ -ray coincidence gates. Of course, the prominence of the SD transitions in Fig. 7.1 only occurs because this band carries such a large fraction ($34 \pm 3\%$ in this experiment) of the ^{60}Zn channel intensity. It should, however, be noted that the absolute cross section (on the order $300 \mu\text{b}$) for this band is smaller than is typical for yrast superdeformed bands in heavy nuclei populated via (HI, xn) reactions, and the unprecedented identification of this superdeformed band in the γ -ray singles spectrum shown in Fig. 7.1 is only possible because of the very clean selection of the weak ^{60}Zn channel.

The excellent peak-to-background ratio provided by the clean selection of the ^{60}Zn channel and the strong population of the doubly-magic superdeformed band enabled the mutual coincidence of all the transitions in this band to be confirmed by setting singles gates on the individual transitions in a γ - γ coincidence matrix. Figure 7.2(a) shows a complete spectrum of the observed band, obtained by summing

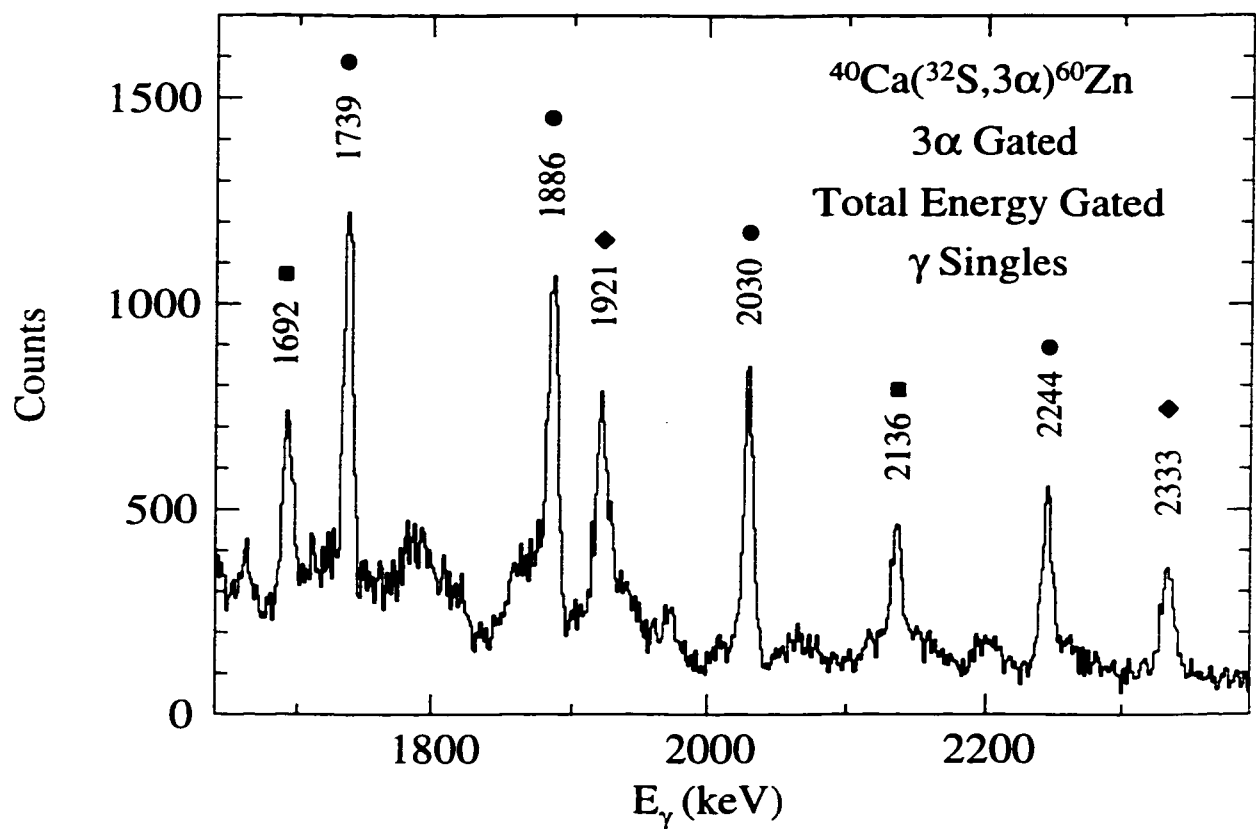


Figure 7.1: A portion of the total γ -ray spectrum for events from the GSFMA9 experiment selected for the weak ^{60}Zn channel. Transitions in the doubly-magic superdeformed band (circles), as well as in the normal-deformed bands ND1 (diamonds) and ND2 (squares) identified in ^{60}Zn , are clearly visible without making any use of γ -ray coincidence information.

coincidence gates set on all of the band members in the matrix from the GS90 experiment, where the SD band was populated at slightly ($\sim 2\hbar$) higher spin than in the GSFMA9 experiment. A partial decay scheme for ^{60}Zn from this work, which builds on the previously known 2^+ and 4^+ excited states [Kin 93], is shown in Fig. 7.3, and the γ -ray energies and intensities relative to the ^{60}Zn channel, as measured in the GS90 experiment, are given in Table 7.1.

In addition to the members of the ^{60}Zn ground-state band and the members of the doubly-magic superdeformed band (circles), Fig. 7.2(a) clearly reveals several

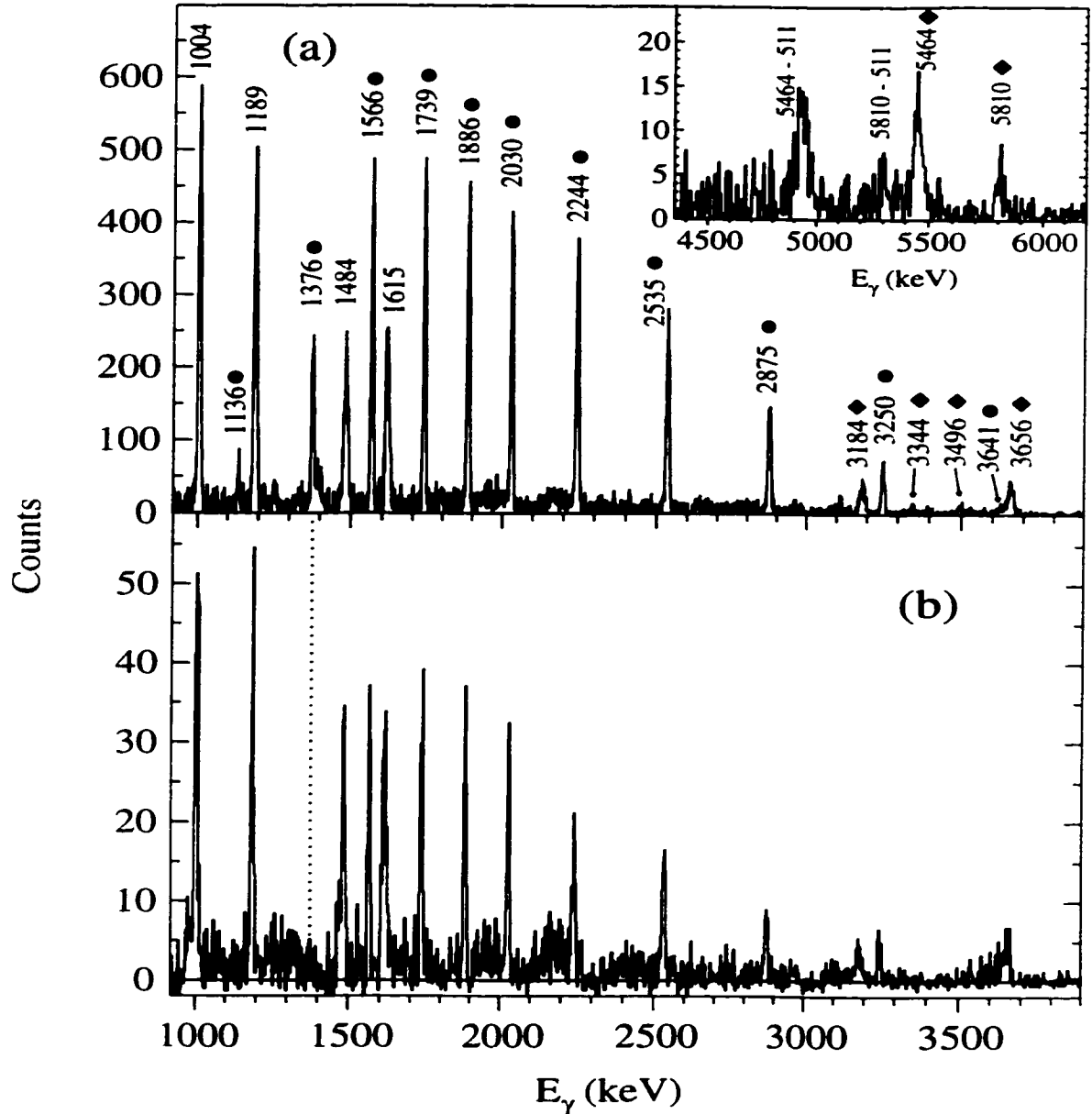


Figure 7.2: Gamma-ray spectra from the GS90 experiment obtained by summing coincidence gates set on (a) the members of the ^{60}Zn SD band (circles) and (b) the 3184 and 3656 keV transitions. Gamma rays connecting the SD band to the ground band are labeled by diamonds in (a) and the inset shows the two high-energy linking transitions at 5464 and 5810 keV. The peaks 511 keV below these transitions result from events in which the incident high-energy γ ray produces an electron-positron pair in the HPGe detector and one of the two 511-keV γ rays from the annihilation of the positron escapes from the Ge detector and does not trigger the BGO Compton suppression shield. Note the absence of the 1376 keV SD transition in (b).

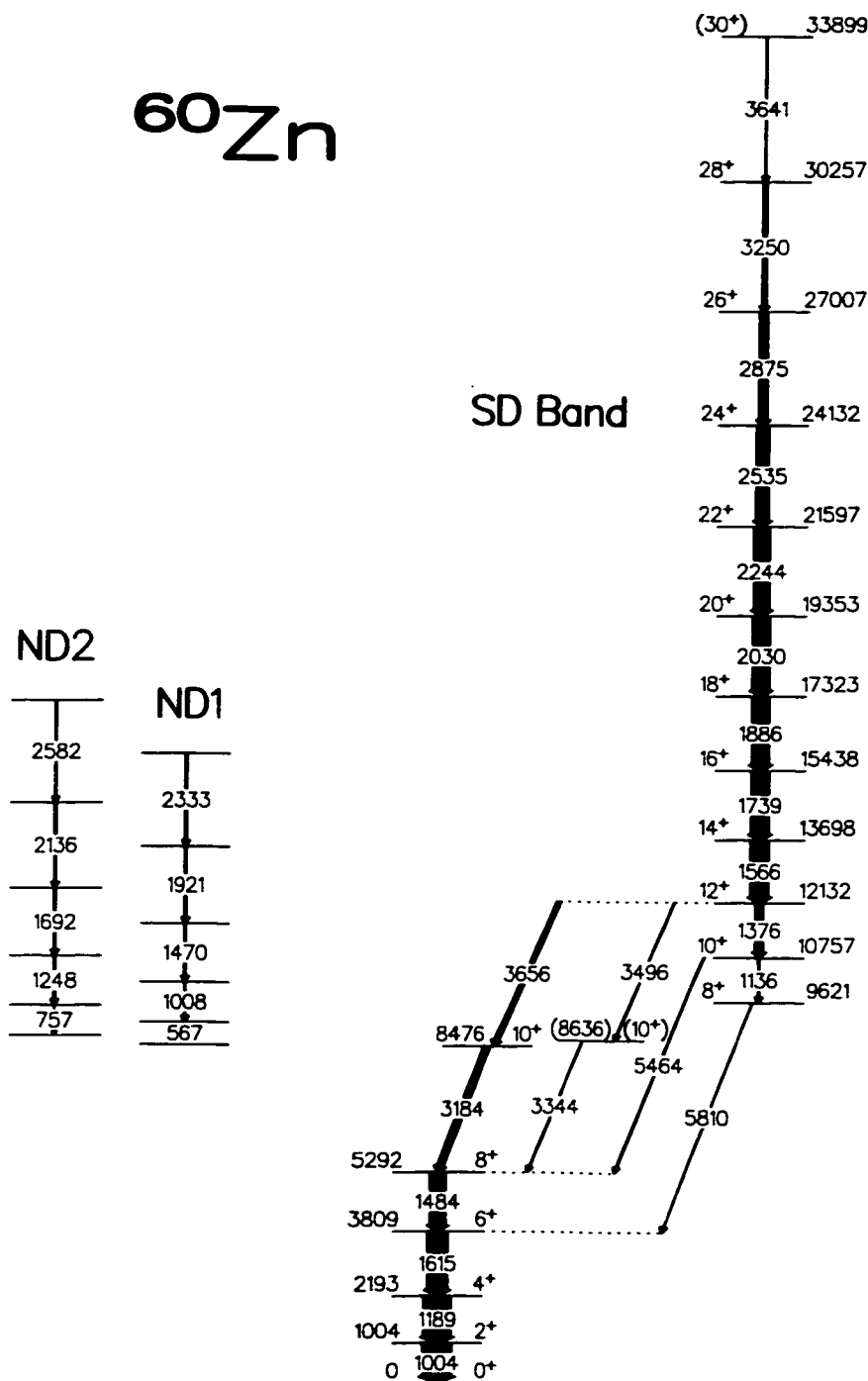


Figure 7.3: Partial decay scheme of ^{60}Zn . The transition and level energies are given to the nearest keV. The order of the 3496 and 3344 keV linking transitions is uncertain, as are the energies and spins of the unlinked normal-deformed bands ND1 and ND2.

I_i^π	I_f^π	E_γ (keV)	Intensity
2^+	0^+	1004.4 (4)	100.0
4^+	2^+	1189.0 (4)	92.5 (36)
6^+	4^+	1615.4 (5)	69.3 (32)
8^+	6^+	1483.7 (6)	53.4 (27)
10^+	8^+	3183.6 (12)	21.3 (16)
(10_2^+)	8^+	3344.1 (20)	2.7 (4)
8_{SD}^+	6^+	5810.0 (48)	1.5 (4)
10_{SD}^+	8_{SD}^+	1135.9 (9)	5.3 (5)
10_{SD}^+	8^+	5464.3 (39)	3.2 (6)
12_{SD}^+	10_{SD}^+	1375.6 (7)	26.8 (16)
12_{SD}^+	10^+	3656.4 (14)	14.6 (12)
12_{SD}^+	(10_2^+)	3495.7 (20)	3.0 (5)
14_{SD}^+	12_{SD}^+	1565.9 (6)	60.4 (35)
16_{SD}^+	14_{SD}^+	1739.3 (6)	59.6 (32)
18_{SD}^+	16_{SD}^+	1885.5 (7)	58.0 (34)
20_{SD}^+	18_{SD}^+	2029.8 (7)	57.1 (32)
22_{SD}^+	20_{SD}^+	2244.2 (8)	52.7 (30)
24_{SD}^+	22_{SD}^+	2535.0 (9)	41.7 (25)
26_{SD}^+	24_{SD}^+	2874.8 (10)	27.3 (16)
28_{SD}^+	26_{SD}^+	3250.5 (12)	12.1 (11)
(30_{SD}^+)	28_{SD}^+	3641.3 (35)	2.5 (7)
ND Band 1		567.3 (9)	1.2 (3)
		1008.3 (21)	4.2 (12)
		1470.1 (12)	4.5 (6)
		1921.2 (9)	6.5 (7)
		2332.5 (11)	5.0 (6)
ND Band 2		756.6 (9)	1.5 (3)
		1248.4 (9)	4.8 (5)
		1692.0 (8)	5.7 (6)
		2135.6 (10)	5.0 (5)
		2581.7 (12)	2.7 (4)

Table 7.1: Energies and intensities of γ -ray transitions in ^{60}Zn , as measured in the GS90 experiment. The intensities are normalized to 100 for the $2^+ \rightarrow 0^+$ transition.

high-energy transitions (diamonds) in coincidence with the SD band. As indicated in Fig. 7.3, these have been identified as linking transitions that decay out of the low-spin SD states and connect the SD band to the ground band. The low-spin nature of these transitions can, in fact, be determined from Fig. 7.2(a) by inspection. This spectrum has been Doppler-shift corrected for the full recoil velocity of the ^{60}Zn nuclei following particle evaporation, which provides the best energy resolution for the very fast transitions at the top of the SD band. This Doppler-shift correction is not optimal for the linking transitions, which are emitted at a lower recoil velocity following the decay of the SD band, and the peak widths for the high-energy linking transitions are therefore noticeably larger than those of the high-spin SD transitions in Fig. 7.2(a). The resolution for these decay-out transitions can be improved, at the expense of the resolution for the high-spin SD transitions, by applying a Doppler-shift correction appropriate for the attenuated recoil velocity, and several such Doppler-shift corrections were employed during the analysis in order to obtain optimal energy resolution at various points in the decay scheme.

The coincidence relationships for the linking transitions indicated in Fig. 7.3 were directly confirmed by setting γ -ray coincidence gates. An example of this is illustrated in Fig. 7.2(b), where the γ -ray spectrum in coincidence with gates set on the 3184 and 3656 keV linking transitions is shown. All of the transitions in the ^{60}Zn ground band, as well as all of the transitions in the SD band above and including the 1566 keV γ ray, are clearly visible in this spectrum. The appearance of the 3184 and 3656 keV transitions in this spectrum also confirms that these γ rays are in coincidence with each other. Note, however, that in accordance with Fig. 7.3, the 1376 and 1136 keV SD transitions are absent in this spectrum. Although no other discrete γ rays that decay into or out of the 8476 keV level could be identified,

the order of the 3184 and 3656 keV transitions, and hence the energy of this level, was established from intensity relationships. As can be seen in Fig. 7.2(a), the 3184 and 3656 keV transitions have equal intensity when gates are set on members of the SD band. However, when gates are set on the members of the ^{60}Zn ground band, the 3184 keV transition is considerably more intense (see Table 7.1), implying that additional unobserved intensity feeds into the 8476 keV level and the 3184 keV transition decays out of this level. Although the coincidence of the weak 3344 and 3496 keV linking transitions was also confirmed, in this case it was not possible to establish an order based on intensity arguments. The energy of the intermediate state between these transitions can therefore be either 8636 keV or 8788 keV, and no evidence for any other transitions feeding into or decaying out of this level could be found for either possible energy. The choice of 8636 keV shown in Fig. 7.3 is arbitrary.

The two normal-deformed bands identified in ^{60}Zn , labeled ND1 and ND2 in Fig. 7.3, were populated more weakly than the SD band, as can be seen in Fig. 7.1 for the GSFMA9 experiment and Table 7.1 for the GS90 experiment. While these bands are in coincidence with the transitions in the ^{60}Zn ground-state band, it was not possible to link them conclusively to the remainder of the decay scheme. As shown in Fig. 7.3, the spins, parities, and excitation energies of these ND bands were therefore not determined by this work.

The linking transitions for the superdeformed band shown in Figs. 7.2 and Fig. 7.3 establish the excitation energies of the SD states. Angular distribution measurements for the transitions in the ^{60}Zn ground-state band and the transitions in the SD band confirm their stretched- $E2$ character, with the exception of the weak 3641 keV transition at the top of the SD band, for which an angular distribution measurement was not possible and stretched- $E2$ character is simply assumed from

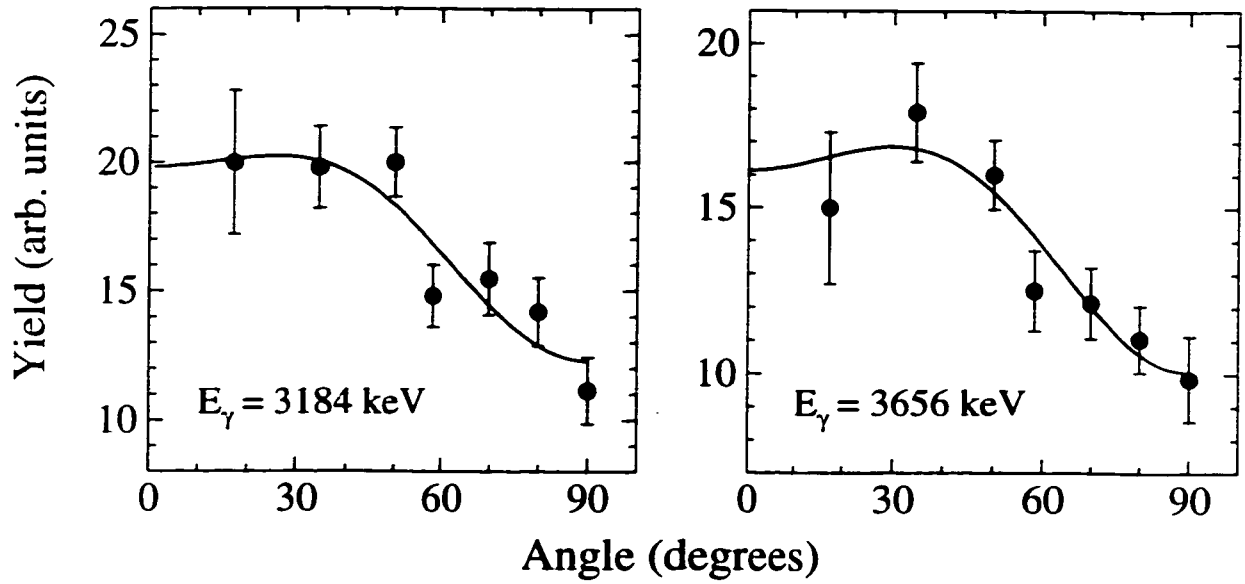


Figure 7.4: Angular distributions for the 3184 keV (left) and 3656 keV (right) linking transitions measured relative to the beam axis in the GSFMA9 experiment. The solid lines are Legendre polynomial fits that give angular distribution coefficients $a_2 = 0.37 \pm 0.08$, $a_4 = -0.16 \pm 0.10$ and $a_2 = 0.38 \pm 0.09$, $a_4 = -0.20 \pm 0.11$ for the 3184 and 3656 keV γ rays, respectively.

the systematic energies of the in-band $E2$ transitions. The spins and parity of the SD states can therefore be determined if the multiplicities of the linking transitions can be established. As shown in Fig. 7.4, sufficient statistics were collected to measure the angular distributions of the 3184 and 3656 keV linking transitions. These measurements were performed with the data from the GSFMA9 experiment, and the data from the HPGe detectors at angles of θ and $180^\circ - \theta$ relative to the beam axis have been combined. The solid lines in Fig. 7.4 are Legendre polynomial fits to the experimental measurements and yield angular distribution coefficients (see Eq. 3.7) $a_2 = 0.37 \pm 0.08$, $a_4 = -0.16 \pm 0.10$ for the 3184 keV γ ray and $a_2 = 0.38 \pm 0.09$, $a_4 = -0.20 \pm 0.11$ for the 3656 keV γ ray. These measurements favour stretched- $E2$ assignments for both of these linking transitions, and hence positive parity and the spins indicated in Fig. 7.3 for the states in the doubly-magic superdeformed band.

It should be noted that the angular distribution measurements for the 3184 and 3656 keV linking transitions shown in Fig. 7.4 are not sufficiently accurate to rule out $\Delta I = 0$ mixed $M1/E2$ assignments, and such assignments would also be consistent with the expectation that the yrast superdeformed band in ^{60}Zn should have positive parity and even spins. Note, however, that if either, or both, of these transitions are assigned $\Delta I = 0$ mixed $M1/E2$ character, a 6840 keV $E2$ transition from the 12132 keV level of the SD band directly to the 8^+ state of the ground band would be allowed. If the 3184 keV transition were assumed to be mixed $M1/E2$ and the 3656 keV transition stretched- $E2$, one would expect, from the E_γ^5 factor in the $E2$ transition rate (see Eq. A.6), that the 6840 keV decay-out transition would be approximately 20 times more intense than the 3656 keV transition. Even if the 3656 keV transition were assumed to be of $\Delta I = 0$ mixed $M1/E2$ character, the measured angular distribution requires a substantial (~ 10 – 50%) $E2$ component, and the 6840 keV transition would still be expected to be ~ 2 – 10 times more intense than the 3656 keV transition. The absence of any evidence for such a 6840 keV transition with an intensity $\gtrsim 5\%$ that of the 3656 keV transition thus argues strongly against the assignment of $\Delta I = 0$ mixed $M1/E2$ character to either the 3184 keV or the 3656 keV linking transition. Both these transitions are therefore assigned stretched- $E2$ character. As shown in Fig. 7.3, the spins, parity, and excitation energies of the SD states are thereby established from the 8^+ state at 9.621 MeV to the 30^+ state at an excitation energy of 33.90 MeV. An extrapolation of the superdeformed band to lower spin places the 0^+ SD state at an excitation energy of approximately 7.5 MeV.

The other linking transitions shown in Fig. 7.3 were too weak for reliable angular distribution measurements, and their multipolarities were therefore not directly determined. However, based on the assigned spins and parity of the SD states, the

5464 and 5810 keV linking transitions each change the nuclear spin by $2\hbar$ while leaving the parity unchanged. Stretched- $E2$ character is therefore also assigned to these transitions. The combined result of the 3344 and 3496 keV linking transitions is to change the nuclear spin by $4\hbar$ with no parity change. Although an $E1$ - $E3$ combination for this pair of transitions, which would give $I^\pi = 9^-$ or 11^- for the intermediate level at 8.636 or 8.788 MeV, cannot be definitely ruled out, given the stretched- $E2$ character of the other linking transitions, the assignment of stretched- $E2$ character to these γ rays would seem more probable. As shown in Fig. 7.3, the intermediate level is therefore tentatively assigned $I^\pi = (10^+)$.

As was discussed in Section 7.1, part of the motivation for these experiments was to obtain an accurate measurement of the transition quadrupole moment, and hence deformation, of the doubly-magic ^{60}Zn superdeformed core. Fractional Doppler shifts for the transitions in the ^{60}Zn SD band, as measured in the GS90 experiment, are shown in Fig. 7.5. This figure shows that the lifetimes of the low-spin SD states are sufficiently long to produce a significant attenuation of the nuclear recoil velocity during the decay of the band. As in the analysis of the ^{62}Zn SD band discussed in Section 6.2, the decay of the ^{60}Zn SD band was modeled assuming a constant in-band Q_t , and the side feeding into each state was modeled by a single transition with the same lifetime as the precursor in-band transition and an intensity to match the measured intensity profile of the band. The electronic stopping powers of Northcliffe and Schilling, scaled by the Ziegler and Chu stopping powers for ^4He (see Section 3.4.2), were again used to model the slowing of the recoiling nuclei in the thin target. The F curves calculated within this model for various values of Q_t are shown by solid lines in Fig. 7.5. The measured F values for the superdeformed band are best fit by $Q_t = 2.75 \pm 0.25$ eb.

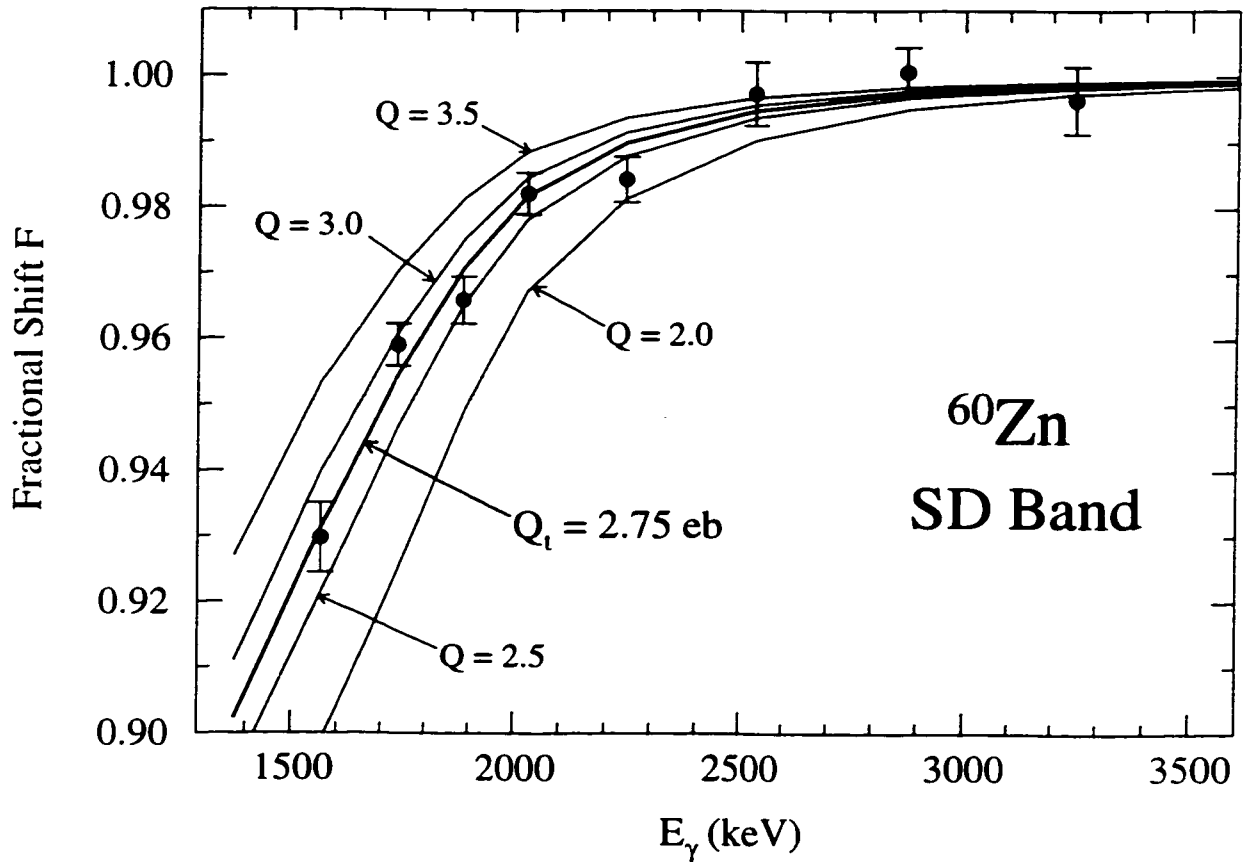


Figure 7.5: Fractional Doppler shifts F for transitions in the ^{60}Zn SD band, as measured in the GS90 experiment. Calculated F curves for various Q_t values are shown by solid lines. The measured F values are best fit by $Q_t = 2.75 \pm 0.25$ eb.

It is evident from the Doppler-shift measurements shown in Fig. 7.5 and the intensities of the transitions in the SD band given in Table 7.1 that the majority of the intensity feeding this band occurs into states which decay at the full Doppler shift $F = 1.00$. The feeding of this band is therefore very fast. As can be seen from the calculated F curves shown in Fig. 7.5, the deduced Q_t value for this band is sensitive primarily to the F measurements for the SD transitions in the plateau region of the band between $I = 22\hbar$ and $I = 12\hbar$, and it is found that any variation of the side-feeding model consistent with the full shift F values measured for the high-spin SD transitions, where the feeding occurs, has little effect on the deduced Q_t value. The

uncertainties associated with the stopping powers are, however, significant, and when combined in quadrature with the statistical uncertainty given above yield a final Q_t value of 2.75 ± 0.45 eb. Assuming an axially symmetric shape, the corresponding quadrupole deformation of the ^{60}Zn superdeformed band is $\beta_2 = 0.47 \pm 0.07$.

It should be noted that the uncertainties in the transition quadrupole moment and deformation of the ^{60}Zn SD band are dominated by the contribution from the uncertainties in the stopping powers, rather than the statistical uncertainties associated with the Doppler-shift measurements. A significant improvement in the precision of the absolute Q_t and β_2 values would therefore require a dedicated experiment to obtain an improved knowledge of the stopping powers for the particular recoil ions and target material relevant to these measurements. It is, however, important to note that the Q_t measurements for the ^{60}Zn and ^{62}Zn SD bands were performed in the same experiment, with the same target, and involved the same model for the decay of the band and the stopping powers. The relative Q_t values for these two bands, with their associated statistical uncertainties, can therefore be directly compared, independent of systematic uncertainties that have the same effect on both measurements.

7.4 Interpretation

Theoretical calculations for ^{60}Zn have been performed by Afanasjev *et al.* [Afa 98] employing both the configuration-dependent shell-correction approach with the cranked Nilsson potential and the cranked relativistic mean field (CRMF) formalism. Pairing correlations were not included in either approach and these calculations are therefore only realistic for high-spin states. The energies of favoured configurations in ^{60}Zn from the cranked Nilsson calculations are shown relative to a rigid rotor reference in Fig. 7.6(a). The doubly-magic superdeformed configuration in ^{60}Zn , corresponding to filling the single-particle energy levels up to the large SD shell gaps at $N, Z = 30$, has two holes in $f_{7/2}$ extruder orbitals and two particles in $g_{9/2}$ intruder orbitals in both the proton and neutron subsystems, the [22,22] configuration in shorthand notation. As shown in Fig. 7.6(a), this superdeformed band is calculated to become yrast at $I = 16\hbar$, and in the spin range from $I \approx 22\hbar$ to $I \approx 32\hbar$ is separated from other states by a large energy gap (the shaded region in Fig. 7.6(a)). This energy gap also appears in the CRMF calculations [Afa 98]. Combined with additional comparisons between experiment and theory discussed below, the highly favoured nature of the [22,22] configuration at high spin leaves little doubt that the observed superdeformed band in ^{60}Zn corresponds to this doubly-magic configuration. It is also worth noting that the existence of the large energy gap between this configuration and other high-spin states predicted by the calculations is supported by the very large fraction of the ^{60}Zn channel intensity observed to feed the superdeformed band in these experiments.

In Fig. 7.6(b), the experimental levels in ^{60}Zn are shown relative to the same $I(I+1)$ reference and are compared with the cranked Nilsson and CRMF calculations for the [22,22] SD configuration (normalized to the experimental 24^+ state). At high spin, where the neglect of pairing in the calculations is valid, the agreement between

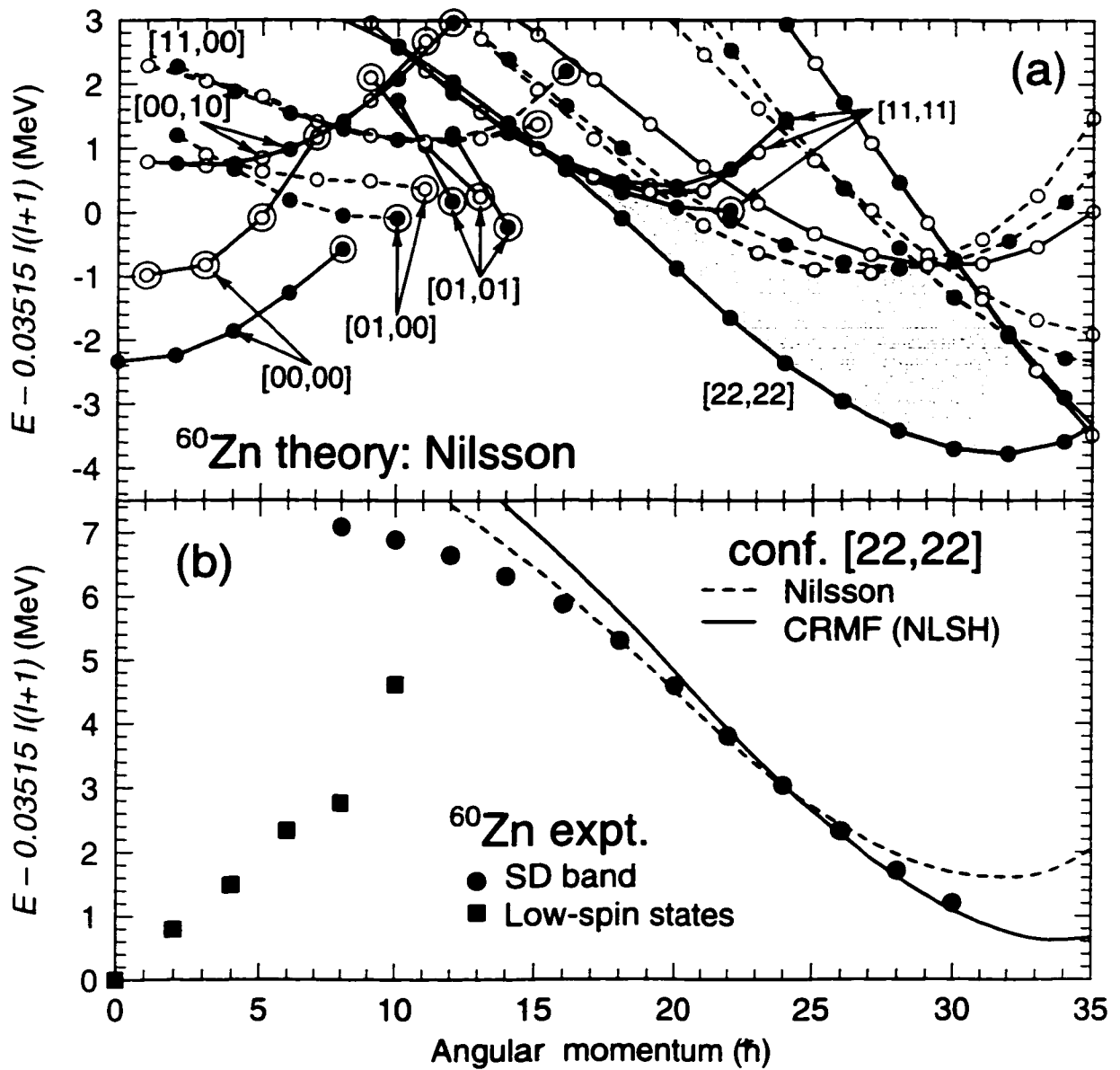


Figure 7.6: Energies of states in ^{60}Zn relative to an $I(I+1)$ reference from (a) theory and (b) experiment. In (a) solid (dashed) lines denote positive (negative) parity, filled (open) symbols are used for signature $\alpha = 0$ ($\alpha = +1$), and terminating states are shown by large open circles. The configurations are labeled by $[p_1 p_2, n_1 n_2]$ where p_1 (n_1) is the number of proton (neutron) $f_{7/2}$ holes, and p_2 (n_2) is the number of proton (neutron) $g_{9/2}$ particles. In (b) the experimental results for the superdeformed band (circles) are compared with cranked Nilsson (dashed line) and cranked relativistic mean field (solid line) calculations for the doubly-magic SD configuration [22.22]. The calculations have been normalized to the experimental energy of the 24^+ state.

theory and experiment is excellent, with the CRMF calculations providing a better description of the highest-spin states [Afa 98]. At low spin, the calculations diverge from the experimental data. As will be discussed below, this failure of the calculations to reproduce the low-spin experimental results is interpreted as an indication of the importance of pairing correlations in the low-spin SD states.

The spins and excitation energies of the unlinked normal-deformed bands identified in ^{60}Zn are not known, and these bands are therefore not shown in Fig. 7.6(b). It can, however, be noted that these bands have the same dynamic moment of inertia $\mathcal{J}^{(2)} \approx 9 \hbar^2/\text{MeV}$ and, to a high degree of accuracy, the transition energies in one band are the averages of consecutive transition energies in the other band. These are the properties expected for a pair of degenerate signature-partner bands (see Section 2.3.3). Based on coincidences with the transitions in the ^{60}Zn ground-state band, the lowest observed states of these ND bands are estimated to have spins in the range $I \approx 8-10 \hbar$. With these estimated spins, the shapes of the energy curves for these bands are in good agreement with the calculations for the [11,11] configuration shown in Fig. 7.6(a), and this configuration, with single proton and neutron holes in the high- Ω extruder orbital from the $f_{7/2}$ shell, is expected to lead to signature-degenerate rotational bands. One might initially expect that the signature-partner bands of this configuration would be connected by strong $M1$ cross-over transitions, as observed for the ND bands in ^{62}Zn with similar single-particle configurations (see Chapter 5). However, ^{60}Zn is an $N = Z$ nucleus, in which isospin-conserving ($\Delta T = 0$) $M1$ transitions are expected to be strongly suppressed [War 69]. The absence of any evidence for such $M1$ transitions connecting ND bands 1 and 2 in ^{60}Zn is therefore not an argument against the proposed configuration. The properties of these ND bands are therefore consistent with an assignment to signature partners of the [11,11] configu-

ration. However, without definite spin, parity, and excitation energy measurements, this assignment must be considered tentative.

The decreasing collectivity in $A \sim 60$ superdeformed bands, associated with the limited spin content of their single-particle configurations, was discussed in Section 6.3 in the context of the superdeformed band identified in ^{62}Zn . This feature of $A \sim 60$ superdeformation is even more important for the doubly-magic superdeformed band in ^{60}Zn , which is observed to within three transitions of the maximum spin $I_{\text{max}} = 36 \hbar$ available from the orbitals occupied in the $[22,22]$ configuration at low spin. The predicted decrease in collectivity in this band is reflected in the calculated transition quadrupole moments, which decrease from 3.05 eb at $I = 8 \hbar$ to 2.06 eb at $I = 30 \hbar$ in the Nilsson-Strutinsky calculations. Unfortunately, the uncertainties in the Doppler-shift measurements for the high-energy transitions at the top of the ^{60}Zn SD band were too large to test this predicted spin dependence of the transition quadrupole moment. As was noted in Section 7.3, the experimental Q_t value for the SD band in ^{60}Zn is determined almost entirely by transitions in the spin range $I = 12\text{--}22 \hbar$. The measured Q_t of 2.75 ± 0.45 eb may be regarded as an average value for the band over this range, and it can be noted that this mean value is in good agreement with the calculated Q_t values for the $[22,22]$ SD configuration, which decrease from 2.97 eb at $I = 12 \hbar$ to 2.54 eb at $I = 22 \hbar$.

Although the predicted decrease in collectivity in the ^{60}Zn SD band could not be directly tested with lifetime measurements, the high energy cost of building high angular momentum states in this band is predicted to result in a dynamic moment of inertia $\mathcal{J}^{(2)}$ that decreases with rotational frequency, and falls well below the kinematic moment of inertia $\mathcal{J}^{(1)}$ at high spin. In the case of the ^{60}Zn superdeformed band, the spins of the SD states have been established experimentally. The kinematic,

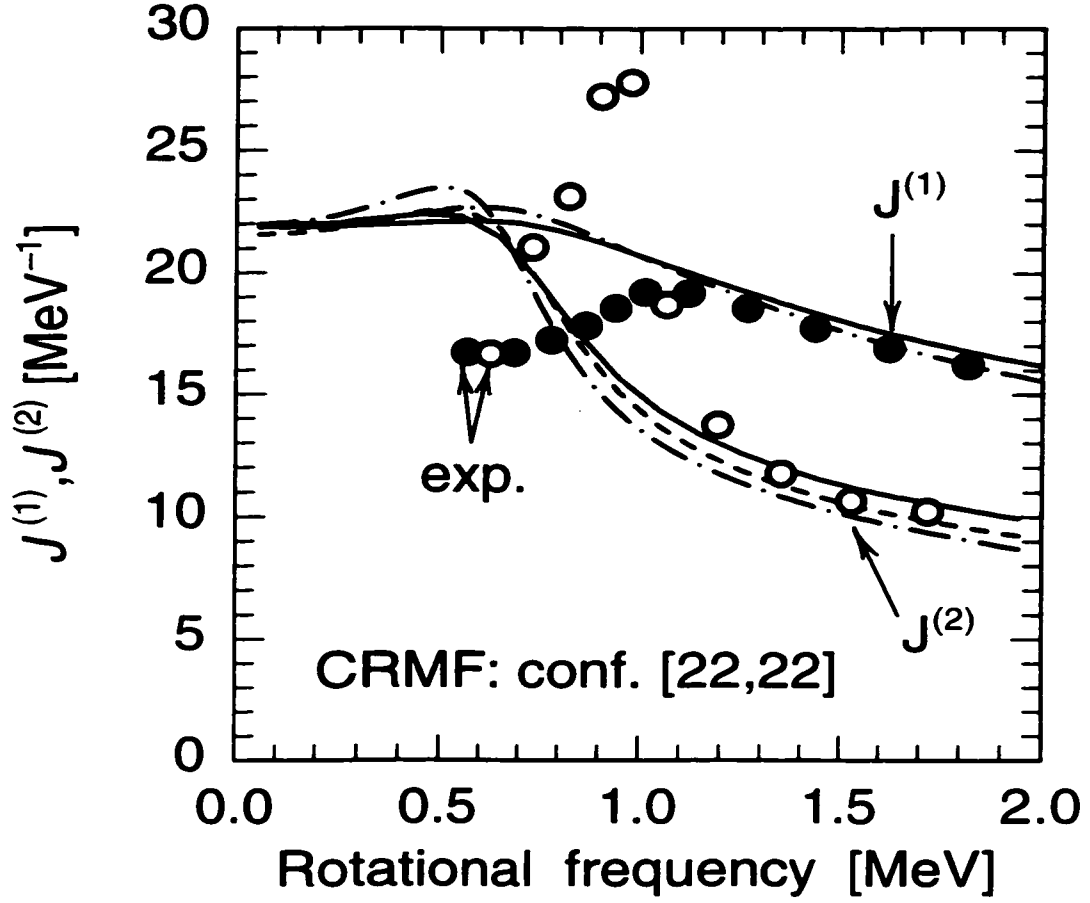


Figure 7.7: Comparison of the experimental $\mathcal{J}^{(2)}$ values (open circles) and $\mathcal{J}^{(1)}$ values (solid circles) for the SD band in ^{60}Zn with the results of cranked relativistic mean field calculations for the doubly-magic [22,22] superdeformed configuration. Different line types are used for different parametrizations of the RMF; NL1 (solid), NL3 (dashed), and NLSH (dot-dashed). From [Afa 98].

as well as the dynamic, moment of inertia is therefore determined and this prediction can be directly tested. The experimental $\mathcal{J}^{(1)}$ and $\mathcal{J}^{(2)}$ values for the ^{60}Zn SD band are shown in Fig. 7.7. At high-spin, the $\mathcal{J}^{(2)}$ values do indeed decrease with rotational frequency and lie well below the $\mathcal{J}^{(1)}$ values. The moments of inertia for the doubly-magic [22,22] configuration from the CRMf calculations are also shown in this figure, and it can be seen that at high rotational frequency the agreement between these calculations and the experimental results is excellent.

Although the unpaired calculations are able to reproduce the experimental $\mathcal{J}^{(1)}$ and $\mathcal{J}^{(2)}$ values at high rotational frequency, Fig. 7.7 shows that these calculations do not provide an adequate description of the low-spin properties of the superdeformed band. As mentioned above, this divergence of the experimental results and the calculations is interpreted as an indication of pairing correlations in the low-spin SD states. In particular, the strong upbend in the experimental $\mathcal{J}^{(2)}$ values seen in Fig. 7.7 is interpreted as a manifestation of the alignment of the $g_{9/2}$ neutrons and protons. In the 0^+ superdeformed ground state, the two $g_{9/2}$ protons and the two $g_{9/2}$ neutrons would each be paired to spin 0. At high rotational frequency, however, these pairs are broken by the Coriolis interaction and the high- j , low- Ω , $g_{9/2}$ particles are aligned with the rotation axis, the alignment process producing the characteristic upbends in the moments of inertia apparent in Fig. 7.7 (see Section 2.4.2).

It was noted in Section 7.1 that the observation of the doubly-magic superdeformed band in the $N = Z$ nucleus ^{60}Zn would provide an ideal case for investigating the role of $T = 0$ neutron-proton pairing at high rotational frequency. In particular, Sheikh *et al.* [She 90] have investigated the alignment of $g_{9/2}$ protons and neutrons in the presence of residual neutron-proton interactions and found that, for $N = Z$ systems, a finite n - p interaction shifts the simultaneous alignment of all four neutrons and protons to lower rotational frequency than would occur for the individual two-quasiparticle alignments. However, these calculations focused on the idealized case of isolated $g_{9/2}$ particles in a spherical system, where the alignment frequencies are sharp; although it was noted that the mixing of the paired and aligned bands in a deformed system would spread the alignment over a range of rotational frequencies, as observed in the ^{60}Zn SD band. At present, no detailed calculations for ^{60}Zn that include pairing correlations are available for direct comparison with the experimental

results presented here. It is, however, hoped that the observation of the doubly-magic superdeformed band in this $N = Z$ nucleus will motivate such theoretical studies in the near future. As discussed in the following section, pairing may also play a crucial role in explaining the observed decay-out properties of the ^{60}Zn superdeformed band.

7.5 Decay Out of the ^{60}Zn SD Band

The decay out of superdeformed bands was briefly discussed in Section 1.3.3. Because of the potential energy barrier separating the superdeformed and normal-deformed states (see Fig. 1.9), the superdeformed band does not decay out immediately after crossing the ND yrast line. Rather, the decay continues within the SD band until it is highly excited relative to the ND yrast line and the SD states are surrounded by a high density of ND levels. In what may be referred to as the standard model of the decay out of high-spin superdeformed bands [Vig 90a, Vig 90b, Shi 93], the weak mixing of SD states and nearby ND levels associated with a small, but finite, barrier penetration probability introduces a small normal-deformed component into the superdeformed wavefunction, through which the SD band decays to ND states. The highly excited ND states with which the SD levels mix are similar to the compound nuclear states formed in neutron capture reactions and, like the γ decay following such reactions, the depopulation of the superdeformed band is characterized by a highly-fragmented statistical decay dominated by $E1$ transitions. It is because of this fragmentation of the decay-out intensity that discrete linking transitions have not been identified for the vast majority of the more than 150 [Sin 96] superdeformed bands now known.

As was noted in Section 1.3.3, discrete linking transitions have recently been identified for superdeformed bands in ^{194}Hg [Kho 96, Hac 97] and ^{194}Pb [Lop 96a, Hau 97]. These observations, combined with lifetime measurements for low-spin SD

states [Krü 94, Krü 97] and detailed statistical studies of the decay-out γ -ray quasi-continuum [Hen 94, Lop 96b, Lau 97], have provided a consistent description of the decay out of $A \sim 190$ SD bands based on the weak-mixing statistical model mentioned above. This progress in understanding the decay out of superdeformed bands has, however, been largely concentrated in a single mass region, and the applicability of these results to other regions of superdeformation remains an open question. The observation of linking transitions for the doubly-magic SD band in ^{60}Zn provides an opportunity to investigate the decay out of superdeformed bands in a new mass region. As will be discussed below, the decay out of the ^{60}Zn SD band shares some similarities with that observed in the $A \sim 190$ region, but also differs in many ways and, in general, does not appear to be well described by the statistical decay-out model that has proved so successful for superdeformed bands in the mercury region.

As shown in Fig. 7.3, the superdeformed band in ^{60}Zn is observed down to its 8^+ state, which lies 4.329 MeV above the yrast 8^+ level. The decay out of this band occurs over the lowest three observed SD states, and the identified linking transitions have energies in the 3–6 MeV range. These numbers are very similar to those for the yrast superdeformed band in ^{194}Hg [Kho 96, Hac 97], which is also observed to its 8^+ state, lying 4.281 MeV above the yrast spin 8 level, and decays out over the last three observed states with identified linking transitions in the 3–5 MeV range. They are also comparable to the observations for the yrast SD band of ^{194}Pb [Lop 96a, Hau 97], in which the 6^+ SD state lies 2.742 MeV above the yrast 6^+ level, and ~ 2 –3 MeV decay-out transitions from the lowest three observed SD states have been identified. It can be noted from Table 7.1 that the 4 observed primary decay-out transitions for the ^{60}Zn SD band account for only $37 \pm 3\%$ of the decay-out intensity. The corresponding numbers are $\sim 5\%$ of the intensity in 5 linking transitions for the

yrast SD band in ^{194}Hg , and 21% of the intensity in 12 linking transitions for the yrast SD band in ^{194}Pb . Although fluctuations in the intensity carried by single-step linking transitions are expected within the statistical decay model (see [Lau 97], for example), the somewhat greater intensity of the linking transitions identified in ^{60}Zn compared to the two cases in the $A \sim 190$ mass region may also simply result from the lower level density (at the same spin and excitation energy) in the $A \sim 60$ mass region. Despite this greater intensity of the observed linking transitions, it should be noted that the majority (63%) of the decay-out intensity from the ^{60}Zn SD band was not identified, implying a fragmentation of this intensity into a large number of weak decay pathways. From the intensities of the γ rays in the ^{60}Zn ground-state band in coincidence with gates set on the SD band (see Fig. 7.2(a)), it can also be noted that much of this unobserved decay-out intensity bypasses the yrast 8^+ and 6^+ states and feeds into the ground band at the 4^+ and 2^+ levels, implying multi-step decay pathways. This fragmentation of the decay-out intensity over a large number of weak multi-step pathways, with a few high-energy single-step linking transitions, is characteristic of the statistical decay-out process observed for superdeformed bands in the $A \sim 190$ mass region (see [Lop 96b], for example).

Based on the above comparisons, it would initially seem plausible that a relatively trivial modification of the statistical decay-out model used in the $A \sim 190$ mass region, to account for the lower level density in the $A \sim 60$ region, would also provide a successful description of the observed decay-out properties for the ^{60}Zn SD band. However, one striking difference between these mass regions is that the observed linking transitions for the ^{60}Zn SD band are assigned stretched- $E2$ character, whereas the decay out of the $A \sim 190$ SD bands is dominated by the $E1$ transitions expected in a statistical decay process. Although stretched- $E2$ decay directly to the

yrast line is energetically favoured, low-lying negative parity states (not observed in these experiments) to which the SD band could decay by $E1$ transitions are expected in ^{60}Zn (see Fig. 7.6(a)), and such $E1$ transitions would be expected to compete favourably in a statistical decay process. It should be noted that ^{60}Zn is an $N = Z$ nucleus, in which isoscalar $T = 0 \rightarrow T = 0$ $E1$ transitions are forbidden by isospin selection rules [War 69]. However, there is strong evidence for an intense $5^- \rightarrow 4^+$ $E1$ transition in the neighbouring even-even $N = Z$ nucleus ^{64}Ge , which suggests that the degree of isospin mixing in $A \sim 60$ $N = Z$ nuclei effectively removes this selection rule [Enn 91]. It therefore seems unlikely that isospin suppression of dipole transitions can explain the failure to observe $E1$ decay out of the ^{60}Zn SD band.

It is worth noting that stretched- $E2$ decay out of highly-deformed rotational bands has been observed in a number of $A \sim 130$ Nd nuclei [Baz 94, Lun 95, Del 95, Pet 96]. However, in these nuclei the “highly-deformed” ($\beta_2 \sim 0.30\text{--}0.35$) bands and the “normally-deformed” ($\beta_2 \sim 0.20\text{--}0.25$) bands to which they decay have similar deformations, and both theoretical calculations and the experimental observations suggest that no well-defined barrier exists between these shapes at the decay-out point. The highly-deformed and normally-deformed bands thus mix substantially and the decay out of the highly-deformed band occurs when it lies close to the yrast line, often via decay-out transitions with energies similar to, and in some cases even lower than, the in-band transitions. In ^{60}Zn , the deformation change between the superdeformed band and the near-spherical states to which it decays is larger, and the observation of the SD band to 4.329 MeV above the yrast line suggests a substantial barrier between the ND and SD minima, as in the $A \sim 190$ superdeformed bands.

Additional information about the decay-out process can be obtained from estimates of the decay-out transition strengths. In the weak-mixing model discussed

above, these decay-out strengths should be strongly suppressed, independent of multipolarity, by the barrier separating the ND and SD wells, and such hindered decay-out transitions are in fact observed for the $A \sim 190$ SD bands. In ^{194}Pb , for example, the decay-out $B(E1)$'s are of order 10^{-8} W.u. and upper limits of $\sim 10^{-6}$ W.u. and $\sim 10^{-4}$ W.u. (before correcting for the small ND/SD mixing amplitudes) have been set on the decay-out $B(M1)$ and $B(E2)$ values [Krü 97]. Assuming that the average in-band Q_t of 2.75 ± 0.45 eb measured for the ^{60}Zn SD band in the spin range $I = 12\text{--}22 \hbar$ remains constant[†] during the decay-out process, the measured in-band to decay-out branching ratios in ^{60}Zn (see Table 7.1) give $B(E2)$'s of 0.8 ± 0.2 W.u. and 0.04 ± 0.02 W.u. for the 3656 keV and 5464 keV linking transitions, respectively. Further assuming a γ -ray energy of 900 keV and the upper limit of $\sim 4\%$ of the SD band intensity for the unobserved $8^+ \rightarrow 6^+$ SD transitions gives a lower limit of ~ 0.01 W.u. for the $B(E2)$ of the 5810 keV linking transition. If the tentative stretched- $E2$ assignments are adopted for the 3496 and 3344 keV linking transitions, a decay-out $B(E2)$ of 0.2 ± 0.1 W.u. is obtained for either order of these transitions. It should be noted that these decay-out $B(E2)$ values are 2–4 orders of magnitude larger than the abovementioned upper limit set on the ^{194}Pb decay-out $B(E2)$'s, and are particularly difficult to reconcile with the weak-mixing statistical decay-out model.

A possible explanation for the relatively large decay-out transition strengths for the ^{60}Zn band may involve the onset of pairing correlations in the low-spin SD states. The important role of pairing correlations in mediating the decay-out of superdeformed bands in heavier nuclei has been pointed out by a number of authors

[†]As noted in Section 7.4, the calculations for ^{60}Zn predict that the in-band Q_t increases with decreasing spin. However, even for the lowest observed SD state, the calculated Q_t of 3.05 eb is within the uncertainty on the measured average value, and assuming a larger in-band Q_t would only increase the deduced decay-out $B(E2)$ values and would not affect the conclusions drawn in this section. It is also worth noting that the assumption of a constant in-band Q_t during the decay-out process has been experimentally confirmed in the case of the ^{194}Pb SD band [Krü 97].

[Bon 90, Shi 92, Shi 93, Ber 94], and it is clear from the alignment observed in the ^{60}Zn SD band (see Section 7.4) that pairing is significant in the low-spin states of this band. Furthermore, it should be noted that the single-particle configurations of the ground-state band and doubly-magic superdeformed band in ^{60}Zn differ only by the movement of a pair of protons and a pair of neutrons from $f_{7/2}$ to $g_{9/2}$ orbitals. The mixing of these configurations in the presence of pairing correlations is therefore expected to be even more significant than in the $A \sim 150$ and $A \sim 190$ mass regions, where the ND and SD configurations differ by the rearrangement of on the order of 10 pairs of nucleons. As was noted in Section 7.4, no theoretical calculations that include pairing correlations are presently available for ^{60}Zn , and it is therefore not clear at this time whether such pairing-mediated mixing can account for the relatively large decay-out $B(E2)$ values observed for the ^{60}Zn SD band. It is, however, hoped that the experimental results discussed here will motivate such theoretical studies, as they will undoubtedly lead to a more complete understanding of both superdeformation in light nuclei such as ^{60}Zn and the decay out of superdeformed bands in general.

7.6 Summary

The doubly-magic superdeformed band in the $N = Z$ nucleus ^{60}Zn has been identified. The observed band consists of a cascade of 11 γ rays with a mean transition quadrupole moment $Q_t = 2.75 \pm 0.45$ eb, corresponding to a deformation $\beta_2 = 0.47 \pm 0.07$ for an axially symmetric shape. While the high-spin properties of this band are in excellent agreement with unpaired Nilsson-Strutinsky and cranked relativistic mean field calculations, an upbend in the dynamic moment of inertia at low rotational frequency is interpreted as a result of the alignment of $g_{9/2}$ protons and neutrons and provides a clear indication of the importance of pairing correlations in the low-spin states of this superdeformed band.

Linking transitions connecting the ^{60}Zn SD band to the yrast line have been identified. These transitions establish the spins, parity, and excitation energies of the SD states from the $I^\pi = 8^+$ SD state at 9.621 MeV to the $I^\pi = 30^+$ SD state at an excitation energy of 33.90 MeV. These results represent the first definite quantum number assignments for any superdeformed band below the $A \sim 190$ mass region. Although the observation of this superdeformed band to 4.329 MeV above the yrast line suggests a substantial barrier between the SD and ND minima, the stretched- $E2$ character and relatively large $B(E2)$ values of the decay-out transitions are difficult to reconcile with the weak-mixing statistical decay-out model that successfully describes the decay-out properties observed for SD bands in the $A \sim 190$ mass region. It is possible that pairing correlations play an important role in mediating the decay out of the ^{60}Zn superdeformed band. A detailed test of this hypothesis, however, requires paired calculations. It is hoped that these first experimental results on the decay out of the doubly-magic superdeformed band in ^{60}Zn will motivate such theoretical studies in the near future.

Chapter 8

Conclusions and Future Prospects

8.1 Summary

The recent coupling of large γ -ray spectrometers and 4π charged-particle detector arrays, and the development of the total energy channel selection technique discussed in Chapter 4, have provided an opportunity to perform detailed high-spin spectroscopic studies of proton-rich ($N \approx Z$) nuclei in the $A \sim 60$ mass region. The results of such investigations of ^{62}Zn and the $N = Z$ nucleus ^{60}Zn presented in this thesis have revealed that nuclei in this mass region exhibit a rich pattern of nuclear structure phenomena with increasing angular momentum; from noncollective spherical shell model states, to well-deformed collective rotational bands, to fully-aligned noncollective terminating states, to highly-collective superdeformed bands.

High-spin states in ^{62}Zn were studied via the $^{40}\text{Ca}(^{28}\text{Si}, \alpha 2p)^{62}\text{Zn}$ reaction in experiments conducted with the 8π Spectrometer and the Miniball charged-particle detector array, and with the Gammasphere array and the Microball charged-particle detector. These experiments led to the identification of two sets of strongly coupled rotational bands in ^{62}Zn . Based on comparisons with configuration-dependent cranked Nilsson-Strutinsky calculations, these bands were interpreted as being built on a proton particle-hole excitation across the $Z = 28$ spherical shell gap from the $f_{7/2}$

to the $g_{9/2}$ orbital, and were assigned the [11,01] and [11,02] single-particle configurations (in the shorthand notation introduced in Section 5.4). With these configuration assignments, and firm spin assignments for the bands established by the identification of transitions linking them to the rest of the ^{62}Zn decay scheme, it was concluded that these bands were observed up to their respective terminating states at $I^\pi = 21^+$ and $I^\pi = 24^-$. Lifetime measurements for these bands were possible all the way to the terminating states, and these measurements revealed transition quadrupole moments that decrease as termination is approached [Sve 98a]. Together with concurrent lifetime measurements for terminating bands in ^{108}Sn and ^{109}Sb [Wad 98], these results represent the first experimental confirmation of the predicted loss of collectivity associated with the smooth termination of rotational bands.

The first superdeformed band in the $A \sim 60$ mass region was also identified in ^{62}Zn . The observed band consists of a cascade of six γ rays covering an estimated spin range from $I = 18\hbar$ to $I = 30\hbar$. The high collectivity and large deformation of this band were confirmed by thin-target Doppler-shift attenuation lifetime measurements. Assuming an axially symmetric shape, the measured transition quadrupole moment of $Q_t = 2.7_{-0.5}^{+0.7} \text{ eb}$ for this band corresponds to a quadrupole deformation $\beta_2 = 0.45_{-0.07}^{+0.10}$. Although a candidate for a primary decay-out transition at 3656 keV was identified, this band could not be linked conclusively into the remainder of the ^{62}Zn decay scheme. The spins, parity, and excitation energies of the SD states were therefore not determined, and a definite configuration assignment was not possible. Comparison of the dynamic moment of inertia of this band with the results of cranked relativistic mean field and cranked Hartree-Fock calculations favour an assignment to the [22,24] SD configuration, although the [22,23] SD configurations cannot be ruled out at this time. These results confirm the longstanding prediction of high-spin superdeformation

in the proton-rich $A \sim 60$ mass region, and establish a new region for the study of superdeformation in light nuclei with proton and neutron numbers $N, Z \approx 30$.

High-spin states in the $N = Z$ nucleus ^{60}Zn were populated and studied via the $^{40}\text{Ca}(^{28}\text{Si}, 2\alpha)^{60}\text{Zn}$ and $^{40}\text{Ca}(^{32}\text{S}, 3\alpha)^{60}\text{Zn}$ reactions in two experiments with Gammasphere and the Microball charged-particle detector array. In addition to two normally-deformed rotational bands, tentatively assigned as signature partners of the $[11,11]$ configuration, the doubly-magic superdeformed band in ^{60}Zn was identified in these experiments. The observation of this superdeformed band, with the $[22,22]$ configuration corresponding to filling the single-particle energy levels up to the large SD shell gaps at $N, Z = 30$, establishes the natural reference core for the study of $A \sim 60$ superdeformation. The mean transition quadrupole moment $Q_t = 2.75 \pm 0.45$ eb measured for this band in the $I = 12\text{--}22 \hbar$ spin range corresponds to a quadrupole deformation $\beta_2 = 0.47 \pm 0.07$ for an axially symmetric shape. High-energy ($\sim 3\text{--}6$ MeV) linking transitions connecting this superdeformed band to the yrast line were identified. These transitions enabled the spins, parity, and excitation energies of the SD states to be established from the $I^\pi = 8^+$ SD level at 9.621 MeV to the $I^\pi = 30^+$ SD state at an excitation energy of 33.90 MeV, the first time such information has become available for any superdeformed band below the $A \sim 190$ mass region. Although the observation of the ^{60}Zn SD band to 4.329 MeV above the yrast line suggests a substantial barrier between the SD and ND minima, and the failure to identify the majority ($\sim 63\%$) of the decay-out intensity implies a fragmentation of this intensity into a large number of weak multi-step decay pathways, the stretched- $E2$ character and relatively large ($\sim 0.01\text{--}1$ W.u.) $B(E2)$'s of the observed decay-out transitions are difficult to reconcile with the weak-mixing statistical decay-out model that successfully describes the decay-out properties observed in the $A \sim 190$ mass region.

These decay-out properties in ^{60}Zn are not well understood at present, although it is possible that significant pairing correlations in the low-spin SD states play an important role in mediating the decay out of this superdeformed band.

8.2 Future Research

The results presented in this thesis suggest several directions for future research into the high-spin structure of proton-rich $A \sim 60$ nuclei. A few of these are briefly discussed in this section.

Because of the limited spin content of the single-particle configurations in $A \sim 60$ nuclei, band termination should be a common feature in this mass region. Although the lifetime measurements for the terminating bands in ^{62}Zn provide clear evidence for decreasing transition quadrupole moments, and hence decreasing collectivity, these measurements are subject to uncertainties associated with the exact nature of the unobserved side feeding of these bands, as discussed in Section 5.4. Lifetime measurements for other terminating bands in this mass region would therefore be highly desirable in order to reduce the sensitivity of these results to the detailed feeding structure of any particular band and to obtain a more systematic understanding of the gradual loss of collectivity in these rotational structures. A particularly promising case for such measurements is the terminating band in ^{64}Zn studied by Galindo-Uribarri *et al.* [Gal 98] with the 8π Spectrometer and the Miniball array. This band was also populated at high-spin and with significant cross section via the $^{40}\text{Ca}(^{28}\text{Si}, 4p)^{64}\text{Zn}$ reaction in the GS90 experiment discussed in this thesis. The higher sensitivity of the Gammasphere plus Microball data should enable lifetime measurements up to, or close to, the terminating state of this band, and the detailed analysis of these data, which are already in hand, will definitely be worthwhile.

The study of superdeformation in the $A \sim 60$ mass region has only just begun. In addition to the superdeformed bands in ^{62}Zn and ^{60}Zn discussed in this thesis, SD bands have also recently been identified in ^{61}Zn and ^{65}Zn [Yu 98] (see also Fig. 1 in [Sve 98d]). However, no excited superdeformed bands have yet been observed in this mass region and linking transitions have only been identified for the doubly-magic SD band in ^{60}Zn . As was noted in Section 6.3, the $[22,24]$ SD configuration in ^{62}Zn , tentatively assigned to the observed SD band based on its dynamic moment of inertia, is not calculated to be the yrast SD configuration in either the cranked Nilsson-Strutinsky or the cranked relativistic mean field calculations performed by Afanasjev *et al.* [Afa 98]. In order to determine the correct ordering and spacing of the single-particle energy levels in the vicinity of the $N, Z = 30$ SD shell gaps, and to refine the mean field parametrizations used in this mass region, it would be highly desirable to identify excited SD bands in this region and establish linking transitions for bands with particles outside the ^{60}Zn SD core. Because of the substantial cross section with which it can be populated, and the relatively large number of SD bands calculated to lie close to the yrast line at high spin (see Section 6.3), ^{62}Zn is a particularly promising case for such studies. Although only one SD band in ^{62}Zn was identified in the GS90 experiment discussed in this thesis, the number of unpacked γ - γ - γ coincidences for ^{62}Zn could easily be quadrupled by simply repeating this experiment with Gammasphere's full complement of 110 HPGe detectors, rather than the 83 detectors used in the GS90 experiment. Such a data set would, of course, provide a higher sensitivity to weakly-populated superdeformed bands in this nucleus.

The identification of the doubly-magic superdeformed band in ^{60}Zn provides a number of exciting opportunities for nuclear structure research. As was noted in Chapter 7, this is the only superdeformed band below the $A \sim 190$ mass region that

has been linked to the remainder of the decay scheme, it is the only SD band in the $A \sim 60$ mass region likely to be observed to low enough rotational frequency that pairing correlations become significant, and this doubly-magic superdeformed band is observed to be populated with an unprecedented fraction of the channel intensity in the reactions employed during this work. Of particular interest will be further studies of the feeding and decay of this unique superdeformed band. Firstly, statistical analyses of the γ -ray quasi-continuum from the decay out of the superdeformed band may provide a direct probe of the pairing strength [Dø85b]. Secondly, because intense decay-out transitions have been identified for this band, gates can be set on these linking transitions in order to eliminate the decay-out quasi-continuum in the γ -ray spectrum and isolate the continuum of statistical transitions that feed the superdeformed band. It would be particularly interesting to investigate whether this statistical feeding spectrum can be used to experimentally determine the energy gap separating the doubly-magic superdeformed band from other states at high spin, as it can be hypothesized that this spectrum will have a low-energy cut-off resulting from the absence of states in this gap. Finally, the ^{60}Zn SD band provides an ideal opportunity to investigate deformation effects during the particle-evaporation process at very high spin. Assuming that thermal shape fluctuations do not completely wash out the correlation between the nuclear symmetry and rotation axes at high excitation energy, the lower Coulomb barrier at the tips of a prolate nucleus should favour charged-particle emission along the long axis, particularly for low-energy alpha particles, which are most strongly influenced by the Coulomb barrier. The result of such preferential emission would be an alpha-particle angular distribution that peaks more strongly in the plane perpendicular to the nuclear spin axis than would otherwise be expected, and evidence for this effect has indeed been observed in the

channel-averaged alpha-particle spectra from the decay of heavy compound systems [Maj 87, Nic 90]. In order to perform a more sensitive investigation of this effect one would desire a nucleus that can be populated at high-spin via an alpha-particle evaporation channel, in which a large fraction of the channel intensity feeds a highly-deformed structure, and in which the γ -ray emission is dominated by stretched- $E2$ transitions so that the nuclear spin axis can be deduced on an event-by-event basis from the angular distribution of the γ rays [Hon 87]. This very demanding set of criteria is particularly well satisfied by ^{60}Zn . Because of the very large fraction of the ^{60}Zn channel intensity feeding the doubly-magic superdeformed band, and the ability to select this pure charged-particle channel very cleanly (see Section 7.2), all of the above investigations can be performed with an excellent peak-to-background ratio in the γ -ray data. These studies will therefore be limited only by the statistics for the weak ^{60}Zn channel. Although long experiments will be required to collect the necessary statistics with the present generation of γ -ray and charged-particle detector arrays, the many exciting opportunities offered by the doubly-magic superdeformed band in ^{60}Zn certainly make such experiments worthwhile.

While, in the author's opinion, the results presented in this thesis represent a good beginning to the study of high-spin nuclear structure phenomena in proton-rich $A \sim 60$ nuclei, there is clearly much exciting research to be done in this mass region.

Appendix A

Electromagnetic Transitions

The electromagnetic decay of an excited nuclear state is characterized by a transition probability T , which is the reciprocal of the mean lifetime τ of the state and is proportional to the square of the matrix element of the electromagnetic interaction operator H_{int}^{EM} between the initial $|i\rangle$ and final $|f\rangle$ nuclear states,

$$T \propto |\langle f | H_{int}^{EM} | i \rangle|^2. \quad (\text{A.1})$$

As is usual in electromagnetic theory, H_{int}^{EM} is expanded in a series of multipole operators $\mathcal{M}_{\sigma\lambda\mu}$, where $\sigma = E(M)$ for electric (magnetic) transitions, $\lambda = 0, 1, 2, \dots$ is the angular momentum associated with monopole, dipole, quadrupole, \dots transitions, and $\mu = -\lambda, -\lambda+1, \dots, \lambda$ is the projection of this angular momentum on the chosen quantization axis. Conservation of angular momentum and parity enforces a number of selection rules on the multipole operators that can contribute to a transition between a given initial $|I_i m_i \pi_i\rangle$ and final $|I_f m_f \pi_f\rangle$ nuclear state:

$$|I_i - I_f| \leq \lambda \leq I_i + I_f, \quad (\text{A.2})$$

$$m_f - m_i = \mu, \quad (\text{A.3})$$

$$\pi_i \pi_f = (-1)^\lambda \quad (\text{electric}), \quad \pi_i \pi_f = (-1)^{\lambda+1} \quad (\text{magnetic}). \quad (\text{A.4})$$

In the special case $I_i - I_f = \lambda$ the transition is said to be “stretched”. It should also be noted that, because of the intrinsic spin 1 of the photon, there are no $\lambda = 0$ γ -ray transitions. Electromagnetic monopole transitions such as $0^+ \rightarrow 0^+$ can, however, proceed by the emission of an atomic electron in an internal conversion process. Internal conversion also contributes to higher multipolarity transitions and can, in fact, dominate γ -ray emission for low-energy transitions in heavy nuclei. However, for the relatively high transition energies and relatively light nuclei which are the focus of this thesis, internal conversion is generally negligible and thus the remainder of this discussion will focus on γ -ray transitions.

In many situations, the orientation of the initial and final nuclear angular momenta are not observed and it is useful to define a reduced matrix element $B(\sigma\lambda)$ by summing over all final orientations and averaging over all initial orientations:

$$B(\sigma\lambda; I_i \rightarrow I_f) = \frac{1}{2I_i + 1} \sum_{m_i, m_f} |\langle I_f m_f | \mathcal{M}_{\sigma\lambda(m_f - m_i)} | I_i m_i \rangle|^2. \quad (\text{A.5})$$

The transition probability for radiation of type $\sigma\lambda$ is then given by

$$T(\sigma\lambda; I_i \rightarrow I_f) = \frac{8\pi(\lambda + 1)}{\hbar\lambda[(2\lambda + 1)!!]^2} \left(\frac{E_\gamma}{\hbar c} \right)^{2\lambda+1} B(\sigma\lambda; I_i \rightarrow I_f). \quad (\text{A.6})$$

The $B(\sigma\lambda)$ values contain all of the information about the nuclear wavefunctions, and to evaluate these matrix elements a knowledge of these wavefunctions is thus clearly required. However, by assuming that the transition involves a single nucleon and by making a number of simplifying assumptions about the single-particle wavefunctions and magnetic moments (see [Wei 51]) crude estimates for single-particle transition strengths can be readily obtained:

$$B(E\lambda) = \frac{e^2}{4\pi} \left(\frac{3}{\lambda + 3} \right)^2 R_0^{2\lambda}, \quad (\text{A.7})$$

$$B(M\lambda) = \frac{10}{\pi} \left(\frac{3}{\lambda + 3} \right)^2 \mu_N^2 R_0^{2(\lambda-1)}, \quad (\text{A.8})$$

λ	$B(E\lambda)$	$T(E\lambda)$	$B(M\lambda)$	$T(M\lambda)$
1	$6.446 \times 10^{-2} A^{2/3}$	$1.023 \times 10^{14} A^{2/3} E^3$	1.790	$3.184 \times 10^{13} E^3$
2	$5.940 \times 10^{-2} A^{4/3}$	$7.265 \times 10^7 A^{4/3} E^5$	$1.650 A^{2/3}$	$2.262 \times 10^7 A^{2/3} E^5$
3	$5.940 \times 10^{-2} A^2$	$3.385 \times 10^1 A^2 E^7$	$1.650 A^{4/3}$	$1.054 \times 10^1 A^{4/3} E^7$
4	$6.285 \times 10^{-2} A^{8/3}$	$1.065 \times 10^{-5} A^{8/3} E^9$	$1.746 A^2$	$3.316 \times 10^{-6} A^2 E^9$

Table A.1: Weisskopf estimates of $B(\sigma\lambda)$ and $T(\sigma\lambda)$. $B(E\lambda)$ values are in units of $e^2\text{fm}^{2\lambda}$, $B(M\lambda)$ in $\mu_N^2\text{fm}^{2(\lambda-1)}$, $T(\sigma\lambda)$ in s^{-1} , and E_γ in MeV. Adapted from [RS 80].

where R_0 is the nuclear radius and μ_N is the nuclear magneton. Although actual transitions may be either strongly enhanced or suppressed relative to these estimates depending on the initial and final nuclear wavefunctions involved, these single-particle, or Weisskopf, estimates do provide a convenient scale by which to measure transition rates. For reference their numerical values are summarized in Table A.1.

Two important observations can be made from the Weisskopf estimates. Firstly, for a given multipolarity, $T(E\lambda)/T(M\lambda) = 3.212A^{2/3}$ so that electric transitions are estimated to be as much as two orders of magnitude faster in heavy and intermediate-mass nuclei than magnetic transitions of the same multipolarity. Secondly, for either electric or magnetic transitions, an increase in λ by 1 typically decreases the transition probability by 4 or 5 orders of magnitude. Excited nuclear states will thus tend to decay by the lowest allowed multipolarities, accounting for the observed predominance of dipole and quadrupole transitions in nuclei. In fact, the observation of electric quadrupole transitions in situations where dipole transitions are allowed only occurs because collective excitation modes often strongly enhance $E2$ transition rates (see below). For a given transition it is therefore usually necessary to consider only the lowest one or two multipolarities allowed by the selection rules. Parity-changing $|\Delta I| \leq 1$ transitions will generally be of $E1$ character, with negligible $M2, E3, \dots$ contributions, while parity-conserving transitions will be dominantly of $E2$ character

for $|\Delta I| = 2$ and, in general, a mixture of $M1$ and $E2$ for $|\Delta I| \leq 1$.

For the collective rotational wavefunctions of a deformed prolate nucleus with angular momentum projection K on the symmetry axis (Fig. 2.2), the $B(E2)$ values are related to the electric quadrupole moment Q_{20} by the expression [BM 75]

$$B(E2; I_i K \rightarrow I_f K) = \frac{5}{16\pi} Q_{20}^2 |\langle I_i K 20 | I_f K \rangle|^2. \quad (\text{A.9})$$

Defining $F = I_f$, the Clebsch-Gordon coefficients, and their high-spin ($F \gg 1$, $F \gg K$) asymptotic values, for the interesting cases of $F + 2 \rightarrow F$ and $F + 1 \rightarrow F$ transitions can be expressed in the analytic form [War 83]:

$$|\langle (F+2) K 20 | F K \rangle|^2 = \frac{3(F+K+1)(F+K+2)(F-K+2)(F-K+1)}{(2F+5)(2F+4)(2F+3)(F+1)} \longrightarrow \frac{3}{8}, \quad (\text{A.10})$$

$$|\langle (F+1) K 20 | F K \rangle|^2 = \frac{3(F+K+1)(F-K+1)K^2}{(F+2)(2F+3)(F+1)F} \longrightarrow \frac{3K^2}{2F^2}. \quad (\text{A.11})$$

Two interesting observations can be made from these expressions. Firstly, from Eq. 2.7 we note that, to first order, Q_{20} is proportional to β_2 so that the $B(E2)$ values and transition rates in rotational bands are approximately proportional to β_2^2 and can become very large (hundreds or even thousands of Weisskopf units) for highly deformed nuclei. Secondly, from the high-spin asymptotic values of the Clebsch-Gordon coefficients we note that $3/8 \gg 3K^2/2F^2$ when $F \gg K$ and, combined with the E_γ^5 factor in the expression for $T(E2)$ (Eq. A.6), it becomes clear that $I \rightarrow I - 2$, $E2$ transitions will dominate over $I \rightarrow I - 1$, $E2$ transitions in rotational bands, explaining the observed separation of $K \neq 0$ bands into two $\Delta I = 2$ sequences even when the two signatures are degenerate (of course, in some cases there may still be strong $M1$ transitions connecting the two signatures).

The equations given so far are most suited to the theorist, who would calculate a deformation for the nucleus, use this deformation in Eq. 2.7 to calculate Q_{20} , then

substitute the result in Eq. A.9 to obtain a $B(E2)$ value, and finally substitute this in Eq. A.6 to obtain a transition probability, the reciprocal of which gives the mean state lifetime. The experimentalist, on the other hand, reverses this procedure. The state lifetimes, and hence the transition probabilities, are the experimentally measurable quantities (see Section 3.4). Assuming the validity of the rotational model, a transition quadrupole moment Q_t is determined from these transition probabilities by the expression:

$$T(E2; IK \rightarrow (I-2)K) = 1.219 Q_t^2 E_\gamma^5 |\langle IK20 | (I-2)K \rangle|^2 \text{ ps}^{-1}, \quad (\text{A.12})$$

which results from substituting Eq. A.9 in Eq. A.6 and evaluating the constants with Q_t in eb and E_γ in MeV. Assuming that the nucleus is prolate, a β_2 value can then be deduced by substituting Q_t in Eq. 2.7. For the general case of a triaxial nucleus, Q_t is related to Q_{20} by [BM 75]

$$Q_t = Q_{20} \frac{\cos(\gamma + 30^\circ)}{\cos(30^\circ)}, \quad (\text{A.13})$$

and we note that Q_t does indeed go to zero for noncollective oblate ($\gamma = 60^\circ$) shapes where the “rotation” axis coincides with the symmetry axis of the nucleus. This dependence of Q_t on γ has particularly important consequences for the loss of collectivity in smoothly terminating bands, in which the nucleus is predicted to gradually change shape from prolate to oblate with increasing spin (see Section 2.5.1).

Appendix B

Symbols

The following is a list of the symbols used in this thesis. These symbols are, to a large extent, dictated by convention. Although this leads to multiple definitions in a number of cases, the meaning of a given symbol should always be clear from the context in which it is used.

α	Signature. (Section 2.3.2)
$\alpha_{\lambda\mu}$	Spherical harmonic coefficient in nuclear shape parametrization. (Section 2.1.1)
β	Velocity, as a fraction of the speed of light. (Section 3.2.3)
β	Quadrupole deformation parameter. (Section 2.1.1)
β_2	Quadrupole deformation parameter. (Section 2.1.1)
β_4	Hexadecapole deformation parameter. (Section 2.1.1)
γ	Quadrupole deformation parameter. (Section 2.1.1)
Δ	Pairing gap. (Section 2.4.1)
δ_{ij}	Kronecker delta, equal to unity if $i = j$, and zero otherwise. (Section 2.4.1)
ϵ	Single-particle energy. (Section 1.1.1)
ϵ	Detector efficiency. (Section 3.1.4)
ε	Nilsson deformation parameter. (Section 1.3.1)

ε_2	Nilsson deformation parameter. (Section 2.1.1)
ε_4	Nilsson deformation parameter. (Section 2.1.1)
$\tilde{\Theta}$	Euler angles. (Section 2.1.3)
κ	Nilsson potential parameter. (Section 2.2.1)
Λ	Projection of the single-particle orbital angular momentum on the 3-axis. (Fig. 2.2)
λ	Photon angular momentum. (Appendix A)
λ	Fermi energy. (Section 2.2.3)
λ	de Broglie wavelength. (Section 1.2.1)
μ	Reduced mass. (Section 1.2.1)
μ	Nilsson potential parameter. (Section 2.2.1)
μ	Photon magnetic substate quantum number. (Appendix A)
ν	Prefix to neutron configurations.
π	Prefix to proton configurations.
π	Parity.
ρ	Nuclear charge density. (Section 2.1.1)
Σ	Projection of the single-particle intrinsic spin on the 3-axis. (Fig. 2.2)
σ	Cross section. (Section 1.2.1)
τ	Mean lifetime. (Section 3.4.1)
ϕ	Single-particle wavefunction. (Section 1.1.1)
Ψ	Nuclear wavefunction. (Section 1.1)
Ω	Projection of the single-particle angular momentum on the 3-axis. (Fig. 2.2)
Ω	Detector solid angle. (Section 3.2)
ω	Oscillator frequency. (Section 1.3.1)
ω	Rotational frequency. (Section 2.1.2)

A	Nuclear mass number.
a	Nuclear “skin-thickness”. (Section 1.1.1)
a	Decoupling parameter. (Section 2.1.3)
B	Reduced transition matrix element. (Appendix A)
C	Nilsson potential parameter. (Section 2.2.1)
c	The velocity of light.
D	Nilsson potential parameter. (Section 2.2.1)
D	Wigner rotation function. (Section 2.2.1)
E	Generic energy.
e^ω	Single-particle energy in the rotating frame, i.e. the Routhian. (Section 2.3.3)
F	Spin of the final nuclear state in a transition. (Appendix A)
f	Gamma-ray coincidence fold. (Section 3.2)
G	Pairing strength parameter. (Section 2.4.1)
g	Level density. (Section 2.2.3)
H	Total γ -ray energy. (Section 3.2)
H	Nuclear Hamiltonian operator. (Section 1.1)
h	Single-particle Hamiltonian operator. (Section 1.1.1)
I	Total nuclear angular momentum.
\mathcal{J}	Generic moment of inertia. (Section 2.1.1)
$\mathcal{J}^{(1)}$	Kinematic moment of inertia. (Section 2.1.2)
$\mathcal{J}^{(2)}$	Dynamic moment of inertia. (Section 2.1.2)
j	Single-particle angular momentum. (Section 1.1.1)
K	Projection of the total nuclear angular momentum on the 3-axis. (Fig. 2.2)
K	Gamma-ray multiplicity. (Section 3.2)

l	Single-particle orbital angular momentum. The symbols s , p , d , f , g , h , ... are used to denote $l = 0, 1, 2, \dots$ (Section 1.1.1)
l	Angular momentum in a heavy-ion collision. (Section 1.2.1)
M	Projection of the total nuclear angular momentum on the laboratory frame x -axis. (Fig 2.2)
\mathcal{M}	Electromagnetic multipole operator. (Appendix A)
m	Nucleon mass. (Section 1.1)
m	Magnetic substate quantum number. (Appendix A)
N	Neutron number.
N	Principal oscillator quantum number. (Section 1.3.1)
n	Oscillator quantum number. (Section 1.3.1)
n	ADC channel number. (Section 3.1.4)
P_l	Legendre polynomial function. (Section 3.3.3)
Q	Energy released in a reaction. (Section 1.2.1)
Q_{20}	Electric quadrupole moment of the nucleus. (Section 2.1.1)
Q_t	Transition quadrupole moment. (Appendix A)
R	Rotational angular momentum. (Fig. 2.2)
$R(\theta, \phi)$	Function in spherical coordinates defining the nuclear surface. (Section 2.1.1)
R_0	Radius of a spherical nucleus, equal to $r_0 A^{1/3}$. (Section 1.1.1)
\mathcal{R}	The Routhian operator, i.e. the Hamiltonian in the rotating frame. (Section 2.3.1)
r_0	Nuclear radius parameter, ~ 1.2 fm. (Section 1.1.1)
s	Single-particle intrinsic angular momentum. (Section 1.1.1)
T	Transmission coefficient. (Section 1.2.1)
T	Kinetic energy. (Section 4.3)
T	Isospin. (Section 6.1)

T	Transition probability. (Appendix A)
U	Unitary rotation operator. (Section 2.3.1)
V	Mean field potential. (Section 1.1.1)
$v(i, j)$	Two-body interaction. (Section 1.1)
v	Nuclear recoil velocity. (Section 3.4.1)
W	Angular distribution function. (Section 3.3.3)
$Y_{\lambda\mu}$	Spherical harmonic function. (Section 2.1.1)
Z	Proton number.

Bibliography

- [Åbe 82] S. Åberg, *Physica Scripta* **25**, 23 (1982).
- [ÅFN 90] S. Åberg, H. Flocard, and W. Nazarewicz, *Ann. Rev. Nucl. Part. Sci* **40**, 439 (1990).
- [Afa 95] A.V. Afanasjev and I. Ragnarsson, *Nucl. Phys.* **A591**, 387 (1995).
- [Afa 96a] A.V. Afanasjev, J. König, and P. Ring, *Nucl. Phys.* **A608**, 107 (1996).
- [Afa 96b] A.V. Afanasjev and I. Ragnarsson, *Nucl. Phys.* **A608**, 176 (1996).
- [Afa 98] A.V. Afanasjev, I. Ragnarsson, and P. Ring, *Phys. Lett. B*, submitted, (1998).
- [Ale 72] T.K. Alexander, O. Häusser, A.B. McDonald, A.J. Ferguson, W.T. Diamond, and A.E. Litherland, *Nucl. Phys.* **A179**, 477 (1972).
- [And 76] G. Andersson, S.E. Larsson, G. Leander, P. Möller, S.G. Nilsson, I. Ragnarsson, S. Åberg, R. Bengtsson, J. Dudek, B. Nerlo-Pomorska, K. Pomorski, and Z. Szymański, *Nucl. Phys.* **A268**, 205 (1976).
- [Ari 77] A. Arima, T. Ohtsuka, F. Iachello, and I. Talmi, *Phys. Lett. B* **66**, 205 (1977).

- [Bak 85] C. Baktash, Y. Schutz, I.Y. Lee, F.K. McGowan, N.R. Johnson, M.L. Halbert, D.C. Hensley, M.P. Fewell, L. Courtney, A.J. Larabee, L.L. Riedinger, A.W. Sunyar, E. der Mateosian, O.C. Kistner, and D.G. Sarantites, *Phys. Rev. Lett.* **54**, 978 (1985).
- [Bak 95] C. Baktash, D.M. Cullen, J.D. Garrett, C.J. Gross, N.R. Johnson, W. Nazarewicz, D.G. Sarantites, J. Simpson, and T.R. Werner, *Phys. Rev. Lett.* **74**, 1946 (1995).
- [Bal 89] D.P. Balamuth, T. Chapuran, and J.W. Arrison, *Nucl. Instrum. Methods Phys. Res., Sect. A* **275**, 315 (1989).
- [Bas 80] R. Bass, *Nuclear Reactions with Heavy Ions*, Springer-Verlag, Berlin (1980).
- [Baz 94] D. Bazzacco, F. Brandolini, R. Burch, S. Lunardi, E. Maglione, N.H. Medina, P. Pavan, C. Rossi-Alvarez, G. de Angelis, D. De Acuna, M. De Poli, J. Rico, D. Bucurescu, and C. Ur, *Phys. Rev. C* **49**, R2281 (1994).
- [BCS 57] J. Bardeen, L.N. Cooper, and J.R. Schrieffer, *Phys. Rev.* **108**, 1175 (1957).
- [Bea 95] C.W. Beausang, D. Prevost, M.H. Berstrom, G. de France, B. Haas, J.C. Lisle, Ch. Theisen, J. Timár, P.J. Twin, and J.N. Wilson, *Nucl. Instrum. Methods Phys. Res., Sect. A* **364**, 560 (1995).
- [Bec 87] E.M. Beck, M.A. Deleplanque, R.M. Diamond, R.J. McDonald, F.S. Stephens, J.C. Bacelar, and J.E. Draper, *Z. Phys. A* **327**, 397 (1987).
- [Ben 75] R. Bengtsson, S.E. Larsson, G. Leander, P. Möller, S.G. Nilsson, S. Åberg, and Z. Szymański, *Phys. Lett. B* **57**, 301 (1975).
- [Ben 79] R. Bengtsson and S. Frauendorf, *Nucl. Phys. A* **327**, 139 (1979).

- [Ben 81] T. Bengtsson, M.E. Faber, G. Leander, P. Möller, M. Ploszajczak, I. Ragnarsson, and S. Åberg, *Physica Scripta* **24**, 200, (1981).
- [Ben 83] T. Bengtsson and I. Ragnarsson, *Physica Scripta* **T5**, 165 (1983).
- [Ben 85] T. Bengtsson and I. Ragnarsson, *Nucl. Phys.* **A436**, 14, (1985).
- [Ben 89] R. Bengtsson, J. Dudek, W. Nazarewicz, and P. Olanders, *Physica Scripta* **39**, 196 (1989).
- [Ber 94] G.F. Bertsch, *Nucl. Phys.* **A574**, 169c (1994).
- [BFM 86] R. Bengtsson, S. Frauendorf, and F.R. May, *Atomic Data and Nuclear Data Tables* **35**, 15 (1986).
- [BG 77] P.J. Brussaard and P.W.M. Glaudemans, *Shell-Model Applications in Nuclear Spectroscopy*, North Holland, Amsterdam, (1977).
- [BH 87] M.J. Berger and J.H. Hubbell, program xCOM, National Bureau of Standards Report No. NBSIR 87-3597, (1987).
- [Bla 66] A.E. Blaugrund, *Nucl. Phys.* **88**, 501 (1966).
- [BM 69] A. Bohr and B.R. Mottelson, *Nuclear Structure*, Benjamin, New York, Vol. 1, (1969).
- [BM 75] A. Bohr and B.R. Mottelson, *Nuclear Structure*, Benjamin, New York, Vol. 2, (1975).
- [BMP 58] A. Bohr, B.R. Mottelson, and D. Pines, *Phys. Rev.* **110**, 936 (1958).
- [Bog 58] N.N. Bogolyubov, *Nuovo Cimento Series 10* **7**, 794 (1958).

- [Bon 87] P. Bonche, H. Flocard, and P.H. Heenen, Nucl. Phys. **A467**, 115 (1987).
- [Bon 90] P. Bonche, J. Dobaczewski, H. Flocard, P.H. Heenen, S.J. Krieger, J. Meyer, and M.S. Weiss, Nucl. Phys. **A519**, 509 (1990).
- [Bra 98] F. Brandolini, S.M. Lenzi, D.R. Napoli, R.V. Ribas, H. Somacal, C.A. Ur, D. Bazzacco, J.A. Cameron, G. de Angelis, M. De Poli, A. Gadea, C. Fahlander, S. Lunardi, G. Martinez-Pinedo, N.H. Media, C. Rossi Alvarez, J. Sanchez-Solano, and C.E. Svensson, Nucl. Phys. **A**, in press, (1998).
- [Bru 76] J.F. Bruandet, Tsan Ung Chan, M. Agard, J.P. Longequeue, C. Morand, and A. Giorni, Z. Phys. A **279**, 69 (1976).
- [Cam 90] J.A. Cameron, M.A. Bentley, A.M. Bruce, R.A. Cunningham, W. Gelletly, H.G. Price, J. Simpson, D.D. Warner, and A.N. James, Phys. Lett. B **235**, 239 (1990).
- [Cam 96] J.A. Cameron, J. Jonkman, C.E. Svensson, M. Gupta, G. Hackman, D. Hyde, S.M. Mullins, J.L. Rodriguez, J.C. Waddington, A. Galindo-Uribarri, H.R. Andrews, G.C. Ball, V.P. Janzen, D.C. Radford, D. Ward, T.E. Drake, M. Cromaz, J.H. DeGraaf, and G. Zwartz, Phys. Lett. B **387**, 266 (1996).
- [Cam 98] J.A. Cameron, J.L. Rodriguez, J. Jonkman, G. Hackman, S.M. Mullins, C.E. Svensson, J.C. Waddington, L. Yao, T.E. Drake, M. Cromaz, J.H. DeGraaf, G. Zwartz, H.R. Andrews, G.C. Ball, A. Galindo-Uribarri, V.P. Janzen, D.C. Radford, and D. Ward, Phys. Rev. C. **58**, 808 (1998).
- [Can 79] M.J. Canty, P.A. Gottschalk, and F. Pühlhofer, Nucl. Phys. **A317**, 495 (1979).

- [Cas 90] R.F. Casten, *Nuclear Structure from a Simple Perspective*, Oxford University Press, New York (1990).
- [Cau 94] E. Caurier, A.P. Zuker, A. Poves, and G. Martínez-Pinedo, Phys. Rev. C **50**, 225 (1994).
- [Ced 95] B. Cederwall, I.Y. Lee, S. Asztalos, M.J. Brinkman, J.A. Becker, R.M. Clark, M.A. Deleplanque, R.M. Diamond, P. Fallon, L.P. Farris, E.A. Henry, J.R. Hughes, A.O. Macchiavelli, and F.S. Stephens, Nucl. Instrum. Methods Phys. Res., Sect. A **354**, 591 (1995).
- [Cha 83] R. Chapman, J.C. Lisle, J.N. Mo, E. Paul, A. Simcock, J.C. Willmott, J.R. Leslie, H.G. Price, P.M. Walker, J.C. Bacelar, J.D. Garrett, G.B. Hagemann, B. Herskind, A. Holm, and P.J. Nolan, Phys. Rev. Lett. **51**, 2265 (1983).
- [Cha 95] E. Chabanat, Ph.D. Thesis, Université Claude Bernard Lyon-1, (1995).
- [Cla 97] R.M. Clark, S.J. Asztalos, G. Baldsiefen, J.A. Becker, L. Bernstein, M.A. Deleplanque, R.M. Diamond, P. Fallon, I.M. Hibbert, H. Hübel, R. Krücken, I.Y. Lee, A.O. Macchiavelli, R.W. MacLeod, G. Schmid, F.S. Stephens, K. Vetter, R. Wadsworth, and S. Frauendorf, Phys. Rev. Lett. **78**, 1868 (1997).
- [Col 92] J.D. Cole, T.M. Cormier, J.H. Hamilton, and A.V. Ramayya, Nucl. Instrum. Methods Phys. Res., Sect. B **70**, 343 (1992).
- [Cro 95] B. Crowell, M.P. Carpenter, R.G. Henry, R.V.F. Janssens, T.L. Khoo, T. Lauritsen, and D. Nisius, Nucl. Instrum. Methods Phys. Res., Sect. A **355**, 575 (1995).

- [Dav 92] C.N. Davids, B.B. Back, K. Bindra, D.J. Henderson, W. Kutschera, T. Lauritsen, Y. Nagame, P. Sugathan, A.V. Ramayya, and W.B. Walters, Nucl. Instrum. Methods Phys. Res., Sect. B **70**, 358 (1992).
- [DD 88] M.A. Deleplanque and R.M. Diamond, *GAMMASPHERE, A National Gamma-Ray Facility*, Lawrence Berkeley National Laboratory Report No. LBL-PUB-5202, (1988).
- [Dea 97] D.J. Dean, in *Proceedings of the Conference on Nuclear Structure at the Limits*, Argonne National Laboratory Report No. ANL/PHY-91/1, p. 232, (1997).
- [Del 95] M.A. Deleplanque, S. Frauendorf, R.M. Clark, R.M. Diamond, F.S. Stephens, J.S. Becker, M.J. Brinkman, B. Cederwall, P. Fallon, L.P. Farris, E.A. Henry, H. Hubel, J.R. Hughes, W. Korten, I.Y. Lee, A.O. Macchiavelli, M.A. Stoyer, P. Willsau, J.E. Draper, C. Duyar, and E. Rubel, Phys. Rev. C **52**, R2302 (1995).
- [Dev 96] M. Devlin, L.G. Sobotka, D.G. Sarantites, and D.R. LaFosse, Nucl. Instrum. Methods Phys. Res., Sect. A **383**, 506 (1996).
- [DF 82] F. Dönau and S. Frauendorf, in *Proceedings of the International Conference on High angular Momentum Properties of Nuclei*, p. 143, Harwood Academic, New York, (1982).
- [Dob 98] J. Dobaczewski, W. Nazarewicz, W. Satulá, and C. Baktash, private communication (1998).
- [Døs 95a] T. Døssing and E. Vigezzi, Nucl. Phys. **A587**, 13 (1995).

- [Døs 95b] T. Døssing, T.L. Khoo, T. Lauritsen, I. Ahmad, D. Blumenthal, M.P. Carpenter, B. Crowell, D. Gassmann, R.G. Henry, R.V.F. Janssens, and D. Nisius, Phys. Rev. Lett. **75**, 1276 (1995).
- [DS 80] R.M. Diamond and F.S. Stephens, Ann. Rev. Nucl. Part. Sci **30**, 85 (1980).
- [Dud 81] J. Dudek, Z. Szymański, and T. Werner, Phys. Rev. C **23**, 920 (1981).
- [Dud 82] J. Dudek, A. Majhofer, W. Nazarewicz, and Z. Szymański, Phys. Lett. B **112**, 1 (1982).
- [Dud 87] J. Dudek, W. Nazarewicz, Z. Szymański, and G.A. Leander, Phys. Rev. Lett. **59**, 1405 (1987).
- [End 79] P.M. Endt, Atomic Data and Nuclear Data Tables, **23**, 547 (1979).
- [Enn 91] P.J. Ennis, C.J. Lister, W. Gelletly, H.G. Price, B.J. Varley, P.A. Butler, T. Hoare, S. Ćwiok, and W. Nazarewicz, Nucl. Phys. **A535**, 392 (1991).
- [FH 59] L.W. Fagg, and S.S. Hanna, Rev. Mod. Phys. **31**, 711 (1959).
- [Fir 96] R.B. Firestone, *Table of Isotopes, Eighth Edition*, John Wiley & Sons Inc., New York, Vol. 2, (1996).
- [Fli 92] S. Flibotte, U.J. Hüttmeier, P. Bednarczyk, G. de France, B. Hass. P. Romain, Ch. Theisen, J.P. Vivien, and J. Zen, Nucl. Instrum. Methods Phys. Res., Sect. A **320**, 325 (1992).
- [Fos 94] D.B. Fossan, D.R. LaFosse, H. Schnare, C.W. Beausang, K. Hauschild. I.M. Hibbert, J.R. Hughes, V.P. Janzen, S.M. Mullins, E.S. Paul, D.C. Radford, I. Ragnarsson, I. Thorslund, P. Vaska, R. Wadsworth, and M.P. Waring,

- in *Proceedings of the Conference on Physics from Large γ -Ray Detector Arrays*, Lawrence Berkeley National Laboratory Report No. LBL-35687, p. 194 (1994).
- [Fra 93] S. Frauendorf, Nucl. Phys. **A557**, 259c (1993).
- [Fur 97] K. Furutaka, T. Hayakawa, H. Nakada, Y. Hatsukawa, M. Kidera, M. Oshima, S. Mitarai, H. Kusakari, T. Komatsubara, M. Matsuda, and K. Furuno, Z. Phys. A **358**, 279 (1997).
- [Gal 92] A. Galindo-Uribarri, Prog. Part. Nucl. Phys. **28**, 463 (1992).
- [Gal 98] A. Galindo-Uribarri, D. Ward, G.C. Ball, V.P. Janzen, D.C. Radford. I. Ragnarsson, and D. Headly, Phys. Lett. B **422**, 45 (1998).
- [GC 65] A. Gilbert and A.G.W. Cameron, Can. J. Phys. **43**, 1446 (1965).
- [GG 71] J. Gilat and J.R. Grover, Phys. Rev. C. **3**, 734 (1971).
- [GM 96] W. Greiner and J.A. Maruhn, *Nuclear Models*, Springer-Verlag, Berlin (1996).
- [Hac 95a] G. Hackman, Ph.D. Thesis, McMaster University, (1995).
- [Hac 95b] G. Hackman and J.C. Waddington, Nucl. Instrum. Methods Phys. Res., Sect. A **357**, 559 (1995).
- [Hac 97] G. Hackman, T.L. Khoo, M.P. Carpenter, T. Lauritsen, A. Lopez-Martens. I.J. Calderin, R.V.F. Janssens, D. Ackermann, I. Ahmad, S. Agarwala, D.J. Blumenthal, S.M. Fischer, D. Nisius, P. Reiter, J. Young, H. Amro, E.F. Moore, F. Hannachi, A. Korichi, I.Y. Lee, A.O. Macchiavelli, T. Døssing, and T. Nakatsukasa, Phys. Rev. Lett. **79**, 4100 (1997).

- [Hac 98] G. Hackman, R.V.F. Janssens, E.F. Moore, D. Nisius, I. Ahmad, M.P. Carpenter, S.M. Fischer, T.L. Khoo, T. Lauritsen, and P. Reiter, *Phys. Lett. B* **416**, 268 (1998).
- [Has 94] D.S. Haslip, G. Hackman, and J.C. Waddington, *Nucl. Instrum. Methods Phys. Res., Sect. A* **345**, 534 (1994).
- [Hau 72] O. Häusser, A.J. Ferguson, A.B. McDonald, I.M. Szöghy, T.K. Alexander, and D.L. Disdier, *Nucl. Phys.* **A179**, 465 (1972).
- [Hau 97] K. Hauschild, L.A. Bernstein, J.A. Becker, D.E. Archer, R.W. Bauer, D.P. McNabb, J.A. Cizewski, K.Y. Ding, W. Younes, R. Krücken, R.M. Diamond, R.M. Clark, P. Fallon, I.Y. Lee, A.O. Macchiavelli, R. MacLeod, G.J. Schmid, M.A. Deleplanque, F.S. Stephens, and W.H. Kelly, *Phys. Rev. C* **55**, 2819 (1997).
- [Hee 98] P.H. Heenen and R.V.F. Janssens, *Phys. Rev. C* **57**, 159 (1998).
- [Hen 94] R. G. Henry, T. Lauritsen, T.L. Khoo, I. Ahmad, M.P. Carpenter, B. Crowell, T. Døssing, R.V.F. Janssens, F. Hannachi, A. Korichi, C. Schuck, F. Azaiez, C.W. Beausang, R. Beraud, C. Bourgeois, R.M. Clark, I. Deloncle, J. Duprat, B. Gall, H. Hubel, M.J. Joyce, M. Kaci, Y. Lecoq, M. Meyer, E.S. Paul, N. Perrin, N. Foffe, M.G. Porquet, N. Redon, H. Sergolle, J.F. Harpey-Schafer, J. Simpson, A. G. Smith, R. Wadsworth, and P. Willsau, *Phys. Rev. Lett.* **73**, 777 (1994).
- [Hil 79] D.L. Hillis, J.D. Garrett, O. Christensen, B. Fernandez, G.B. Hagemann, B. Herskind, B.B. Back, and F. Folkmann, *Nucl. Phys.* **A325** 216 (1979).
- [HJS 49] O. Haxel, J.H.D. Jensen, and H.E. Suess, *Phys. Rev.* **75**, 1766 (1949).

- [Hon 87] K.J. Honkanen, F.A. Dilmanian, D.G. Sarantites, and S.P. Sorensen, Nucl. Instrum. Methods Phys. Res., Sect. A **257**, 233 (1987).
- [HW 53] D.L. Hill and J.A. Wheeler, Phys. Rev. **89**, 1102 (1953).
- [Ing 54] D.R. Inglis, Phys. Rev. **96**, 1059 (1954).
- [Ing 56] D.R. Inglis, Phys. Rev. **103**, 1786 (1956).
- [Jam 88] A.N. James, T.P. Morrison, K.L. Ying, K.A. Connel, H.G. Price, and J. Simpson, Nucl. Instrum. Methods Phys. Res., Sect. A **267**, 144 (1988).
- [Jan 95] V.P. Janzen, D.R. LaFosse, H. Schnare, D.B. Fossan, A. Galindo-Uribarri, J.R. Hughes, S.M. Mullins, E.S. Paul, L. Persson, S. Pilotte, D.C. Radford, I. Ragnarsson, P. Vaska, J.C. Waddington, R. Wadsworth, D. Ward, J. Wilson, and R. Wyss, Phys. Rev. Lett. **72**, 1160 (1995).
- [Jan 97] V.P. Janzen, A.V. Afanasjev, H.R. Andrews, G.C. Ball, J.A. Cameron, M. Cromaz, J. DeGraaf, T.E. Drake, S. Flibotte, A. Galindo-Uribarri, G. Hackman, D.M. Headly, J. Jonkman, S. Mullins, D.C. Radford, I. Ragnarsson, J.L. Rodriguez, C.E. Svensson, J.C. Waddington, D. Ward, and G. Zwartz, in *Proceedings of the Conference on Nuclear Structure at the Limits*, Argonne National Laboratory Report No. ANL/PHY-91/1, p. 171. (1997).
- [JK 91] R.V.F. Janssens and T.L. Khoo, Annu. Rev. Nucl. Part. Sci. **41**, 321 (1991).
- [Joh 72] A. Johnson, H. Ryde, and S.A. Hjorth, Nucl. Phys. **A179**, 753 (1972).

- [Kho 93] T.L. Khoo, T. Lauritsen, I. Ahmad, M.P. Carpenter, P.B. Fernandez, R.V.F. Janssens, E.F. Moore, F.L.H. Wolfs, Ph. Benet, P.J. Daly, K.B. Beard, U. Garg, D. Ye, and M.W. Drigert, Nucl. Phys. **A557**, 83c (1993).
- [Kho 96] T.L. Khoo, M.P. Carpenter, T. Lauritsen, D. Ackermann, I. Ahmad, D.J. Blumenthal, S.M. Fischer, R.V.F. Janssens, D. Nisius, E.F. Moore, A. Lopez-Martens, T. Døssing, R. Krücken, S.J. Asztalos, J.A. Becker, L. Bernstein, R.M. Clark, M.A. Deleplanque, R.M. Diamond, P. Fallon, L.P. Farris, F. Hannachi, E.A. Henry, A. Korichi, I.Y. Lee, A.O. Macchiavelli, and F.S. Stephens, Phys. Rev. Lett. **76**, 1583 (1996).
- [Kin 93] M.M. King, Nucl. Data Sheets **69**, 1 (1993).
- [Kno 89] G.F. Knoll, *Radiation Detection and Measurement*, John Wiley & Sons, New York (1989).
- [Koe 89] W. Koepf and P. Ring, Nucl. Phys. **A493**, 61 (1989).
- [Kra 88] K.S. Krane, *Introductory Nuclear Physics*, John Wiley & Sons, New York (1988).
- [Krü 94] R. Krücken, A. Dewald, P. Sala, C. Meier, H. Tiesler, J. Altmann, K.O. Zell, P. von Brentano, D. Bazzacco, C. Rossi-Alvarez, R. Burch, R. Menegazzo, G. de Angelis, G. Maron, and M. de Poli, Phys. Rev. Lett. **73**, 3359 (1994).
- [Krü 96] R. Krücken, A. Dewald, P. von Brentano, D. Bazzacco, and C. Rossi-Alvarez, Phys. Rev. C **54**, 1182 (1996).
- [Krü 97] R. Krücken, S.J. Asztalos, J.A. Becker, B. Busse, R.M. Clark, M.A. Deleplanque, A. Dewald, R.M. Diamond, P. Fallon, K. Hauschild, I.Y. Lee, A.O.

- Macchiavelli, R.W. MacLeod, R. Peusquens, G.J. Schmid, F.S. Stephens, K. Vetter, and P. von Brentano, *Phys. Rev. C* **55**, R1625 (1997).
- [Lal 97] G.A. Lalazissis, J. König, and P. Ring, *Phys. Rev. C* **55**, 540 (1997).
- [Lau 92] T. Lauritsen, Ph. Benet, T.L. Khoo, K.B. Beard, I. Ahmad, M.P. Carpenter, P.J. Daly, M.W. Drigert, U. Garg, P.B. Fernandez, R.V.F. Janssens, E.F. Moore, F.L.H. Wolfs, and D. Ye, *Phys. Rev. Lett.* **69**, 2479 (1992).
- [Lau 97] T. Lauritsen, G. Hackman, T.L. Khoo, M.P. Carpenter, R.V.F. Janssens, A. Lopez-Martens, D. Ackermann, I. Ahmad, H. Amro, D.J. Blumenthal, S.M. Fischer, D.T. Nisius, F. Hannachi, A. Korichi, and E.F. Moore, *Heavy Ion Physics* **6**, 229 (1997).
- [Lee 90] I.-Y. Lee, *Nucl. Phys.* **A520**, 641c (1990).
- [Len 96] S.M. Lenzi, D.R. Napoli, A. Gadea, M.A. Cardona, D. Hojman, M.A. Nagarajan, C. Rossi-Alvarez, N.H. Medina, G. de Angelis, D. Bazzacco, M.E. Debray, M. De Poli, S. Lunardi, and D. de Acuña, *Z. Phys. A* **354**, 117 (1996).
- [Len 97] S.M. Lenzi, C.A. Ur, D.R. Napoli, M.A. Nagarajan, D. Bazzacco, D.M. Brink, M.A. Cardona, G. de Angelis, M. De Poli, A. Gadea, D. Hojman, S. Lunardi, N.H. Medina, and C. Rossi-Alvarez, *Phys. Rev. C* **56**, 1313 (1997).
- [Leo 87] W.R. Leo, *Techniques for Nuclear and Particle Physics Experiments*. Springer-Verlag, Berlin (1987).
- [Lop 96a] A. Lopez-Martens, F. Hannachi, A. Korichi, C. Schück, E. Gueorguieva, Ch. Vieu, B. Hass, R. Lucas, A. Astier, G. Baldsiefen, M.P. Carpenter,

- G. de France, R. Duffait, L. Ducroux, Y. Le Coz, Ch. Finck, A. Gorgen, H. Hübel, T.L. Khoo, T. Lauritsen, M. Meyer, D. Prévost, N. Redon, C. Rigollet, H. Savajols, J.F. Sharpey-Schafer, O. Stezowski, Ch. Theisen, U. Van Severen, J.P. Vivien, and A.N. Wilson, *Phys. Lett. B* **380**, 18 (1996).
- [Lop 96b] A. Lopez-Martens, F. Hannachi, T. Døssing, C. Schück, R. Collatz, E. Gueorguieva, Ch. Vieu, S. Leoni, B. Herskind, T.L. Khoo, T. Lauritsen, I. Ahmad, D.J. Blumenthal, M.P. Carpenter, D. Gassmann, R.V.F. Janssens, D. Nisius, A. Korichi, C. Bourgeois, A. Astier, L. Ducroux, Y. Le Coz, M. Meyer, N. Redon, J.F. Sharpey-Schafer, A.N. Wilson, W. Korten, A. Bracco, and R. Lucas, *Phys. Rev. Lett.* **77**, 1707 (1996).
- [Lun 95] S. Lunardi, R. Venturelli, D. Bazzacco, C.M. Petrache, C. Rossi-Alvarez, G. de Angelis, G. Vedovato, D. Bucurescu, and C. Ur, *Phys. Rev. C* **52**, R6 (1995).
- [LVH 70] K.E.G. Löbner, M. Vetter, and V. Hönig, *Nucl. Data Tables* **A7**, 495 (1970).
- [Mac 94] A.O. Macchiavelli, I.Y. Lee, B. Cederwall, R.M. Clark, M.A. Deleplanque, R.M. Diamond, P. Fallon, and F.S. Stephens, in *Proceedings of the Conference on Physics from Large γ -Ray Detector Arrays*, Lawrence Berkeley National Laboratory Report No. LBL-35687, p. 149 (1994).
- [Mac 98] A.O. Macchiavelli, R.M. Clark, P. Fallon, M.A. Deleplanque, R.M. Diamond, R. Krücken, I.Y. Lee, F.S. Stephens, S. Asztalos, and K. Vetter, *Phys. Rev. C* **57**, R1073 (1998).

- [Maj 87] Z. Majka, D.G. Sarantites, L.G. Sobotka, K. Honkanen, E.L. Dines, L.A. Adler, L. Ze, M.L. Halbert, J.R. Beene, D.C. Hensley, R.P. Schmitt, and G. Nebbia, *Phys. Rev. Lett.* **58**, 322 (1987).
- [Mar 97] G. Martínez-Pinedo, A.P. Zuker, A. Poves, and E. Caurier, *Phys. Rev. C* **55**, 187 (1997).
- [May 49] M.G. Mayer, *Phys. Rev.* **75**, 1969 (1949).
- [Moo 89] E.F. Moore, R.V.F. Janssens, R.R. Chasman, I. Ahmad, T.L. Khoo, F.L.H. Wolfs, D. Ye, K.B. Beard, U. Garg, M.W. Drigert, Ph. Benet, Z.W. Grabowski, and J.A. Cizewski, *Phys. Rev. Lett.* **63**, 360 (1989).
- [Moo 97] E.F. Moore, T. Lauritsen, R.V.F. Janssens, T.L. Khoo, D. Ackermann, I. Ahmad, H. Amro, D. Blumenthal, M.P. Carpenter, S.M. Fischer, G. Hackman, D. Nisius, F. Hannachi, A. Lopez-Martens, A. Korichi, S. Asztalos, R.M. Clark, M.A. Deleplanque, R.M. Diamond, P. Fallon, I.Y. Lee, A.O. Macchiavelli, F.S. Stephens, J.A. Becker, L. Bernstein, L.P. Farris, and E.A. Henry, *Phys. Rev. C* **55**, R2150 (1997).
- [Mot 60] B.R. Mottelson and J.G. Valatin, *Phys. Rev. Lett.* **5**, 511 (1960).
- [MS 74] E. der Mateosian and A.W. Sunyar, *Atomic Data and Nuclear Data Tables* **13**, 407 (1974).
- [Mul 79] L. Mulligan, R.W. Zurmühle, and D.P. Balamuth, *Phys. Rev. C* **19**, 1295 (1979).
- [Mül 82] E.M. Müller, K. Mühlhans, K. Neergård, and U. Mosel, *Nucl. Phys.* **A383**, 233 (1982).

- [Naz 85] W. Nazarewicz, J. Dudek, R. Bengtsson, T. Bengtsson, and I. Ragnarsson, Nucl. Phys. **A435**, 397 (1985).
- [Nee 75] K. Neergård and V.V. Pashkevich, Phys. Lett. B **59**, 218 (1975).
- [Nic 90] N.G. Nicolis, D.G. Sarantites, L.A. Adler, F.A. Dilmanian, K. Honkanen, Z. Majka, L.G. Sobotka, Z. Li, T.M. Semkow, J.R. Beene, M.L. Halbert, D.C. Hensley, J.B. Naowitz, R.P. Schmitt, D. Fabris, G. Nebbia, and G. Mouchaty, Phys. Rev. C **41**, 2118 (1990).
- [Nil 55] S.G. Nilsson, Mat. Fys. Medd. Dan. Vid. Selsk. **29**, No. 16 (1955).
- [Nil 69] S.G. Nilsson, C.F. Tsang, A. Sobiczewski, Z. Szymański, S. Wycech, C. Gustafson, I.L. Lamm, P. Möller, and B. Nilsson, Nucl. Phys. **A131**, 1 (1969).
- [Nol 85] P. Nolan, A. Kirwan, D.J.G. Love, A.H. Nelson, D.J. Unwin, and P.J. Twin, J. Phys. G **11**, L17 (1985).
- [NS 70] L.C. Northcliffe and R.F. Schilling, Nucl. Data. Tables **A7**, 233 (1970).
- [Nya 84] B.M. Nyakó, J.R. Cresswell, P.D. Forsyth, D. Howe, P.J. Nolan, M.A. Riley, J.F. Sharpey-Schafer, J. Simpson, N.J. Ward, and P.J. Twin, Phys. Rev. Lett. **52** 507 (1984).
- [Nyb 92] J. Nyberg, D. Seweryniak, C. Fahlander, P. Unsua-Cao, A. Johnson, E. Adamides, A. Atac, B. Cederwall, E. Ideguchi, R. Julin, S. Juutinen, W. Karczmarczyk, J. Kownacki, S. Mitarai, L.-O. Norlin, M. Piiparinen, R. cshubaart, S. Törmänen, and A. Virtanen, *Proceedings of the Conference on Nuclear Structure at High Angular Momentum*, Atomic Energy of Canada Limited Report No. AECL 10613, p. 423, (1992).

- [OLe 97] C.D. O'Leary, M.A. Bentley, D.E. Appelbe, D.M. Cullen, S. Ertürk. R.A. Bark, A. Maj, and T. Saitoh, *Phys. Rev. Lett.* **79**, 4349 (1997).
- [Pal 85] G. Palameta and J.C. Waddington, *Nucl. Instrum. Methods Phys. Res., Sect. A* **234**, 476 (1985).
- [Pau 95] E.S. Paul, P.J. Woods, T. Davinson, R.D. Page, P.J. Sellin, C.W. Beausang, R.M. Clark, R.A. Cunningham, S.A. Forbes, D.B. Fossan, A. Gizon. J. Gizon, K. Hauschild, I.M. Hibbert, A.N. Jamies, D.R. LaFosse, I. Lazarus. H. Schnare, J. Simpson, R. Wadsworth, and M.P. Waring, *Phys. Rev. C* **51**, 78 (1995).
- [PB 75] M.A. Preston and R.K. Bhaduri, *Structure of the Nucleus*. Addison-Wesley. Reading (1975).
- [Per 62] V.P. Pereygin, S.P. Almazova, B.A. Gvozdev, and Yu. T. Chuburkov. *Sov. Phys. JETP* **15**, 1022 (1962).
- [Pet 96] C.M. Petrache, D. Bazzacco, S. Lunardi, C. Rossi-Alvarez, R. Venturelli. P. Pavan, N.H. Medina, M.N. Rao, R. Burch, G. de Angelis, A. Gadea. G. Maron, D.R. Napoli, L. Zhu, and R. Wyss, *Phys. Rev. Lett.* **77**, 239 (1996).
- [Pol 62] S.M. Polikanov, V.A. Druin, V.A. Karnaukhov, V.L. Mikheev, A.A. Pleve. N.K. Skobelev, V.G. Subbotin, G.M. Ter-Akop'yan, and V.A. Fomichev. *Sov. Phys. JETP* **15**, 1016 (1962).
- [Rad 93] D.C. Radford, A. Galindo-Uribarri, G. Hackman, and V.P. Janzen. *Nucl. Phys.* **A557**, 311c (1993).
- [Rad 95a] D.C. Radford, *Nucl. Instrum. Methods Phys. Res., Sect. A* **361**, 297 (1995).

- [Rad 95b] D.C. Radford, Nucl. Instrum. Methods Phys. Res., Sect. A **361**, 306 (1995).
- [Rad 98] D.C. Radford, in *Proceedings of the Nuclear Structure 98 Conference*. in press, (1998).
- [Rag 81] I. Ragnarsson, S. Åberg, and R. K. Sheline, Physica Scripta **24**, 215 (1981).
- [Rag 85] I. Ragnarsson, T. Bengtsson, W. Nazarewicz, J. Dudek, and G.A. Leander, Phys. Rev. Lett. **54**, 982 (1985).
- [Rag 86] I. Ragnarsson, Z. Xing, T. Bengtsson, and M.A. Riley, Physica Scripta **34**, 651 (1986).
- [Rag 90] I. Ragnarsson, in *Proceedings of the Workshop on the Science of Intense Radioactive Ion Beams*, Los Alamos National Laboratory Report LA-11964-C, p. 199 (1990).
- [Rag 95] I. Ragnarsson, V.P. Janzen, D.B. Fossan, N.C. Schmeing, and R. Wadsworth, Phys. Rev. Lett. **74**, 3935 (1995).
- [Rag 97] I. Ragnarsson and A.V. Afanasjev, private communication (1997).
- [Rei 86] P.-G. Reinhard, M. Rufa, J. Maruhn, W. Greiner, and J. Friedrich, Z. Phys. A **323**, 13 (1986).
- [Rod 98] T. Rodinger, D.S. Haslip, C.E. Svensson, and J.C. Waddington, Nucl. Instrum. Methods Phys. Res., Sect. A, submitted, (1998).
- [RS 80] P. Ring and P. Schuck, *The Nuclear Many-Body Problem*, Springer-Verlag, New York (1980).

- [Rud 96] D. Rudolph, C.J. Gross, J.A. Sheikh, D.D. Warner, I.G. Bearden, R.A. Cunningham, D. Foltescu, W. Gelletly, F. Hannachi, A. Harder, T.D. Johnson, A. Jungclaus, M.K. Kabadiyski, D. Kast, K.P. Lieb, H.A. Roth, T. Shizuma, J. Simpson, O. Skeppstedt, B.J. Varley, and M. Weiszflog, *Phys. Rev. Lett.* **76**, 376 (1996).
- [Rud 97] D. Rudolph, C. Baktash, M.J. Brinkman, M. Devlin, H.-Q. Jin, D.R. LaFosse, M. Leddy, I.Y. Lee, A.O. Macchiavelli, L.L. Riedinger, D.G. Sarantites, and C.-H. Yu, *Z. Phys. A* **358**, 379 (1997).
- [Rud 98] D. Rudolph, C. Baktash, J. Dobaczewski, W. Nazarewicz, W. Satula, M.J. Brinkman, M. Devlin, H.-Q. Jin, D.R. LaFosse, L.L. Riedinger, D.G. Sarantites, and C.-H. Yu, *Phys. Rev. Lett.* **80**, 14 (1998).
- [Sar 96] D.G. Sarantites, P.-F. Hua, M. Devlin, L.G. Sobotka, J. Elson, J.T. Hood, D.R. LaFosse, J.E. Sarantites, and M.R. Maier, *Nucl. Instrum. Methods Phys. Res., Sect. A* **381**, 418 (1996).
- [Sav 96] H. Savajols, A. Korichi, D. Ward, D. Appelbe, G.C. Ball, C. Beausang, F.A. Beck, T. Byrski, D. Curien, P. Dagnall, G. de France, D. Disdier, G. Duchêne, S. Erturk, C. Finck, S. Flibotte, B. Gall, A. Galindo-Uribarri, B. Hass, G. Hackman, V.P. Janzen, B. Kharraja, J.C. Lisle, J.C. Merdinger, S.M. Mullins, S. Pilotte, D. Prévost, D.C. Radford, V. Rauch, C. Rigollet, D. Smalley, M.B. Smith, O. Stezowski, J. Styczen, Ch. Theisen, P.J. Twin, J.P. Vivien, J.C. Waddington, K. Zuber, and I. Ragnarsson, *Phys. Rev. Lett.* **76**, 4480 (1996).
- [Sch 89] R.B. Schubank, J.A. Cameron, and V.P. Janzen, *Phys. Rev. C* **40**, 2310 (1989).

- [Sch 98] G.J. Schmid, A.O. Macchiavelli, S.J. Asztalos, R.M. Clark, M.A. Deleplanque, R.M. Diamond, P. Fallon, R. Kruecken, I.Y. Lee, R.W. MacLeod, F.S. Stephens, and K. Vetter, *Nucl. Instrum. Methods Phys. Res., Sect. A* **417**, 95 (1998).
- [Sew 94] D. Seweryniak, J. Nyberg, C. Fahlander, and A. Johnson, *Nucl. Instrum. Methods Phys. Res., Sect. A* **340**, 353 (1994).
- [Sha 93] M.M. Sharma, M.A. Nagarajan, and P. Ring, *Phys. Lett. B* **312**, 277 (1993).
- [She 72] R.K. Sheline, I. Ragnarsson, and S.G. Nilsson, *Phys. Lett. B* **41**, 115 (1972).
- [She 90] J.A. Sheikh, N. Rowley, M.A. Nagarajan, and H.G. Price, *Phys. Rev. Lett.* **64**, 376 (1990).
- [She 91] R.K. Sheline, P.C. Sood, and I. Ragnarsson, *Int. J. Mod. Phys. A* **6**, 5057 (1991).
- [Shi 92] Y.R. Shimizu, F. Barranco, R.A. Broglia, T. Døssing, and E. Vigezzi, *Phys. Lett. B* **274**, 253 (1992).
- [Shi 93] Y.R. Shimizu, E. Vigezzi, T. Døssing, and R.A. Broglia, *Nucl. Phys. A* **557**, 99c (1993).
- [Sie 77] S.H. Sie, D. Ward, J.S. Geiger, R.L. Graham, and H.R. Andrews, *Nucl. Phys. A* **291**, 443 (1977).
- [Sin 96] B. Singh, R.B. Firestone, and S.Y.F. Chu, *Nucl. Data Sheets* **78**, 1 (1996).
- [Sko 98] S. Skoda, T. Steinhardt, F. Becker, J. Eberth, U. Hermkens, O. Thelen, H.B. Thomas, D. Weisshaar, D. Rudolph, Ch. Fischbeck, D. Gassmann,

- P.G. Thirolf, C. Baktash, D.J. Dean, S.D. Paul, M.M. Aleonard, F. Bourguine, J.N. Scheurer, B. Cederwall, D.M. Cullen, D.S. Haslip, C.E. Svensson, J.C. Waddington, J.N. Wilson, W. Weintraub, D.R. LaFosse, D.G. Sarantites, G. de Angelis, C. Fahlander, A. Gadea, E. Farnea, C. Ur, and M. Weiszflog, *Phys. Rev. Lett.*, submitted, (1998).
- [Sky 59] T.H.R. Skyrme, *Nucl. Phys.* **9**, 615 (1959).
- [Spe 72] H.J. Specht, J. Weber, E. Konecny, and D. Heunemann, *Phys. Lett. B* **41**, 43 (1972).
- [Ste 72] F.S. Stephens and R.S. Simon, *Nucl. Phys.* **A183**, 257 (1972).
- [Ste 85] F.S. Stephens, M.A. Deleplanque, R.M. Diamond, A.O. Macchiavelli, and J.E. Draper, *Phys. Rev. Lett.* **54**, 2584 (1985).
- [Str 67] V.M. Strutinsky, *Nucl. Phys.* **A95**, 420 (1967).
- [Str 68] V.M. Strutinsky, *Nucl. Phys.* **A122**, 1 (1968).
- [Str 90] D.W. Stracener, D.G. Sarantites, L.G. Sobotka, J. Elson, J.T. Hood, Z. Majka, V. Abenante, A. Chbihi, and D.C. Hensley, *Nucl. Instrum. Methods Phys. Res., Sect. A* **294**, 485 (1990).
- [Sve 97a] C.E. Svensson, J.A. Cameron, S. Flibotte, G. Gervais, D.S. Haslip, J.M. Nieminen, J.C. Waddington, J.N. Wilson, G.C. Ball, A. Galindo-Uribarri, V.P. Janzen, D.C. Radford, D. Ward, M. Cromaz, and T.E. Drake, *Nucl. Instrum. Methods Phys. Res., Sect. A* **396**, 228 (1997).
- [Sve 97b] C.E. Svensson, J.A. Cameron, S. Flibotte, G. Gervais, D.S. Haslip, J.M. Nieminen, J.C. Waddington, J.N. Wilson, G.C. Ball, A. Galindo-Uribarri,

- V.P. Janzen, D.C. Radford, D. Ward, M. Cromaz, and T.E. Drake, in *Proceedings of the Conference on Nuclear Structure at the Limits*, Argonne National Laboratory Report No. ANL/PHY-97/1, p. 209 (1997).
- [Sve 97c] C.E. Svensson, C. Baktash, J.A. Cameron, M. Devlin, J. Eberth, S. Flibotte, D.S. Haslip, D.R. LaFosse, I.Y. Lee, A.O. Macchiavelli, R.W. MacLeod, J.M. Nieminen, S.D. Paul, L.L. Riedinger, D. Rudolph, D.G. Sarantites, H.G. Thomas, J.C. Waddington, W. Weintraub, J.N. Wilson, A.V. Afanasjev, and I. Ragnarsson, *Phys. Rev. Lett.* **79**, 1233 (1997).
- [Sve 98a] C.E. Svensson, C. Baktash, G.C. Ball, J.A. Cameron, M. Devlin, J. Eberth, S. Flibotte, A. Galindo-Uribarri, D.S. Haslip, V.P. Janzen, D.R. LaFosse, I.Y. Lee, A.O. Macchiavelli, R.W. MacLeod, J.M. Nieminen, S.D. Paul, D.C. Radford, L.L. Riedinger, D. Rudolph, D.G. Sarantites, H.G. Thomas, J.C. Waddington, D. Ward, W. Weintraub, J.N. Wilson, A.V. Afanasjev, and I. Ragnarsson, *Phys. Rev. Lett.* **80**, 2558 (1998).
- [Sve 98b] C.E. Svensson, D. Rudolph, C. Baktash, M.A. Bentley, J.A. Cameron, M.P. Carpenter, M. Devlin, J. Eberth, S. Flibotte, A. Galindo-Uribarri, G. Hackman, D.S. Haslip, R.V.F. Janssens, D.R. LaFosse, T.J. Lampman, I.Y. Lee, F. Lerma, A.O. Macchiavelli, J.M. Nieminen, S.D. Paul, D.C. Radford, P. Reiter, L.L. Riedinger, D.G. Sarantites, B. Schaly, D. Seweryniak, O. Thelen, H.G. Thomas, J.C. Waddington, D. Ward, W. Weintraub, J.N. Wilson, C.H. Yu, A.V. Afanasjev, and I. Ragnarsson, *Phys. Rev. Lett.*, submitted, (1998).
- [Sve 98c] C.E. Svensson, S.M. Lenzi, D.R. Napoli, A. Poves, C.A. Ur, D. Bazzacco, F. Brandolini, J.A. Cameron, G. de Angelis, A. Gadea, D.S. Haslip, S.

- Lunardi, E.E. Maqueda, G. Martínez-Pinedo, M.A. Nagarajan, C. Rossi Alvarez, A. Vitturi, and J.C. Waddington, *Phys. Rev. C* **58**, R2621 (1998).
- [Sve 98d] C.E. Svensson, in *Proceedings of the Nuclear Structure 98 Conference*, in press, (1998).
- [Szy83] Z. Szymański, *Fast Nuclear Rotations*, Clarendon Press, Oxford, (1983).
- [TA 81] T. Troudet and R. Arvieu, *Annals of Physics* **134**, 1 (1981).
- [Tar 83] P. Taras, J.C. Waddington, H.R. Andrews, and D. Ward, *The 8π Spectrometer - Proposal for a National Facility*, Atomic Energy of Canada Limited Report No. AECL-8329, (1983).
- [Tjø 85] P.O. Tjøm, R.M. Diamond, J.C. Bacelar, E.M. Beck, M.A. Deleplanque, J.E. Draper, and F.S. Stephens, *Phys. Rev. Lett.* **55**, 2405 (1985).
- [Twi 86] P.J. Twin, B.M. Nyakó, A.H. Nelson, J. Simpson, M.A. Bentley, H.W. Cranmer-Gordon, P.D. Forsyth, D. Howe, A.R. Mokhtar, J.D. Morrison, J.F. Sharpey-Schafer, and G. Sletten, *Phys. Rev. Lett.* **57**, 811 (1986).
- [Vig 90a] E. Vigezzi, R.A. Broglia, and T. Døssing, *Phys. Lett. B* **249**, 163 (1990).
- [Vig 90b] E. Vigezzi, R.A. Broglia, and T. Døssing, *Nucl. Phys.* **A520**, 179c (1990).
- [Wad 98] R. Wadsworth, R.M. Clark, J.A. Cameron, D.B. Fossan, I.M. Hibbert, V.P. Janzen, R. Krücken, G.J. Lane, I.Y. Lee, A.O. Macchiavelli, C.M. Parry, J.M. Sears, J.F. Smith, A.V. Afanasjev, and I. Ragnarsson, *Phys. Rev. Lett.* **80**, 1174 (1998).
- [War 69] E.K. Warburton and J. Weneser, in *Isospin in Nuclear Physics*, ed. D.H. Wilkinson, North-Holland, Amsterdam (1969), Ch. 5.

- [War 81] N.J. Ward, L.P. Ekström, G.D. Jones, F. Kearns, T.P. Morrison, O.M. Mustaffa, D.N. Simister, P.J. Twin, and R. Wadsworth, *J. Phys. G.* **7**, 815 (1981).
- [War 83] D. Ward, H.R. Andrews, B. Haas, P. Taras, and N. Rud, *Nucl. Phys.* **A397**, 161 (1983).
- [War 91] D. Ward, V.P. Janzen, H.R. Andrews, D.C. Radford, G.C. Ball, D. Horn. J.C. Waddington, J.K. Johansson, F. Banville, J. Gascon, S. Monaro. N. Nadon, S. Pilotte, D. Prevost, P. Taras, and R. Wyss, *Nucl. Phys.* **A529**, 315 (1991).
- [WD 92] T.R. Werner and J. Dudek, *Atomic Data and Nuclear Data Tables* **50**, 179 (1992).
- [WD 97] P.J. Woods and C.N. Davids, *Annu. Rev. Nucl. Part. Sci.* **47**, 541 (1997).
- [Wei 51] V.F. Weisskopf, *Phys. Rev.* **83**, 1073 (1951).
- [Wil 94] J.N. Wilson, Ph.D. Thesis, University of Liverpool, (1994).
- [Wil 97] J.N. Wilson, R.A.E. Austin, D.S. Haslip, and J.C. Waddington, *Nucl. Instrum. Methods Phys. Res., Sect. A* **399**, 147 (1997).
- [Wil 98] J.N. Wilson, R.A.E. Austin, G.C. Ball, J. DeGraaf, M. Cromaz, S. Flibotte. A. Galindo-Uribarri, G. Gervais, D.S. Haslip, V.P. Janzen, S.M. Mullins. J.M. Nieminen, D.C. Radford, C.E. Svensson, D. Ward, and J.C. Waddington, *Phys. Rev. C* **57**, R2090 (1998).
- [WS 54] R.D. Woods and D.S. Saxon, *Phys. Rev.* **95**, 557 (1954).
- [Yam 67] T. Yamazaki, *Nuclear Data A* **3**, 1 (1967).

- [Yam 98] M. Yamagami and K. Matsuyanagi, in *Proceedings of the Nuclear Structure 98 Conference*, in press, (1998).
- [Yu 98] C.-H. Yu, private communication, (1998).
- [Zaw 78] D. Zawischa, J. Speth, and D. Pal, Nucl. Phys. **A311**, 445 (1978).
- [ZC 74] J.F. Ziegler and W.K Chu, Atomic Data and Nuclear Data Tables **13**, 463 (1974).